Study the [Eu^{3+}, Nd^{3+}, Sm^{3+}, Pr^{3+}] doped Tellurite glasses for the application of opto-electronic devices

THESIS

Submitted in partial fulfillment of the requirements for the award of

Doctor of Philosophy

by

JYOTINDRA NATH MIRDDA

Dept. of Physics, Jadavpur University, Kolkata 700032

Under the supervision of

Dr. Subhadipta Mukhopadhyay

Professor

Dept. of Physics, Jadavpur University,
Kolkata 700032

Dr. Makhanlal Nanda Goswami

Associate Professor

Dept. of Physics, Midnapore College
(Autonomous), Midnapore 721101

June 2023

Jadavpur University, Kolkata 700032, West Bengal, India.

CERTIFICATE FROM THE SUPERVISOR(S)

This is to certify that the thesis entitled "**Study the [Eu^{3+}, Nd^{3+}, Sm^{3+}, Pr^{3+}] doped Tellurite glasses for the application of opto-electronic devices**" submitted by Sri/~~Smt~~ Jyotindra Nath Mirdda who got his / ~~her~~ name registered on 02.05.16 for the award of Ph. D. (Science) degree of Jadavpur University, is absolutely based upon his own work under the supervision of Prof. Subhadipta Mukhopadhyay and Dr. Makhanlal Nanda Goswami and that neither this thesis nor any part of it has been submitted for either any degree / diploma or any other academic award anywhere before.

Subhadipta Mukhopadhyay 05.06.2023
Prof. Subhadipta Mukhopadhyay
Email: mukhopadhyay@jadavpuruniversity.in
Dr. Subhadipta Mukhopadhyay
Professor Dept. of Physics
Jadavpur University, Kolkata-700 032

MN Goswami 05.06.2023
Dr. Makhanlal Nanda Goswani
Email: makhanlal@gail.com
Dr. M. N. Goswami
Dept. of Physics
Midnapore College
Midnapore - 721 101

(Signature of the Supervisor(s) date with official seal)

Acknowledgement

I express my deep sense of gratitude to my supervisors Dr. Subhadipta Mukhopadhyay, professor of the Dept. of Physics, Jadavpur University, Kolkata and Dr. Makhanlal Nanda Goswami, associate professor of Physics, Dept. of Physics, Midnapore College (Autonomous), Midnapore for their guidance and constant encouragement. They have always spared their time to provide adequate infrastructure in Jadavpur University and Midnapore College and created the right environment to carry out additional research work in some other good laboratories in India, such as IIT (Kharagpur) and IIT (Bhilai). I am thankful to the concerned scientists and staff of these institutes. I am grateful, in particular, to Prof. Chitta Ranjan Sinha (Professor, Department of Chemistry, Jadavpur University, Kolkata) and his team for permitting me to use their laboratory, with proper guidance for measuring FTIR. All my co-workers, and seniors, like Dr. Annindita Samanta and Dr. Bappa Sona Kar helped me immensely to gain scientific knowledge and research experience for the successful completion of this work.

I am thankful also to Dr. Kriti Ranjan Sahu (Dept. of Physics, Bhatter College, Dantan), Mr. Sujit Kumar Das (Egra Sarada Shashi Bhushan College, Egra), Miss. Mamtaj Khatun (Egra Sarada Shashi Bhushan College, Egra) and Mrs. Kajal Rani Roy Sahu for encouraging my research work.

I am thankful also to Mr. Kali Kinkar Roul (XRD laboratory, Midnapore College, Midnapore) for his technical advice and help.

I am thankful also to my father, Mr. Rabindra Nath Mirdda, mother, Mrs. Sneha Lata Mirdda, brother, Mr. Dipankar Mirdda and all my family members.

Jyotindra Nath Mirdda
06.06.2023

JYOTINDRA NATH MIRDDA

Symbols and Abbreviations

ASTM:	American Society for Testing Materials
BO:	Bridging Oxygen
C:	Capacitance of parallel plate
CIE:	Commission Internationale de l'Elcairage
COD:	Crystallographic Open Database
CR:	Cross Relaxation
CVD:	Chemical Vapor Deposition
CW:	Constant Wave
DFT:	Discrete Fourier Transform
DTA:	Differential Thermal Analysis
DSC:	Differential Scanning Calorimeter
DTG:	Derivative Thermo-gravimetric
E:	Free energy required to excitation
EBF:	Exposure Buildup Factor
ESR:	Erythrocyte Sedimentation Rate
ET:	Energy Transfer
F:	Field Strength
FTIR:	Fourier Transform Infrared
FWHM:	Full Width Half Maximum
H:	Hruby’s parameter
IR:	Infrared
IC:	Integrated Circuit
LED:	Light-emitting diode
LP:	Lone Pair
LMO:	Localized Molecular Orbitals
mid-IR:	mid-Infrared
MFP:	Mean Free Path
N:	Ion density of rare-earth ions
NBO:	Non-Bridging Oxygen
NIR:	Near-Infrared
NZT:	Na_2O-ZnO-TeO_2

PAT:	Process Analytical Technology
POWD:	An Interactive Program for Powder Diffraction Data
PL:	Photo- Luminescence
RE:	Rare Earth
SPH:	Small Polaron Hopping
SSL:	Solid-State Lighting
TA:	Thermal Analysis
TG:	Thermo-gravimetry
TGA:	Thermal Gravimetric Analysis
TMO:	Transition Metal Oxide
TNPs:	Titanium nanoparticles
UV:	Ultraviolet
VIS:	Visible
VRH:	Variable Range Hopping
WLEDs:	White Light-Emitting Diodes
XRD:	X-Ray Diffraction
YAG:	Yttrium Aluminium Garnet
$\chi^{(3)}$:	Susceptibility
μ:	Attenuation Coefficient
ρ_m:	Mass Density
μ/ρ_m:	Mass Absorption Coefficient
Ne:	Electron Density
Z_{eff}:	Effective Atomic Number
τ_{exp}:	Experimental Lifetimes
η:	Quantum Efficiency
2θ:	Bragg angle
d:	Inter planar spacing
$\boldsymbol{\varepsilon}_0$:	Dielectric Constant in free space
A:	Area of the sample
$\boldsymbol{\sigma}_{dc}$:	DC Conductivity
ρ:	Resistivity
R:	Resistance
t:	Thickness of the sample
E_a:	Activation Energy

σ_0:	Pre-exponential Factor
K_B:	Boltzmann Constant
λ_α:	Wavelength of X-Ray = 1.5418 Å
T_g:	Glass Transition Temperature
T_c:	Softening Temperature /Critical Temparature
ΔT:	Thermal Stability
T_m:	Melting Temperature
tbp:	Trigonal-bipyramidal
$\alpha(\nu)$:	Absorption Coefficient
A_b:	Absorbance
$\log(I_0/I)$:	Absorbance = A_b
I_0:	Intensity of incident Beam
I_t:	Intensities of transmitted Beam
E_g:	Band gap Energy
r_i:	Inter-ionic Distance
n:	Refractive Index
r_p:	Polaron Distance
$\sigma_{ab}(\lambda)$:	Absorption Cross-section
$\sigma_{emi}(\lambda)$:	Emission Cross-section
ν:	Phonon Frequency
ε:	Permittivity/Dielectric Constant
T:	Absolute Temperature
p:	Order number
m:	Index number
B:	Constant
h:	Planck's Constant
Hz:	Hertz
kHz:	Kilo-hertz $=10^3$Hz
MHz:	Mega- hertz = 10^6 Hz
eV:	Electron Volt
cm:	Centimeter
nm:	Nano-meter
μm:	micro-meter = 10^{-6} m
Å:	Angstrom, 1 Å$=10^{-10}$ m

Publications related to the Thesis

International Journals

[1] **J. N. Mirdda**, S. Mukhopadhyaya, K. R. Sahu, M. N. Goswami, “Enhancement of optical emission and dielectric properties of Eu^{3+}-doped Na_2O–ZnO–TeO_2 glass material”, ISSN 1087-6596, Glass Phys. Chem., 2020, vol. 46, no. 3, pp. 218-227.https://doi.org/10.1134/S1087659620030104.

[2] **J. N. Mirdda**, S. Mukhopadhyay, K. R. Sahu, M. N. Goswami, “Optical and electrical properties of Nd^{3+} doped Na_2O-ZnO-TeO_2 material”, Biointerface Res. Appl. Chem., 2022, vol. 12, no. 6, pp. 7927-7941. https://doi.org/10.33263/BRIAC126.79277941.

[3] **J. N. Mirdda**, S. Mukhopadhyay, K. R. Sahu and M. N. Goswami, “Enhancement of optical properties and dielectric nature of Sm^{3+} doped Na_2O–ZnO–TeO_2 Glass materials”, J. Phys. Chem. Solids, 2022, vol. 167, pp. 110776-1-9. https://doi.org/10.1016/j.jpcs.2022.110776.

[4] **J. N. Mirdda**, S. Mukhopadhyay, K. R. Sahu and M. N. Goswami, “Enhancement of optical and electrical properties of Pr^{3+} doped Na_2O–ZnO–TeO_2 glass materials”, Glass Phys. Chem. 2023 (Accepted).

Conference Proceedings

[1] **J. N. Mirdda**, M. N. Goswami, S. Mukhopadhyay, K. R. Sahu, “Enhancement of optical and electrical property of Na_2O-ZnO-TeO_2 compound doped by Eu^{3+}”, Lap Lambert Academic publishing, Proceedings of NPCRDA, 2022, pp. 26-43. ISBN-978-620-4-98114-7.

International/National seminar/Webinar Presentations

[1] **J. N. Mirdda**, K. R. Sahu, S. Mukhopadhyay and M. N. Goswami,"Optical and Electrical Properties of Nd^{3+}ions incorporated Na_2O-ZnO-TeO_2 compounds," RIES, Hokkaido University, Japan, 6-7th December, 2021. https://www.es.hokudai.ac.jp/symposium/2021/

[2] **J. N. Mirdda**, K. R. Sahu, S. Mukhopadhyay, M. N. Goswami, "Enhancement of Optical and Electrical Property of Na_2O-ZnO-TeO_2 compound doped by Eu^{3+}," 2021, National Webinar on NPCRDA, Narajole Raj College, West Bengal, India, 11th July and 12th July, 2021.

[3] **J. N. Mirdda**, K. R. Sahu, S. Mukhopadhyay, M. N. Goswami, "Instrumentation and application of UV-Visible Spectroscopy", Webinar Series-II (PDPAS), BASIS, West Bengal, India, 6th -7th and 13th - 14th February, 2021.

[4] **J. N. Mirdda**, S. Mukhopadhyay, K. R. Sahu, M. N. Goswami, "Optical property enhancement of Te base glass material: Doped by Nd^{3+}", National Seminar on Recent Trends in Advanced Functional Materials, Midnapure College, Midnapur, West Bengal, India, 13th -14th January, 2020.

[5] **J. N. Mirdda**, S. Mukhopadhyay, K. R. Sahu and M. N. Goswami, "Optical property enhancement of Te base glass material: Doped by Eu^{3+}", CMDAYS19, VU, Midnapore, West Bengal, India, 29th -31th August, 2019.

[6] **J. N. Mirdda**, S. Mukhopadhyay, K. R. Sahu, M. N. Goswami, "Modeling of wave length Conversion, Phase shifting, electromagnetic immunity, compactness using switching bistability in a Vertical Micro cavity Semiconductor Saturable Absorbers (VMCSSAs)", 2nd Time PDPAS-2017, ESSBC, West Bengal, India, 31st January, 2017.

List of Figures

List of Tables

Study the [Eu^{3+}, Nd^{3+}, Sm^{3+}, Pr^{3+}] doped Tellurite glasses for the application of opto-electronic devices

Contents

Chapter 1: **Introduction and Literature Review 1-20**

Chapter 2: **Preparation and Characterization techniques 21-39**

Chapter-1

Introduction and Literature Review

1.1 General Introduction

Glass is a non-crystalline solid material, often transparent amorphous solid and usually transparent or translucent. It is hard as well as brittle and impermeable to the natural particles applied in optics and houseware [1]. The American Society for Testing Materials (ASTM) described glass as an inorganic compound of fusion that has been cooled to a solid and hard condition without crystallizing. The amorphous nature of glasses is obtained by melting and cooling at a sufficient rate to avoid crystallization. Glass is also described as an amorphous solid material that can exhibit a glass transition and the material is characterized by a distinct changes in heat capacity, thermal expansively, enthalpy, etc.

Glass materials are an essential part of our daily life. The history of the glass fabrication process of the devolvement of mankind is nearly six hundred years old. But the research on glass materials is still dynamic and productive in the assessment the of the last few decades due to the very simple fabrication technique and novel applications with better performance of glasses than the solid crystalline materials. Day by day the usefulness of glass materials is gaining interest for scientific components in many fields such as fiber optics, laser, electronics, and optoelectronics. The application of glass materials in optoelectronics devices is also increasing for the increasing technological advancement and the rising demand for technical grade glasses [2-5]. The hybrid formulation of glass and other materials can explore a new area for future technology due to the advancement of the fabrication process.

1.2 Types of Glasses

There are different types of glasses exist for various technological applications depending on their composition and structure. According to their composition, oxide and non-oxide glasses are the two types of glasses. Historically, Oxide glasses are familiar as the oldest glasses because they can be simply made by melt quenching method. Most oxide glasses are familiar as non-crystalline materials with their competing properties as compared to chalcogenide glass materials. The oxide glasses hold oxygen as an anion, which takes place continuation as bridging oxygen during the melting of glass compositions. The radius ratio of cation/oxygen ions are varied by the coordination number of oxide glasses.

These glasses are produced using different oxides generally GeO_2, TeO_2, SiO_2, P_2O_5, B_2O_3, etc. Although the main apprehension of the research effort is to detail the tellurite glass, from a historical view point here we discuss some essential oxide glasses at a glance.

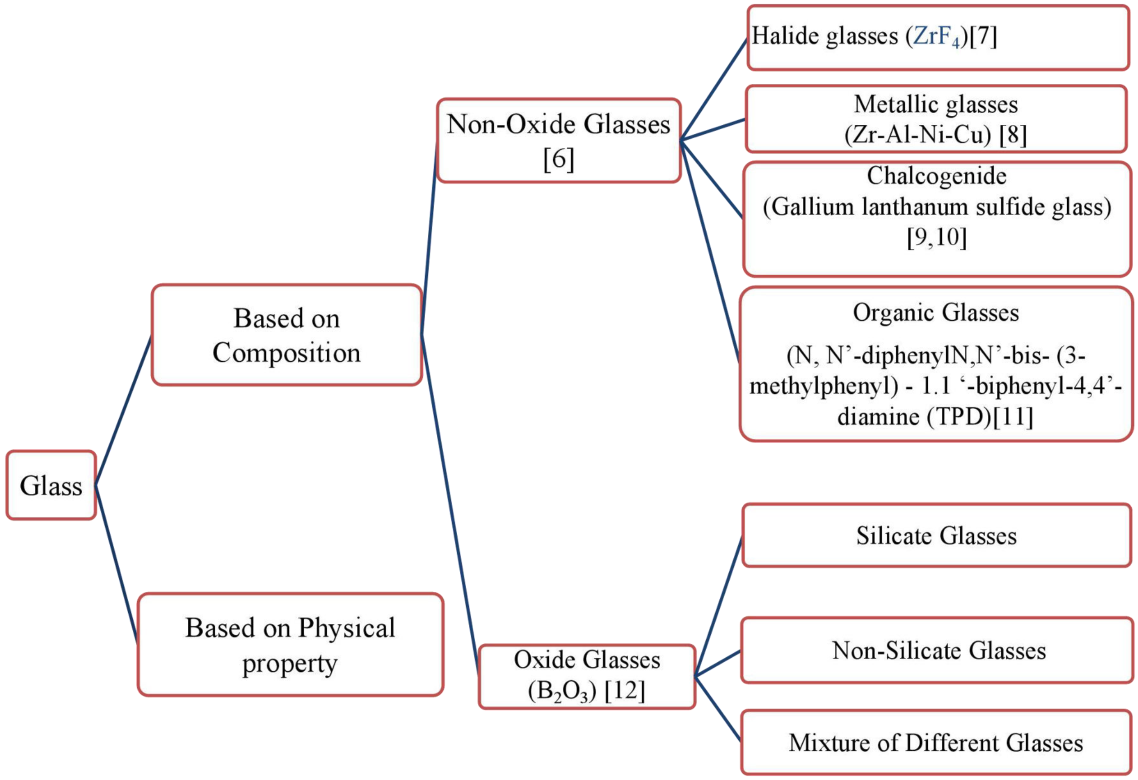

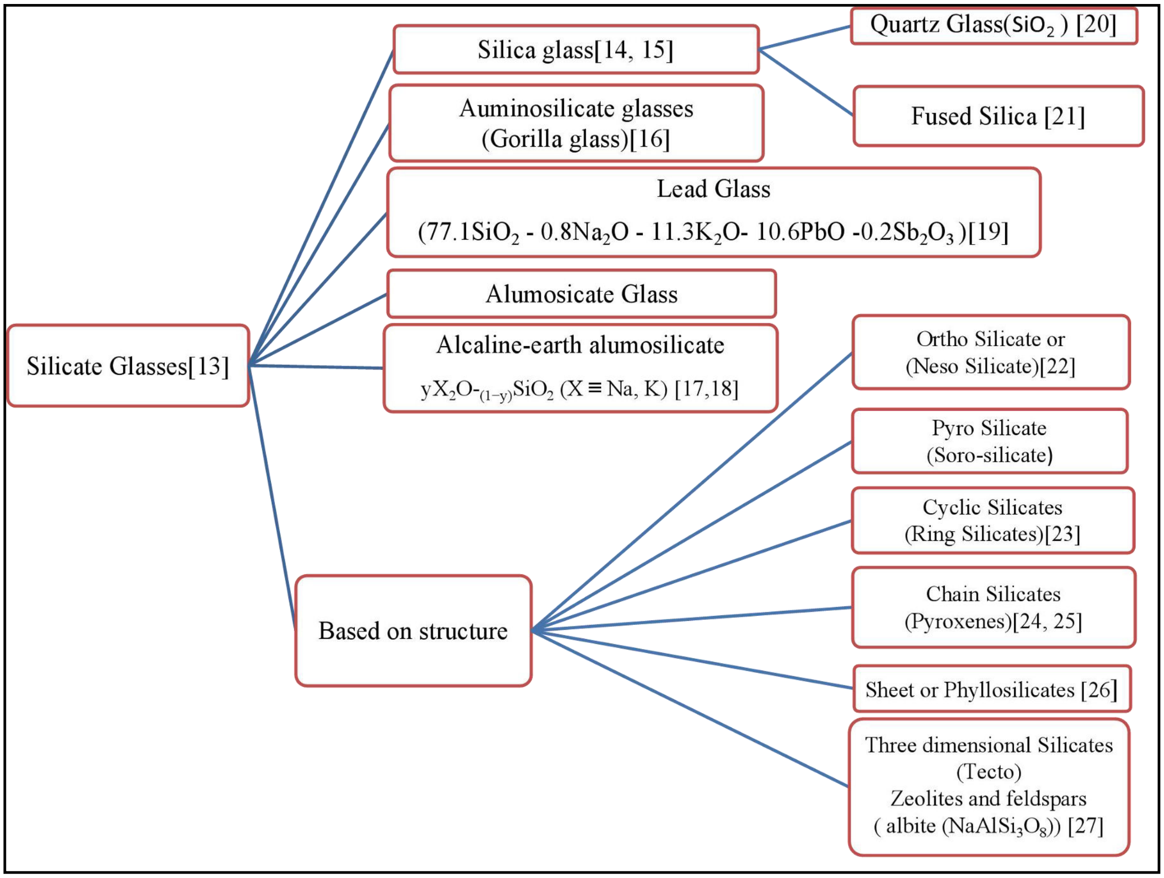
Silicate Glasses[13]
Silica glass[14, 15]
Quartz Glass(SiO_2) [20]
Fused Silica [21]
Auminosilicate glasses (Gorilla glass)[16]
Lead Glass
($77.1SiO_2$ - $0.8Na_2O$ - $11.3K_2O$- $10.6PbO$ -$0.2Sb_2O_3$)[19]
Alumosicate Glass
Alcaline-earth alumosilicate
yX_2O-$_{(1-y)}SiO_2$ (X ≡ Na, K) [17,18]
Based on structure
Ortho Silicate or (Neso Silicate)[22]
Pyro Silicate (Soro-silicate)
Cyclic Silicates (Ring Silicates)[23]
Chain Silicates (Pyroxenes)[24, 25]
Sheet or Phyllosilicates [26]
Three dimensional Silicates (Tecto)
Zeolites and feldspars
(albite ($NaAlSi_3O_8$)) [27]

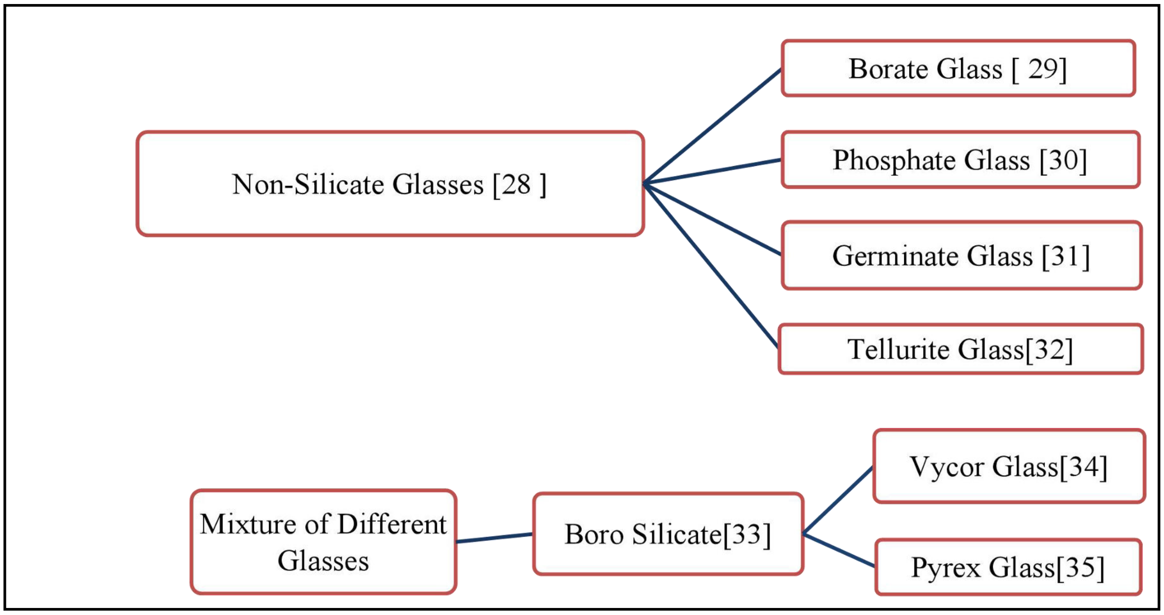
Non-Silicate Glasses [28]
Borate Glass [29]
Phosphate Glass [30]
Germinate Glass [31]
Tellurite Glass[32]
Mixture of Different Glasses
Boro Silicate[33]
Vycor Glass[34]
Pyrex Glass[35]

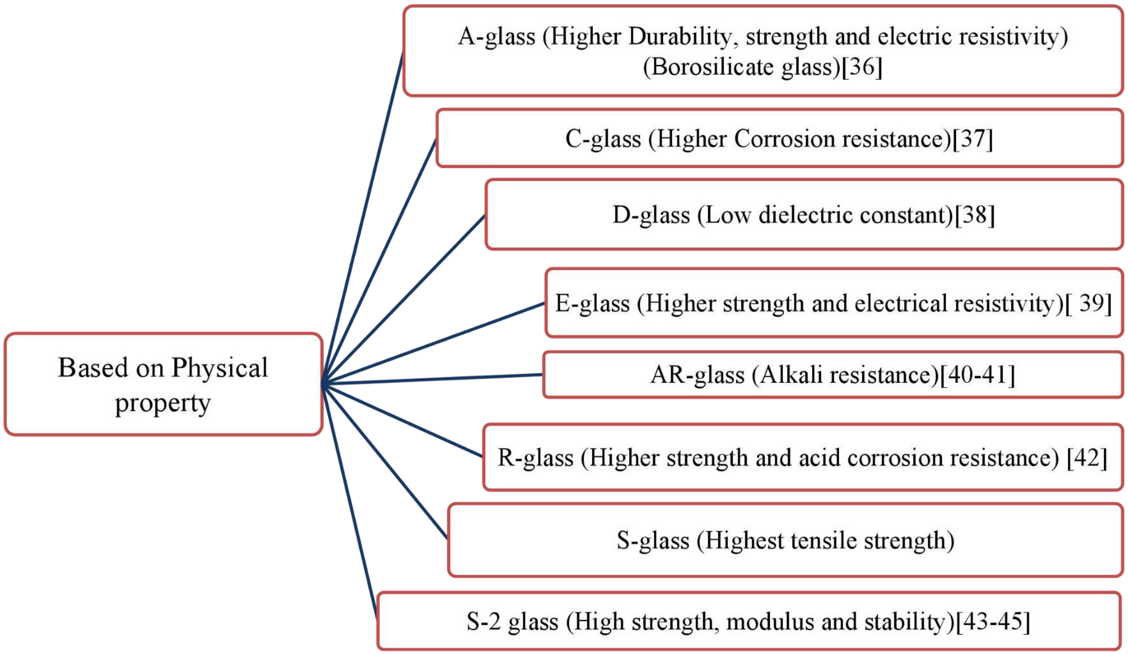

Fig 1.1 Block diagram of classification for different glass materials.

Glass materials are classified into two types depending on their properties. There are three types of glass classified according to the composition of glass materials. These are silicate, non-silicate, and the mixture of different glasses.

1.2.1 Silicate Glasses

Silicate glasses are used in the chemical laboratory as glassware like a crucible, beakers, evaporators, etc. It is also very much useful for high-quality watch glass. These glasses are structured by three dimensional networks with intermediate ionic/covalent bonds. A similar structure has been observed in alkali phosphate glass but the alkali phosphate glasses are described as chains. The basic units of a silicate glass network having silicon-oxygen tetrahedron are shown in Fig.1.2. The formation of three dimensional structures is obtained by linking all the tetrahedra together by their corners. The center of the linked tetrahedral is occupied by a common oxygen atom between two silicon atoms. The structure of this network may be easily distorted by changing the Si-O-Si bond angle and also the bond lengths between the adjacent tetrahedrons. These glasses are also used in optics, optoelectronics, and electronics [46].

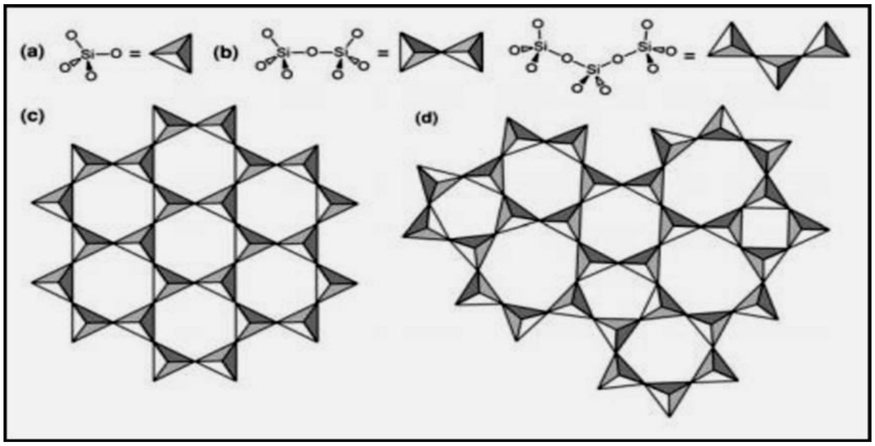

Fig 1.2 Structure of silicate glass showing basic silicon tetrahedron and SiO_4 network.

1.2.2 Borate Glasses

Borate glass is widely used in linear and non-linear optical applications for its high transmittance and thermal stability. The structure of these oxide glasses (shown in Fig. 1.3) consists of five boron-oxygen bonds for forming a glass network.

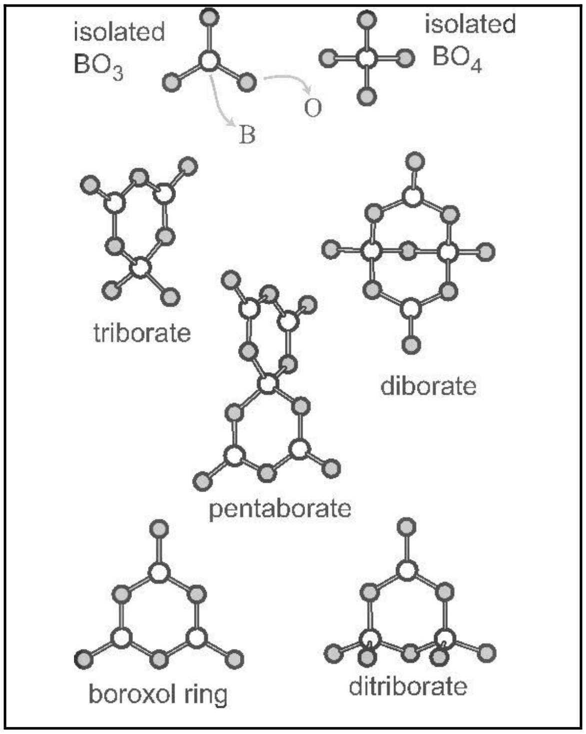

Fig 1.3 Structure of tetra-borate glass materials.

These glasses form BO_3 triangles and BO_4 tetrahedra with alumina, alkaline, and alkali earth combination and are compatible to other elements. Due to the small size of the B^{3+} ion, it can adjust well into the trigonal void generated by three mutually linked oxygen ions [47-49].

1.2.3 Bismuthate Glasses

Bi_2O_3 is not only a glass former but also in combination with some other glass formers such as SiO_2, B_2O_3, etc., it forms glass relatively in bulk [50]. Bi_2O_3 doped glass has a large number of applications in optical, electronic devices, thermal and mechanical sensing, etc. [51-55]. Annealed Bi_2O_3 doped glass exhibits few interesting characteristics of a high-temperature super conductors [56]. Since the transmission range is high and sharp cut off in UV-VIS and IR regions, these glasses are used in spectral devices. The physical properties of the bismuth borate glasses can be modified by introducing the alkali oxide [57].

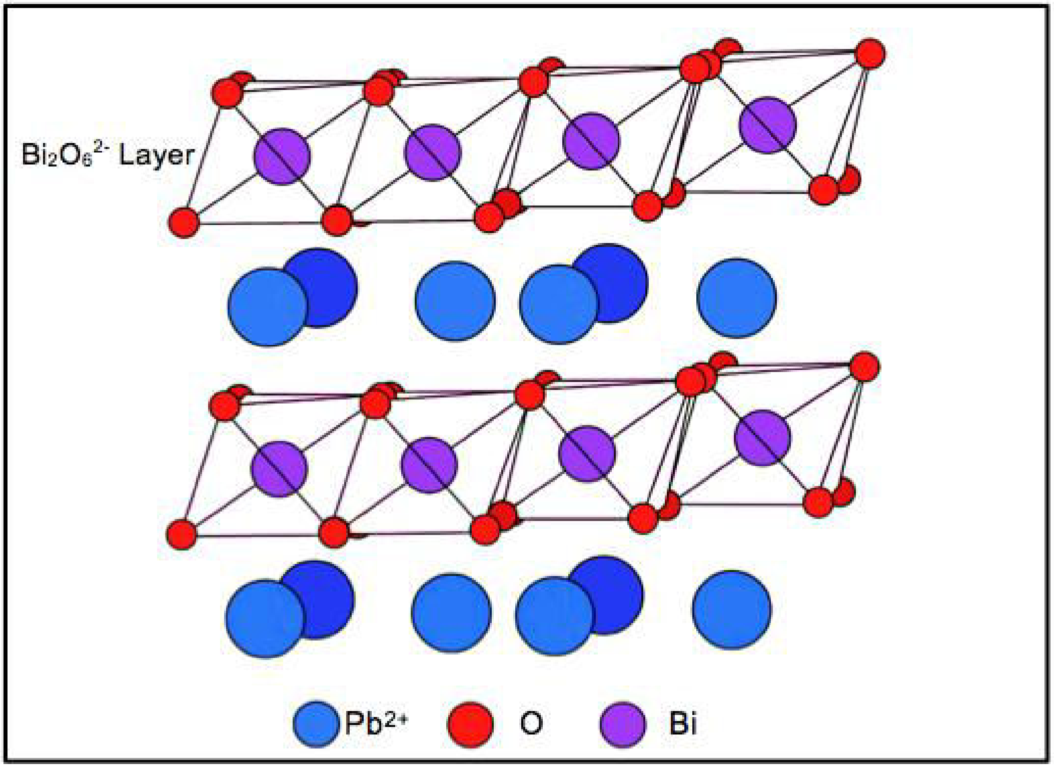

Fig 1.4 Structure of bismuthate glass materials.

1.2.4 Germanate Glasses

GeO_2 glass gets high academic interest for its high performance and large-scale application in fiber optic devices. GeO_2 can be used to make glass and it is expected to have structural similarities with SiO_2. It can form a glass network in coordination with oxygen's [58]. There is a number of germanates glasses such as Bismuth germanates, lead germanates, etc. These glasses are very much useful in optical devices due to their interesting properties like high density, nonlinear refractive index, and high IR transmission [59].

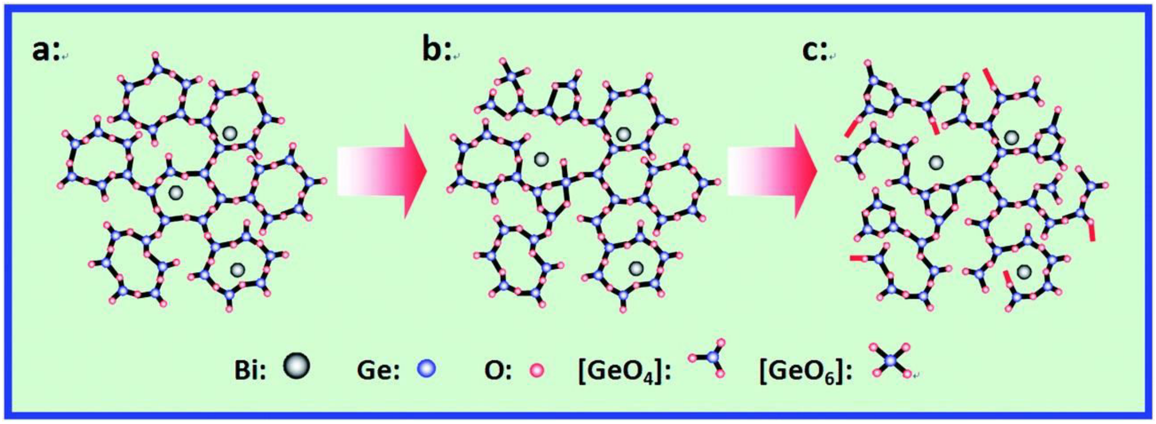

Fig 1.5 Structure of germanate glass materials.

1.2.5 Tellurite Glass

The study of tellurite glass receives tremendous interest among researchers in the recent time because of its many interesting properties like low melting temperature, relatively high refractive indices, large relative permittivity, and low phonon energies (640-790 cm^{-1}) considerable chemical and thermal stabilities. Tellurite glasses are eco-friendly and safe from environmental pollution for their hygroscopic nature. These are useful for optical fiber applications as the materials have low melting points and low glass transition temperatures. The transparency and absorption percentage in tellurite glasses is controlled by the vibration of the structural subunits of tellurite. Therefore, to achieve a stable and wide transmission or absorption window, the preparation of raw materials must be pure [60-62].

The polarizability of TeO_2 glass is very high, so they have large nonlinear refractive indices. Therefore, these glasses are suitable for nonlinear optical devices. Tellurite glass has wide range of optical transmission from 400 nm and 5μm due to the low level of phonon energy, so these are applicable efficiently for visible and mid-IR spectroscopic devices.

Tellurium oxide has been found in 1934. Though the material has been observed nearly 190 years ago the investigation of the properties of many tellurite glasses has been started in the 1950s [63]. Since then, many different TeO_2-based glass systems have been observed and the development of tellurite glass fiber has been reported in1990s [60, 64]. Research is still going on actively in tellurite glasses for their unique and interesting properties [60, 65].

The interesting properties such as transparency at room temperature, highly corrosion resistance, and satisfactory strength of hardness have been observed in tellurite glass materials. Recently, the applications of rare-earth doped tellurite glasses are used in the region of visible optical instruments, particularly for white LED applications like indicators, automobile headlights, back-light, and general illumination [66]. White LED can be the next generation system of solid-state lighting devices and the technology has become very familiar because of its various potential applications in lighting technology. The solid-state LED is of great significance to reduce the global electricity utilization convention of fossil fuels. Doping of rare-earth in tellurite glass helps to increase the densities of tellurite glasses and their thermal properties as well as a network structure. The nature of these glasses allows the doping of rare-earth ions with large concentrations depending on the final applications.

The melting point of tellurium dioxide (TeO_2) is 733ºC and is more stable than the other oxide form of tellurium (Te). TeO_2 has band gap of ~3.0 eV. The stability of tellurium oxide makes it the material of intensive attention for researchers towards the tellurite glasses. A large number of elements can be permitted to mix in tellurite glass compositions for the inherent stability of tellurium oxides [1]. Tellurite glass materials are of unique interest for the purity of TeO_2 approached 98.5 mol% in recent years due to improvement in synthesis technology and ultra-pure ingredients [67, 68]. Again, pure TeO_2 is not a good glass former, but with the addition of a network modifier, it can simply form glass, therefore, it is classified as a conditional glass former [69]. Recently, tellurite glass materials are the topic of intensive research because of their high homogeneity, high chemical stability, and electrical conductivity. These properties make them appropriate for applications in optical, electronics, electric, laser, and fiber optics fields.

1.3 Structure of Tellurite Glass

TeO_2 shows worthy non-linear optical properties. Especially, the value of susceptibilities ($\chi^{(3)}$) is 50–100 times larger than that of SiO_2 glass and probably the highest value among the oxide glasses [70]. The silicates are mainly focused as the glass materials because of their technological usefulness in the field of chemistry and physics. In the present study, the focus has been put to understand the dynamical processes that occur in rare-earth doped tellurium oxide glasses. In order to achieve this, it must be understood the molecular structure of prepared tellurium oxide glass. It has been reported earlier that the structural unit of tellurite is similar to the tellurite crystal according to Zachariasen random network theory. Tellurites are not tetrahedral as silicates but distorted octahedral/trigonal bipyramid. The trigonal bipyramidal structure is the fundamental unit of tellurium oxide, composed of two long bonds to oxygen identified as Bridging Oxygen's (BO) and two relatively shorter bonds to an electron pair, corresponding to the fifth place, shown in Fig. 1.6 below [71,72].

A three-dimensional network structure with the trigonal bipyramid units in random orientations is involved to compose the tellurium oxide glass shown in Fig. 1.6. This structure is maintained to the connection of the direct bonding of tellurium atoms via four oxygen atoms. The non-bridging oxygen's (NBOs) are generally created by the addition of modifier oxides.

Breaking of the covalent network structure (de-polymerization) due to the addition of modifier oxides creates mobile ions in the material. The tellurite structural units modify as the form of TeO_3/TeO_{3+1} [Fig. 1.6]. The structure of TeO_2 has been ascribed that the oxygen atoms are bonded to the lone pair (LP) of tellurium (IV) atoms in its electronic configuration of ($5s^2$) lone pair [70]. These LPs of tellurium atoms seemed to be electron structures of TeO_2 glass and were capable to show linear and nonlinear polarizability.

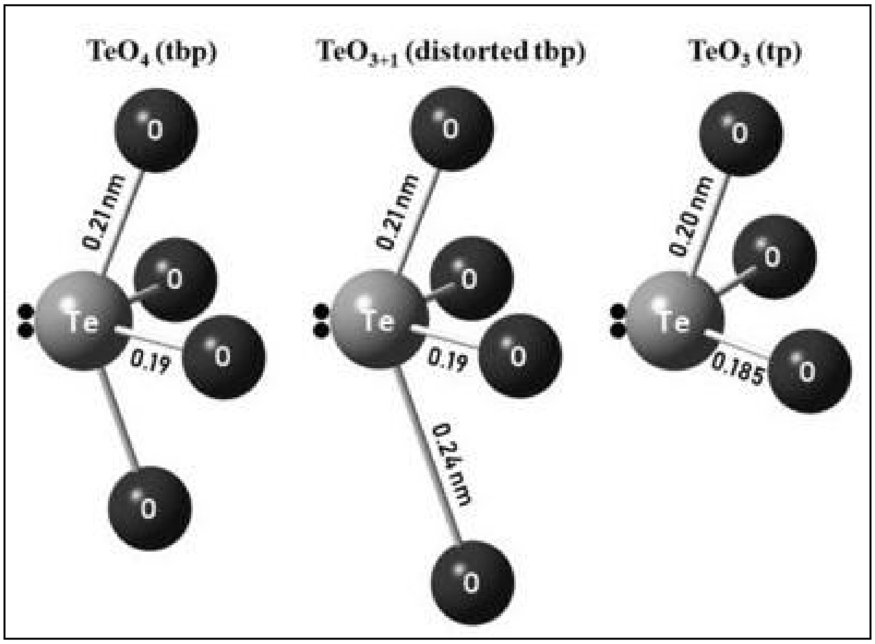

Fig 1.6 TeO_4 trigonal bipyrimidal, TeO_{3+1}, and TeO_3 structure.

Recent studies have shown that the form of Te–O–Te bridges is mainly responsible for the nature of the structure of TeO_2 glass [70]. Pure tellurite glass is not much stable because of the presence of electronic lone pair of TeO_4 units, at the equatorial position. These are actually the limits of the structural rearrangement for the necessary conditions to make the glass formation. However, the addition of alkali metal oxides like Na_2O with a very small amount makes TeO_2 as good glass-former [73]. The O=Te⟨O…O⟩Te⟨O…O...⟩Te=O chains as the chemical particularity is reflected in the structure of TeO_4 coordination polyhedrons and this particular form is known as bisphenoid or trigonal bipyramid. Te-O bonds form an O-Te-O angle of about 100°. The lone pair of Te atoms form an equatorial plane of the polyhedrons. Therefore, these bonds are known as equatorial bonds, Te-O_{eq}. The other two longer Te-O bonds are almost normal to the equatorial plane and are known as axial bonds, Te-O_{ax}. The Te-O_{eq} bonds are generally covalent in nature [74]. Thus, the O_{eq}-Te-O_{eq} units are similar to the TeO_2 molecules. The Te-O_{ax} bonds are relatively weaker and considered as intermolecular contact with the electrostatic origin [74]. Actually, the total molecular dipole moment of the chains has decayed due to the localized molecular orbitals (LMO). This localized molecular orbital can be assigned to a lone-pair of the Te atoms [75]. Accordingly, it seems that the structure of alkali-based tellurite crystals is used as the basic model for tellurite glass structures.

1.4 Literature Review

J T. Berzelius investigated the glass forming capacity of the glass combination of TeO_2 and BaO [1]. After a long period J E. Stanworth studied systematically the properties of tellurite glass materials and made an analogy to phosphorous oxide according to the same electro-negativity in 1952 [60]. He incorporated outstanding glass former into the Pauling scale and consider whether tellurium oxide or tellurites or tellurates will make the glass. In 1957, Barady studied the structure and distribution of electrons in the glass and informed unusual behavior of tellurite glass as it is octahedral to the faces that demonstrate a close-order configuration. He also included that TeO_2 like Li_2O or Na_2O are act as a modifier to convert the material into glass materials by sudden cooling [76]. Initially, he identified TeO_2 as a potential glass material for the application of fiber optics in the host glass for the losing ion process in 1976. Burger et al. prepared a material with the binary combination of 60 mol% TeO_2 and 40 mol% B_2O_3 compositions in 1984 and found the distribution of different compositional elements in this material [77]. Analysis of XRD, found a depositing of 80% tellurium at the middle portion, decreasing to about 4% at the tail. E F. Lambson et al. found that the prepared glass materials were contaminated by the material of the crucible (SiO_2 or Al_2O_3) in which the initial glass composition melts. The concentrations of the mixture were very high to affect largely the properties of glass [78]. El-Zaidia et al. observed in 1985 that the infrared transmittance occurred in the spectral region a far 2.5 μm tellurite glass samples. These glasses can be used to make mid-infrared optical fiber devices [79]. A. Ghosh observed the nature of electrical conductivity of semiconducting glass materials in 1993. He explained the experimental results with the help of polaron hopping theories. The hopping mechanism of tellurium in glass materials has been investigated from non-adiabatic to adiabatic changes due to the presence of bismuth oxide [80]. M M. Elkholy et al. found in 1995 that the ac conductivity increased with increasing frequency. They also observed that the value of the frequency exponent was reduced with increasing temperature. The conductivity spectra revealed a strong dependence on the transition of metal ions in the glass materials [81]. M R. Sahar et al. investigated the optical and thermal characteristics of TeO_2 –ZnO–$ZnCl_2$ glasses using FTIR and DTA in 1997 [82]. They found that the glass materials display transmission beyond 6 µm.

M H. Bhat et al. reported the conductivity of the glass material was increased due to the higher concentration of non-bridging oxygen. It was found that total conductivity spectra slightly changed by the doping of LiCl. AC conductivity and dielectric properties discovered that it does not change in conductivity mechanism in all materials and temperatures [83]. S. Szu et al. showed in 2005 that the conductivity of glasses increased due to the low content of BaO. They worked out the electric modulus depending upon exponential relaxation. They calculated the activation energy from DC conductivity and relaxation time spectra, which are similar [84]. M M. El-Desoky found in 2005, that glass transition temperature and the density of the glass samples were decreased due to the increase of V_2O_5 [85]. The conduction was followed by the adiabatic small polaron hopping due to the V^{2+} ions mechanism. Small polaron hopping (SPH) Mott model was maintained at high temperatures and the Greave's Variable Range Hopping (VRH) model was followed at a medium range of temperature. J. Ozdanova et al. investigated the optical band gap and found 3.55 eV for the glass materials in 2007. They also determined the optical band gap dependent on temperature [86]. Raman scattering measurements analyze that the content of TeO_2, and TeO_4 trigonal bi-pyramidal transformation leads to making TeO_3 trigonal pyramids. In 2008, D. Saritha et al. observed that the glass transition temperature (473 ºC to 449 ºC) and optical band gap of glass samples were decreased due to the increase of bismuth. They also found that the glass network system becomes loosely packed and the degree of disorder increases by increasing bismuth content [87]. In 2008, S. Rada et al. observed that the structural variations of TeO_2-B_2O_3 glass materials are explained by Fourier Transform Infrared (FTIR) spectroscopy and Discrete Fourier Transform (DFT) calculations. They observed that the tetrahedral [BO_4] units were frequently changed to trigonal [BO_3] units for a large number of non-bridging oxygen (NBO) atoms present in the glass system. They also studied the formation of [TeO_6] distorted octahedral and changing coordination of the Te atom [88]. M P. Kumar and T. Sankarappa investigated alkali-doped vanado-tellurite glasses in 2008 and reported the variation of conductivity with the density of vanado-tellurite glass materials. The conductivity decreases up to 40-mol% doping of Li_2O and then increases for further increase of Li_2O doping concentration [89]. These changes may be due to structural changes at $x = 0.4$ and changes in the conduction mechanism. M. Pant et al. studied the large range of frequencies for DC and AC conductivity in 2009. DC activation energy is obtained from the relaxation principle. The DC activation energies were calculated from the impedance and modulus spectra which followed the hopping mechanism due to the presence of silver ions in the host glass matrix. It can occur harmonic electron-phonon interactions during the hopping process [90].

B. Sujatha et al. observed the temperature and frequency dependent DC conductivity of B_2O_3 doped tellurite glass materials in 2010. DC conductivity obeyed the Arrhenius mechanism over the large temperature range. Scaling property has also been described that the transport mechanism does not follow the composition and temperature [91]. R. El-Mallawany et al. found in 2010, the relaxation process correlated with changing of peak position to high temperature in high frequency regions. The acoustic activation energy and relaxation frequency both were linked with the relaxation strength and the potential for structural deformation present in the prepared tellurite glass materials [92]. In 2011, J N. Ayuni et al. studied the IR spectra of glass network with Zn^{2+} ions as modifiers forming BO_4 units. The absorption edge transferred towards lower energy with the higher concentration of ZnO. The direct and indirect optical band gap energy decreased with the incorporation of ZnO in the host glass system. These glass samples followed the Urbach rule. The refractive index of glass material increases but the molar refractivity decrease for the higher concentration of ZnO content [93]. P G. Pavani et al. in 2011 calculated the Urbach energy and optical band gap energy which decreased while the refractive index of the glass materials increased due to the large concentration of ZnO. They also studied the various physical parameters like density, optical basicity, molar volume and also the oxygen packing density etc [94]. K. Maheshvaran et al. investigated the structural properties from FTIR spectra in 2011. They reported the structure of Te-O bending vibrations and Te-O-Te linkage associated with the TeO_6 and TeO_3 units respectively. It is also studied that the ionic character decreases with the increase in TeO_2 content [95]. In 2011, R. Punia et al. studied that the density, molar volume, optical band gap energy, and thermal stability increased due to the higher concentration of Bi_2O_3 in host glass materials. They investigated the conversion of tetrahedral VO_4 to trigonal-bi-pyramid VO_5 configuration. The DC conductivity and hopping carrier mobility of the zinc vanadate glass system were found to increase due to the incorporation of Bi_2O_3. The experimental data obeyed Mott's Variable Range Hopping (VRH) models and the magnitude of inverse localization length was found much higher than the obtained value for transition metals by using Mott's model [96].

In 2012, H M. Oo et al. found that the molar volume, density, and refractive index increase with increasing bismuth content may be attributed to the increased polarization of Bi^{3+} ions. Optical band gap energy was also found to decrease with bismuth content [97]. H A A. Sidek et al. exposed the prepared glass materials having amorphous nature by using an X-Ray diffraction pattern in 2012. They reported the various physical parameters of the glass materials like molar volume and density were changed due to the incorporation of fluoride [98]. V. Kamalaker et al. investigated the physical parameters like molar volume, density etc., and glass transition temperature was determined from Differential Scanning Calorimetry (DSC) measurement in 2012. Band gap energy and Urbach energy were estimated from optical absorption spectral data [99]. In 2013, G. Zhao et al. observed that the physical properties like density, optical basicity and refractive index of the glasses increased for the larger concentration of Bi_2O_3 content. They analyzed the glass network structure made by the [BiO_6] octahedra, [TeO_3] trigonal pyramid, [TeO_4] trigonal bipyramidal, [BO_3] trigonal pyramid, and [BO_4] tetrahedral by using Raman spectra [100]. In 2014, V. Sreenivasulu et al. studied the Raman spectra, optical properties of the glasses, Differential Scanning Calorimetry (DSC), Erythrocyte Sedimentation Rate (ESR) etc. Structural studies showed that V^{4+} ions survive as VO^{2+} in octahedral coordination along with tetragonal distortion. The glass network consists of TeO_4, TeO_{3+1}/TeO_3 and ZnO_4 units as fundamental structural units [101]. In 2014, R S. Kundu et al. found that the molar volume of glass materials increase and the glass transition temperature decrease with increasing of Bi_2O_3. The percentage of transmittance of the glass materials is increased with the increase in bismuth ions and band gap is decreased with the increase in bismuth ions [2]. In 2015, N. Berwal et al. shows that molar volume, crystalline volume and the density of glass materials decreased with the increase of B_2O_3. However, the glass transition temperature follows the reverse tendency. The optical band gap shows nonlinear properties due to the induced structural variation [102]. Nanda et al. showed in 2015 that the molar volume, density and equivalent crystalline volume are increased with the incorporation of Nd_2O_3 in glass materials. The doping Nd^{3+} ions decrease the optical band gap energy [103]. S. Dhankhar et al. investigated that the presence of zinc in glass materials increases the activation energy of the glass [104]. They also observed that dc conduction can be understood via variable range hopping (VRH), initially proposed by Mott and then with some alteration suggested by Punia et al. The AC conduction in glass materials is occurred by tunneling of overlapped large polaron.

N. Berwal et al. found the nonlinear properties of prepared glass materials with the variation of structure interrelated to optical band gap energy. The optical band gap energy was determined by fitting Hydrogenic Excitonic Model and Mott-Davis's Model [105]. O A. Zamyatin et al. calculated the molar refraction, Urbach energy, optical band gap and criterion of the metallization of glass structure in 2017. The optical band gap energy decreases due to the incorporation of copper content whereas the Urbach energy decreases due to the possible structural defect in the host glasses [106]. The luminescence for the transition corresponding to the cross-relaxation process has shown the non-exponential behavior. The decay curves in the NIR region represented simple exponential behavior. The calculated lifetime of Er^{3+} doped zinc-tellurite glasses is found large [107]. P. Yasaka et al. studied the structural and spectroscopic properties of zinc-tellurite glasses mixing with different concentrations of BaO. O-H and Te-O bonds are observed in the measurement of FTIR spectroscopy in the tellurite glass system. Refractive index, colour coordinates and brightness are increased with the increase of BaO concentration [108]. N N. Yusof et al. observed the spectral properties and self-cleaning features of the glass materials. A relationship between Titanium nanoparticles (TNPs) and self-cleaning properties has been established. The influence of embedded Titanium nanoparticles (TNPs) on the spectral properties and self-cleaning is examined and established their correlation for the first time [109]. A I. Yakovlev et al. observed that the glasses are transparent in the NIR and mid-IR regions. This stability against devitrification has been demonstrated and found to be very high for the investigated glasses. This type of glass was used for magneto-optical fiber waveguides or magneto-optical devices [110].

S A. Tijani et al. found that this glass has better radiation protective characteristics than lead glass. These glass materials are recommended for preparing radiation protective glasses and building barriers for both Computed Tomography facilities and general diagnostic centers [111]. In 2018, Sayyed et al. calculated the mass absorption coefficient (μ/ρ_m) values, electron density (Ne), mean free path (MFP), the effective atomic number (Zeff) and Exposure Buildup Factor (EBF) values using Geometric Progression for fitting method. The cross-section for fast neutrons is evaluated for their potential applications as neutron radiation and γ-ray shielding materials. The obtained results demonstrated that the mass absorption coefficient increase with the increase of concentration of Sb_2O_3 and Bi_2O_3 modifiers in the B_2O_3-Sb_2O_3 and B_2O_3-Bi_2O_3 glasses, respectively [112].

Al-Buriahi et al. and Tonguc et al. have shown shielding properties of gamma-ray for the high concentration of Bi_2O_3 in glasses [113, 114]. Gaikwad et al. has also reported the best shielding properties of the glass composed of higher concentration of Bi_2O_3 [115]. Matori et al. has studied buildup factors for gamma-ray in phosphate glasses [116]. The shielding properties of these glasses can be improved by the substitution of ZnO for PbO. But lead (Pb) material is harmful to the environment and human health due to the toxicity and hazardous nature of the element. So, lead (Pb) material is replaced by other high atomic number elements such as Mo, Ba, W, Bi, Gd etc. to save the environment and human health. Therefore, many efforts are being put to supply suitable substitution instead of lead to get equivalent shielding, physical and chemical properties. Tellurite glass has also been used to protect the X-ray radiations and other ionizing radiations coming from radioactive materials. Radiation exposure can have negative effects on the human body coming from different nuclear sources like radioactive mining, nuclear power plants etc. There is number of disadvantages have been observed in case of lead as a shielding material. Material scientists have proposed the efficiency of the shielding material using the tellurite/borate glasses without any environmental pollution. P. Vani et al. and Sayyed et al. have synthesized and investigated different types of Pb-free tellurite-based glass materials [117, 118].

The rare-earth doped tellurite glasses are more suitable for designing and fabricating optoelectronic devices. Reddy et al calculated the emission cross-sections of rare-earth doped tellurite glass and its quantum efficiencies. It has been observed that the designing of optoelectronic devices is more suitable for tellurite glass with 1 mol% of Sm^{3+} ions. It is also used as a laser active medium for laser applications at 601 nm emission wavelength. Branching ratios and emission cross-sections were estimated from the luminescence spectra. The measurement of quantum efficiencies of as-prepared glasses is correlated with the experimental lifetimes (τ_{exp}) corresponding to decay spectral profiles. All the mentioned results of these glasses are suitable for the fabrication of optoelectronic devices like WLEDs and lasers [119].

The chromaticity coordinates have also been estimated to find the suitability of these tellurite glasses as red luminescence devices. Sharma et al. studied the emission spectra and determined the band-widths, emission cross-sections and branching ratios. To find out the quantum efficiency (η) of the host glasses the experimental lifetimes and radiative lifetimes are calculated. Relatively higher values of cross-section, branching ratios, and quantum efficiency (η) are found [120]. It can be used for visible photonic devices. Y. Ruan et al found the Magnetic effect of the glass materials. Tellurite glass has been applied to realize the magnetic field sensitive object. The physical properties like structure, fluorescence, and decay times of the glasses have been studied. To produce high sensitive device it has been better to choose the low doping sample indicating the possibility of high power laser. It is also described the up-conversion processes and sensitivity of these glasses [121]. R. Kaur et al. calculated the emission cross-sections, Commission Internationale de l'Elcairage (CIE) coordinates and quantum efficiency in 2019. Pr_2O_3-doped tellurite glasses have been used for preparing visible optoelectronic devices [122]. The doping of Pr^{3+}/Er^{3+} ions in tellurite glass materials is used for the ultra-broadband and amplifiers covering the explanation of low-loss communication window. The Judd-Ofelt parameter, spontaneous transition probability, fluorescence branching ratio, and radiative lifetime are calculated from fluorescence decay curves

[123]. Yu et al. photoluminescence properties were investigated. The doping of Dy^{3+} and Eu^{3+} ions in tellurite glass matrix can perform for the UV converted WLEDs. L. Yuliantini et al. observed the molar volume, density, and refractive index of the quenched glass materials. It has also been calculated branching ratios of $^4F_{3/2} \rightarrow {}^4I_{11/2}$ transition (1072 nm) and that represents the possibility of application in NIR under 584 nm excitation [124].

1.5 Motivation and Objectives of Study

As explained above, pure and rare-earth doped NZT glass materials are extensively applicable in different devices due to their structural, thermal, optical, and electrical properties. The doping of various rare earth ions like Eu^{3+}, Nd^{3+}, Sm^{3+}, and Pr^{3+} in host glass materials, NZT has grown interest among scientists and researchers for their various application potentialities. Individual rare-earth ions with their specific size, charge and spin arrangement improve the optical and electrical properties of the host glass material. The optical and electrical properties are enhanced for the doping of rare-earth (RE) ions in the host glass matrix which act as efficient photo luminescence centers. In chapter 2, the various synthesis techniques used for the preparation of NZT and rare-earth doped NZT glass materials with their merits and drawbacks have been discussed in detail. In this chapter, a brief outline of the different characterization techniques used for the structural, thermal, optical, and electrical properties of the prepared glasses has also been presented.

In Chapters 3, 4, 5, and 6 we have reported our investigation on Eu^{3+}, Nd^{3+}, Sm^{3+}, and Pr^{3+} doped NZT glass materials respectively. Rare-earth doped NZT glass materials are prepared by the melt quenching method. The study for each of the doped samples is carried out for four different doping concentrations of 0.5, 1.0, 1.5, and 2.0 %. Thermal properties like Differential Thermal Analysis (DTA) and also Thermo-gravimetric Analysis (TGA) studies have been carried out to find out the glass transition temperature, critical temperature, and melting temperature for each of the different doping concentrations. Thermal stability has been calculated using glass transition temperature, critical, and melting temperatures. The X-ray diffractogram (XRD) and Fourier Transform Infrared (FTIR) studies have been presented in this work for the structural analysis of the prepared glass samples. The absorption and emission spectra are characterized by using a UV-VIS spectrophotometer and photoluminescence measurement for these samples. The absorption and emission spectra are used to investigate the optical properties of pure and doped NZT glass materials. The band gap energy is estimated from Tauc's plot using absorption spectra. The absorption and emission cross-section for a particular transition is also calculated for specific applications in optoelectronic devices. The electrical properties have been studied through the measurement of dielectric constant with the variation of frequency at room temperature and DC conductivity with temperature for the pure and doped samples of NZT glass materials. The variation of conductivity with temperature is used to investigate the conduction mechanism and to find out the value of activation energy of NZT glass materials. Finally, the conclusions of our findings and the further scope of work have been arranged in Chapter 7.

Chapter-2

Preparation and Characterization techniques

2.1 Introduction

Amorphous materials like glass, polymer, plastics and polycrystalline materials like ceramics, thin films, and hetero-structure materials can be prepared using various modern techniques. These techniques are mainly categorized as physical and chemical routes. The chemical route deserves the techniques like chemical precipitation method, sol-gel method, hydrothermal method, solid-state reaction technique, chemical vapor deposition method (CVD), and melt-quenching processes which are useful for the synthesis of amorphous glass materials [125-130]. In this chapter, we have discussed the three methods: sol-gel method, CVD method and melt-quenching process briefly. Here, the melt-quenching method is mainly used for the preparation of pure and rare-earth doped NZT glass materials for its various advantages.

The properties of the prepared glass materials have been obtained through the characterization of the samples. The structural characterization of pure and rare-earth doped tellurite glass materials has been studied by performing X-ray diffraction (XRD), Fourier Transform Infrared (FTIR), and also Raman spectroscopy. Glass transition and glass melting temperature have been investigated using the Differential Thermal Analysis (DTA) and also Thermo-gravimetric Analysis (TGA). The characterization of optical properties like absorption and emission spectra is made by UV-VIS spectrophotometer and Photoluminescence measurement set up respectively. The electrical properties regarding the conduction mechanism etc. are achieved using computer-controlled LCR meter.

2.2 Sol-gel Method

The sol-gel method is known as the wet chemical process for the formation of various crystalline and non-crystalline materials, especially metal oxide nanoparticles and glass. In this process, the molecular precursor (generally metal alkoxide) is formed as gel dissolving in water or alcohol by heating land stirring by hydrolysis/alcoholysis [131]. It should be dried up using suitable methods depending on the preferred application and properties of the gel. After drying, the formed gels are milled and then calcined. Various steps of glass formation through the sol-gel method are shown in Fig. 2.1 [132].

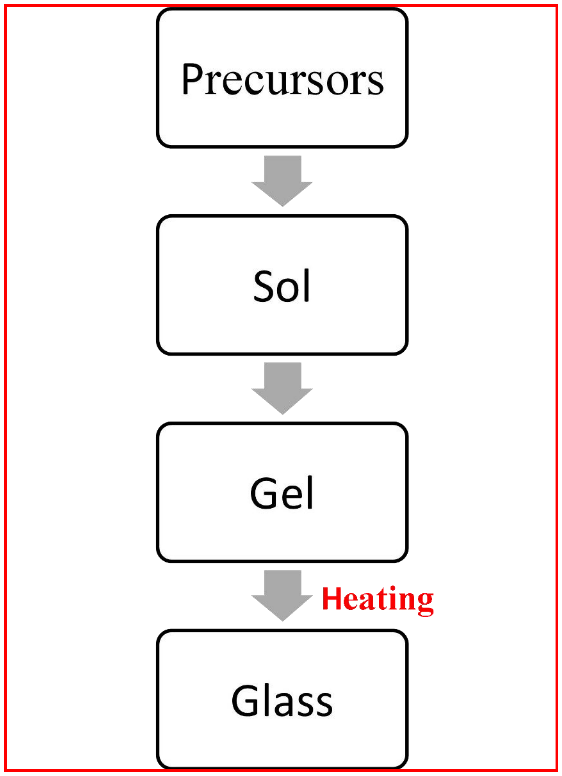

Fig 2.1 Schematic flow chart of a sol-gel method for the development of glass particles.

The generic form of metal alkoxides is $M(OR)_n$, where R is usually a simple organic alkyl group. The metal alkoxides $M(OR)_n$, have been prepared by the sol-gel method. Usually, in the formation of tellurium metal alkoxides, these compounds Te has the tetravalent state. Initially, $TeCl_4$ is prepared through the dissolution of research-grade TeO_2 in HCl. $TeCl_4$ reacts with alkoxide like sodium methoxide to produce tellurium methoxide. In the same way, higher alkoxides like tellurium isopropoxide were prepared.

$$TeCl_4 + 4\ Na(OCH_3) = Te(OCH_3)_4 + 4\ NaCl \quad \ldots \quad \ldots \quad \ldots \quad (2.1)$$

Telluric acid $Te(OH)_6$ and allotelluric acid $[TeO_2(OH)_2]n$ derived by autoclave heating of telluric acid at 100–150 °C are soluble precursors for tellurium oxides. These are not suitable for device/film fabrication as they precipitate due to drying to form coarse powders. However, organo-metallic compounds of tellurium like tellurium catecholate or tellurium methoxide are synthesized using the ingredients of these acids to generate telluric esters. According to Eq. (2.2), allotelluric ethyl ester is developed by the reaction of ethanol and allotelluric acid.

$$[TeO_2(OH)_2]_n + nC_2H_5OH = [TeO_2(OC_2H_5)_2]_n + nH_2O \quad \ldots \quad \ldots \quad \ldots \quad (2.2)$$

This compound presents some advantages in sol-gel processing and holds a remarkable hexavalent structure of tellurium [133].

However, some specific problems have been observed in these tellurium alkoxides. Tellurium alkoxides and tellurium isopropoxide are both moisture sensitive. It is difficult to handle the precursors for conventional sol-gel processes and make precipitates instead of gels. The alkoxide compounds oligomerize suddenly in the presence of very small amounts of water and modify their reactivity. They are contaminated with sodium chloride frequently from the preparation process and have limited thermal stability [133].

It creates a problem with preferential precipitation of a particular oxide during sol formation due to the different reactivity of the alkoxide precursors. It is difficult to avoid residual porosity and OH-group. For this result, the materials lead to fracture due to the shrinkage of a wet gel upon drying. The sol-gel method is not a cost-effective process. It is a time taking process for deposition and a very costly process for the fabrication of glass. It is impossible to connect a thick layer of nanoparticles on the substrate. In this method, high temperature is required to prepare anatase nano-crystals.

2.3 Chemical Vapor Deposition

Chemical vapor deposition (CVD) is the deposition of solid through the chemical reaction on a heated surface [134]. Chemical vapor deposition is a method that occupies the reaction of a volatile precursor which is inserted into a chamber (vacuum). This vacuum chamber is heated to a particular temperature at which the ancestor gas to respond for the reaction. After this reaction the required coating material deposits on the surface and makes a coating throughout the surface of the substrate [135, 136]. CVD is a versatile technique and is broadly applied for coatings, synthesis of powders, thin films, glass fibers, and other monolithic components [134]. It is possible to make alloys and compounds through the CVD process of metallic and non-metallic materials. Recently, this method can also be used to prepare tellurite glass materials [137-139].

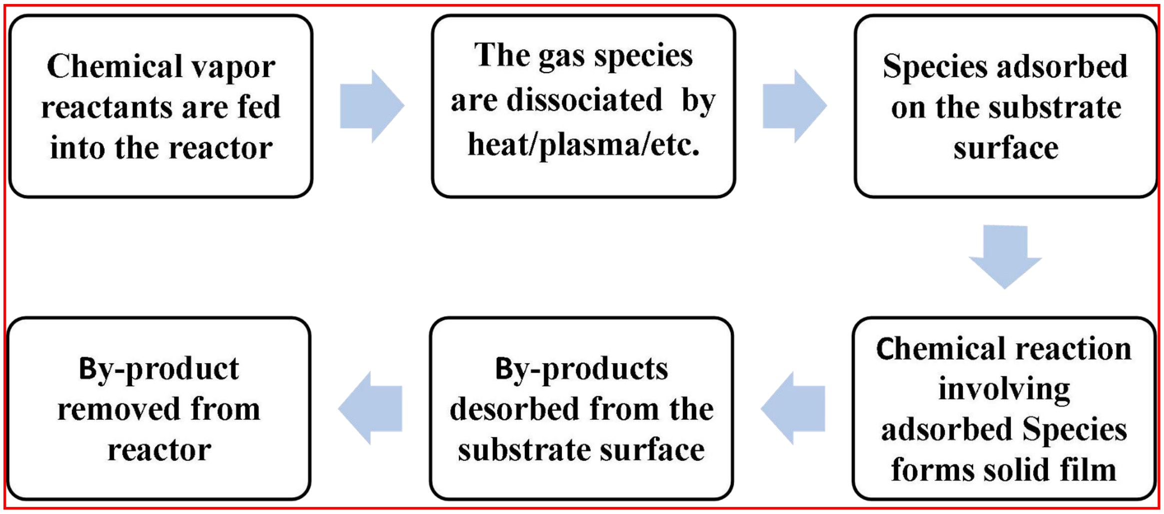

Fig 2.2 Schematic diagram of chemical vapor deposition method for the glass deposition on the substrate.

The zinc-tellurite glass can be made by using the CVD technique with alkyl organo-metallic compounds as the initial volatile precursors of tellurium and zinc such as diethyltellurium ($Te(C_2H_5)_2$), dimethyltellurium ($Te(CH_3)_2$, diethylzinc ($Zn(C_2H_5)_2$) and dimethylzinc ($Zn(CH_3)_2$). These compounds were taken based on the high reactivity of organo-metallic compounds compare to oxygen and water and with highly saturated vapor pressure. The metal impurities in these compounds should not be more than 10^{-5} mass % [139]. Carrier gas for organo-metallic compounds was argon and the compounds with argon gas were interacting in an oxy-hydrogen burner with the required temperature of reactions. The formation of the condensed phase was made by this process. Then the mixtures are ready for tellurite glass.

However, the CVD method is not the entire coating panacea [134]. It also has some disadvantages. The major disadvantage is to supply a high temperature than the room temperature to control the reactions. Normally, the substrates are not stable at that high temperature. Again, the organic exhaust soot is usually toxic to human health and endangers the environmental problem without proper treatment.

2.4 Melt-quenching Process

The most common technique is the melt-quenching technique for the preparation of photonic/electro-optic glass materials. Melt-quenching is the conventional technique of glass making and it includes heating up to a temperature well above the melting point of the mixed ingredients and then quenching of melting glass [140]. This melt-quenching technique has the flexibility of preparing with different compositions of the glass of borate, phosphate, silicate, and other oxide systems. In this method, the thermal stability of the prepared glass materials is high. However, the melt-quenching technique represents a valuable glass fabrication process and recent research has depicted its potential and is not yet explored thoroughly. The doping of different active ions in the glass matrix is quite easy by using this technique. We have chosen this method to increase the hardness and toughness of the glass materials. The melt-quenching technique is also used to refine the structure of the system.

Initially, raw materials are ground into powder form by an agate mortar. For obtaining a more homogenous particle size, the mixture of raw materials is transferred to the agate mortar and ground for several hours initially in a wet medium such as acetone, ethanol etc. [141]. The grounded mixture of raw materials is transferred to the alumina crucible and melted in a furnace. The melted substance is poured into molds for the fabrication of a disk, cylindrical shape, or any other desired size and shape. To get quenched of melting material in air, stainless steel plate can also be used for as prepared glass. The quenched glass is annealed to avoid the internal stresses present within the glasses [142]. The following schematic diagram represents the steps of the melt-quenching technique for the development of dense and transparent glass for photonic applications [143, 144].

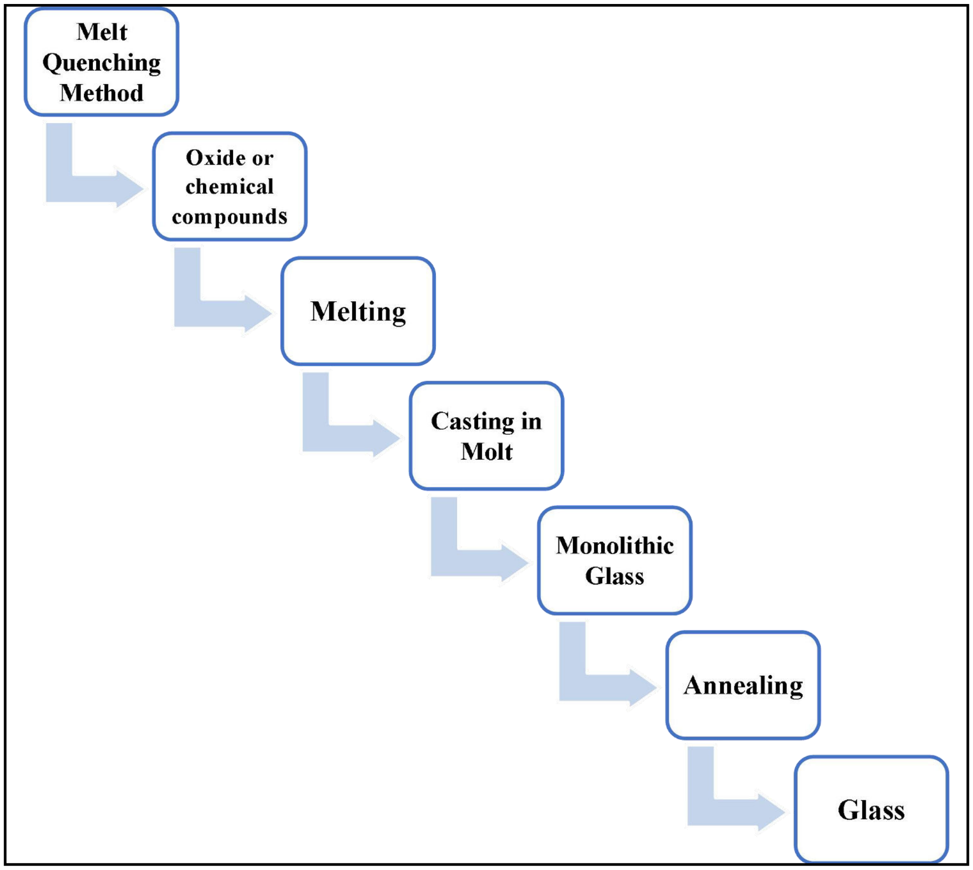

Fig 2.3 Schematic diagram of melt-quenching method for the fabrication of glass.

Na_2O-ZnO-TeO_2 (NZT**)** glasses have been prepared by conventional melt-quenching technique, using high purity precursors ZnO (Zinc Oxide), TeO_2 (Tellurium oxide) and Na_2CO_3 (Sodium Carbonate) manufactured by Merck. ZnO, TeO_2 and Na_2CO_3 powders have been mixed in such a ratio Na_2O: ZnO: TeO_2 is 1:2:7 as a host glass matrix. Rare-earth Oxide like (Eu_2O_3, Nd_2O_3, Sm_2O_3, Pr_2O_3) was added to the host glass as a dopant for (0-2 wt%). The starting materials have been weighed by using an electronic balance after the calculation of the required raw materials. The required amount of mixture has been well ground in an agate mortar and pestle for 2 hours for better homogeneity. The organic material acetone is evaporated from the resulting mixture when the mixture is dried in the air. To get good quality tellurite glass, the melting has been done in two stages at 550 °C for 1 hour and then 650 °C for ½ hour in an electrical box furnace. The mixture is heated up to different temperatures for different rare-earth doped materials.

The alumina crucible is used for the melting purpose of raw materials at relatively low temperatures. If the melting temperature of the glass composition is very high then the alumina crucible will not be used to avoid the diffusion of alumina into the glass composition. Hence, for making the glass material at high temperatures, a platinum crucible can be used for the preparation of melt quench glass. The stainless steel plate is covered with a mica sheet which is cut according to its size from a large mica sheet. The produced melt sample was poured onto a smooth surfaced stainless steel plate (depth 0.15 cm and diameter 3 cm) and cooled down slowly to room temperature to remove internal stress present in the glass samples. The prepared samples were polished using fine emery papers of different grades to increase the brightness. The prepared samples are translucent with different colour according to the rare-earth doped ions.

2.5 Characterization Techniques

An outline of the characterization techniques has been presented in this section to study the various properties of amorphous and or semi-crystalline pure and rare-earth doped NZT glass samples.

2.5.1 Structural characterization by XRD

X-ray diffraction can supply information about crystal structure and unit cell parameters a, b, c, α, β, γ of a crystalline material, crystallinity and crystal size, certain structural defects, phase composition, micro-stress and -strain and texture (orientation of the crystallites in a polycrystalline material). Samples have been ground in an agate mortar to prepare for X-ray powder diffraction.

2.5.1.1 Principle of X-ray Diffraction

X-ray diffraction was performed to establish the actual structural properties of the materials and their crystalline or amorphous phase. The XRD data also supply information about the amorphous or crystallinity nature of the material, inter-planar spacing and average crystalline size. When the selected wavelength of X-ray incident on an atom, the scattering will occur in all directions. If the atomic arrangement is encountered by X-ray, the scattered beams will make stronger in particular directions and diminish in others. When an X-ray strikes a specified group of planes, the scattered beams produce constructive interference due to the arrival at the detector in the same phase [145]. The beams are realized due to constructive interference in a direction with Bragg angle 2θ obeying Bragg's law (shown in Fig. 2.4).

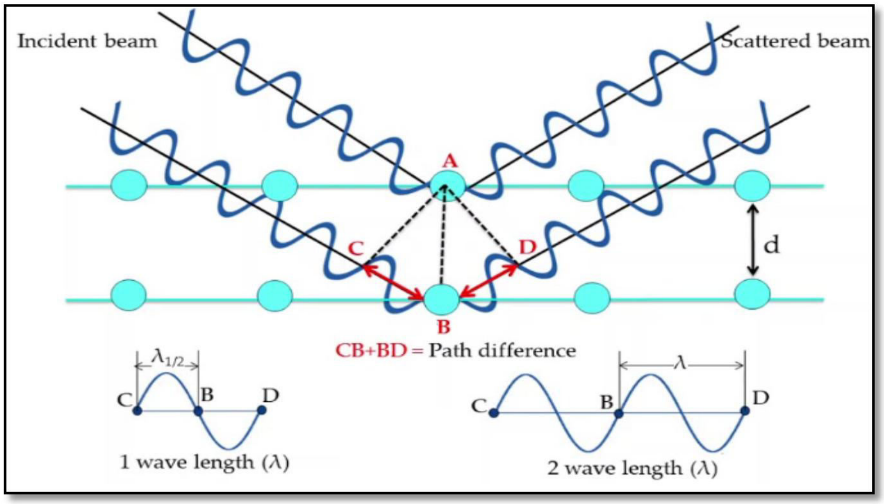

Fig 2.4 Presentation of Bragg's diffraction of X-ray beam from atomic planes.

Fig 2.5 Photograph of X-ray diffractometer experimental set-up.

The constructive interference of the beams arises when the path difference of two beams is an integral multiple of wavelength λ, i.e.,

$$2d \sin\theta = p\lambda \quad \ldots \quad \ldots \quad \ldots \quad (2.3)$$

Where p is as an order number, d is the interplanar spacing, and the grazing angle is θ.

Fig. 2.5 shows the experimental set-up of XRD. Rigaku Mini Flex-600 with CuKα (λ = 1.5418 Å) is used for the X-ray characterization of the materials with the angle of deviation 2θ between 10° and 80°. The peak intensity of X-ray spectra is changed due to the doping in the host glass materials and the peak intensity varies with the variation of dopant concentration. These peaks offer important information of glass materials. The XRD pattern of each glass sample displays different significance. The determination of crystal or amorphous structure of the unknown materials can be obtained by investigation of the XRD data using appropriate software like POWD, COD and also through comparing with known database. The Scherrer equation has been used to calculate the average crystalline size of the particles.

$$D = k\lambda/\beta \cos\theta \quad \ldots \quad \ldots \quad \ldots \quad (2.4)$$

Where D = average crystalline diameter, k = 0.89 a constant, λ = wavelength of X-ray, θ = Bragg's angle, and β = FWHM of the diffraction peak for the Bragg angle θ.

Broad peak identified that the materials give an amorphous nature and sharp peak gives the information about the specific crystal structure of the materials.

2.5.2 Structural Characterization by FTIR spectroscopy

Fourier Transform Infrared (FTIR) spectroscopic analysis methodology is used in industry, organic chemistry, forensic science and academic laboratories to realize the structure of separated molecules, and the component of molecular mixtures. The vibrational band energy of atoms or molecules is absorbed infrared beam at a particular frequency. Various wavelengths of FTIR radiation are absorbed to vibrate by the different bonds in a molecule at different energies. The peak positions and intensity of FTIR spectra of absorption bands create a characteristic fingerprint of the atoms or molecules. FTIR spectroscopy has been widely used in the chemical, pharmaceutical and polymer industries [146]. It is also applied in industry and academic laboratories to better understand the molecular structure kinetics, pathways in chemical reactions, mechanism and catalytic cycles. FTIR spectra identified the particular specification of final products, raw materials and intermediate materials. It is also applied to build up the scale of chemical reactions and optimize the by-product impurities. FTIR spectra can be used to control and achieve the final product of the samples. It is also applied in process analytical technology (PAT). The working formula of FTIR and Michelson interferometer are the same.

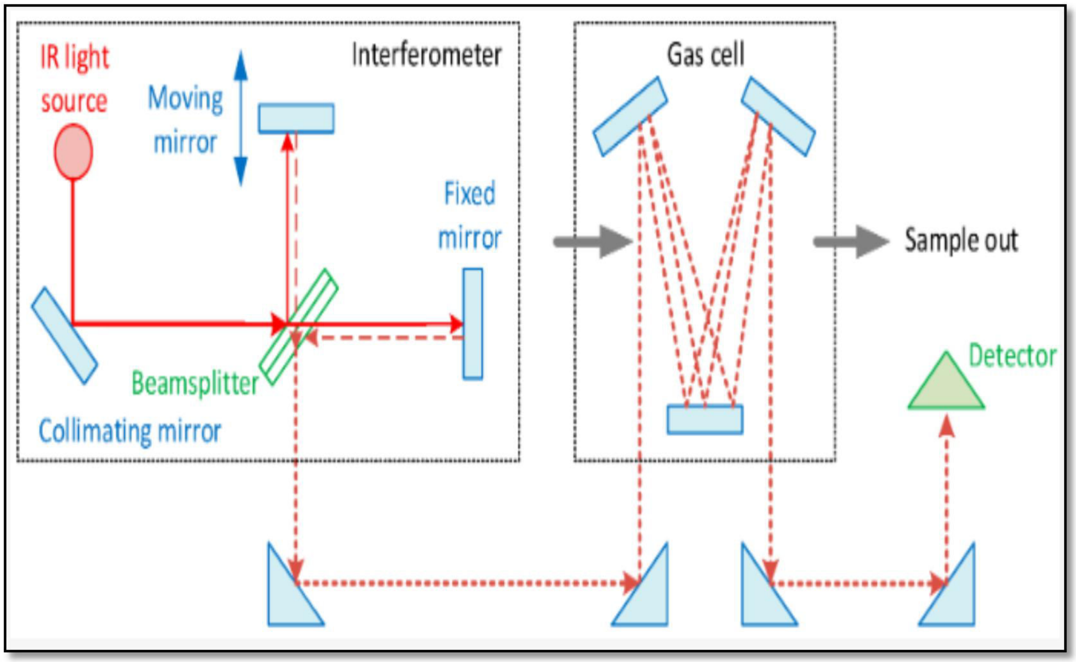

Fig 2.6 Schematic view of FTIR spectrophotometer.

A specific wavelength which is absorbed by covalent bonds of molecule changes the vibrational energy in the bond. The vibration (stretching or bending) induced by IR radiation depends on the atomic bonding. The transmission pattern is different for different types of molecules and functional groups due to the absorption of different frequencies. To get the spectrum of FTIR one can plot transmittance along Y axis and wave number (cm^{-1}) along X-axis. All the data are taken using BX-II spectrophotometer within the wave number range of 400-4000 cm^{-1} to find out the vibrational bond and bond angle in the present work. Peaks of the FTIR spectra are fitted to their separate positions with the help of Gaussian and Origin software. The study of FTIR has been performed in open-air condition. Fourier transform infrared (FTIR) spectroscopy has been used to characterize the chemical bonds and/or detect the molecular structure of organic/inorganic samples, using the techniques of absorption/transition, emission and or photoconductivity of solid [147-148]. The schematic diagram of the FTIR spectrometer has been shown in Fig. 2.6. Our FTIR spectrometer (RX1 Perkin Elmer FTIR) collected spectral data with the resolution of 1 cm^{-1} for 50 scans in the wave number range 400 to 4000 cm^{-1}.

2.5.3 Thermal Characterization by DTA/TGA

The study of the thermal properties i.e., the temperature-dependence properties of materials can be studied by a group of technique known as Thermal Analysis (TA). It provides the characterization of mass changes, enthalpy and coefficient of heat expansion and thermal capacity of the prepared materials with the variation of temperature [149]. It is also applied in solid-state chemistry to investigate the thermal degradation reactions, reactions in the solid state, phase transitions and phase diagrams. Differential Thermal Analysis (DTA) curve can be explained by the change in crystal structure, melting temperature, critical temperature, glass transition temperature etc. DTA can be explored the thermal properties of polymers, minerals and biological materials. DTA can explain the change in the crystal structure, and the chemical reaction whether the reaction is endothermic or exothermic. It can determine Crystallization temperature (exothermic), Melting temperature (endothermic, Vaporization temperature (endothermic) and Sublimation temperature (endothermic).

TGA can be applied to investigate the characterization of metals, plastics, inorganic and organic materials, ceramics, composite materials, and glasses. Thermo gravimetric analysis (TGA) determines mass change, thermal stability, presence of moisture, material purity, etc. as a function of temperature.

Fig 2.7 Experimental set-up of DTA/TGA.

2.5.4 Optical property analysis by UV-Visible Spectroscopy

Ultraviolet and visible (UV-Vis) spectroscopy is a simple and powerful tool for detecting the presence of ultraviolet to visible optically active molecules/components in the sample. Arnold Beckman in July 1941, first time introduced a UV-Vis spectrophotometer, based on the UV and Visible light absorption mechanism [150]. A beam of light is reflected or transmitted from a sample, and a part of the incident light is absorbed. According to Bohr's law, excitation and de-excitation states are taking place in molecules of the sample due to the absorption of light. Collecting the transmitted and or reflected light beam from the sample by detector we found a discrete spectrum. Analyzing the spectrum, we detect the presence of molecules/chemical bonds and calculate various optical and or physical properties of the sample [151-152]. Basic mechanisms, structure, some specific applications and accuracy have been discussed in this work.

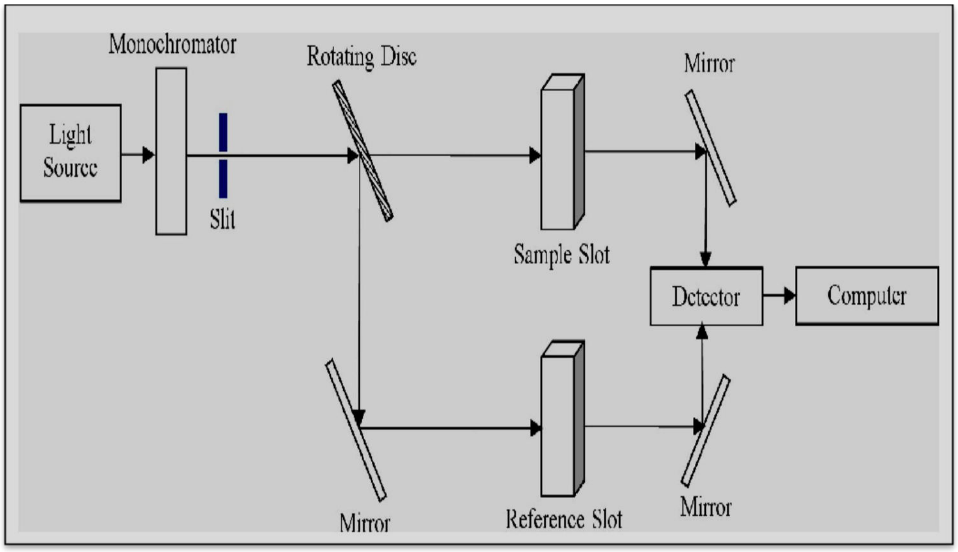

Fig 2.8 Schematic view of the absorption spectrophotometer.

Fig 2.9 Photograph of UV-Visible spectrophotometer (Perkin-Elmer).

2.5.5 Optical and Electronic properties analysis by Photoluminescence Spectroscopy

In the photoluminescence process, xenon lamp is used as an excitation source due to its emitted wavelength lying from ultraviolet to the infrared region. A specific wavelength of light is produced by an excitation monochromator for excitation and then a preferable slit is used to control the intensity of the incident beam striking the material. The sample absorbs the incident light beam for exciting one of its electrons to the higher electronic excited state. The materials release energy through the radiation of electromagnetic waves due to the return of electrons to a lower energy state. These electromagnetic radiations are detected by the detector with a secondary monochromator, positioned, perpendicular to the arriving light and then associated with a computer for receiving the emission data. Fluorescence is one of the main characteristics of photoluminescence spectroscopy. Different types of parameters of the samples like a defect, impurity level, and band gap, etc. are described with the help of photoluminescence characterization.

(i) The PL energy attributed to various defects and energy levels of impurity can be predicted with the PL intensity and detect the amount of impurity present in the materials.

(ii) Recombination is connected to the radiative and nonradiative mechanisms. The recombination mechanism depends on the temperature of the photo-excitation and provides the PL intensity.

(iii) The PL spectra occur due to the transition between various states of the conduction and valence bands of the materials and in effect calculate the optical band gap of the materials. Band gap energy determination is generally useful when working with prepared semiconductor materials.

The fluorescence spectrometer (Perkin Elmer LS 55) has been used to study the luminescence properties and the samples are excited with Xe-Laser of wavelength 325 nm.

Fig 2.10 Photograph of photoluminescence spectrometer.

2.5.6 Electrical Characterization by LCR Meter

Dielectric properties of pure NZT and rare-earth doped NZT glass materials have been measured by 3522-50 LCR-meter Hi TESTER (HIOKI, Japan). Dielectric constant can be measured in frequencies of 10 Hz to 8 MHz. The dielectric constant depends on the polarization method such as dipolar, ionic, interfacial and electronic polarization remaining in the sample. The electrical property of the glass materials has been performed at desired temperatures for the different rare-earth doped NZT compounds. A small part of the large glass slab is cut as a round-shaped pallet and polished on both the flat faces. The flat faces are painted with thin silver paint to form the electrodes. The polished pellets are heated at the required temperature to avoid moisture.

Fig 2.11 Experimental set-up of LCR meters.

Then the sample is ready for measurement by using LCR-meter. This measurement supplies the phase angle, impedance, capacitance of parallel plate, dielectric loss, and other parameters at room temperature for different frequencies [153].

$$\varepsilon = \frac{Ct}{\varepsilon_0 A} \quad \dots \dots \dots \quad (2.5)$$

Where t is the thickness of the samples, C is the capacitance of the parallel plate, $\boldsymbol{\varepsilon}_0$ is the dielectric constant in free space, and the area of the samples is denoted by A. The thickness and radius are measured with the help of a screw gauge. The dielectric constant ($\boldsymbol{\varepsilon}$) of the samples is determined using Eq. 2.5

2.5.7 DC Conductivity

Electrical conductivity measurement is required for a production method for quality control and as well as quality assurance. Specifically, it is applied to determine the conduction of an electrical current through the material. The DC conductivity depends on the temperature [154]. The pure and rare-earth doped NZT glass materials are prepared as a round-shaped pallet. The flat faces of the pellets are electroded and studied the DC conductivity measurement with temperature.

Fig. 2.12 shows the schematic circuit diagram of DC conductivity measurement. The current data in nano-ampere order with various temperatures are collected using a simple Ohms circuit. The DC electrical conductivity (σ_{dc}) can be determined using the following formula

$$\rho = \frac{RA}{t} \quad \dots \dots \dots \quad (2.6)$$

$$\sigma_{dc} = \frac{t}{RA} \quad \dots \dots \dots \quad (2.7)$$

Where ρ is the resistivity, R is the resistance, A is the area and t is the thickness of the sample. The actual experimental set up for the measurement of DC conductivity is displayed in Fig. 2.13.

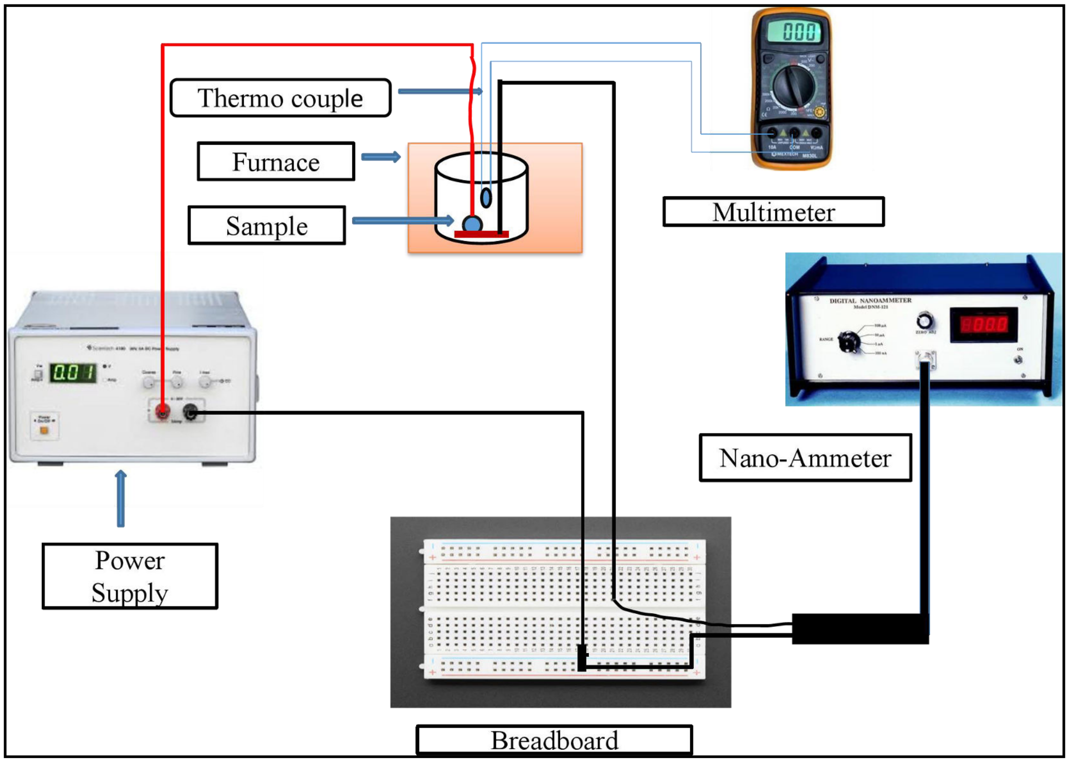

Fig 2.12 Schematic circuit diagram of DC conductivity measurement.

Fig 2.13 Experimental set-up for temperature dependent DC conductivity measurement.

Now, the activation energy E_a can be estimated from the DC conductivity measurement, and the conduction mechanism can be explored from this measurement. The activation energy is related to the DC conductivity and expressed by Arrhenius empirical relation as follows [155]

$$\sigma_{dc} = \sigma_0 exp^{\frac{E_a}{K_B}}T \quad \dots \dots \dots \quad (2.8)$$

Where, σ_0 = pre-exponential factor, K_B = Boltzmann constant, and T = absolute temperature.

Chapter-3

Enhancement of optical emission and dielectric properties of Eu^{3+}-doped Na_2O-ZnO-TeO_2 glass material

3.1 Introduction

Rare-Earth ions (RE^{3+}) doped tellurite glasses have drawn much attention recently due to their large potential applications in optoelectronic devices such as solid-state lasers, three-dimensional displays, optical amplifiers, planar waveguides, field emission displays, white light emitting diodes and high-density frequency domain optical data storage [156, 157]. Glass scintillators are an important component of optical devices that can be fabricated easily depending on the various shapes and sizes. During the last two decades, the precise properties of tellurite glass have been investigated for demonstration of various spectroscopic and nonlinear optical device applications such as broadband light emission and optical communications network [158].

TeO_2 is a very important material to form glass and glass ceramics along with the alkali-based or alkaline earth, and transitional element or transition metal oxide (TMO) [159]. TeO_2 is a semiconducting material with strong covalent bonding between oxygen with tellurium. This bonding does not allow creating the required level of deformation to form the glass itself by TeO_2 [160-163]. In comparison with the other families of glasses like borate, silicate, fluoride, chalcogenide or lead-based glass, tellurite glass has interesting physical properties such as high thermal stability and corrosion resistance in accountability with this strong tellurium oxygen bond. It has been reported that tellurite glass fibers are very good broadband amplifiers than the normal rare-earth, like neodymium and/or erbium doped silica optical fibers. This broadband amplifier is more applicable to the optical communications devices and data transfer technology [64]. Tellurite glass matrix produces a wide band frequency window (from the visible to the mid-infrared region) with low cutoff phonon energy (~ 700 cm^{-1}), high refractive index (~ 2.0), and large chemical stability. This family of glasses has been used as a host matrix for studies in large wavelength ranges with the doping of trivalent rare-earth ions [164].

Again, the study of luminescence properties of the rare-earth elements hosted in tellurite non-crystalline glass, and glass ceramics are strongly attractive because of their applications in optoelectronics devices. Europium (Eu) is a rare-earth element which is more suitable as a dopant ion in the TeO_2 glass matrix for photonics devices because the Eu^{3+} ions are useful for photo conversion due to the $4f^6$ electronic configuration. Eu^{3+}

doped tellurite glass can carry out attentively persistent spectral hole-burning in the $^7F_0$ → $^5D_0$ transition among all glasses [165]. However, little attention has been made to investigate thoroughly the Eu^{3+}doped tellurite glass, and glass ceramics.

In this present work, the focus has been made to study thoroughly the glass formation, optical, dielectric constant, and conduction mechanism of the Eu^{3+} doped Na_2O-ZnO-TeO_2 glass ceramics with various doping concentrations.

3.2 Experimental Outline

Na_2O-ZnO-TeO_2 (NZT**)** glasses have been prepared by conventional melt-quenching technique, using high purity precursors ZnO (Zinc Oxide), TeO_2 (Tellurium oxide), Na_2CO_3 (Sodium Carbonate) and Eu_2O_3 (Europium Oxide), manufactured by Merck. ZnO, TeO_2 and Na_2CO_3 powders have been mixed in such a ratio Na_2O: ZnO: TeO_2 is 1:2:7 as a host glass matrix. The host glasses were doped with (0-2) wt% Eu_2O_3. The required amount of mixture has been well ground in an agate mortar and pestle for 2 hours for better homogeneity. To get a good quality telluride glass, the melting has been done in two stages at 400 °C for 1 hour, and then 475 °C for ½ hour in an electrical box furnace. The alumina crucible was used as a molt mixture materials container. The produced melt sample was poured onto a smooth surfaced stainless steel plate (depth 0.15 cm and diameter 3 cm) and cooled down slowly to room temperature to remove internal stress present in the glass samples. A Perkin Elmer Instrument (Pyris Diamond TG/DTA, thermo-gravimetric/differential thermal analyzer) was used for the thermal characterization and analysis of the mixtures of precursors to form the telluride glasses in the presence of an argon environment. The rate of scanning was 10 °C/min between the temperature range of room temperature (30 °C) and 600 °C.

An X-ray diffractometer (RIGAKU model: Japan, XRD 6000, λ_α = 01.5418 Å) was used to study the X-ray diffraction of these samples. Optical measurements of pure, and doped glasses were carried out using Perkin-Elmer UV/VIS/NIR (Lambda-35) a double beam optical spectrophotometer for optical absorption spectrum in the wavelength range 350-800 nm, and using fluorescence spectrophotometer HITACHI Model F-7000 for fluorescence measurements from the wavelength 500 - 775 nm at room temperature. The dielectric constants (ε) of these samples were studied using HIOKI MI- 3536 LCR HiTESTER at room temperature for the frequency range 100 Hz - 8 MHz. The conductivity of these samples was measured using laboratory-made experimental set-up in the temperature range 50 ^{o}C to 160 ^{o}C.

3.3 Results and Discussion

3.3.1 Thermal Analysis

DTA curve of the pure, and Eu_2O_3 doped NZT glasses from the temperature 35 °C to 650 °C at a heating rate of 10 °C/min is shown in Fig. 3.1. Three consecutive endothermic peaks are observed on the DTA curve between (92 - 162) °C for the pure sample and Eu_2O_3 doped NZT glasses. These endothermic peaks on the DTA curve are ascribed to the desorption or removal of moisture [166]. DTA curve attributed the exothermic peaks that occurred when the CO_2 is released from the precursor powders in the temperature range (392 - 415) °C for pure, and (1 and 2) wt% Eu_2O_3 doped NZT glasses respectively.

These curves also suggest that the phase transition occurred due to the transition of solid powder form to liquid form through melting at around 446 °C. Actually, the melting point of TeO_2 is around 730 ^{o}C [167] which is decreased due to the presence of Na_2CO_3 mixed with ZnO. This decrement in melting point can be explained by the decomposition of Na_2CO_3 and the mixture of TeO_2-ZnO compounds.

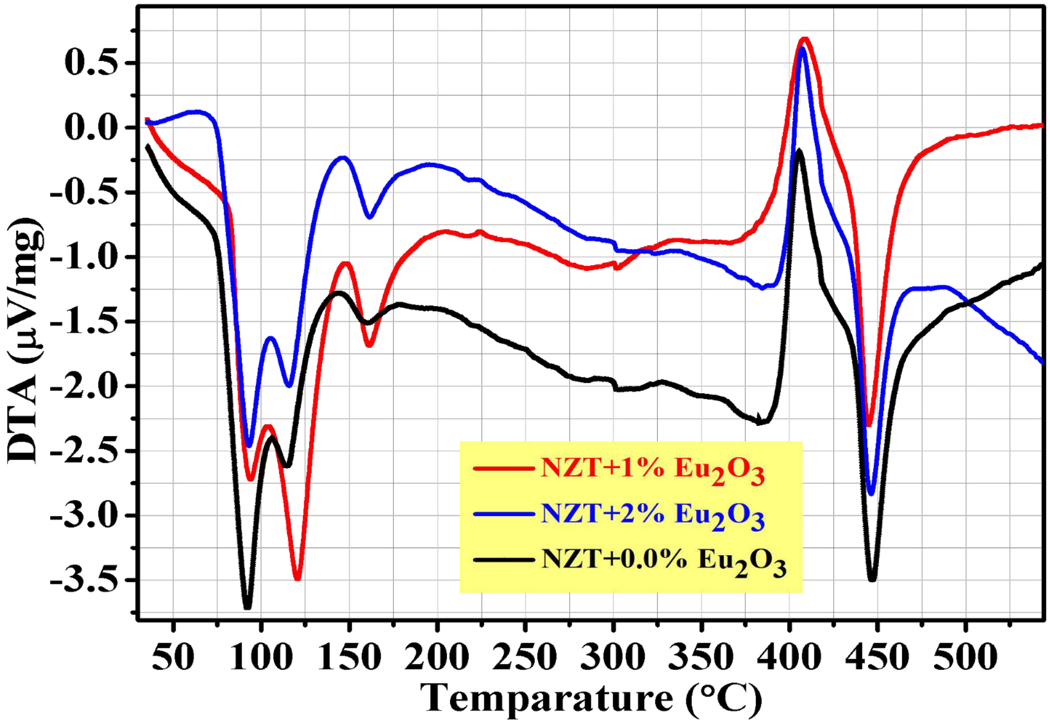

Fig 3.1 DTA curves for pure, 1.0 wt%, and 2 wt% of Eu_2O_3-doped NZT glass materials.

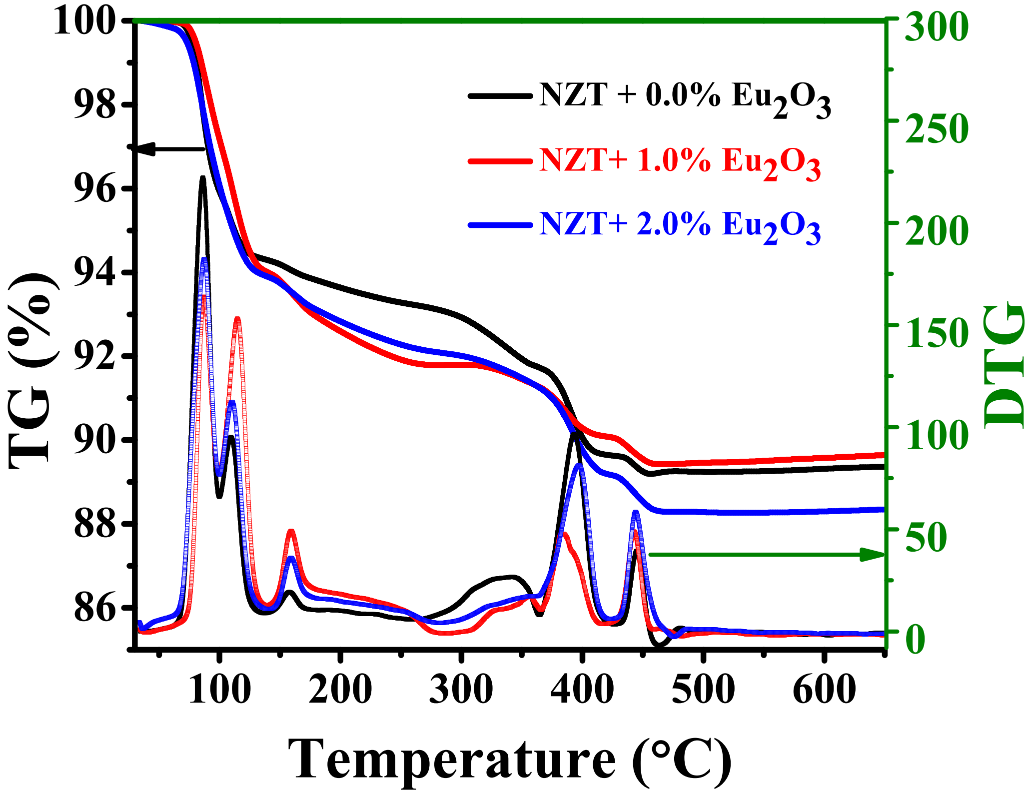

Fig 3.2 TGA and DTG curves of pure, 1.0wt%, and 2wt% Eu_2O_3-doped NZT glass materials.

Fig. 3.2 represents the TG with DTG curve of the pure and Eu_2O_3 doped NZT glasses. The weight loss started when the powders heated beyond 70 °C. TG/DTG curve represents the 10.6% mass loss out of total mass from room temperature (35 °C) up to 650 °C through stepwise decomposition of the compounds, and release of volatile substances, like water, and carbon dioxide. It is found from Fig. 3.2 that the mass losses 5.46% of its weight at about 92 - 160 °C attributed to the removal of moisture [168]. The DTG analysis curve shows the confirmation of weight loss due to the escape of absorbed water, and other volatile materials through displayed three maxima at 86 °C, 115°C, and 159 °C. The DTG peak is observed near 395 °C for all the samples because of the decomposing of anhydrous Na_2CO_3. The CO_2 evolved through the reaction mechanism $Na_2CO_3 \rightarrow Na_2O + CO_2$ at that particular temperature which is also predicted from the DTA curve of Fig. 3.1. The CO_2 produced at 380-409 °C was identified by the TGA curve. However, the decomposition temperature of the Na_2CO_3 was decreased when it was mixed with TeO_2 and decomposition occurred at 392 °C for the first time.

The last peak in the DTG curve at 444 °C has shown a small change of mass loss during the melting of the solid powder samples. This may be suggesting that remain part of Na_2CO_3 completely decomposes, and evolve CO_2 with a small mass at that temperature and also with some volatile materials. After the temperature of 460 °C there is no weight loss revealing that the samples have been prepared as glass materials.

3.3.2 X-ray Diffraction

The XRD pattern of pure NZT and (0.5 wt% - 2 wt%) Eu_2O_3 doped samples have been recorded by using an X-ray diffractometer with CuK_α radiation, λ_α= 0.15418 nm, and shown in Fig. 3.3. The pattern of XRD shows no discrete sharp peaks, and there are two broad peaks have been found in the region of the glancing angle at 18° to 34°.

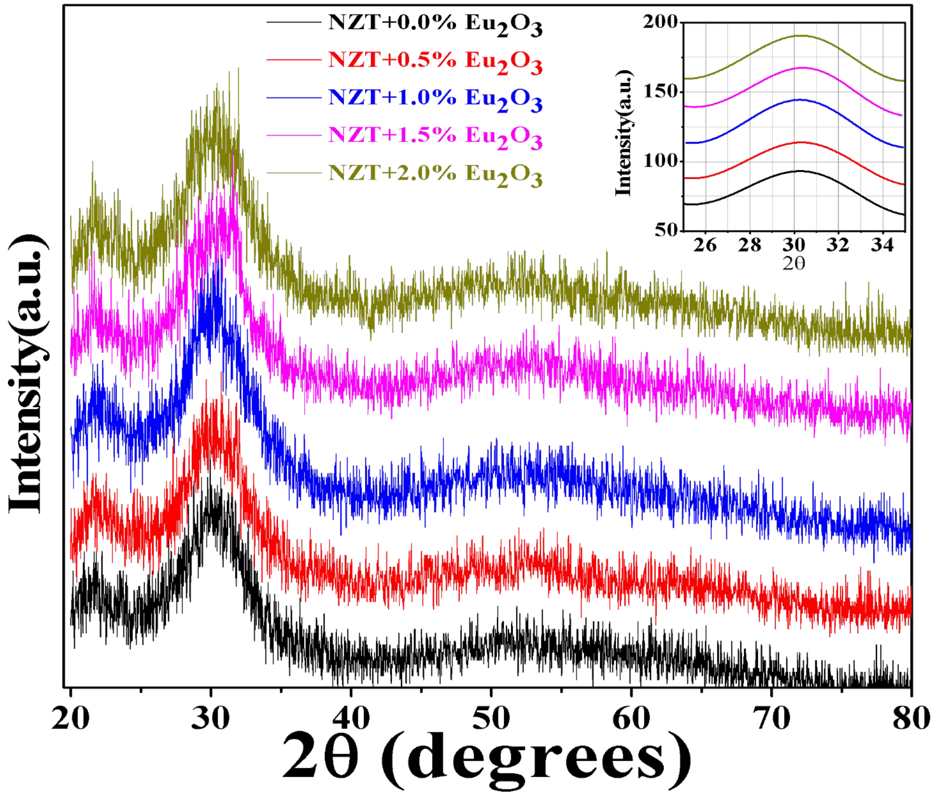

Fig 3.3 XRD pattern of pure and various concentrations of Eu^{3+}-doped NZT glass samples.

A large broad peak around 2Θ ≈ 28°-33° has been displayed, which is typically the characteristics of long-range structural disorder. The broad continuous pattern of X-ray diffraction, therefore, reveals the amorphous nature of these glasses [169-170].

3.3.3 Optical Properties

3.3.3.1 Optical Absorption

The optical absorption spectra of Eu_2O_3-doped NZT glasses have been displayed in Fig. 3.4. The recording of absorption intensity was carried out in the visible region (350 - 800 nm) at room temperature with the band assignments. It is found from Fig. 3.4, the absorption intensity increases gradually with the increase of doping concentration of Eu_2O_3. There is a very small anomaly present in the absorption spectra of Eu^{3+}doped glasses at wavelength 535 nm.

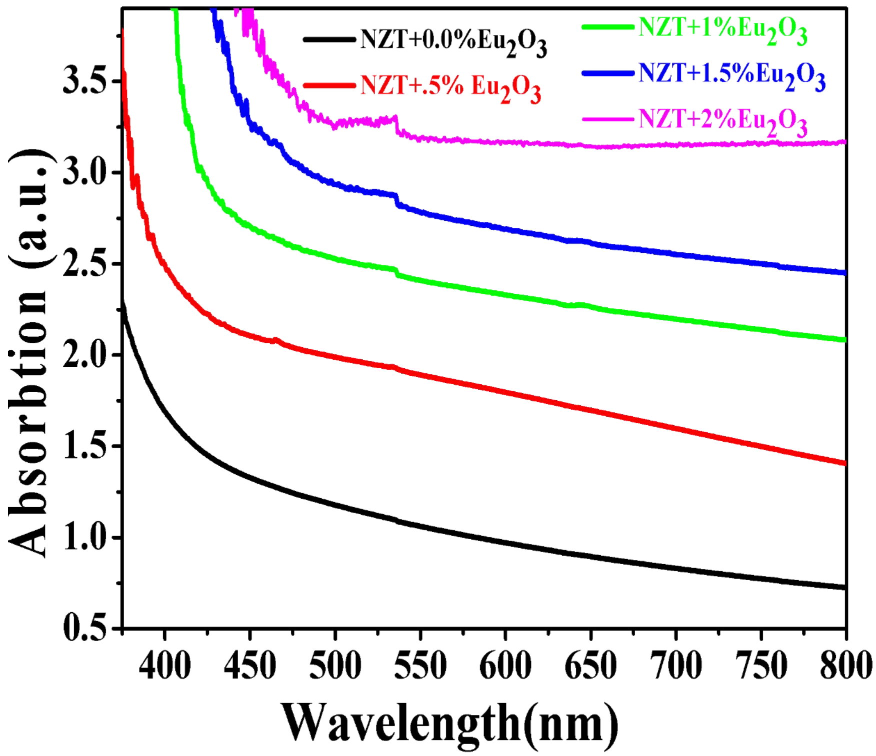

Fig 3.4 The absorption spectra of pure and different concentrations of Eu^{3+}-doped NZT glass samples.

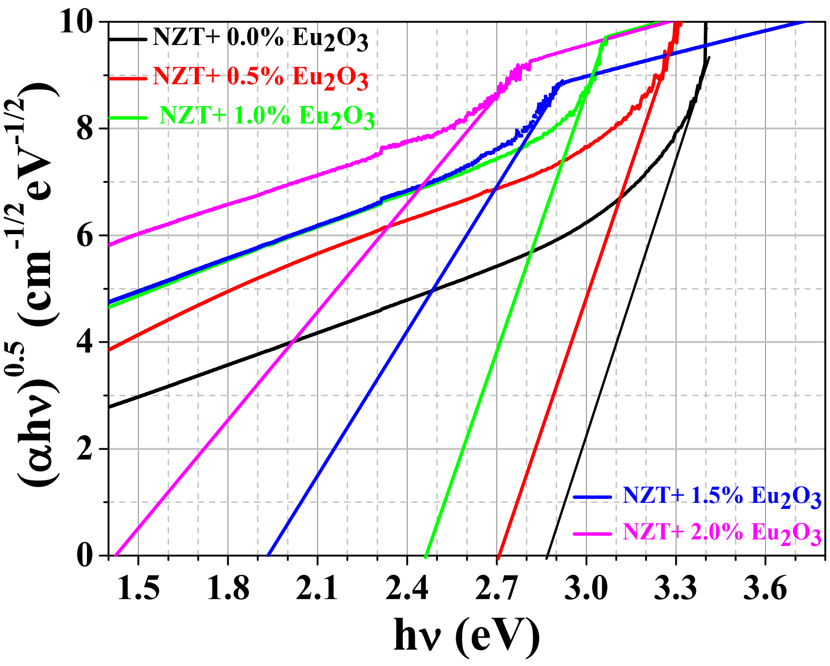

Fig 3.5 Tauc's plots for pure and various concentrations of Eu^{3+}-doped with NZT glass samples.

This anomaly predicts the transitions from the ($^7F_1$) ground state to ($^5D_1$) for the doping of Eu^{3+} ions. The weak anomaly occurs due to the spin-forbidden transitions for the absorption lines $^7F_J \rightarrow {}^5D_J$ [171]. The increment of this anomaly in the absorption band edge may be due to the internal conversion of the ZnO by oxy-telluride groups which has been already confirmed through fluorescence measurement [71]. ZnO is interlinked to the oxy-telluride groups through the axial Te-O bonds. It has been found that the number of non-bridging oxygen increases due to the modification of ZnO and oxy-telluride group exchange interaction.

The optical band gap has been studied using the formula of Davis and Mott for the coefficient of absorption $\alpha(\nu)$ from the optical absorption spectrum and band edge measurement

$$\alpha(\nu) = \left(\frac{1}{t}\right) \ln\left(\frac{I_0}{I_t}\right) \quad \dots \dots \dots \quad (3.1)$$

Where t is the thickness of the sample, and I_0 and I_t are the intensities of the incident and transmitted radiation respectively [172].

The variation of $(\alpha h\nu)^{1/2}$ with hν (Tauc's plot) is shown in Fig. 3.5 for some of the glass samples of the NZT with different concentrations of Eu_2O_3 doped series. The indirect band gap energy varied between 2.86 eV, 2.71 eV, 2.47 eV, 1.94 eV, and 1.43 eV due to increasing concentration of the Eu_2O_3 from 0 to 2 wt% respectively. The values of band gap energy of pure and doped samples are tabulated in Table 3.1 and depicted a continuous decreasing trend with the increase of Eu_2O_3 concentration [172]. This results in an increase in the structural compactness in the network of the glass [169]. The decrease in the values of band gap energy may be carried out by the accumulation of electron localization caused by the glass network's structural changes.

Table 3.1 Band gap energies of pure and Eu_2O_3-doped NZT glass samples.

Sample name	Band gap energy (Eg in eV)
NZT+0.0% Eu_2O_3	2.86
NZT+ 0.5% Eu_2O_3	2.71
NZT+ 1.0% Eu_2O_3	2.47
NZT+ 1.5% Eu_2O_3	1.94
NZT+ 2.0% Eu_2O_3	1.43

3.3.3.2 Fluorescence Spectra

Fig. 3.6 shows the emission spectra for different concentrations (0.5 wt% - 2 wt%) of Eu^{3+} ions doped with NZT glasses. The spectra have been recorded for samples with four different concentrations of Eu_2O_3 at an excitation wavelength of 395 nm in the range 520 - 775 nm. It is found that there is no transition occurred for the pure glass sample whereas the intensity of the emission due to transition increases with increasing the doping concentration of Eu^{3+} ions gradually. The peak positions of emission spectra of Eu^{3+} ions doped glasses are similar to $^5D_0 \rightarrow {}^7F_J$ (J = 0 to 4) transitions. Six emission bands are displayed corresponding to $^5D_1 \rightarrow {}^7F_1$ at 537 nm, $^5D_1 \rightarrow {}^7F_2$ at 556nm, $^5D_0 \rightarrow {}^7F_1$ at 591 nm, $^5D_0 \rightarrow {}^7F_2$ at 614 nm, $^5D_0 \rightarrow {}^7F_3$ at 653 nm, $^5D_0 \rightarrow {}^7F_4$ at 703 nm with the excitation wavelength λ_{ex} = 395 nm. The energy level diagram of Eu^{3+} ions doped NZT has been shown in Fig. 3.7.

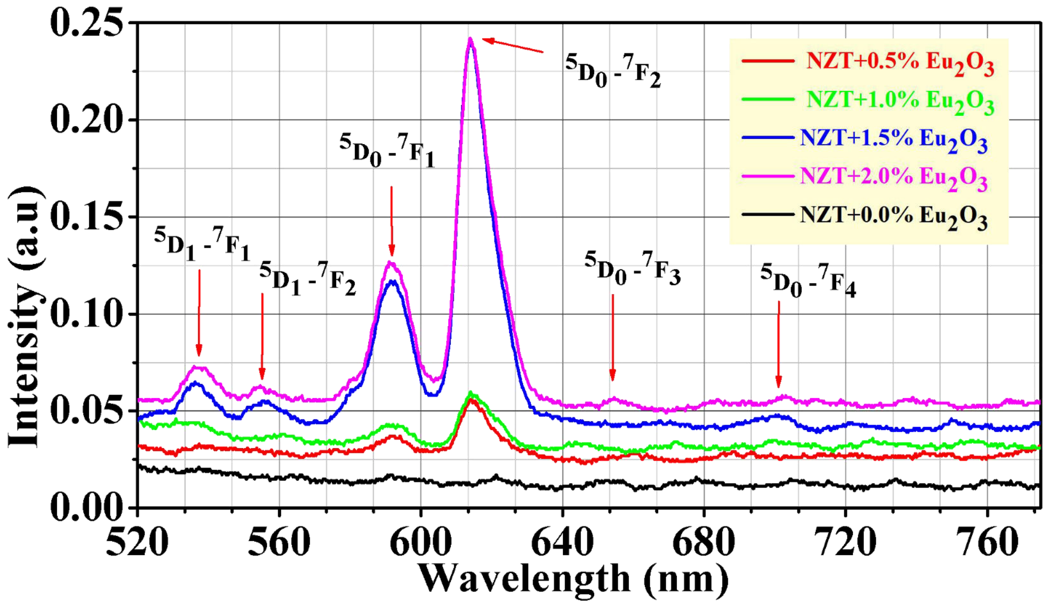

Fig 3.6 Luminescence spectra of pure and Eu^{3+}-doped NZT glass system excited at 395 nm.

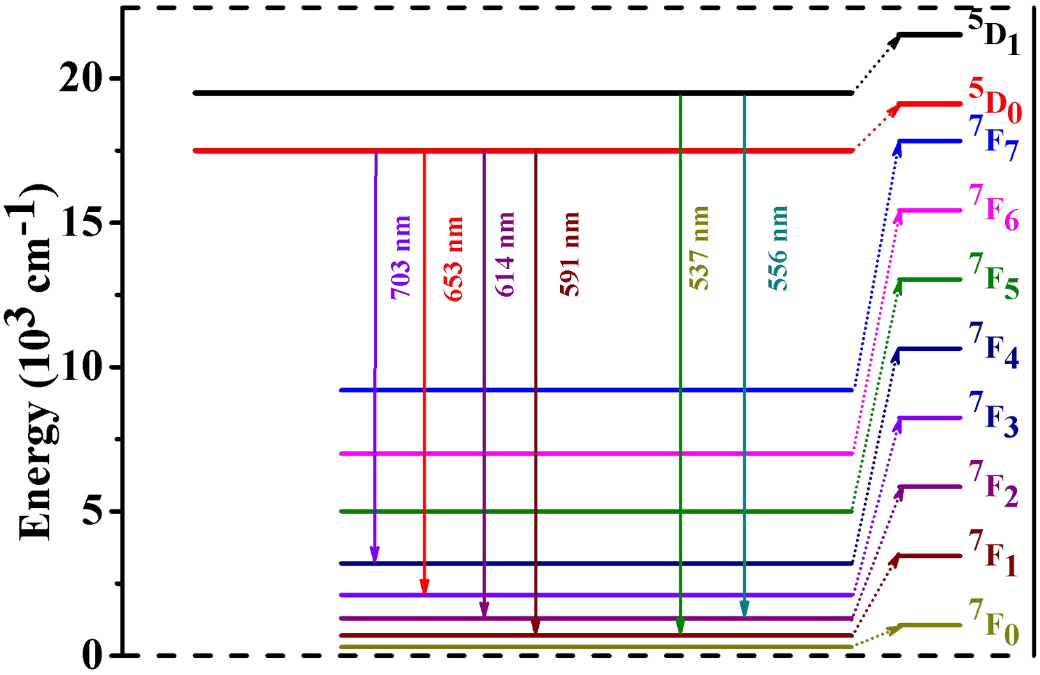

Fig 3.7 Energy levels diagram of Eu^{3+}ions.

The narrow emission bands are produced because of the shielding effect of $4f^6$ electrons by 5s, and 5p electrons in outer shells in the Eu^{3+} ion [165, 172-174]. The $^5D_0$

→ $^7F_3$ and $^5D_0$ → $^7F_4$ emissions are comparatively very weak similar to other reported Eu^{3+} glass systems [174-175].

The spectra displayed very high intense emission at 614 nm with the transition line $^5D_0$ → $^7F_2$. This transition has been produced due to the electric-dipole transition mainly depending on the localized symmetry of coordination surroundings around Eu^{3+} ions in the host matrix of telluride glasses [164, 172]. The transition line $^5D_0$ → $^7F_1$ at 591 nm arises for the magnetic-dipole transition which does not depends on the local symmetry of the surroundings of Eu^{3+} ions [174]. All other transitions in the lower, and higher regions for the lines $^5D_{0,1}$ → $^7F_{2,4}$ and $^5D_{0,1}$ → $^7F_{1,3}$ are carried out due to electric-dipole (ED) and magnetic-dipole (MD) orientations respectively [172].

3.3.3.3 Cross Section

From the Lambert-Beer dependency, the absorption cross-section of the $^5D_0$ → $^7F_2$ transition of Eu^{3+} ions has been determined from the emission absorption spectra using the formula

$$\sigma_{ab}(\lambda) = 2.303 \log(I_0/I)/(N\, t) \quad \ldots \quad \ldots \quad \ldots \quad (3.2)$$

Where $\log(I_0/I)$ is absorbance, t is the sample thickness, and N is the Eu^{3+} ion (ions/cm^3) density in the host matrix telluride glass. There are many ways to find the emission cross-sections. The emission cross-section is calculated using Ma-Cumber (1964) theory [176]. The absorption and emission cross-section are related as

$$\sigma_{emi}(\lambda) = \sigma_{ab}(\lambda) \exp[(E - h\nu)/K_B T] \quad \ldots \quad \ldots \quad \ldots \quad (3.3)$$

Where ν is the phonon frequency, E is the net free energy required to excite one Eu^{3+} from $^5D_0$ → $^7F_2$ state at temperature T, h is the Planck's constant, and K_B is the Boltzmann constant. Fig. 3.8 shows the calculated emission cross-sections for the $^5D_0$ → $^7F_2$ transition of Eu^{3+} ions in different concentrations of tellurite glasses. The emission-cross section is decreasing for the higher concentrations of Eu^{3+}-doped in different concentrations of NZT glass samples, which is shown in Fig. 3.8.

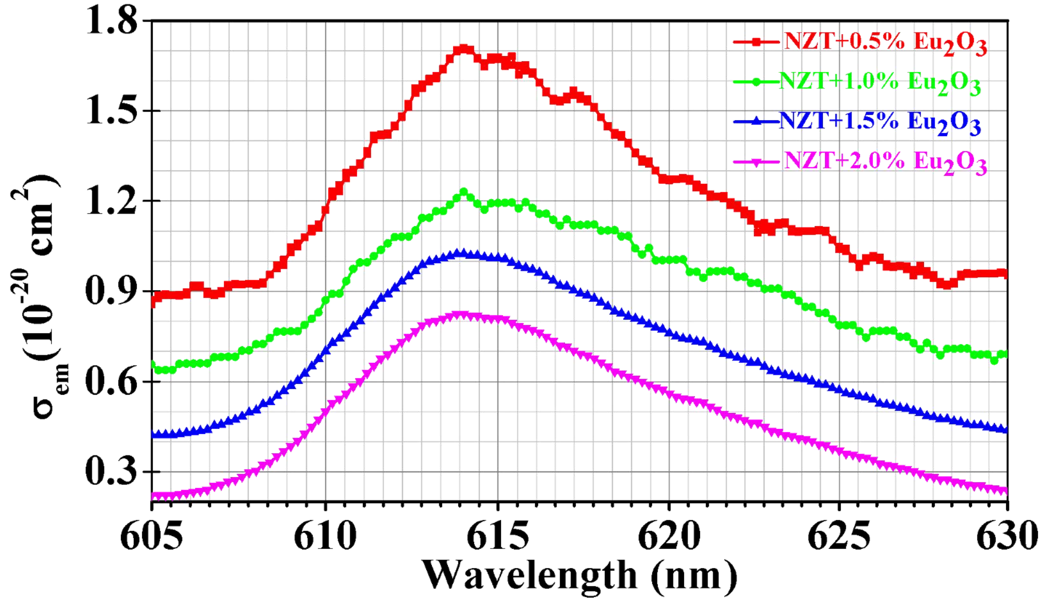

3.8 Emission cross-section spectra for pure and Eu^{3+}-doped NZT glass samples.

3.3.4 Electrical Property

3.3.4.1 Dielectric Constant

The dielectric constant (ε) of Eu^{3+} doped NZT has been measured in the frequency range 100 Hz to 8 MHz at room temperature and shown in Fig. 3.9. This figure depicts that the variation of ε is linear and nearly independent within this wide frequency range. This behavior arises due to the insignificant contribution of ionic, orientation, and space charge polarization in this frequency range [177]. Only the electronic polarization may contribute to the total polarization enhance the dielectric constant remains independent of frequency in the frequencies under investigation. Again, it is also found that the values of ε are increased with increasing the doping concentration of Eu^{3+} ions. This behavior is attributed mainly to the ionic polarizability arising from the contribution of the Eu^{3+} ions in the glassy semiconducting material. Therefore, the numerical values of ε increase with the doping concentration of Eu^{3+} ions.

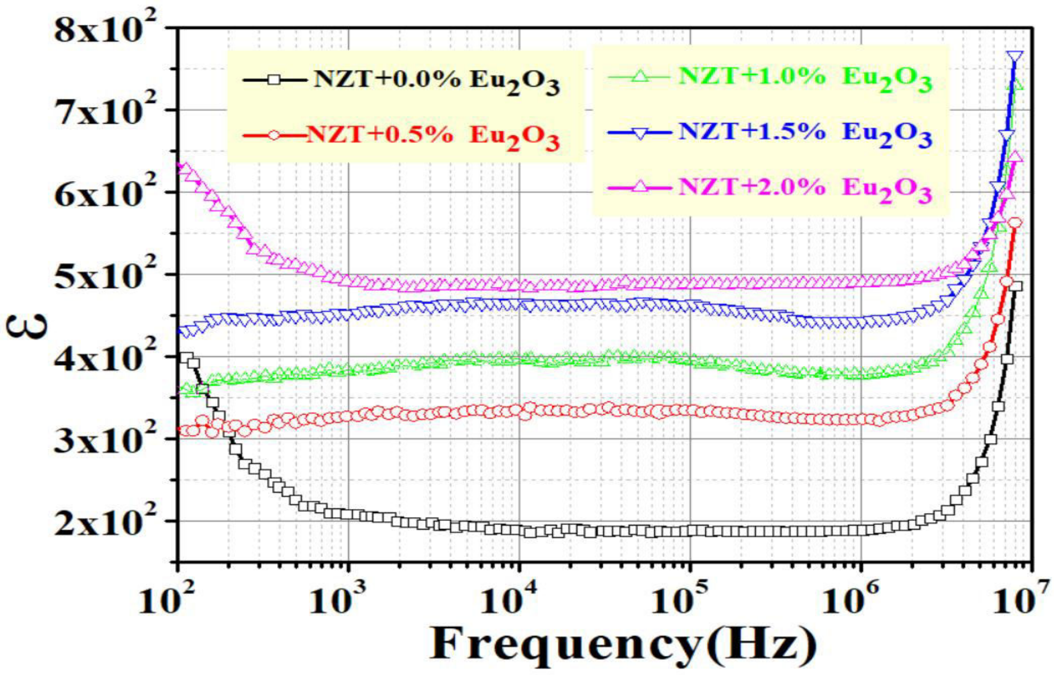

Fig 3.9 The variation of ε with the frequency for pure and Eu^{3+}-doped NZT glass samples at room temperature.

3.3.4.2 DC Conductivity

The temperature dependence of electrical conductivity has been shown in Fig. 3.10. The variation of ln σ with 1000/T plots shows conductivity increases with increasing temperature for all the samples and also increases with a doping concentration of Eu_2O_3. Yilmaz et al. reported in 2011 electrical DC conductivity has increased with increasing concentration of Eu_2O_3 due to the movement of mobile oxygen ions for $(Bi_2O_3)_{1-x}(Eu_2O_3)_x$ ceramic sample [178]. Similarly, we have predicted that the electrical DC conductivity has been attributed due to the movement of mobile oxygen ions with increasing concentrations of Eu_2O_3.

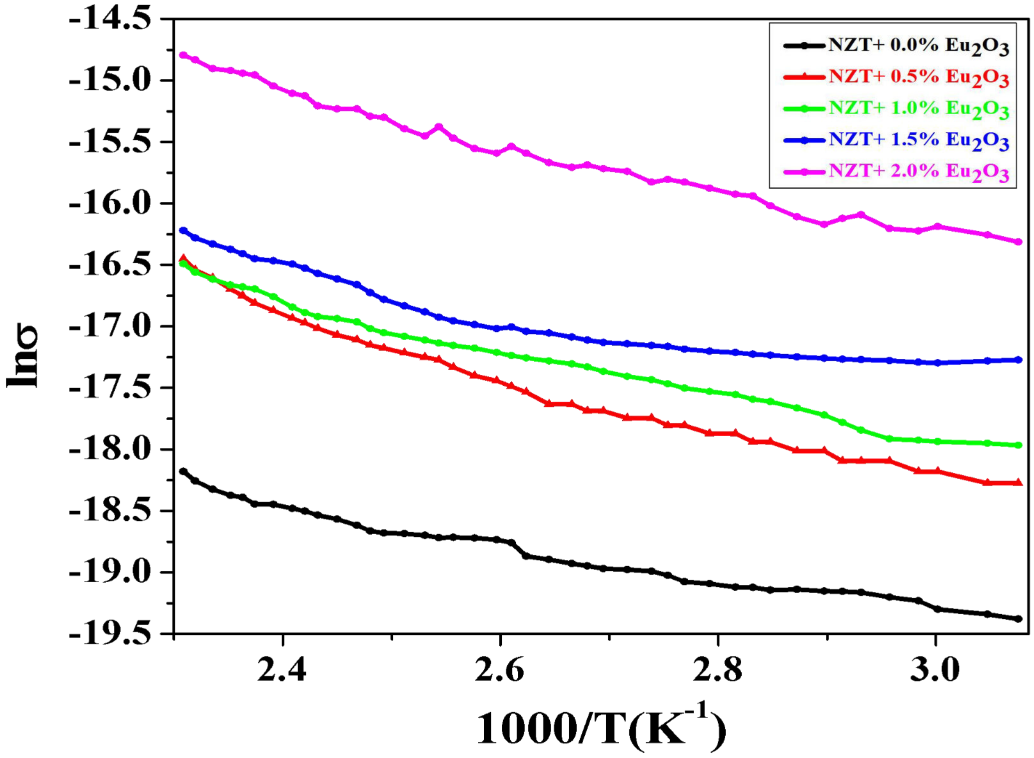

Fig 3.10 Temperature dependence of the electrical conductivity of the pure and Eu_2O_3-doped NZT glass samples.

The activation energy of our samples has been decreased with increasing concentrations of Eu_2O_3, and activation energies were calculated (detail in Table 3.2) using the empirical formula (Arrhenius relation) [178].

$$\sigma_T = \sigma_0 e^{(-E_a}/K_B T) \;\ldots\;\ldots\;\ldots\; (3.4)$$

Where E_a is the activation energy, σ_0 is the pre-exponential factor, T is the absolute temperature and K_B is the Boltzmann constant.

It has been found that the activation energy decreases with increasing concentrations of Eu_2O_3-doped glass samples. It may be possible to increase the oxygen ions due to the increase of doping concentration for the defects states within the bulk samples. This prediction may be confirmed from the measurement of the dielectric constant of the samples as the dielectric constant increases with increasing doping concentration.

Table 3.2 Activation energies of pure and Eu_2O_3-doped NZT glass samples.

Sample name	Activation Energy (E_a in eV)
NZT+0.0% Eu_2O_3	0.64
NZT+0.5% Eu_2O_3	0.59
NZT+1.0% Eu_2O_3	0.58
NZT+1.5% Eu_2O_3	0.58
NZT+2.0% Eu_2O_3	0.53

3.4 Conclusions

In summary, Europium-doped Na_2O-ZnO-TeO_2 (NZT) glasses were successfully synthesized by the melt-quenching method. The X-ray diffraction characterization strongly indicated the amorphous nature of the prepared glasses. We present the results of the preparation and characterization of the luminescent system based on Na_2O-ZnO-TeO_2 (NZT) glasses doped with four different Eu^{3+} concentrations ions (0.5 wt%, 1.0 wt%,1.5 wt%, 2.0 wt%). There are six emission sites of Eu-doped NZT glass samples from the transitions of $^5D_1 \rightarrow {}^7F_1$, $^5D_1 \rightarrow {}^7F_2$, $^5D_0 \rightarrow {}^7F_1$, $^5D_0 \rightarrow {}^7F_2$, $^5D_0 \rightarrow {}^7F_3$, $^5D_0 \rightarrow {}^7F_4$ respectively. The photoluminescence graph made it clear that the small variation in the peak value occurred when the sample was doped with a rare earth element. This indicated that the wavelength of excitation purely depended upon the material composition. The dielectric constant of glass samples was studied for different frequencies at room temperature and found a stable material within the frequency range 1 kHz to 1MHz with dielectric constant 200 to 500. These glass samples may be useful as substrate devices as these materials show high dielectric constant. The variation of conductivity with temperature confirmed the Arrhenius conduction mechanism and the estimated activation energies were in the range of 0.64 eV to 0.53 eV. So, these samples have a high potential for application in optoelectronic devices.

[*This work has been published in Glass Phys. Chem., 2020, vol. 46, pp. 218–227.* ***http://dx.doi.org/10.1134/S1087659620030104***]

Chapter-4

Optical and electrical properties of Nd^{3+}doped Na_2O-ZnO-TeO_2 Material

4.1 Introduction

Tellurite glasses are extremely attractive materials for linear and non-linear applications in optics, due to their important aspects such as their low melting temperature, low phonon energy, high refractive index, high dielectric constant, good chemical durability, high thermal stability, non-hygroscopic, with large transmission window and the possibility to integrate a large number of rare-earth ions [71, 179-185]. It can be used as micro-lenses, IC photo masking glass, hard disks, press modeling of spherical lenses, glass substrates for solar cells, artificial bones, dental implants, and crows. The optical property of rare-earth ions in tellurite glasses depends on the chemical composition, which determines the structure and the nature of the bonds of the glass matrix. Besides, the understanding of their microscopic mechanism of structural and optical behavior gave much thrust and basic interest for both academia and industries. Tellurite glasses doped with rare-earth ions have attracted researchers for their broad spectrum of applications in optoelectronic and photo-electronic devices viz solid-state lasers optical switches, broad-band amplifications, nonlinear optical devices, infra-red (NIR) laser windows, optical fibers [186, 187]. The doping of rare-earth ions in tellurite glasses has shown interesting properties like an amplification of optical signal in the visible and NIR region, optical data storage, white light emission, and planner waveguides which are applicable to micro-chip lasers, biomedical diagnostics, light-emitting diodes and high-density optical data reading [188-190]. Recently, the precise properties of tellurite glass have been investigated for the demonstration of various spectroscopic and nonlinear optical device applications such as broadband light emission and optical communications network.

The applications of neodymium-doped glass materials are most commonly useful than the different types of rare-earth ions-doped glasses [191]. In 1961, Snitzer initiated the application of glass material as a medium for containing neodymium ions (Nd^{3+}) [192]. Neodymium-doped lasers have been used in various applications due to perform within the high-efficiency range at room temperature. The phonon energy is decreased due to the amalgamation of heavy metal oxides into the tellurite glass system [193]. Also, alkaline earth metal oxides such as Na_2O, CaO, and MgO reduce the crystalline structure and increase the amorphous nature of the glass system [194-196]. For this result, the thermal stability of glasses is increased [99]. The fundamental structural units of tellurite glass are adapted to the rare-earth oxides like Nd_2O_3 from 4-coordination to 3-coordination by exchanging TeO_4 trigonal bipyramid units to the TeO_3 trigonal pyramid units [69].

In this present work, the focus has been initiated to study systematically the glass formation, structural, optical, and electrical properties constant at room temperature with frequency variation, and thermal conduction mechanism of the Nd^{3+} doped Na_2O-ZnO-TeO_2 (NZT**)** glass materials with different doping concentrations.

4.2 Materials and Methods

The conventional melt-quenching technique has been used to prepare Na_2O-ZnO-TeO_2 (NZT**)** glasses using research great initial ingredients Zinc Oxide (ZnO), Tellurium di-Oxide (TeO_2), Sodium Carbonate (Na_2CO_3) manufactured by Merck and Neodymium Oxide (Nd_2O_3) made by Loba Chemie. The mixing ratio of Na_2O, ZnO, and TeO_2 is maintained as 1:2:7 to prepare the host glass. Neodymium Oxide (Nd_2O_3) was added to the host glass as a dopant for (0-2) wt%. The homogeneous mixture of these compounds was obtained by grinding the ingredient powders in an agate mortar. The mixture was kept in an alumina crucible, and the crucible was placed in an electrical box furnace. The melt quenching process was obtained by two stages of heating with the temperature at 400 °C for 1 hour and temperature at 475 °C for the next half an hour to produce the quality telluride glass. The cylindrical stainless steel plate was used to hold the melted sample for quenching and the prepared glass was placed again in the furnace at 400°C for 1 hour to anneal the sample. The annealed glass was allowed to reach room temperature gradually through the slow cooling process for avoiding thermal stress.

The thermal properties, differential thermal analysis, and thermo-gravimetry of the initial mixtures (raw materials in the powder form)were analyzed in the argon environment by using Perkin Elmer Instrument (Pyris Diamond TG/DTA, thermo-gravimetric/differential thermal analyzer). These were studied properties for the temperature range of 30 °C to 650 °C with a scanning rate of 10°C/min. X-ray diffraction patterns were obtained using an X-ray diffractometer (RIGAKU model: Japan, XRD 6000, λ = 1.5418 Å) with a slow scanning rate 3°/min between the angle 10º and 70º for all the samples. FTIR spectrometer (HITACHI Model F-700) was used to identify the nature of pure and doped glasses in the wave number range 400-3000 cm^{-1}. Optical absorption and emission spectra of all the glasses were obtained using UV/VIS/NIR spectrophotometer (Perkin Elmer Lambda-35) for the wavelength range 400-800 nm and fluorescence spectrophotometer (HITACHI Model F-7000) for 300-600 nm at room temperature. The dielectric constants (ε) of prepared glass samples were measured using LCR- HiTESTER (HIOKI, Japan) for the large frequency range of 200 Hz- 4 MHz at room temperature. The temperature-dependent DC conductivity of these glasses was studied for the temperature range 36 °C-227 °C using a constant voltage supply and current meter.

4.3 Results and Discussion

The color of the pure NZT glass is white, while Nd^{3+} doped NZT glasses revolved into purple color due to the doping of Nd^{3+}ions in the host glass NZT. The prepared transparent NZT glasses were shown in Fig. 4.1. The color of the glass samples varies from bluish to violet with the increase of doping concentration. It has been found that there are no visible crystallites present in these transparent samples [197].

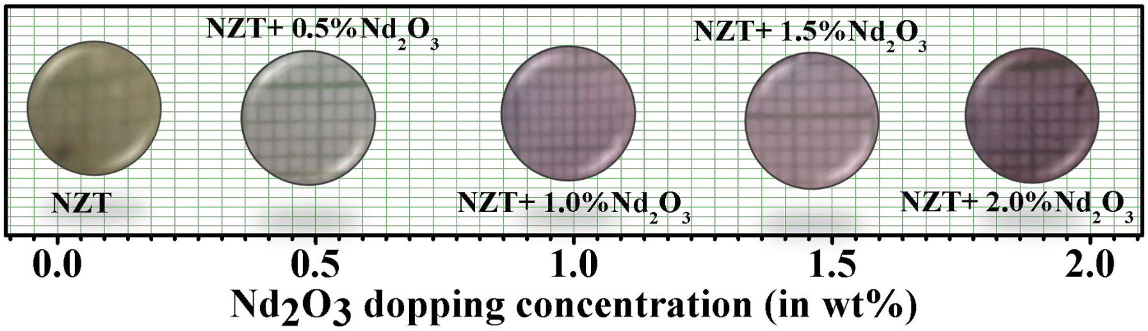

Fig 4.1 Pictorial view of Nd_2O_3-doped NZT glasses.

4.3.1 Thermal analysis

Fig. 4.2 shows the DTA curve of the mixed precursor of pure, and Nd^{3+}ions doped NZT glasses for the temperature range 35 °C to 650 °C. There are three successive endothermic peaks evolved in the temperature range of 72 °C to 160 °C for all the samples. These endothermic peaks in this specified temperature range reveal the desorption or evaporation of the moisture from the precursor ingredients [166]. It has been also observed that there are exothermic peaks present in the DTA curve within the temperature range of 330 °C to 463 °C.

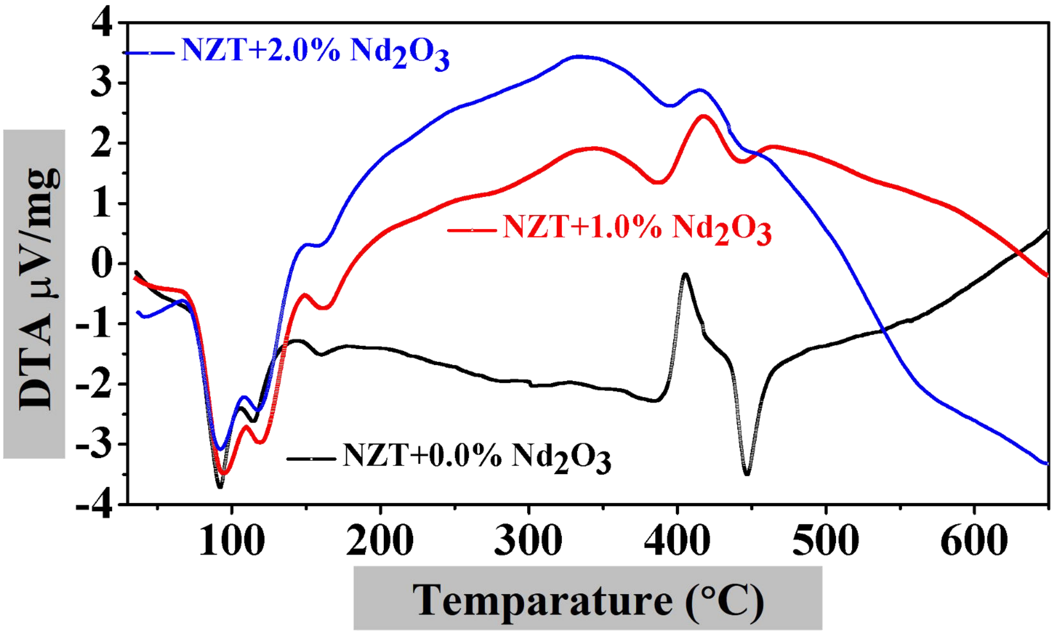

Fig 4.2 DTA graphs of pure, 1.0 wt%, and 2.0 wt% of Nd_2O_3-doped NZT glasses.

These peaks demonstrate the removal of CO_2 through the decomposition of Na_2CO_3 present in the initial ingredients and the phase transition from solid powders to liquid form through melting. The phase transition has come about through the melting at the temperature of 447 °C. The melting point of TeO_2 (730 °C) is reduced to 447 °C due to the existence of Na_2CO_3 and ZnO in the initial mixture [167, 198].

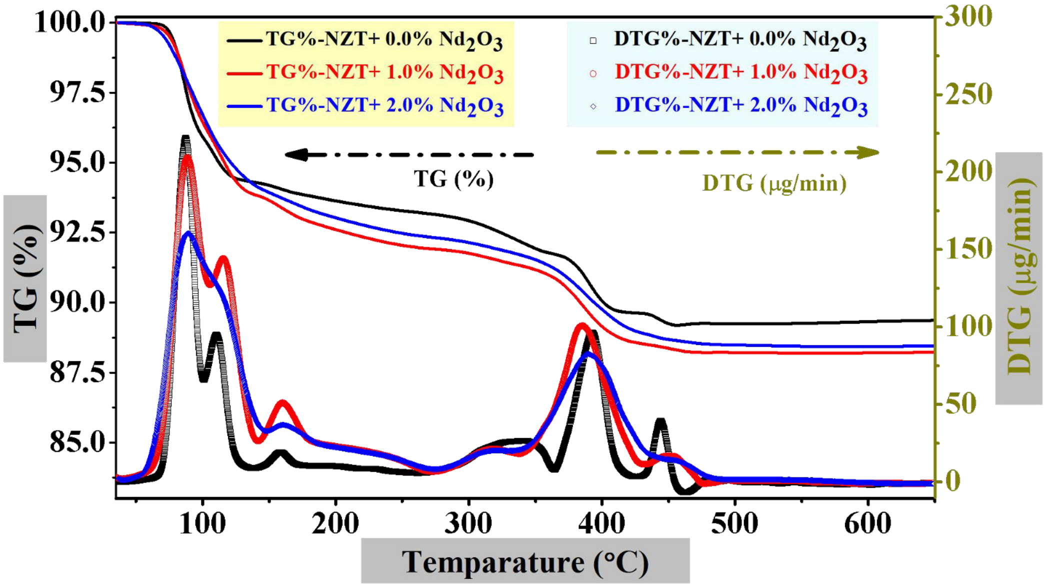

Fig 4.3 TGA and DTG vs temperature graph of pure, 1.0wt%, and 2wt% Nd_2O_3-doped NZT glass samples.

It is also observed that the melting point of the mixture slightly decreases with increasing the concentration of Nd_2O_3.

TG and its differentiation curves of the precursor powders of the samples are shown in Fig. 4.3. These curves for all the samples depict the weight loss during heating at different temperatures. The total weight loss in the measured temperature range 35 °C to 650 °C is 10.71%, and this amount of loss occurred from the removal of moisture, evaporation of the volatile substances, and decomposition of Na_2CO_3 by releasing CO_2, etc. The major mass loss in the temperature range 64-125 °C is taken place due to the desorption of water, and removal of moisture, and other volatile materials which is also confirmed by the DTA curves [168]. The emission of CO_2 is observed at 385 °C to 395 °C which is displayed in DTG curves for pure and doped samples. The little amount of mass is reduced within the temperature range of 442 °C to 460 °C during the melting of solid powders. No weight loss is observed beyond the temperature of 460 °C.

4.3.2 X-ray Diffraction

Fig. 4.4 shows the XRD pattern of the glass samples. The XRD peaks of pure NZT glass are observed at 10.86º, 21.92º, 23.26º, 29.03°, 29.86°, and 31.39° for the corresponding planes (010), (110), (011), (021), (111) and (030) respectively. It has been found that the sharp peak at 13.24° signifies new hybrid compounds and it may develop due to the presence of $Na_2Te_2O_5$, $2H_2O$ [199]. This new hybrid compound has not been formed in case of the addition of doping material Nd_2O_3, as the peak position at 13.24° is absent in the doped NZT glass samples. The broadening of XRD peaks in higher doping concentrations reveals the amorphous nature of the doped samples. The shifting of the peak positions is observed for the higher concentration of Nd_2O_3 doped NZT glass samples and this shifting has ascribed to the modification of the crystalline pattern embedded in the glass samples due to the incorporation of Nd^{3+} ions.

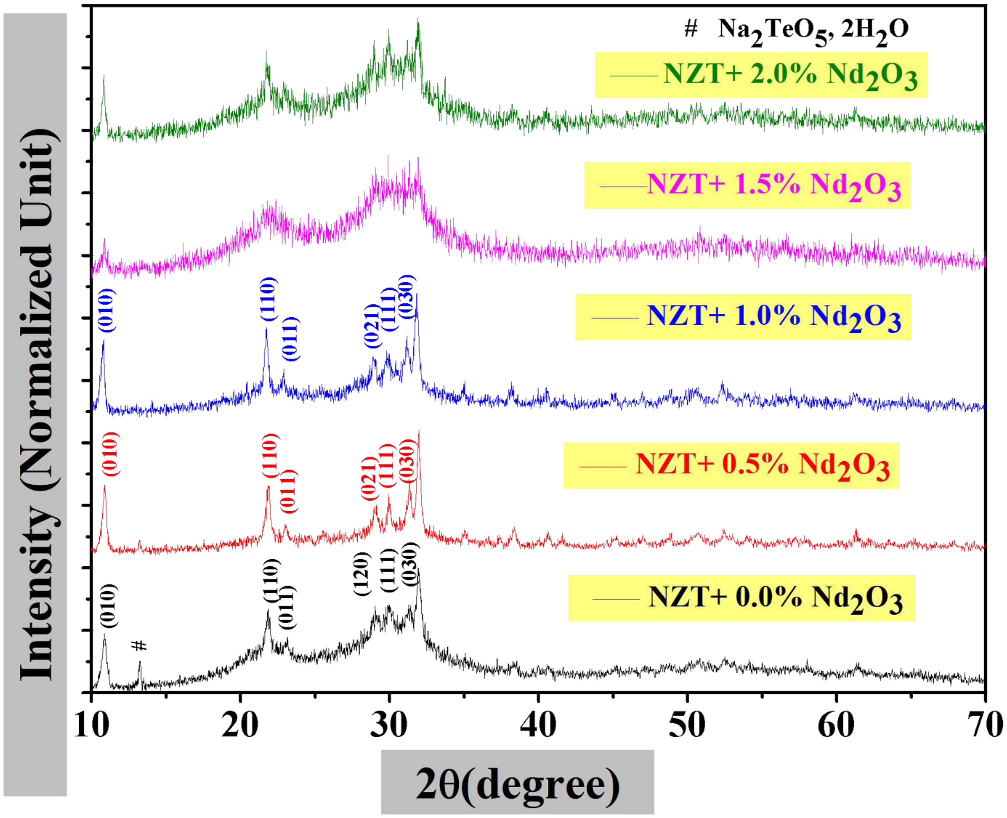

Fig 4.4 XRD pattern of pure and Nd^{3+}-doped with NZT glass samples.

4.3.3 Optical Properties

4.3.3.1 FTIR

The FTIR spectra for pure and doped NZT glasses are shown in Fig. 4.5. The analysis of these spectra is a useful process to investigate structural studies with functional groups and bonding information in the crystalline and non-crystalline systems [200]. The transmission spectra of the various concentration of neodymium oxide doped glass samples are recorded for the region 400-3000 cm^{-1}. The position of the structural unit of ZnO is observed in the band range 424-440 cm^{-1}. The absorption band at 426 cm^{-1} appeared due to the symmetric stretching vibration of the Zn-O bond [201]. The characteristics of tellurite oxide found the structural unit in the range of 600-800 cm^{-1}.

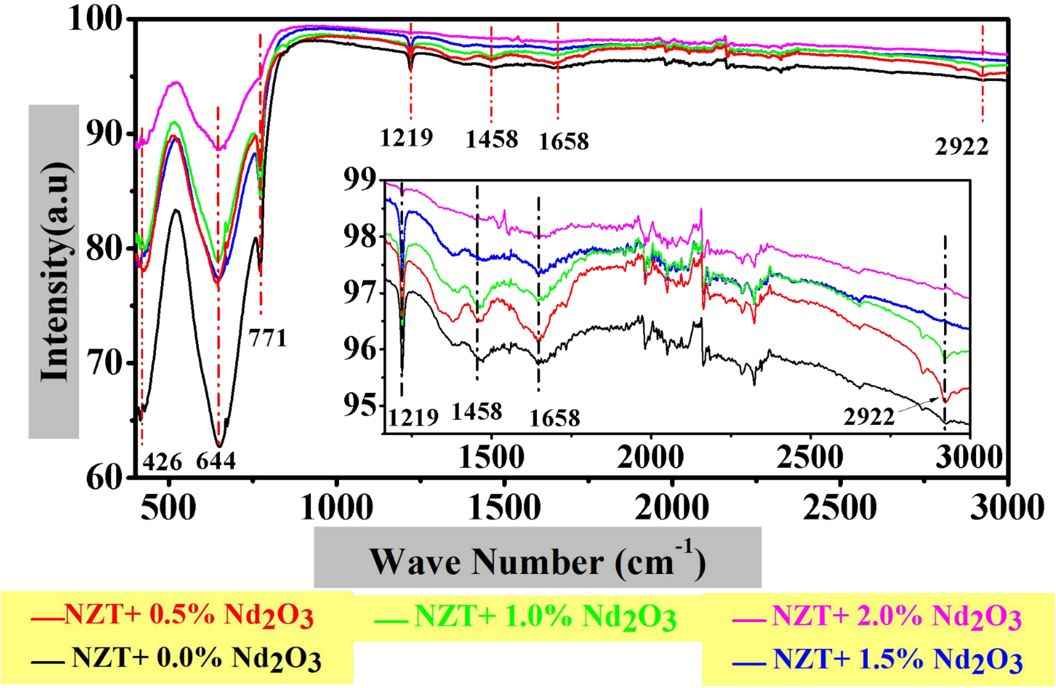

Fig 4.5 FTIR spectra of pure and different concentrations of Nd_2O_3-doped NZT glass materials.

In this broad range, pure TeO_2 is characterized by an infrared absorption at around 644 cm^{-1}. The formation of tellurite glass contains two types of fundamental structural units TeO_4 trigonal bipyramidal, and trigonal pyramidal. Symmetrical stretching vibration of Te–O bond in trigonal bipyramids (TeO_4) and Te–O bending vibrations in trigonal pyramids (TeO_3) in the tellurium network were observed around 644 cm^{-1} [202-205]. The broad peaks can be attributed to the mixing of two groups, and the absorption peaks broaden with the addition of Nd_2O_3. This broadenings of peaks and increase of intensity confirm Nd^{3+} ions in the host glass matrices. The band at 771 cm^{-1} is evolved for pure, and doped glasses due to trigonal pyramidal structural units. This band is attributed to the stretching vibration within the tellurium and the non-bridging oxygen of the trigonal pyramidal structure [195, 206].

The absorption peaks around 1658cm^{-1}, and 2922 cm^{-1} are ascribed to a stretching vibration of hydrogen bonding and mental bonding with the hydroxyl group as the hydroxyl group is coupled with the Te^{4+} glass network [207].

4.3.3.2 Optical Absorption

The absorption spectra of pure and Nd_2O_3-doped NZT glasses are shown in Fig. 4.6 for the visible region (400-800 nm) at room temperature. It has been found that the absorption transition occurs only for Nd^{3+} ions doped glasses, and the intensity of absorption spectra increases with the increase of doping concentrations. There is no transition of the pure glass sample. The peak positions of absorption spectra for Nd^{3+} ions doped glasses are designated as similar to$^4I_{9/2} \rightarrow {}^4F_J$(J = 9/2,7/2) and $^4I_{9/2} \rightarrow {}^4G_J$ (J = 11/2,9/2,7/2,5/2) transitions corresponding to the six absorption band at 430 nm ($^4I_{9/2} \rightarrow {}^4G_{11/2}$), at 512 nm ($^4I_{9/2} \rightarrow {}^4G_{9/2}$), at 525 nm ($^4I_{9/2} \rightarrow {}^4G_{7/2}$), at 583 nm ($^4I_{9/2} \rightarrow {}^4G_{5/2}$), at 683 nm ($^4I_{9/2} \rightarrow {}^4F_{9/2}$), and 746 nm ($^4I_{9/2} \rightarrow {}^4F_{7/2}$). Though the absorption band of rare-earth doped tellurite glasses arises in the ultraviolet region in general, the current glass network displays the absorption in the visible region with large intensity due to the presence of Nd^{3+}ions as a dopant in the glass samples. The introduction of Nd^{3+}ions behaves as crystalline material confirming the sharp absorption band which is also confirmed from XRD. The different forbidden transitions concerning 4f levels are also involved in the exhibition of absorption bands in the visible region [99, 208]. It has been also found from Fig. 4.6 that the peak positions of absorption bands for different dopant concentration of Nd_2O_3 are slightly shifted towards a lower wavelength. This displacement of the absorption band may be occurred due to the change of structural arrangement and various fundamental units of the present glass materials. The peak position of the absorption band may also be shifted due to the change of strength in the oxygen bond in the glass materials. Similar absorption spectra are observed for the addition of rare-earth oxide of the same type in the other tellurite glasses [187, 209-212].

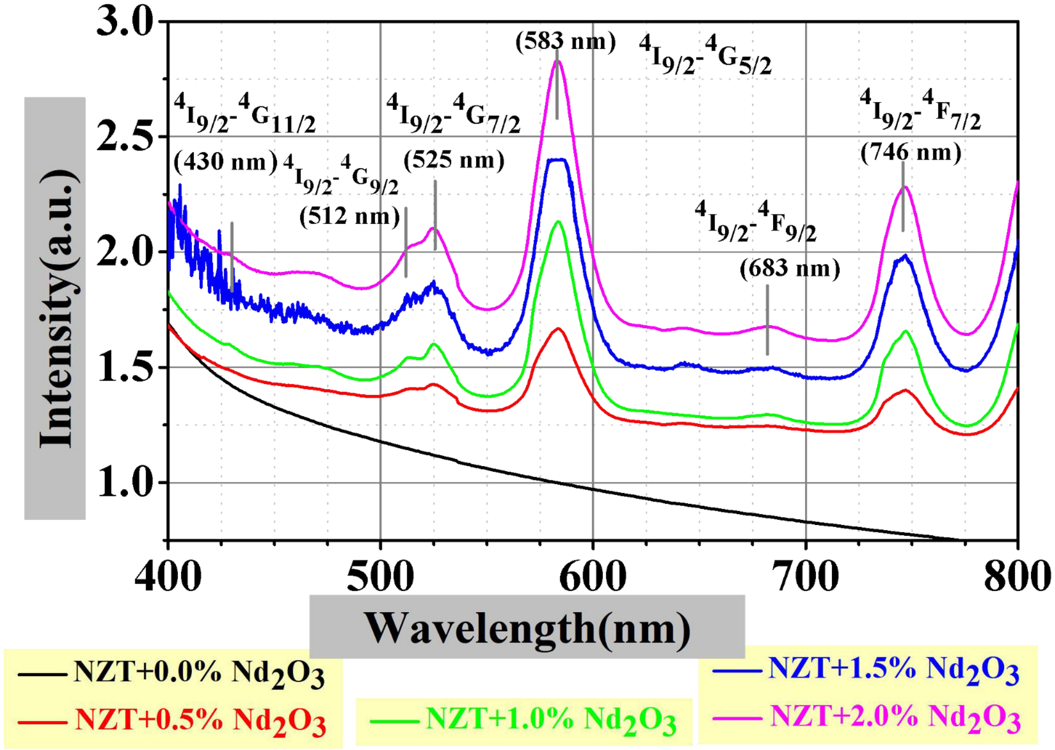

Fig 4.6 Absorption specta of pure and Nd^{3+} ions doped NZT glass materials.

Fig. 4.7 shows the variation of $(\alpha h\nu)^{1/2}$ with $h\nu$ (Tauc plot) for all of the glass-ceramics at room temperature. Here, the coefficient of absorption $\alpha(\upsilon)$ of optical absorption spectra is obtained according to the formula of Davis and Mott

$$\alpha(\nu) = \left(\frac{A_b}{t}\right) \quad \dots \dots \dots \quad (4.1)$$

Where, A_b is the absorbance and t is the thickness of the sample [169, 193, 213].
The indirect band gap energy is decreased from 2.63 eV and 1.32 eV due to the higher concentration of the Nd^{3+}ions.

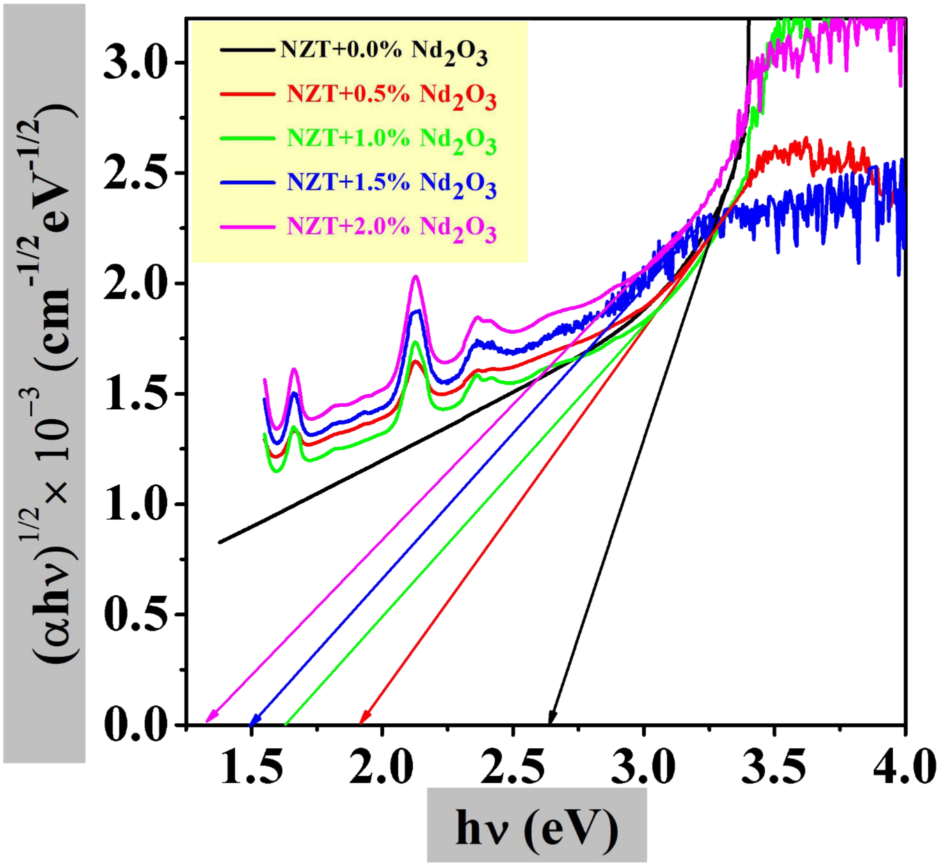

Fig 4.7 Band gap energy of Nd^{3+}ions doped NZT glasses.

The band gap energy and other physical properties of pure and doped glass samples are tabulated in Table 4.1. The physical properties are performing an important part to estimate the optical property of rare-earth doped glasses. The structural efficiency of the glass samples is developed in the glass network. The physical parameters of prepared glasses like concentration ions, inter-ionic distance (r_i), polaron radius (r_p), and field strength (F) are calculated and displayed in Table 4.1. The variation of inter-ionic distance (r_i) and field strength (F) with different ion concentrations of rare-earth ion (Nd_2O_3) is shown in Fig. 4.8.

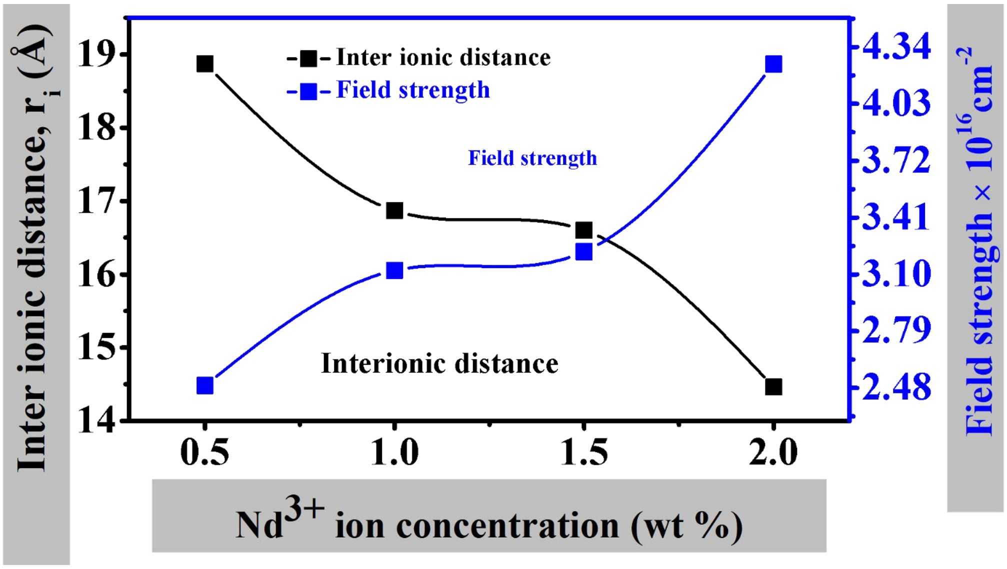

Fig 4.8 Nd^{3+}ion dependence inter ionic distance (r_i) and Field strength (F) for NZT glass compound.

Table 4.1 Band gap energy and physical properties of pure and Nd^{3+}-doped NZT glass materials.

Physical properties	Nd_2O_3 doped different samples				
Doping concentration of Nd_2O_3 in NZT (wt%)	0.0	0.5	1.0	1.5	2.0
Concentration of Nd^{3+}ions N(10^{20} ions/cm^3)	-	1.49	2.08	2.19	3.31
Inter-ionic distance between the Nd^{3+} ions(r_i in Å)	-	18.87	16.87	16.60	14.46
Polaron radius (r_p in Å)	--	7.61	6.80	6.69	5.83
Electric Field strength F(in 10^{16} cm^{-2})	--	2.49	3.12	3.22	4.25
Band gap Energy E_g indirect (n = 2) eV	2.63	1.90	1.63	1.50	1.32

It has been found that the Inter-ionic distance (r_i) decreases and field strength (F) increases with the increase of doping concentration of Nd_2O_3. The stronger field strength evolved around Nd^{3+} ions with the increase of Nd-O bond strength. The compactness of the glass structure is confirmed by the result of density and increasing concentration of Nd^{3+} ions in the doped glasses. The electron localization may be formed due to the decrease of r_i and r_p. This formation of electron localization can affect directly band gap energy according to the structural change of the glass system. The donor centers in the glass matrix increase with the increase of electron localization and the outcome is the decrease of optical band gap energy (E_g) which is also confirmed by Tauc's plot for pure and Nd^{3+} doped glasses [214-218].

4.3.3.3 Fluorescence Spectra

The fluorescence spectra of pure and Nd_2O_3 doped with NZT glasses have shown in Fig. 4.9. The spectra have been obtained at room temperature for the wavelength range 355nm to 600 nm with an excitation wavelength of 325 nm. No transition takes place for a pure NZT glass sample. The intensity of the emission spectra for all the doped glasses increases with increasing the doping concentration of Nd^{3+} ions. It has been found that a broad spectrum of wavelength 370-556 nm is emitted from the doped samples. This spectrum contains several emission lines which are evaluated from the de-convolution of each spectrum. We have observed five emission bands emitted a broad spectrum $^2P_{3/2} \rightarrow {}^4I_{9/2}$ at 371 nm, $^2D_{5/2} \rightarrow {}^4I_{9/2}$ at 421 nm, $^2P_{1/2} \rightarrow {}^4I_{9/2}$ at 431 nm, $^4G_{11/2} \rightarrow {}^4I_{9/2}$at 467 nm, and $^4G_{7/2} \rightarrow {}^4I_{9/2}$ at 546 with the excitation wavelength λ_{exci} = 325 nm. The emission corresponding to the $^2P_{1/2} \rightarrow {}^4I_{9/2}$ transition is stronger than the other emissions bands [188, 219]. As the Nd^{3+} ions are populated in the $^2D_{5/2}$ level some of them relax radiatively to this level by emitting fluorescence. The green emission of Nd^{3+} ion in doped NZT glass is observed due to the decaying transition from $^4G_{7/2} \rightarrow {}^4I_{9/2}$ at 546 nm. The peak position of the transitions shifted towards a higher wavelength for 2% doping of concentration of Nd_2O_3. This shifting may arise due to the presence of excited Nd^{3+} ions in $^2D_{5/2}$ and $^4G_{11/2}$ state for the respective transitions with blue emissions [188].

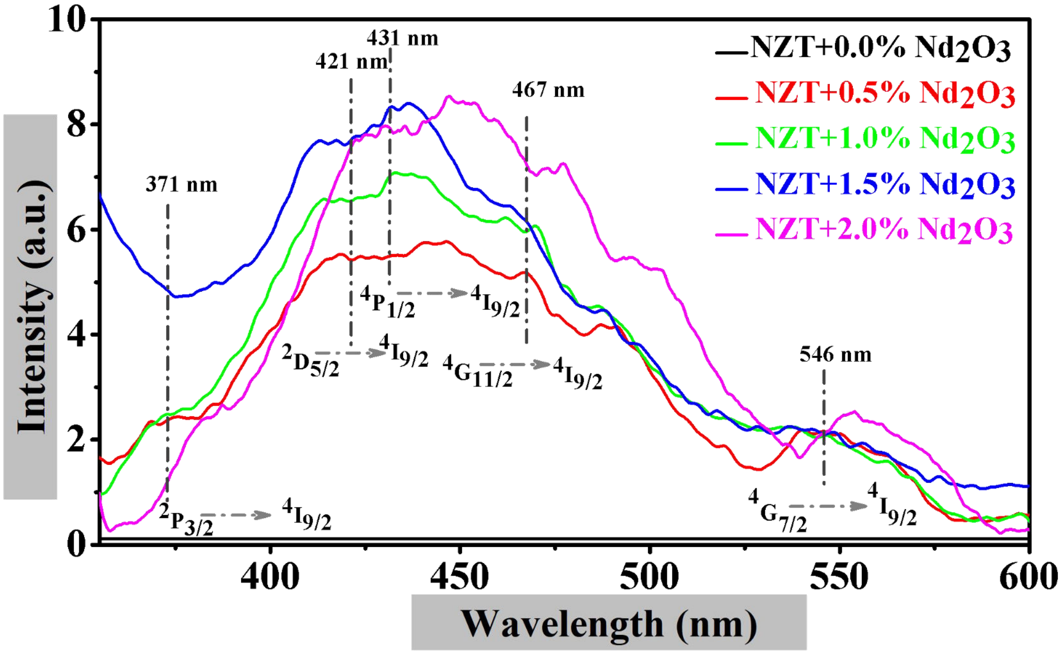

Fig 4.9 Fluorescence spectra of various concentrations of Nd^{3+}ions doped NZT glasses, excited at 325nm.

4.3.3.4 Cross Section

The absorption cross-section of the glass samples for the $^4G_{5/2} \rightarrow {}^4I_{9/2}$ transition has been calculated using the Lambert-Beer formula

$$\sigma_{ab}(\lambda) = 2.303\ A_b/(Nt) \quad \ldots \quad \ldots \quad \ldots \quad (4.2)$$

Where A_b is absorbance, t is the thickness of the sample and N is the density (ions/cm^3) of the Nd^{3+} ion of the telluride glass. Fig. 4.10 shows the absorption cross-section decreasing for increasing the concentration of the Nd^{3+} doped NZT glass samples. The emission cross-section is measured using MaCumber (1964) theory [176].

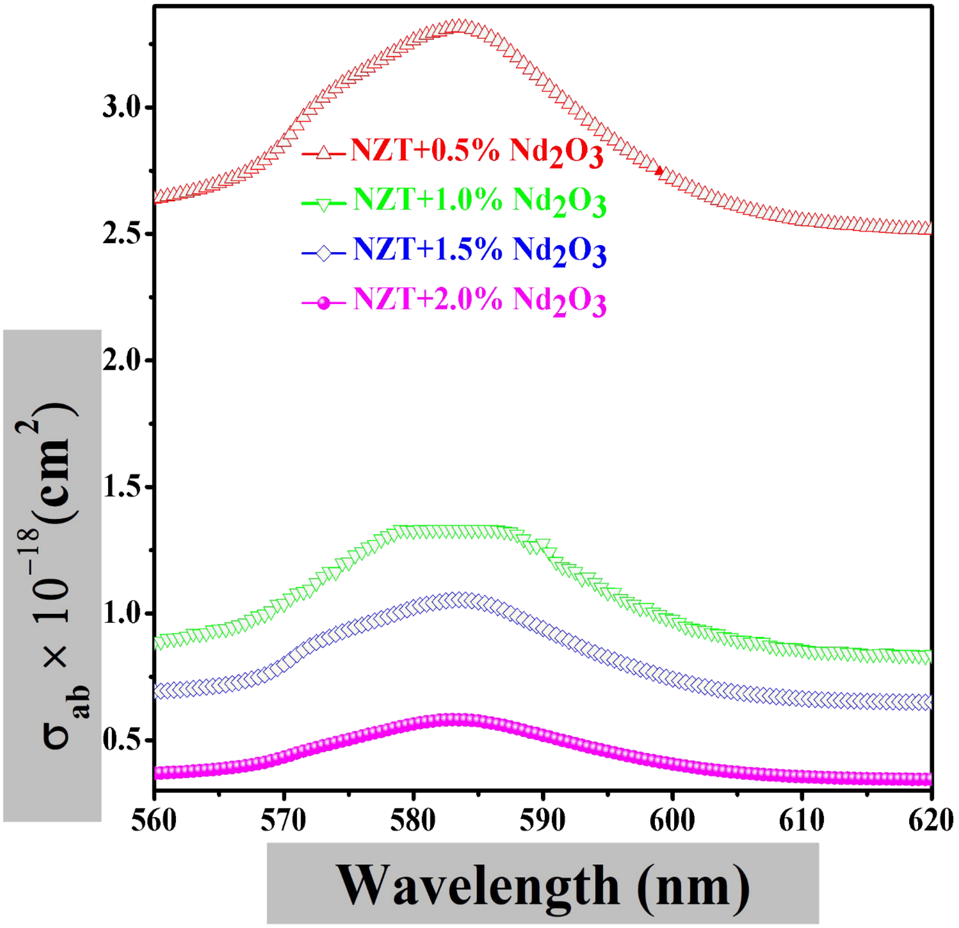

Fig 4.10 Absorption cross-section vs wavelength (nm) for 0.5, 1.0, 1.5, and 2.0 wt% Nd_2O_3-doped NZT glass materials.

The absorption and emission cross-section are associated with the formula

$$\sigma_{em}(\lambda) = \sigma_{ab}(\lambda)\exp[(E - h\nu)/K_BT] \quad \ldots \quad \ldots \quad \ldots \quad (4.3)$$

Where, ν is the phonon frequency, E is the free energy needed to excite Nd^{3+} from $^4I_{9/2} \rightarrow$ $^4G_{5/2}$ state at temperature T, h is the Planck's constant, and K_B is the Boltzmann constant.

The emission cross section for the $^4I_{9/2} \rightarrow {}^4G_{5/2}$ transition of Nd^{3+} doped glasses is shown in Fig. 4.11. The emission cross-section is decreased for a higher concentration of Nd^{3+}ions of NZT glasses.

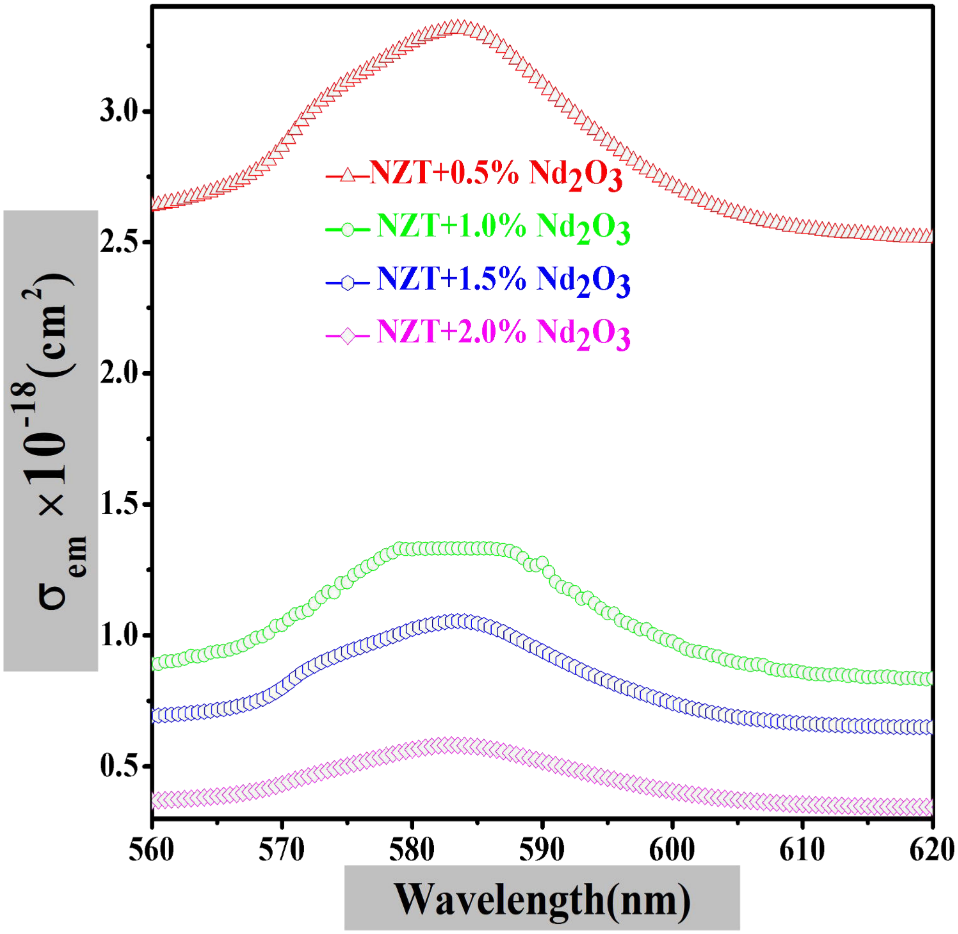

Fig 4.11 Wavelength dependence emission cross-section for Nd_2O_3-doped NZT glass materials.

4.3.4. Dielectric Property

4.3.4.1 Dielectric constant

Fig. 4.12 shows the real part of the dielectric constant (ε) of Nd^{3+} doped NZT at room temperature in the frequency range of 200 Hz to 4 MHz. The value of ε of Nd^{3+}doped NZT glass samples is decreased with increasing frequency from 200 Hz to ~ 2 kHz. At lower frequencies, the value of ε is high due to the absence of spontaneous polarization in oxide glass materials [220]. The values of ε of our samples are almost frequency independent in the frequency range ~ 3kHz to ~ 1MHz due to a decrease of ionic, space charge, and orientation polarization. The dielectric constant is increased in the frequency range ~ 1 MHz to 4 MHz with a higher concentrations of Nd^{3+} ions. A similar result has been observed in Eu^{3+} ions doped NZT glass samples [221].

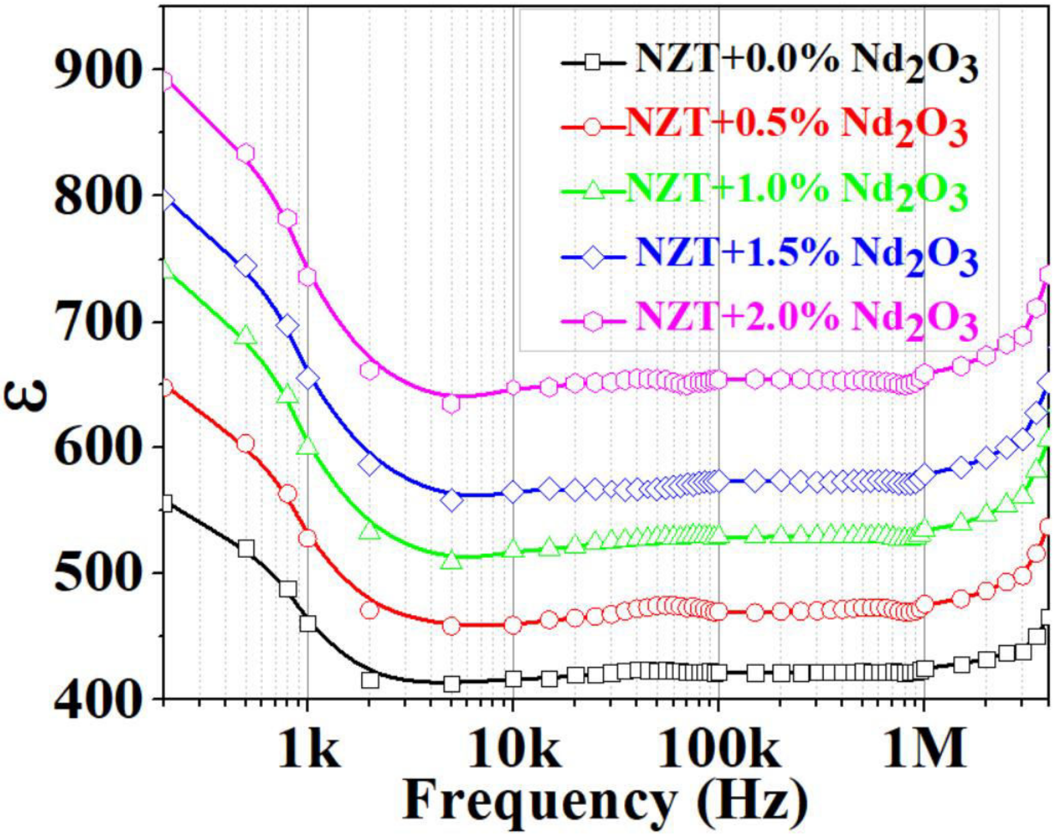

Fig 4.12 The variation of dielectric constant (ε) as a function of frequency for Nd^{3+}-doped NZT glasses at room temparature.

4.3.4.2 DC Conductivity

Fig. 4.13 shows the variation of electrical conductivity with temperature for pure, and Nd^{3+} doped NZT glass materials. It has been found that the conductivity of all the glass samples is increased with increasing temperature, and also with the increase of doping concentration in the host glass. This increment of conductivity with temperature reveals that the electrical conduction mechanism is Arrhenius type. This Arrhenius mechanism of electrical conduction can be used and estimated the activation energy of the samples using the relation

$$\sigma_{dc} = \sigma_0 \exp^{\left(-\frac{E_a}{K_B T}\right)} \quad \ldots \ldots \ldots \quad (4.4)$$

Where E_a is the activation energy, σ_0 is the pre-exponential factor, T is the absolute temperature, and K_B is the Boltzmann constant.

The estimated activation energies for all the samples have been calculated from Fig. 4.13. The activation energy decreases (666 meV to 552 meV) with increasing concentrations of Nd_2O_3 doped glass samples [220].

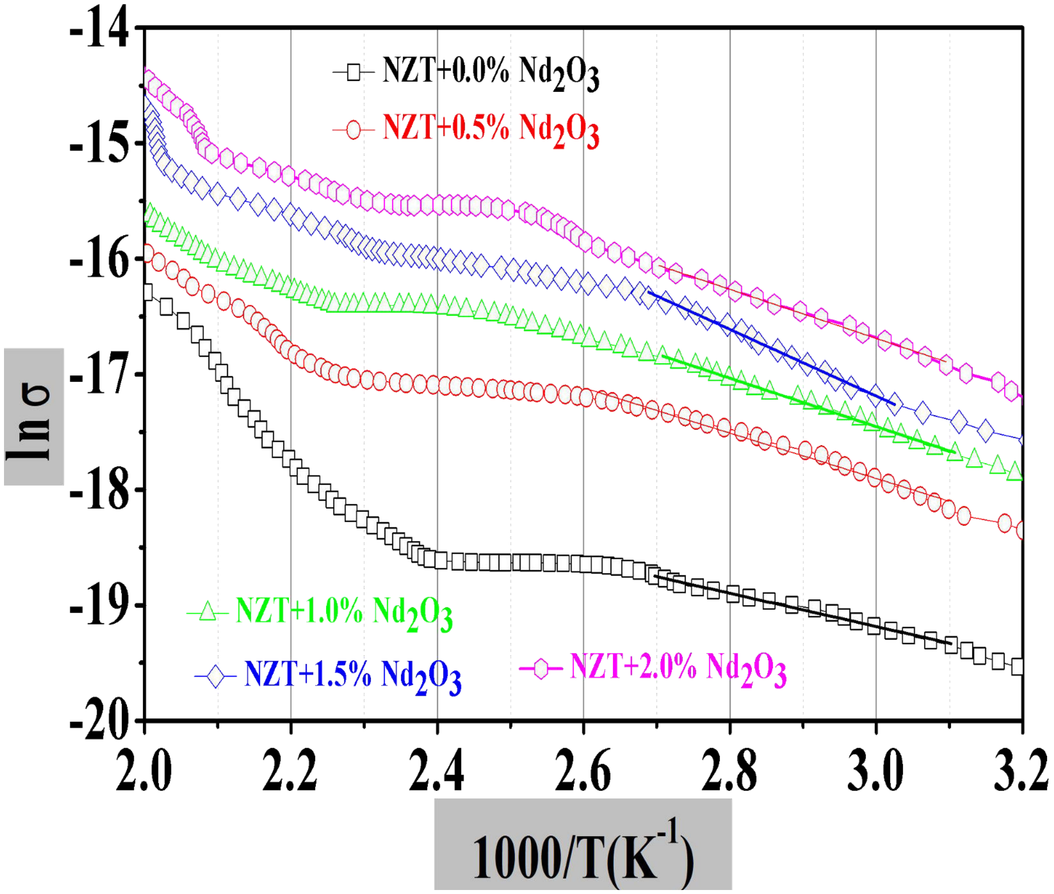

Fig 4.13 Arrhenius plot of lnσ vs 1000/T for Nd^{3+} ions doped NZT glasses.

The increment of conductivity due to the increase of doping concentration of rare-earth ions can be explained based on the interaction between the rare-earth ions and structural units of host glass. The atomic weight, doping concentration, and location of Nd^{3+} ions describe the mechanism of conductivity in the glass structure. The addition of rare-earth ions in the host glass creates a large number of non-bridging oxygen in the glass materials. This is also confirmed from the analysis of obtained FTIR spectra for all the samples. So, the increases of Nd^{3+} ions in the NZT glasses enhance the creation of non-bridging oxygen atoms, and hence the conductivity is increased for all the doped glass samples [154].

4.4 Conclusions

Neodymium (III) doped NZT glasses were effectively manufactured by the melt-quenching method. The X-ray diffraction characterization sturdily signified the amorphous nature of the prepared glasses for the higher concentration of Nd^{3+} ions. The results of the preparation and characterization of the luminescent system are obtained for the addition of various concentrations (0.5 wt%, 1.0 wt%, 1.5 wt%, 2.0 wt%) of NZT glass samples. Six absorption bands are displayed corresponding to 430 nm ($^4I_{9/2} \rightarrow {}^4G_{11/2}$), at 512 nm ($^4I_{9/2} \rightarrow {}^4G_{9/2}$), at 525 nm ($^4I_{9/2} \rightarrow {}^4G_{7/2}$), at 583 nm ($^4I_{9/2} \rightarrow {}^4G_{5/2}$), at 683 nm ($^4I_{9/2} \rightarrow {}^4F_{9/2}$), and 746 nm ($^4I_{9/2} \rightarrow {}^4F_{7/2}$). The peak value of photoluminescence spectra is slightly changed due to the addition of the higher concentration of rare-earth ions in the NZT glass sample. It specifies that the excitation wavelength simply depends upon the glass composition. Field strength (F*)* was observed to increase with increasing the Nd^{3+} ions concentration. Inter-ionic distance (r_i), and polaron radius (r_p) were found to decrease with increasing the Nd^{3+} ions. The role of Nd^{3+} ions in modifying the structural and optical properties has been understood. The decrease in the value of direct optical band gap energy was ascribed to the change in the structure of such glasses. The dielectric constant of Nd_2O_3-doped NZT glasses was measured for various frequencies and seen as a stable substance within the frequency of 3 kHz to 1 MHz. So, Nd_2O_3 doped NZT glass samples have a large prospect for application in optoelectronic devices.

[*This work has been published in Biointerface Res. Appl. Chem., 2022, vol. 12, pp. 7927 -7941.* *https://doi.org/10.33263/BRIAC126.79277941*.]

Chapter -5

Enhancement of optical properties and dielectric nature of Sm^{3+} doped Na_2O-ZnO-TeO_2 Glass materials

5.1 Introduction

Tellurium dioxide (TeO_2) is a promising glass network maker in the existence of alkali, alkaline earth, and transition metal oxides (TMO) as modifiers, but it does not form glass itself. So, TeO_2 is familiar as a conditional glass producer, as it requires a modifier to produce the glassy state of the materials. Tellurite glass materials have some interesting properties like transparency at room temperature, hardness of satisfactory strength, and attractive corrosion resistance [222-224]. Tellurite glasses are very interesting materials for linear and non-linear applications in optics, due to their significant characteristics such as low melting point, small phonon energy, and large refractive index. It has also important for high dielectric constant, good chemical durability, high thermal stability, non-hygroscopic, with a large transmission window and the possibility to integrate a large quantity of rare-earth ions. It can be also applied as micro-lenses in photocopiers and mobile-phone cameras, IC photo masking in photolithography, photosensitive glass, hard disks, substrates for solar cells, artificial bones for mankind, and dental transplants, etc. Besides these applications, tellurite glass has been used for the protection of X-ray radiations, gamma radiations, and other ionizing radiations from radioactive materials. Radiation exposure from different nuclear sources such as nuclear power plants, radioactive mining, conservation of radioactive sources etc. can have a serious negative effect on the human body. Earlier, lead (Pb) has been used to protect these radiations. But several disadvantages have been found to using lead as a shielding material against nuclear radiation. Recently, material scientists have suggested that tellurite/ borate glass can be used as an efficient shielding material of nuclear radiations without any environmental pollution [225-232]. Glass materials are practically used for optical appliances due to their various compositions, physical isotropy and deficiency of grain boundaries. Tellurite glasses are useful to study by industrial researchers not only because of their methodological applications but also owing to a fundamental significance in thoughtful their microscopic mechanisms [233, 234]. The luminescence properties of optical materials have been broadly observed not only for applications in phosphors, scintillators, and laser crystals but also for scientific importance during the last two decays [235-241]. In presence of rare-earth ions, the glass materials are excellent luminescence intensity because of their emission power due to 4f-4f and 4f-5d electronic transitions [217, 242, 243].

Rare-earth ions doped tellurite glasses are applied due to their large potential in optoelectronic instruments such as solid-state lasers optical switches, broadband amplifications, nonlinear optical devices, infra-red (NIR) laser windows, optical fibers three-dimensional displays, optical amplifiers, field emission displays, colour displays white light-emitting diodes, high-density optical data reading, biomedical diagnostics, microchip lasers, planar waveguides, and high-density frequency domain optical data storage [244]. Samarium (Sm^{3+}) can be used as a dopant in glass hosts for powerful emissions in the visible area. Especially, the reddish-orange emission section from Sm_2O_3 doped NZT glasses holds strong photo-luminescence intensity, large emission cross-section, and high quantum efficiency, which could be fit for laser applications. Therefore, Sm^{3+} ions are the significant luminescent activators that are useful in illustrating the fluorescence properties because its $^4G_{5/2}$ level shows comparatively high quantum efficiency [233].

In this present work, the focus has been made to study properly the glass formation, structural, optical, and electrical properties at room temperature of Sm^{3+}-doped Na_2O-ZnO-TeO_2 (NZT) glass compounds.

5.2 Experimental Outline

The melt-quenching process was used to prepare pure and Sm^{3+}doped Na_2O-ZnO-TeO_2 (NZT**)** glasses using research-grade initial composition Zinc Oxide (ZnO), Tellurium di-Oxide (TeO_2), Sodium Carbonate (Na_2CO_3) manufactured by Merck, and Samarium Oxide (Sm_2O_3) made by LobaChemie. The mixing ratio of Na_2O, ZnO, and TeO_2 is continued as 1:2:7 to make the host glass matrix. Samarium Oxide (Sm_2O_3) was added to the glass system as a dopant for (0-2) wt%. The standardized mixture of these precursors was obtained by grinding the ingredient powders in agate mortar. The mixture was put in an alumina crucible and the crucible was kept in an electrical furnace. The melt-quenching method was reached by two stages of heating with the temperature at 400 °C for 1 hour and temperature at 475 °C for half an hour to prepare the good quality telluride glass. The cylindrical stainless-steel plate was used to hold the melted sample for quenching and the prepared glass material was placed again in the furnace at 400°C for 1 hour to anneal the sample. The annealed glass was allowed to reach room temperature gradually through the slow cooling process to avoid thermal stress.

DTA/TGA of the initial mixtures (raw materials in the powder form) were carried out through the argon environment by using Perkin Elmer Instrument (Pyris Diamond TG/DTA, thermo-gravimetric/differential thermal analyzer) for the temperature region of 30 °C to 650 °C with a scanning rate of 10°C/min. X-ray diffraction patterns were obtained using an X-ray diffractometer (RIGAKU model: Japan, XRD 6000, $\lambda = 1.5418$ Å) with a slow-scanning rate 3°/min between the angle 10º and 70º for all the samples. FTIR spectrometer (HITACHI Model F-700) was used to detect the type of pure, and doped glasses in the wavenumber region 400-3000 cm^{-1}. Absorption spectra, and emission band of all the glasses were found using UV/VIS/NIR spectrophotometer (Perkin Elmer Lambda-35) for the wavelength range 400-800 nm, and fluorescence spectrophotometer (HITACHI Model F-7000) for 300-600 nm at room temperature. The dielectric constants (ε) of prepared glass materials were measured using LCR-HiTESTER (HIOKI, Japan) for the wide frequency range of 100 Hz-8 MHz at room temperature. The temperature-dependent DC conductivity of glass samples was studied for the temperature range 36 °C-227 °C using a constant voltage supply and current meter.

5.3 Results and Discussion

Fig. 5.1 shows the transparent Sm_2O_3 doped NZT glass samples. The colour of the pure NZT glass is white, while Sm^{3+} doped NZT glasses are turned into yellowish colour due to the higher doping of Sm^{3+}ions in the NZT glass samples. There are no visible crystallites present in these transparent samples.

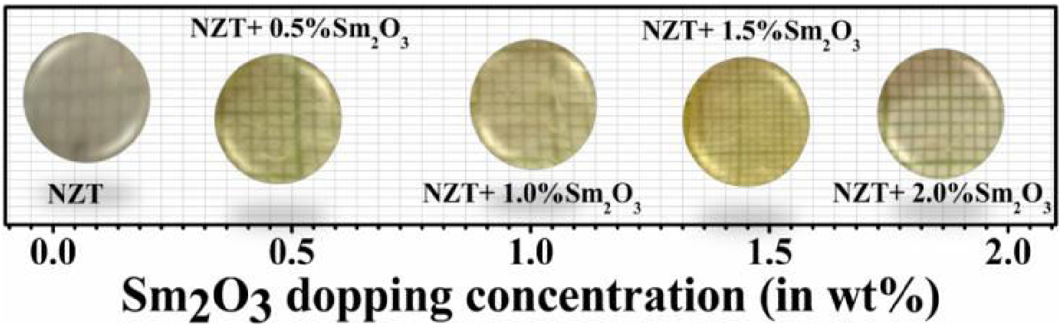

Fig 5.1 Picture of Sm_2O_3-doped NZT glass samples.

5.3.1 Thermal properties

Fig. 5.2 shows the DTA curve of the pure and Sm_2O_3 doped (2.0% wt) NZT glasses from 40 °C to 550 °C at a heating rate of 10 °C/min. The DTA curve for the pure and highest doping concentration of Sm_2O_3 (2.0 % wt) is used to investigate the thermal properties of pure and doped samples. It has been found that there is a small change in peak positions obtained in the DTA curve of pure and highest-doped samples.

Three consecutive endothermic peaks have been found in DTA curve between (72 - 160) °C for pure and doped NZT glasses. These endothermic peaks on the DTA pattern are attributed to the desorption or exclusion of moisture. Generally, endothermic peaks are evolved due to the melting point and exothermic peak indicates the crystallization of the melted glass [245]. Also, the exothermic peaks occurred when the CO_2 is released from the precursor powders and that has been found at around 406°C for pure and 416 °C for doped NZT glass.

These curves also suggest that the phase transition occurred due to the transition of solid powder form to liquid form through melting at around 447 °C. The melting point of TeO_2 is 730 °C which is decreased due to the presence of Na_2CO_3 mixed with ZnO [198]. The glass transition temperature (T_g) of pure and doped NZT glass materials has been observed to be 284 °C and 275 °C.

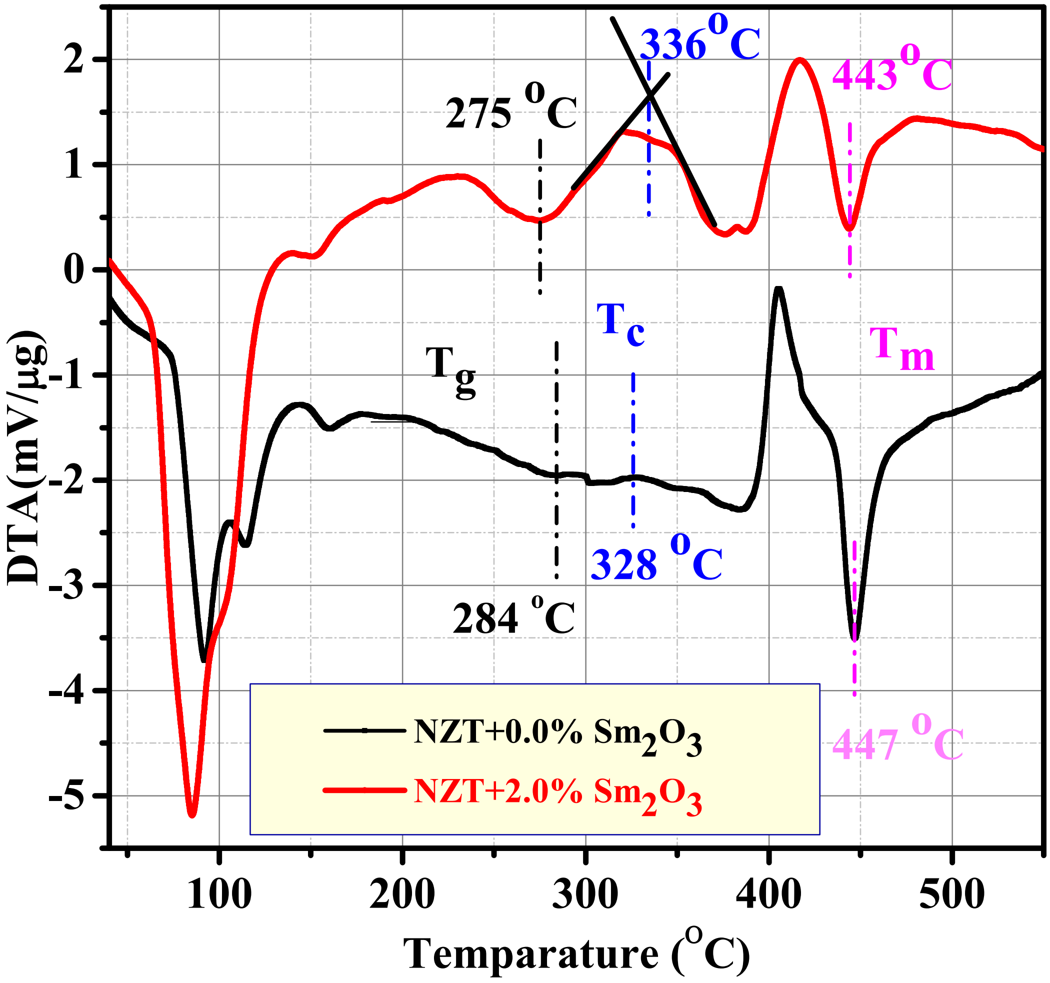

Fig 5.2 DTA curves of Sm_2O_3-doped NZT glass samples.

Table 5.1 Thermal parameters calculated from the DTA traces of pure and Sm_2O_3-doped NZT glasses.

Sample Name	**T_g(°C)**	**T_c(°C)**	**T_m(°C)**	**$\Delta T = T_c - T_g$**	**$H=(T_c-T_g)/(T_m-T_c)$**
NZT+0.0% Sm_2O_3	284	328	447	44	0.37
NZT+2.0% Sm_2O_3	275	336	443	61	0.57

The decreased value of T_g of the doped sample indicates the onward formation of stable glass material. The thermal stability of the glasses is generally defined as the difference between glass transition temperature and crystallization temperature. This thermal stability factor is representing the tough stability against the occurrence of crystallization. Here, the estimated thermal stabilities (ΔT) of the pure and Sm^{3+} doped NZT glass materials have been tabulated in Table 5.1. Glass thermal stability is stronger for a glass host to have ΔT as large as possible [245, 246]. The result specified here that the prepared Sm^{3+} doped NZT glass holds good anti-crystallization ability and thermal stability. The glass-forming tendency can be explained using Eq. (5.1), where H is Hruby's parameter, T_c is the softening temperature and T_m is the melting temperature [247, 248].

$$H = \frac{Tc - Tg}{Tm - Tc} \quad \dots \dots \dots \quad (5.1)$$

The higher value of Hruby's parameter in the case of Sm_2O_3 doped NZT glass sample indicates the improvisation of glass-forming tendency due to doping of Sm^{3+} ions.

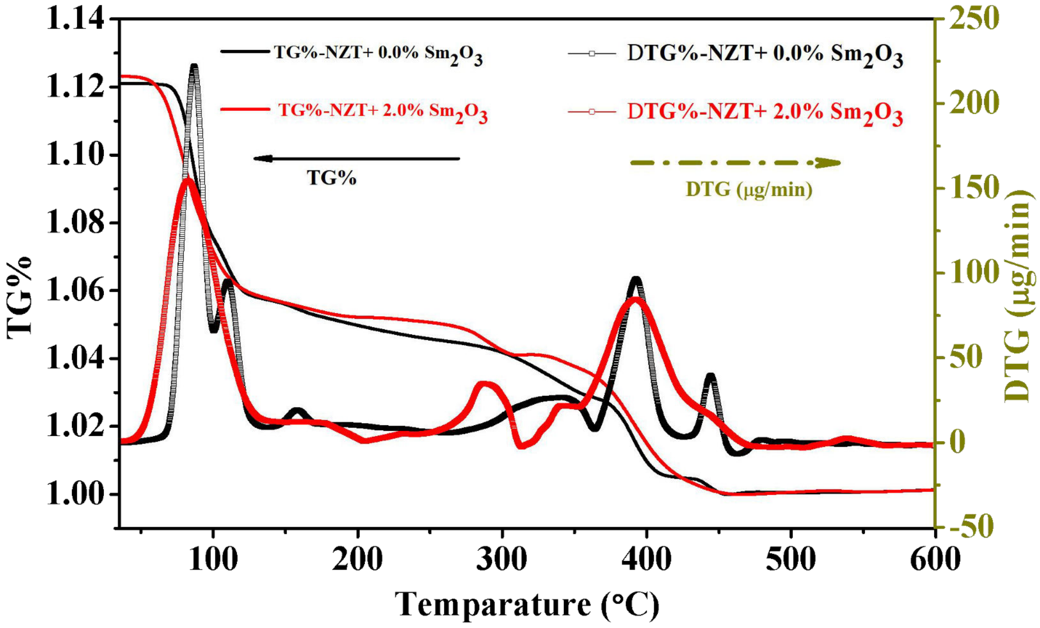

Fig 5.3 TG with DTG curve of the pure and Sm_2O_3-doped NZT glasses.

Fig. 5.3 shows the TG with DTG pattern of the pure and Sm_2O_3 doped NZT glasses. This TG analysis can also be used for the determination of thermal stability and the glass transition temperature. It has been frequently used to study the moisture contained, and decomposition of undesirable organic, and inorganic materials. The weight loss of the precursor mixture has been observed for pure and doped glasses at different temperatures. As mentioned earlier, TG/DTG curve illustrates the 5.37 % mass loss out of total mass due to exclusion of water, the release of moisture and other volatile substances in the temperature region 58-127 °C [168, 249]. The CO_2 is removed at the temperature range of 380 °C to 406 °C for the decomposition of Na_2CO_3 which is found in DTG curves for pure and doped samples. A little amount of mass is also lost within the temperature range of 435 °C to 450°C during the melting of the solid materials. No weight loss is detected beyond the temperature of 450 °C.

5.3.2 XRD

X-ray diffractogram of pure NZT and Sm_2O_3 doped glasses are shown in Fig. 5.4. It has been found from the figure that the XRD of all the samples demonstrates no discrete sharp peaks and a broad peak has been found in the region of the glancing angle at 24° to 34°. This broad peak in the XRD pattern indicates the non-crystalline materials as characteristics of typical long-range structural disorder of the samples. The broad continuous pattern of X-ray diffraction reveals the amorphous nature of these glasses [250, 251].

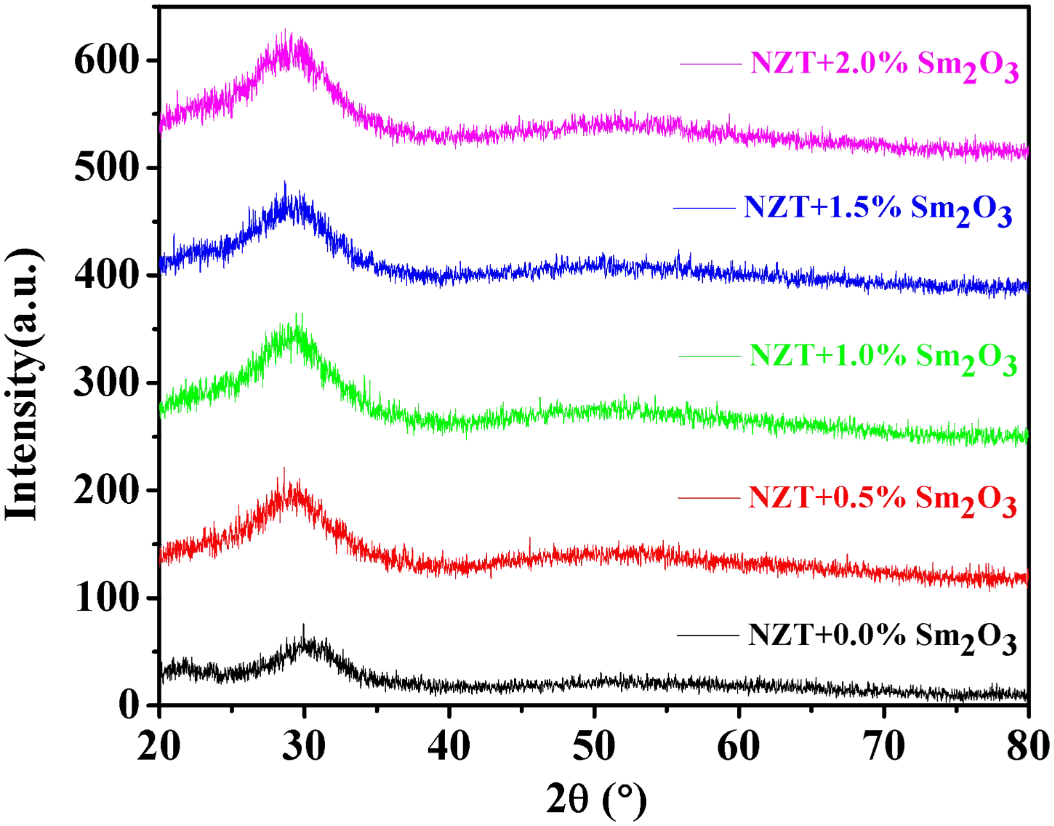

Fig 5.4 XRD pattern of sample pure and Sm^{3+}-doped with NZT glass materials.

5.3.3 Optical Properties

5.3.3.1 FTIR Spectroscopy

Fig. 5.5 represents the FTIR transmission spectra of pure and Sm_2O_3 doped NZT glasses in the wave-number range 400-3000 cm^{-1} at room temperature. The band at 424-440 cm^{-1} comes out due to the symmetric stretching vibration of the Zn-O bond. Zn^{2+} ions perform as an agent to split bonds and generate a modification in the glass structure. For this result, TeO_{3+1} and TeO_3 can be twisted from TeO_4 units making non-bridging oxygen atoms [201, 252, 253]. This is also confirmed from the observation of glass transition temperature in DTA. The band is located at 570–601 cm^{-1} due to the stretching vibration of TeO_4 (trigonal pyramid) [254, 255]. It is observed that transmission intensity slightly changes due to the presence of Sm_2O_3 in the glass system. The band at 670–685 cm^{-1} is observed due to the stretching vibration of TeO_4 trigonal bipyramid (tbp) [254]. The fundamental groups such as (- OH) bond, hydrogen bond, and H-O-H bending appear in the higher region at 1632 cm^{-1} [256]. The broad shoulder corresponds to the hydrogen bonds observed around 2886 cm^{-1}.

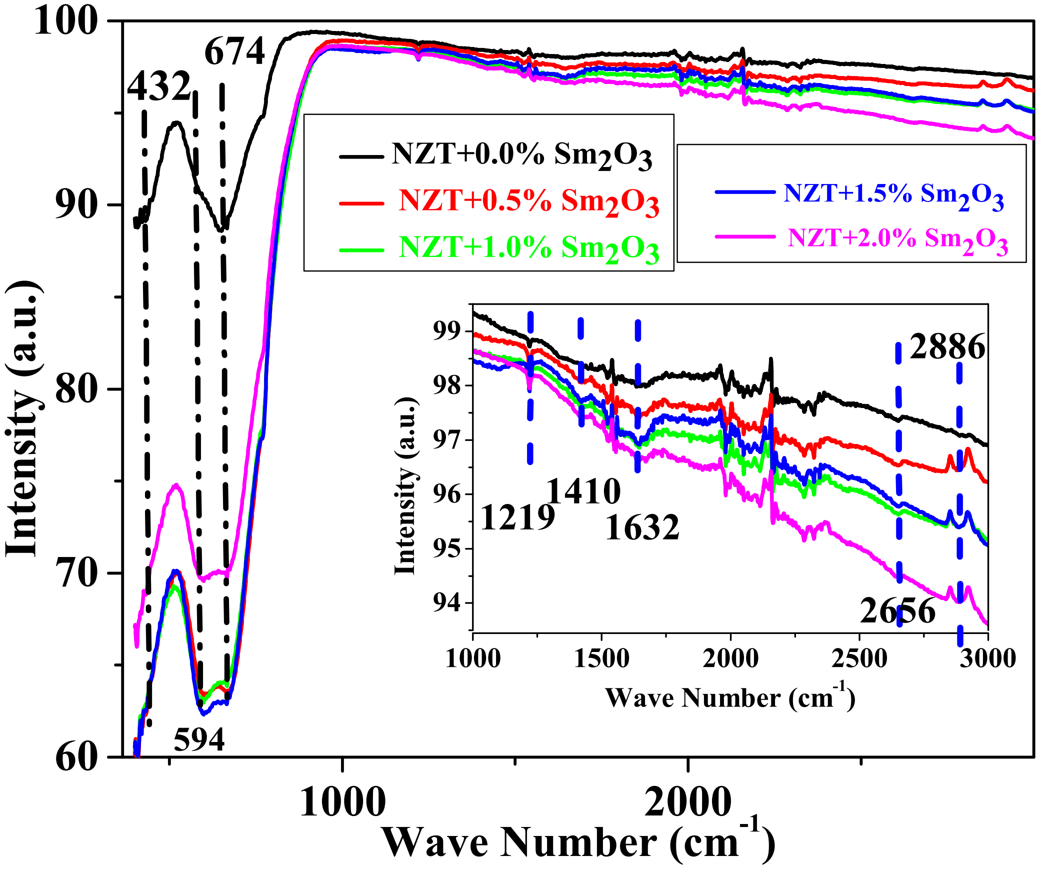

Fig 5.5 FTIR spectra of pure and various Sm^{3+}-doped with NZT glass materials.

5.3.3.2 Absorption Spectroscopy

UV/Viz absorption spectra of pure and Sm_2O_3-doped NZT glasses are displayed in Fig. 5.6. The recording of absorption intensity has occurred in the visible range (350 - 540 nm) at room temperature with the band assignments. It is found from Fig. 5.6, the absorption intensity increases gradually with the increase of doping concentration of

Sm_2O_3. There is no transition occurred for the pure NZT glass sample whereas the absorption peaks appeared at specific transitions in the case of Sm^{3+} ions doping.

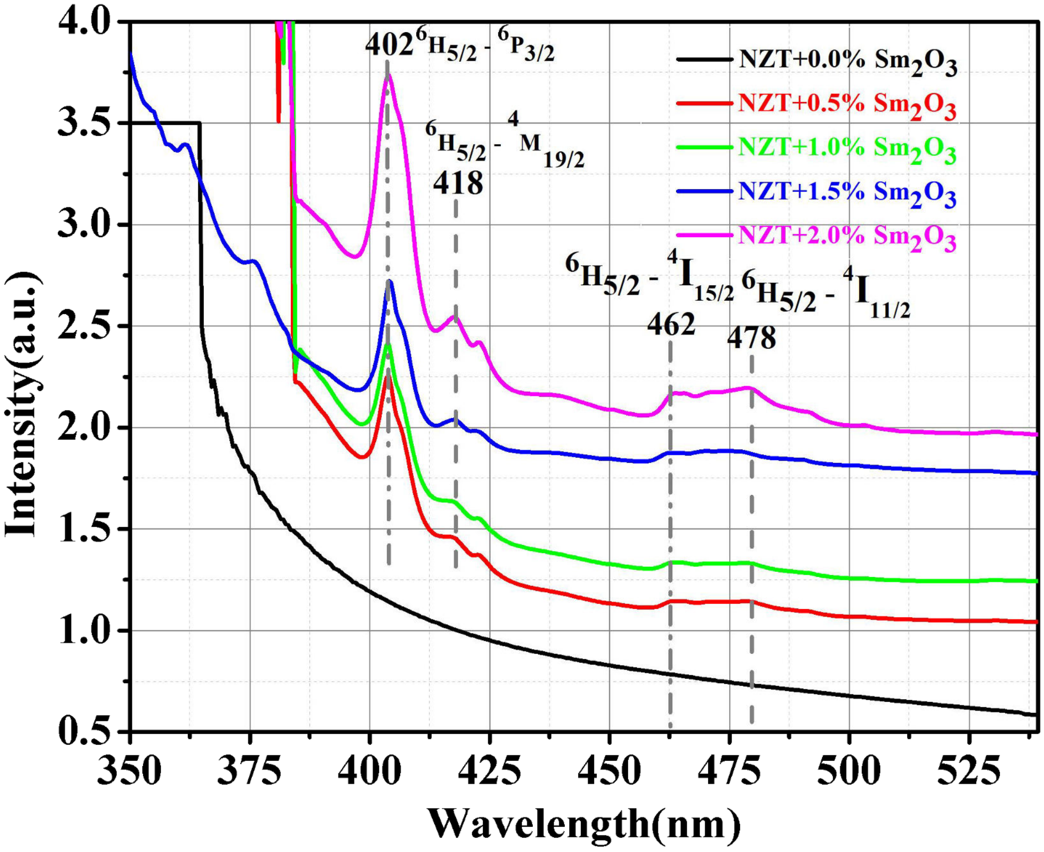

Fig 5.6 Absorption spectra of pure and Sm^{3+}-doped with NZT glass materials.

The tail of the optical absorption band is not strongly identified due to the amorphous nature of glasses which is also established from XRD. The peak value of Sm^{3+} doped NZT samples is obtained for the interaction of 4f -5d electronic configurations [217]. It is observed that there are four absorption peaks for the transitions $^6H_{5/2} \rightarrow {}^4P_{3/2}$ at 402 nm, $^6H_{5/2} \rightarrow {}^4M_{19/2}$ at 418 nm, $^6H_{5/2} \rightarrow {}^4I_{15/2}$ at 462 nm, and $^6H_{5/2} \rightarrow {}^4I_{11/2}$ at 478 nm. Carnall et al. approved these transitions [257, 258]. Optical absorption is expressed due to factors (compositional diversity, dimension, and defect) associated with material [259, 260]. Fig. 5.7 shows the variation of absorption coefficient $\alpha(\nu)$ with corresponding energy.

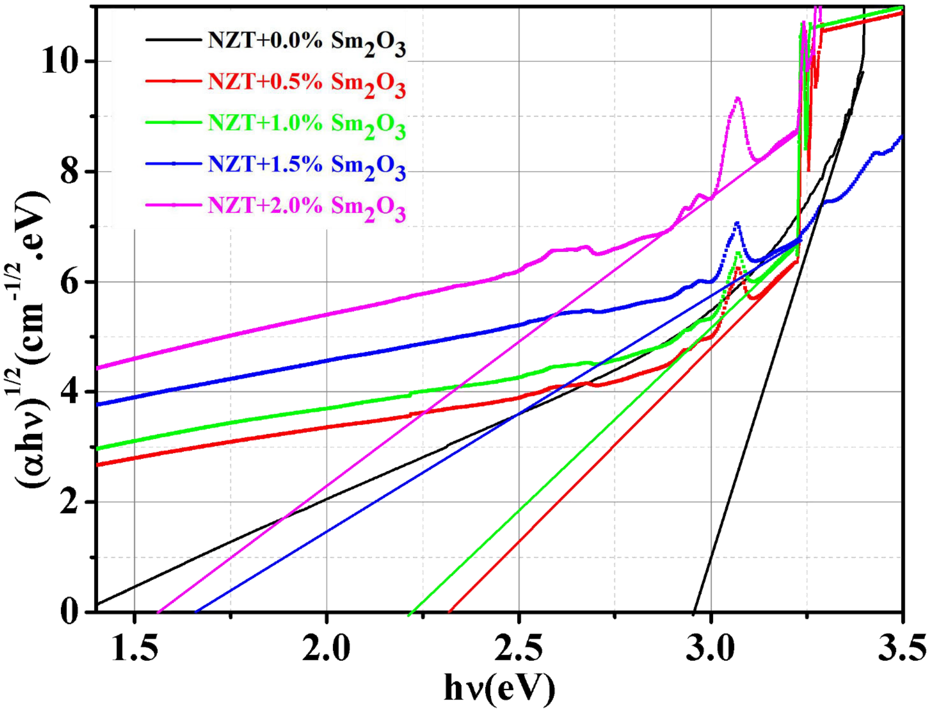

Fig 5.7 Tauc's plot for pure and Sm^{3+}-doped with NZT glass materials.

The absorption coefficient in many non-crystalline materials reflects the density of states at the band tails and can be determined from the optical absorption spectra using Eq. (5.2)

$$\alpha(\nu) = \left(\frac{A_b}{t}\right) \quad \ldots \ldots \ldots \quad (5.2)$$

Where $\alpha(\nu)$ is the absorption coefficient, A_b is the absorbance and t is the thickness of the sample.

$$\alpha(\nu) = \frac{B\left(h\nu - E_g\right)^m}{h\nu} \quad \ldots \ldots \ldots \quad (5.3)$$

Where ν is the phonon frequency, h is the Planck's constant, E_g is the band gap energy, B is a constant, and m is an index number.

Eq. (5.3) gives the relation between the absorption coefficient and photon energy. It has been determined the value of indirect band gap energy for m = 2 from the above Eq. (5.2) by plotting the absorption coefficient to zero absorption in the graph $(\alpha h\nu)^{1/2}$ vs hν.

For the indirect transitions, the corresponding value of E_g is obtained by extrapolating $(\alpha h\nu)^{1/2} = 0$. The values of E_g for the glasses are tabulated in Table 5.2. The band gap energy is a major factor determining the electrical conductivity of a solid. Substances with large band gaps are generally insulators, those with smaller band gaps are semiconductors. The band gap measurement can figure out various parameters like electronic structure, absorption coefficient, and electronic transitions. In case of a large band gap, the sample can be useful for the insulating device while a low band gap sample is used in optoelectronic applications. The decrease of E_g with increasing Sm^{3+} ions in the glass network can be explained by the creation of a large number of NBO in the samples. The negative charges of oxygen ions in the NBO create active electrons with a higher value than that on the bridging oxygen (BO). These active electrons are distributed irregularly because NBOs are softly bounded by the tellurite atoms [261, 262].

The obtained values of the E_g and the refractive index (n) can be estimated using Eq. (5.4) [253, 254].

$$\frac{n^2 - 1}{n^2 + 2} = 1 - \sqrt{\frac{E_g}{20}} \quad \dots \dots \dots \quad (5.4)$$

The refractive index increases with the increasing number of Sm^{3+} ions due to the creation of non-bridging bonds. This effect can be explained by the dissociation of the bridging Te–O–Te bonds and created non-bridging bonds. The bond energies of non-bridging oxygen (NBO) bonds are lower with greater ionic character. The cation refractions have a higher magnitude for the NBO bonds are determined from this explanation [263].

5.3.3.3 Fluorescence Spectra

Fig. 5.8 shows the fluoresce emission spectra for different concentrations of Sm_2O_3 doped with NZT glasses. The spectra have been recorded for samples with four different concentrations of Sm^{3+} ions at an excitation wavelength of 402 nm in the visible range of 500 - 700 nm at room temperature. The photoluminescence (PL) is an active method to study the electronic purity, different allowed transitions, presence of external defects, existence of impurities in the material, and the transitions related to photo-excitation. The PL characteristics of pure and Sm^{3+} doped materials have been investigated using the spectrophotometer (HITACHI Model F-7000) with a slit width of 5 mm. The emission intensity is enhanced up to 1wt% doping of the Sm_2O_3 and then slightly decreases for the higher doping concentration.

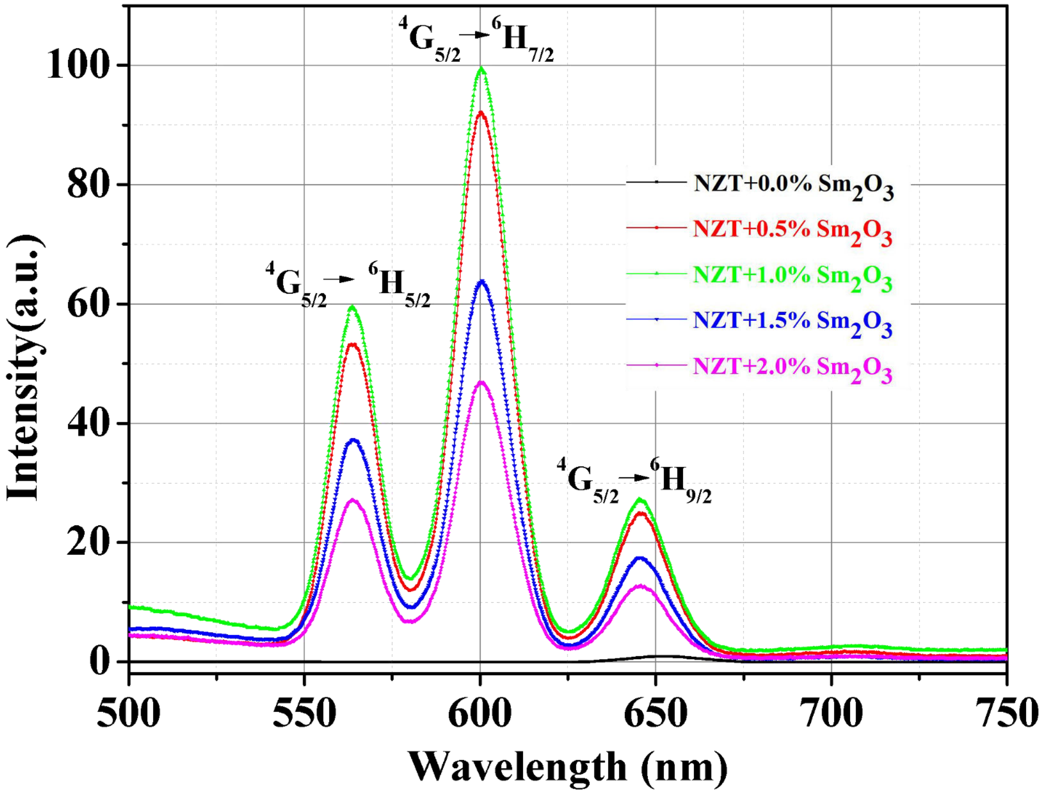

Fig 5.8 Luminescence spectra of pure and Sm^{3+}-doped with NZT glass materials, excited at 402 nm.

PL emission thus confirms the potential credibility of Sm^{3+} doped NZT glass materials. The photoluminescence (PL) is an active method to study the electronic purity, different allowed transitions, presence of external defects, existing of impurities in the material and the transitions related to photo excitation. The PL characteristics of pure and Sm^{3+} doped materials have been investigated using the spectrophotometer (HITACHI Model F-7000) with the slit width 5 mm. The emission intensity is enhanced up to 1% doping of the

Sm_2O_3 and then slightly decreases for the higher doping concentration. PL emission thus confirms the potential credibility of Sm^{3+} doped NZT glass materials [264, 265].

Fig. 5.8 displays the three peaks at the wavelengths 563 nm (green), 600 nm (orange), and 645 nm (red) with the matching to the transitions $^4G_{5/2} \rightarrow {}^6H_{5/2}$, $^4G_{5/2} \rightarrow {}^6H_{7/2}$, $^4G_{5/2} \rightarrow {}^6H_{9/2}$ of Sm^{3+} ions respectively [244, 217, 266-268]. It is found that the emission band at 600 nm ($^4G_{5/2} \rightarrow {}^6H_{7/2}$) is the most outstanding band in all Sm_2O_3-doped NZT glasses. The higher intensity of allowed transition $^4G_{5/2} \rightarrow {}^6H_{7/2}$ (600 nm) occurred due to the contribution of a magnetic dipole in the Sm^{3+}doped NZT glasses. In comparison to the intensity of the three emission peaks, the magnetic transition ($^4G_{5/2} \rightarrow {}^6H_{7/2}$) is greater than the intensity of electric dipole transitions ($^4G_{5/2} \rightarrow {}^6H_{5/2}$) and ($^4G_{5/2} \rightarrow {}^6H_{9/2}$) due to the ionic nature and symmetry of the system. The melt quenching of Sm^{3+} doped NZT glass samples has also been confirmed from the emission band according to the increasing and decreasing intensity conforming to the quenching effect of various doping concentrations. Usually, the quenching effect is created from the non-radiative method consisting of multi-phonon relaxation and the non-radiative cross-relaxation may be obtained by two Sm^{3+} ions through dipole-quadrupole or dipole-dipole or quadrupole-quadrupole interactions [119, 269-272].

The scattering wavelengths of emission in the visible area can be quantified using CIE 1931 colour coordinates, which is a physiologically apparent colour vision of humans. The emission band of Sm_2O_3-doped NZT glass samples was plotted using CIE 1931 (Fig. 5.9). The obtained colour confirmed the different colours of emission of all materials. The colour coordinates were (0.25839, -0.03215), (0.2526, 0.1042), (0.21879, 0.06764), (0.24418, 0.1011), and (0.22123, 0.0711) for Sm^{3+} doped (0.5% wt-2% wt) respectively. The non-emissive nature of the pure glass sample was confirmed from the coordinates out of the CIE plot. The changes in coordinates indicated that with increasing rare-earth oxide percent the emission shifted towards higher wavelengths.

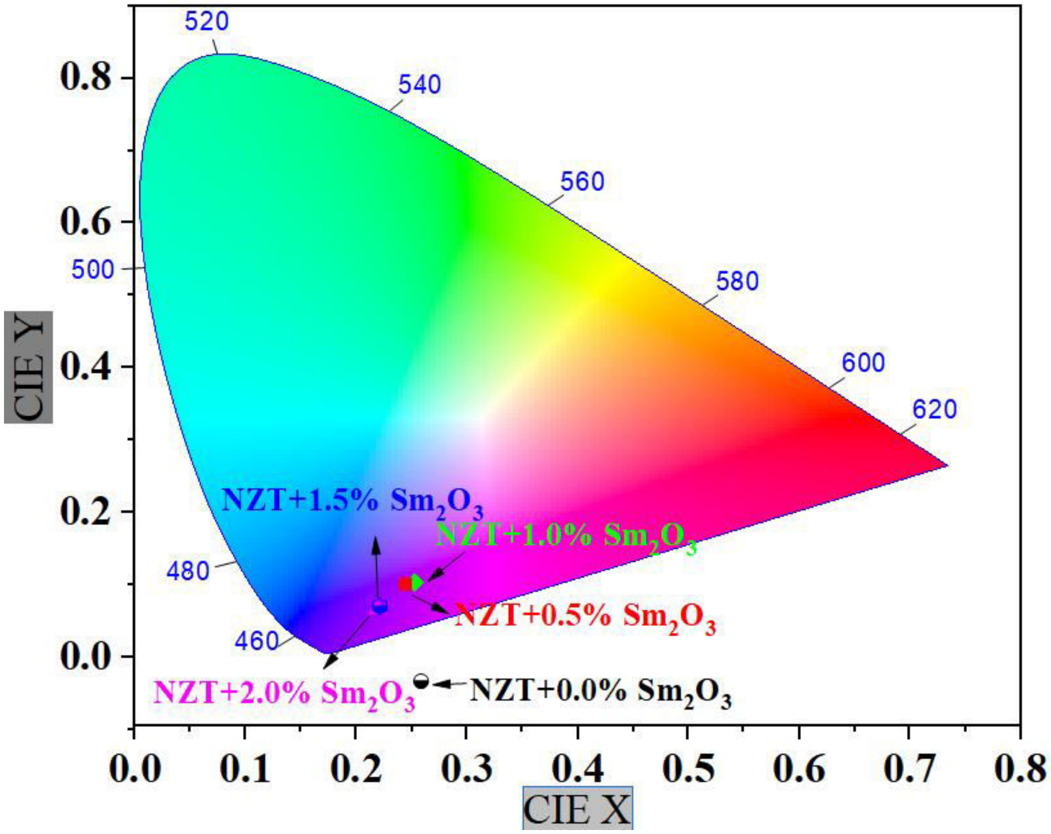

Fig 5.9 CIE chromaticity color coordinate diagram of Sm^{3+}-doped with NZT glass materials, excited at 402 nm.

$$\mathrm{r_i} = \left(\frac{1}{N}\right)^{\frac{1}{3}} \quad \dots\ \dots\ \dots\ (5.5)$$

$$\mathrm{r_p} = \left(\frac{\pi}{48\mathrm{N}}\right)^{\frac{1}{3}} \quad \dots\ \dots\ \dots\ (5.6)$$

$$\mathrm{F} = \left(\frac{\mathrm{Z}}{\mathrm{r_p^2}}\right) \quad \dots\ \dots\ \dots\ (5.7)$$

Fig.5.10 shows the variation of inter-ionic distance (r_i) and field strength (*F*) with ion concentration of Sm^{3+} ions. Inter-ionic distance (r_i) and polaron distance (r_p) decrease up to 1 wt% doping concentration of Sm^{3+} ions. The field strength (F) between Sm^{3+}- Sm^{3+} ions is increased with the ion concentration up to 1 wt% of Sm^{3+} ions obtained using Eq. (5.7).

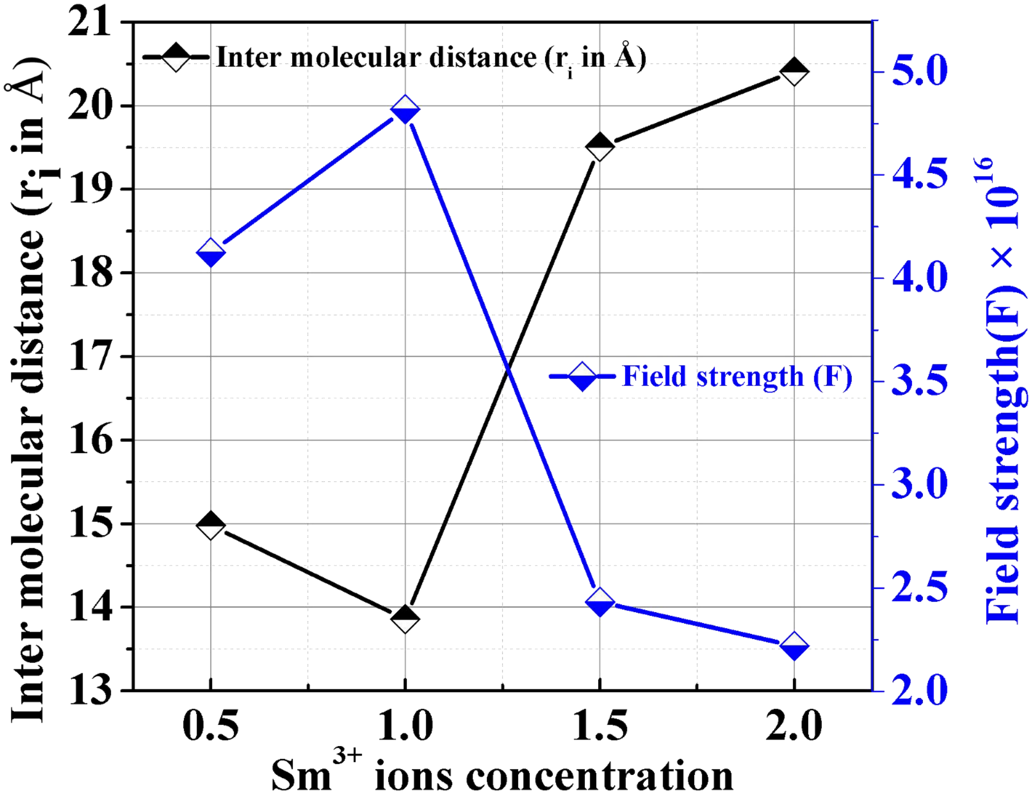

Fig 5.10 Variation of inter-molecular distance and field strength with Sm^{3+} ions concentration.

Again, the inter-ionic and polaron distance increase up to 2 wt% of Sm^{3+} ions and correspondingly the field strength (*F*) decreases due to the variation of Sm^{3+} ions which confirmed the fluoresce emission spectra. As the inter-ionic distance (r_i) decreases between two Sm^{3+} ions for the compactness of the glass structure, the strong interaction of Sm^{3+} ions can transfer the excitation energy from one Sm^{3+} ion to the other [217]. In a similar manner, the ion density varies with the emission intensity for the doped samples.

Table 5.2 Band gap energy, refractive index, and other physical properties of pure and Sm^{3+}-doped NZT glasses.

Samples Name	Band gap energy E_g (eV)	Refractive index(n)	Inter Molecular distance (r_i) in Å	Polaron Distance (r_p) in Å	Field strength (F)× 10^{16}	Ion density $\times 10^{20}$
NZT+0.0% Sm_2O_3	2.95	2.41	--	--	--	--
NZT+0.5% Sm_2O_3	2.28	2.63	14.98	6.037	4.125	2.97
NZT+1.0% Sm_2O_3	2.22	2.65	13.86	5.586	4.819	3.76
NZT+1.5% Sm_2O_3	2.12	2.69	19.51	7.862	2.432	1.35
NZT+2.0% Sm_2O_3	1.58	2.95	20.41	8.228	2.220	1.18

5.3.3.4 Cross Section

The absorption cross-section of the glass materials for the ${}^4G_{5/2} \rightarrow {}^6H_{7/2}$ transition has been measured using the Lambert-Beer formula

$$\sigma_{ab}(\lambda) = 2.303\frac{A_b}{Nt} \quad \dots \dots \dots \quad (5.8)$$

Where A_b is absorbance, t is the width of the glass sample and N is the density (ions/cm^3) of Sm^{3+} ions of the telluride glass.

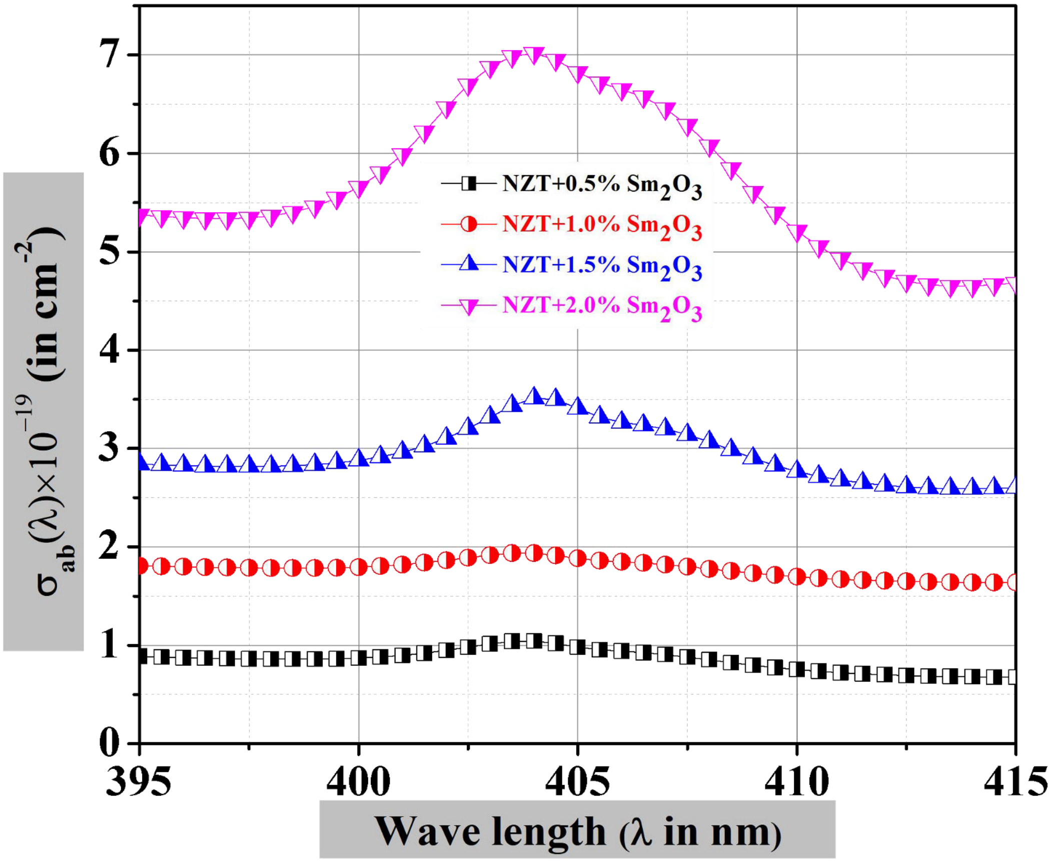

Fig 5.11 Wavelength dependence absorption cross-section of Sm_2O_3-doped NZT glass materials.

Fig. 5.11 shows the absorption cross-section is increasing for increasing the concentration of Sm^{3+} ions in the NZT glass samples. The emission cross-section σ_{emi} is calculated using MaCumber (1964) theory [176].

The absorption and emission cross-section are related with the formula

$$\sigma_{emi}(\lambda) = \sigma_{ab}(\lambda)\exp\left[\frac{E_g - h\nu}{K_B T}\right] \quad \dots \dots \dots \quad (5.9)$$

Where ν is the photon frequency, E_g is the free energy needed to excite Sm^{3+} from $^4G_{5/2} \rightarrow {}^6H_{7/2}$ state at temperature T, h is the Planck's constant, and K_B is the Boltzmann constant.

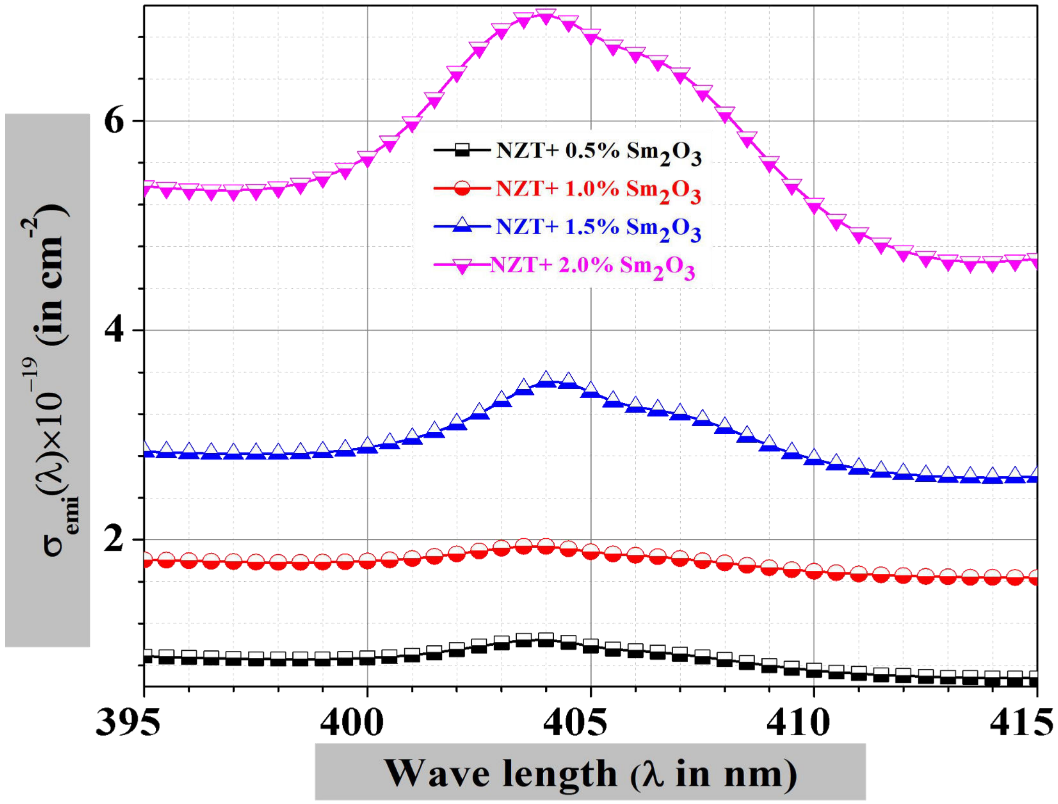

Fig 5.12 Wavelength dependence emission cross-section of Sm_2O_3-doped NZT glasses.

Fig. 5.12 shows the emission cross-section of Sm^{3+} doped glasses for the $^4G_{5/2} \rightarrow {}^6H_{7/2}$ transition. The emission cross-section of Sm^{3+} doped NZT glasses is increased due to the higher concentration of Sm^{3+} ions. The emission cross-section (σ_{emi}) is the main parameter and its value suggests the rate of energy removal from the lasing material [271]. The higher value of emission cross-section proposes the interesting characteristic for high gain laser applications, low threshold, which are applied to achieve constant wave (CW) laser action.

5.3.4 Dielectric Property

5.3.4.1 Dielectric Constant

The values of the dielectric constant are correlated to the electron density and ionic charges. The effect of frequency on dielectric constant for Sm_2O_3 doped NZT glass is observed in Fig. 5.13 for the frequency range 100 Hz - 8 MHz at room temperature. It has been observed that the magnitude of ε decreases swiftly with increasing frequency of 100 Hz to 2 kHz. This could be attributed to the dielectric dispersion resulting from the delay of the polarization process of the molecules behind the interchanges of the applied electric field [273].

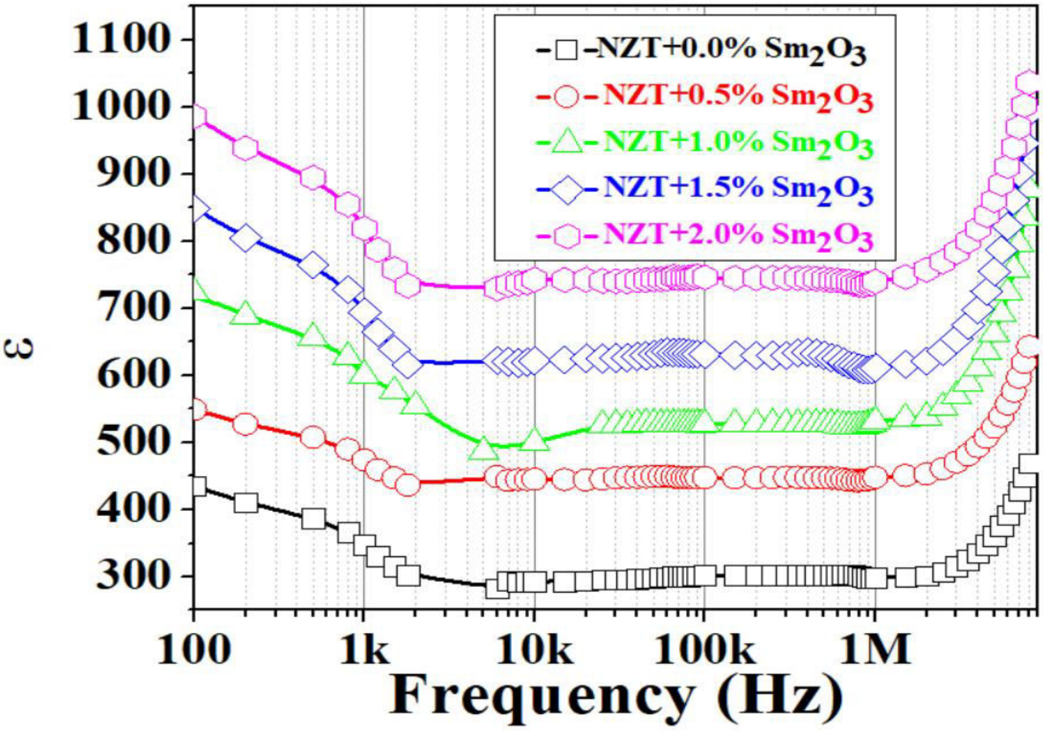

Fig 5.13 Dielectric constant (ε) for Sm^{3+}-doped NZT at room temperature.

At low frequencies, the increase of dielectric constant is also ascribed to the electronic, ionic, dipolar, interfacial polarization and the absence of spontaneous polarization [274-

277]. The magnitude of ε of these glasses is almost constant in the frequency region 3 kHz - 2MHz due to the decrease of ionic, space charge, and orientation polarization [278]. It has been also described that the pure and doped glasses are not maintaining any variation of dielectric constant with frequency because of the stable molecular orientation, and the electron exchange between the ions does not follow a high frequency applied field. On the other hand, this may be explained as the applied frequency increases, the ions are not able to respond quickly and it reveals an almost frequency-independent behavior that may be due to the diminishing number of dipoles which contributes to polarization in the high-frequency region [277].

The dielectric constant increases rapidly beyond the frequency region 2 MHz [221, 279]. It has been observed that the dielectric constant increases from 430 to 980 for Sm_2O_3 doping in the lower frequency as well as advanced frequency. This effect may be explained by the charge accumulation due to rare-earth doping. The increasing concentration of doped ions disrupts the tellurite glass system by producing dangling bonds and NBOs. These bonds and NBOs create the motion of charges and thus generate space charge polarization leading to a sharp rise in the dielectric constant [273]. This result is similar to Eu^{3+} doped NZT glass materials [221].

5.3.4.2 DC Conductivity

The variation of electrical conductivity as a function of temperature is shown in Fig. 5.14. The conductivity increases with temperature and also with the doping concentration of Sm^{3+} ions concentration. This variation of conductivity with temperature establishes that the electrical conduction mechanism is Arrhenius type. This Arrhenius mechanism of electrical DC conductivity can be applied to determine the activation energy of the samples using the connection

$$\sigma_{dc} = \sigma_0 \exp^{\frac{E_a}{K_B T}} \quad \dots \dots \dots \quad (5.10)$$

Where E_a is the activation energy, σ_0 denotes the pre-exponential factor, T is the absolute temperature and K_B is the Boltzmann constant. The assessed activation energies for these samples have been measured from Fig. 5.14. The activation energy reduces (0.63 eV to 0.43 eV) due to the doping of Sm^{3+}ions. The collaboration between the rare-earth ions and structural units of host glass clarified the increment of DC conductivity due to the increasing concentration of rare-earth ions [221]. The technique of conductivity in the glass structure is defined by doping concentration, atomic weight and position of Sm^{3+} ions. The doping concentration of rare-earth ions generates a huge number of NBO in the tellurite glass materials which is also established from FTIR spectra for Sm^{3+} doped NZT glass materials. The higher concentrations of Sm^{3+} ions in the NZT glasses enhance the creation of NBO atoms and hence the conductivity is improved for all the glass materials [154].

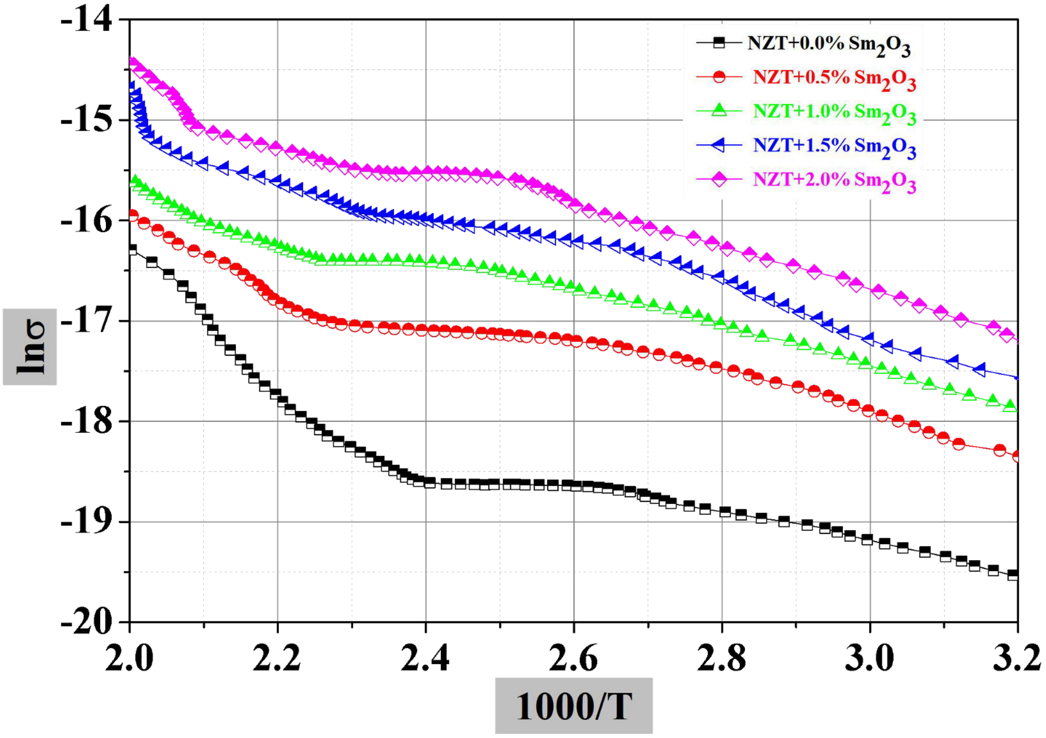

Fig 5.14 The variation of lnσ versus 1000/T.

5.4 Conclusions

Samarium (III) doped NZT glasses have been efficiently prepared by the melt-quenching method. The X-ray diffraction characterization indicates the amorphous nature of the glass materials for the higher doping concentration of Sm^{3+} ions. FTIR spectra reveal the construction of a new glass structure of pure and Sm_2O_3 incorporated NZT glasses. The stability of the glass sample is examined by using Hruby's parameter (H), and thermal stability ΔT from the DTA curve. The value of H is 0.57 for the highest glass stability in the higher doping of Sm^{3+} ions. The refractive index increases from 2.41 to 2.95 with the increase of Sm^{3+} ions. The absorption bands of the glass materials are found corresponding to the transitions $^6H_{5/2} \rightarrow {}^4P_{3/2}$ at 402 nm, $^6H_{5/2} \rightarrow {}^4M_{19/2}$ at 418 nm, $^6H_{5/2} \rightarrow {}^4I_{5/2}$ at 462 nm and $^6H_{5/2} \rightarrow {}^4I_{11/2}$ at 478 nm. The emissions at 563 nm, $^4G_{5/2} \rightarrow {}^6H_{5/2}$, at 600 nm, $^4G_{5/2} \rightarrow {}^6H_{7/2}$, at 645 nm, $^4G_{5/2} \rightarrow {}^6H_{9/2}$ are observed in the photoluminescence spectra. Based on the studied optical properties it is concluded that Sm^{3+} doped NZT glasses may be used as an active medium for laser emission at 600 nm corresponding to the $^4G_{5/2} \rightarrow {}^6H_{7/2}$ transition. Field strength (F) increases with increasing the Sm^{3+} ions concentration and consequently, the inter-ionic distance (r_i) and polaron radius (r_p) are observed to decrease. The value of band gap energy decreases from 2.95 eV to 1.58 eV due to doping. The magnitude of the photonic band gap E_g is decreased due to the change in the structure of such glasses. The dielectric constant increases from 430 to 980 for Sm_2O_3 doping in the lower frequency at room temperature. The dielectric constant of Sm_2O_3 doped NZT glasses has been measured for various frequencies and found as a stable substance within the frequency of 3 kHz-2 MHz. The DC conductivity increases with temperature whereas the activation energy decreases with the increase of ion concentration in the usual manner. So, Sm_2O_3-doped NZT glass samples have a large prospect for application in optoelectronic devices.

[*This work has been published in J. Phys. Chem. Solids, 2022, vol. 167, pp. 110776. https://doi.org/10.1016/j.jpcs.2022.110776.*]

Chapter-6

Enhancement of optical and electrical properties of Pr^{3+} doped Na_2O-ZnO-TeO_2 glass materials

6.1 Introduction

Rare-earth (RE) doped tellurite glasses are displayed in different types of applications in science and technology such as waveguide lasers, bulk lasers, and optical fiber amplifiers. Recently, the applications of rare-earth-doped tellurite glasses are used in the region of visible optical instruments, particularly for white light-emitting diode (w-LED) applications such as indicators, back-light, automobile headlights, and general illumination [66]. White light-emitting diodes (w-LEDs), known as the next generation of solid-state lighting (SSL) technology have become very familiar because of their potential applications in various fields. The SSL is of great significance to decrease the global electricity utilization convention of fossil fuels [280, 281]. In comparison to other conventional light sources like fluorescent tubes and incandescent lamps, the w-LEDs have a large number of qualities such as relatively high luminous power, eco-friendly characteristics, larger operation lifetime, and safety [282]. In recent times, these w-LEDs are developed by the proper arrangement of blue LED and YAG: Ce^{3+} with a yellow phosphor [283]. Recently, rare-earth-doped glass materials maintain a very important role in various scientific and technological applications such as SSL, optical amplifiers, bar code reading, sensors, display devices and telecommunications [284]. Among the glass-forming oxides, rare-earth-doped borate glasses are shown large interest due to their physical parameters and optical properties like lower melting point, large dielectric constant and photon energy. Along with the above potential characteristics, research communities illustrate the enormous attention towards tellurite glass materials due to their benefits such as high density, good durability and mechanical and chemical stability. Tellurite glass materials have some motivating properties like the hardness of suitable strength, transparent at normal temperatures and high corrosion resistance [222-224]. Tellurite-based glasses are very exciting glass materials for linear and non-linear applications in optics, due to their significant characteristics such as their low melting point and large refractive index. It has also essential for high dielectric constant, non-hygroscopic, good chemical durability, and high thermal stability, with a large transmission window and the possibility to integrate a large quantity of rare-earth ions.

The tellurite glass materials are also used for the safety purpose of gamma radiations, X-ray emission, and ionizing radiations from radioactive materials due to radioactive mining, nuclear power plants, etc. Previously, heavy metals like lead (Pb), antimony (Sb), arsenic (As), bismuth (Bi), etc. have been used to save from damage to these radiations but Pb has some disadvantages to environmental pollution. Tellurite/borate glass materials can be used to overcome environmental pollution [285]. Rare-earth doped tellurite glasses also control the solar spectrum to increase solar cell efficiency as renewable energy sources [286]. It can be used as a quantum medium for quantum information [287]. Tellurite glasses are useful to study by industrial research workers not only because of their methodological applications but also remaining of fundamental significance in thoughtful their microscopic mechanisms [233, 234]. The emission characteristics of optical glass materials have not been observed only for application in laser crystals, scintillators and phosphors but also to serve the purpose of technological advancement during the last few decades. In presence of the rare-earth ions, glass materials have shown excellent luminescence properties due to their emissive power of electronic transitions 4f-4f and 4f-5d [235-241]. It has also been observed that the intensity of fluorescence spectra of rare-earth-doped tellurite glass samples is increased when a glass host has low phonon energy, as borate glass(1400 cm^{-1}), silicate glass (1050 cm^{-1}), phosphate glasses (1280 cm^{-1}) [288].

Praseodymium is one of the most interesting optical activators among the rare-earth elements, which suggests the prospect of instantaneous blue, green and red emission for laser activity as well as IR emission for optical amplification [288]. Energy levels of the praseodymium ions reveal the number of meta-stable states. Many of the researchers highlighted the laser transitions $^3P_0 \rightarrow {}^3H_4$ (blue), $^1D_2 \rightarrow {}^3H_4$ (orange) in the visible wavelength region [284]. Pr^{3+} doped tellurite glass materials can also be used as a temperature sensors based on their fluorescence property [289]. Recently, many researchers concentrate on Pr_2O_3-doped tellurite glasses for their potential applications in photonic and optoelectronic devices.

The present study aims to prepare Pr_2O_3-doped NZT glasses and to investigate the transition of the absorption and emission spectra for optical applications. The frequency-dependent dielectric constant and temperature-dependent conductivity of the pure and doped glass materials have also been studied.

6.2 Experimental Outline

The melt-quenching process was used to prepare pure and Pr^{3+} doped Na_2O-ZnO-TeO_2 (NZT**)** glasses using research-grade initial composition Zinc Oxide (ZnO), Tellurium di-Oxide (TeO_2), Sodium Carbonate (Na_2CO_3) manufactured by Merck and Praseodymium Oxide (Pr_2O_3) made by LobaChemie. The mixing ratio of TeO_2, ZnO, and Na_2O is continued as 7: 2: 1 to make the glass matrix. Praseodymium Oxide (Pr_2O_3) was added to the glass system as a dopant for (0-2) wt%. The standardized mixture of these precursors was obtained by grinding the ingredient powders in an agate mortar. The mixture was placed in an alumina crucible and the crucible was kept in an electrical furnace. The mixture was heated in two steps, initially at the temperature of 400 °C for 1 hour and at 475 °C for 30 minutes inside the electrical furnace. The powder materials were melted at 475 °C and the melted compounds were transferred to the stainless-steel plate of cylindrical shape. The slow-cooling method was maintained to arrive the room temperature for the removal of thermal stress. X-ray diffractogram of the glass samples was obtained using an X-ray diffractometer (RIGAKU model: Japan, XRD 6000, λ = 1.5418 Å) with a slow-scanning rate of 3°/min between the angle 10º and 80º for all the materials. FTIR spectrometer (HITACHI Model F-700) was used to detect the type of pure and doped glasses in the wave number region 400 - 1500 cm^{-1}. Absorption spectra and emission band of all the glasses were found using UV/VIS/NIR spectrophotometer (Perkin Elmer Lambda-35) for the wavelength range 400 - 700 nm and fluorescence spectrophotometer (HITACHI Model F-7000) for 470-700 nm at room temperature. The dielectric constants (ε) of prepared glass materials were measured using LCR-HiTESTER (HIOKI, Japan) for the wide frequency range of 100 Hz-8 MHz at room temperature. The temperature-dependent DC conductivity of glass samples was measured for the temperature range 36 °C – 225 °C using a constant voltage supply and current meter.

6.3 Result and Discussion

The colour of the NZT glass material is translucent and colourless, while Pr^{3+}-doped NZT glass materials are turn into green colour due to the doping concentration of Pr^{3+} ions in the host glasses. The prepared Pr^{3+}-doped NZT glasses were shown in Fig. 6.1. The coloured glass materials vary from white to green with the incorporation of Pr_2O_3. It has been found that there are no visible crystallites present in these transparent samples.

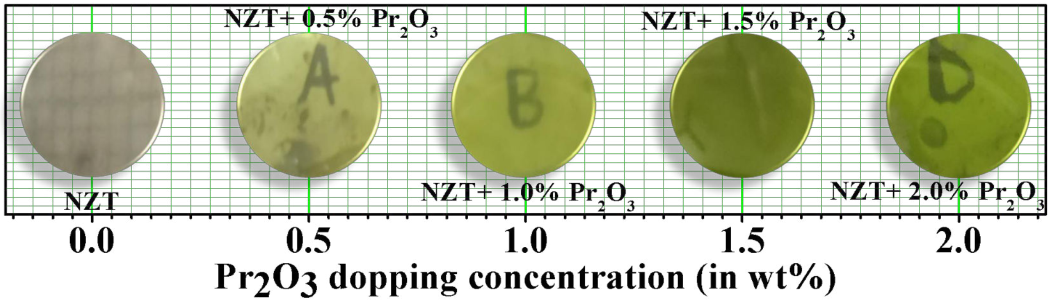

Fig 6.1 Pictorial view of Pr_2O_3-doped NZT glass samples.

6.3.1 Thermal Properties

Fig. 6.2 shows the DTA curve of the pure and Pr_2O_3 doped NZT glass materials for the temperature range 35 °C to 650 °C heating rate of 10 °C/min in the Argon environment. Three consecutive endothermic peaks are displayed on the DTA curve between 72 °C and 165 °C for the precursor samples and depicted to desorption or elimination of moisture from the samples. The endothermic peak at 277 °C is revealed the temperature of glass transition (T_g) and at 447 °C melting point of the samples. It has been found the glass transition temperatures slightly decrease with the higher doping concentration of Pr_2O_3 but the melting temperature decreases with the doping concentration. The addition of rare-earth ions (Pr^{3+}) to the tellurite glass network also causes the decreasing values of bridging oxygen (BO) and creating non-bridging oxygen (NBO) [290]. As a result, the glass transition temperature decreases due to the formation of non-bridging oxygen. The exothermic peak near 400 °C has evolved due to the decomposition of CO_2 from the precursor powders. The decomposition temperature of CO_2 is decreased due to the doping of Pr_2O_3 in the host glass materials can be explained through the strength of the bonds Te–O and Pr–O. The stronger Pr–O bonds replace the Te–O bonds and generate NBO which can decrease the decomposition temperature.

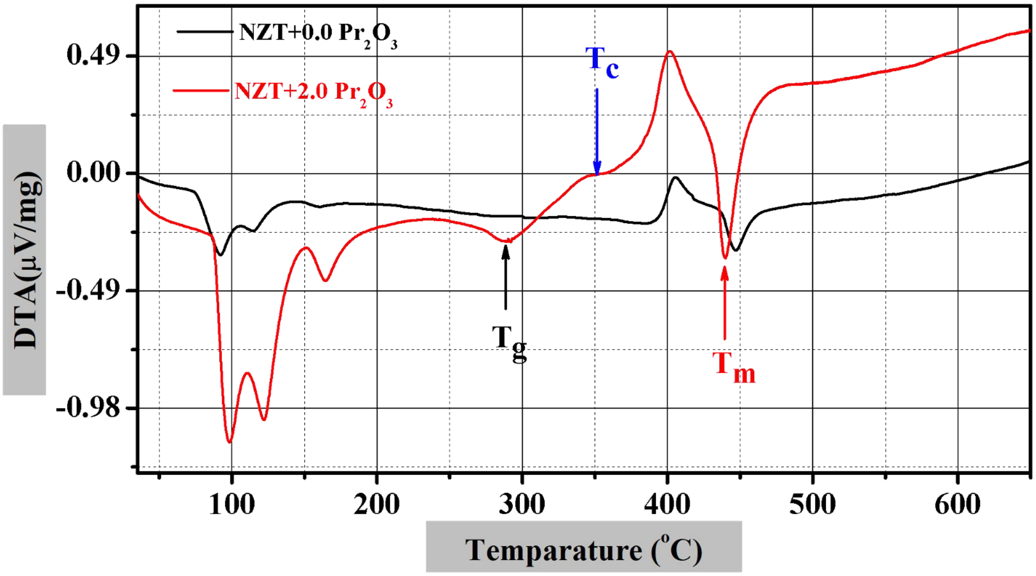

Fig 6.2 DTA curves of pure and Pr_2O_3-doped NZT glasses.

The DTA curves also show the phase transition occurred through melting at around 447 °C for pure host glass. The melting point of TeO_2 is 730 °C which is decreased due to the presence of Na_2CO_3 mixed with ZnO [198]. It is also found that the melting point decreases with the doping of Pr_2O_3. The T_g value of the samples are increasing with the increasing doping concentration of Pr_2O_3. The structural stability is gradually adapted as the glass transition temperature increases [249]. Softening temperature (T_c) is increased for the higher doping concentration of rare-earth ions. The calculation of thermal stabilities ΔT of the Pr^{3+} doped NZT glass samples is tabulated in Table 6.1. The thermal stability of glass materials is estimated for a glass host from the numerical value of ΔT [246]. The nucleation and crystallization will occur with the increased value of ΔT [247, 248]. This result specified that the glass sample possesses good thermal stability.

Hruby's parameter (H) has been calculated by using Eq. (6.1) and found the higher glass forming tendency as the magnitude of Hruby's parameter is improved.

$$H = \frac{T_c - T_g}{T_m - T_c} \quad \ldots \ldots \ldots \quad (6.1)$$

Table 6.1 Thermal parameters determined from the DTA traces of pure and Pr_2O_3-doped NZT glasses.

Sample Name	% Pr_2O_3	T_g (˚C)	T_c (˚C)	T_m (˚C)	ΔT (˚C) = T_c-T_g	H = (T_c-T_g)/(T_m-T_c)
NZT+ 0.0% Pr_2O_3	0.0	284	328	447	44	0.37
NZT+ 2.0% Pr_2O_3	2.0	285	351	439	66	0.75

Fig. 6.3 represents the TG with DTG plot of the powder ingredients for pure and Pr_2O_3 doped NZT glasses. The weight loss started when the powders heated beyond 60 °C. TG/DTG curve represents the 9.23% loss out of total mass from room temperature (35 °C) up to 600 °C through step-wise decomposition of the compounds and release of volatile substances, like water, carbon dioxide etc. It is found from Fig. 6.3 that the mass loses 5.28% of its weight at about 60 - 125 °C attributed to the removal of moisture [168, 249]. The DTG curve supports the weight loss due to the removal of absorbed moisture and other volatile compounds through displayed three peaks at 87 °C, 110 °C, and 160 °C. The peak of the DTG curve is observed near 395 °C for NZT glass samples and 392 °C for 2% Pr_2O_3 doped NZT glasses because of the decomposing of anhydrous Na_2CO_3. The CO_2 evolved at that temperature which is also predicted from the DTA curve of Fig. 6.2. The CO_2 is produced at 365 - 415 °C and is also identified by the TG curve. The decomposition temperature of Na_2CO_3 is reduced in the TeO_2 environment and the corresponding decomposition takes place at 392 °C. The last peak at 447 °C has shown a small change of mass loss during the melting of the solid powder samples.

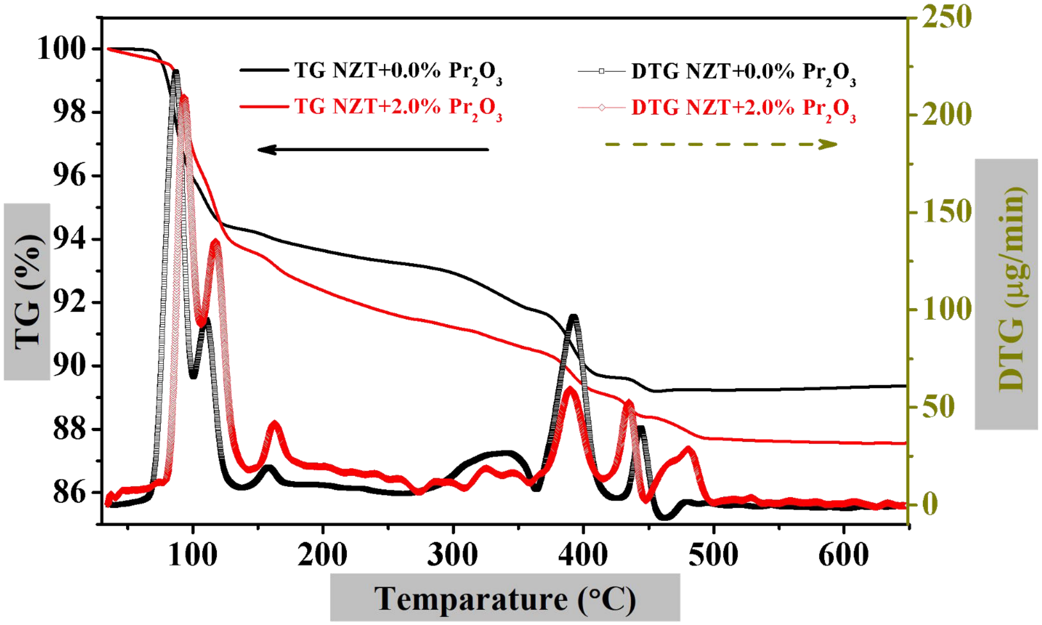

Fig 6.3 TG and DTG curve of ingredients powder for pure and Pr_2O_3-doped NZT glasses.

The peak positions are shifted to the lower temperature for the higher doping concentration of Pr_2O_3 due to decreasing the number of bridging oxygen which implies the increase of non-bridging oxygen. This may be suggesting that the remaining part of Na_2CO_3 decomposes and emission of CO_2 with a small mass at that temperature and also with some volatile substances. After the temperature of 460 °C there is no weight loss revealing that the glass samples have been melted as glass materials.

6.3.2 XRD

X-ray diffractogram of pure NZT and Pr_2O_3 doped glass materials are shown in Fig. 6.4. It is clearly observed that the XRD curve shows mainly the non-crystalline structure with limiting crystallinity of hexagonal phase (space group P 63/m (176); lattice parameters are a = b = 9.410 Å and c = 7.640 Å) of $Na_2Zn_2(TeO_3)_3$. The crystallinity develops for the higher concentration of Pr^{3+} ions i.e. non-crystalline or amorphous nature decrease for the higher concentration of rare-earth ions [291]. Gallerande et al 2022 confirmed that the crystalline nature of TeO_2–ZnO–Na_2O glasses increases for rare-earth doped ions

(Nd^{3+}) [292, 293]. The peak positions of XRD pattern for the present studied samples are observed at 10.87°, 21.83°, 22.45°, 23.07°, 24.95°, 25.49°, 29.01°, 29.95°, 31.29°, 31.95°, 35.05°, 38.29°, 40.60°, 45.13°, 47.13°, 48.73°, 50.67°, 52.83°, 54.03°, 57.87° and 65.29° for the (100), (200), (111), (002), (201), (012), (210), (112), (211), (202), (301), (220), (113/302), (222), (004), (320), (402), (411), (313), (501) and (422) planes of $Na_2Zn_2(TeO_3)_3$ compound. The peak intensity of the XRD pattern is increased due to the incorporation of Pr^{3+} ions.

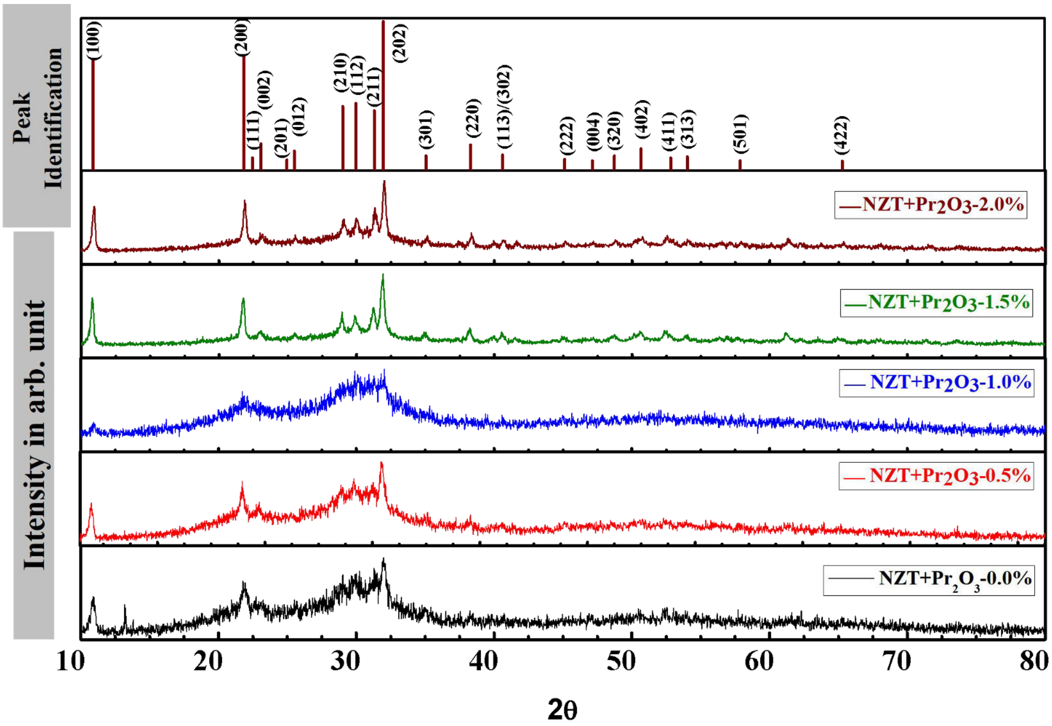

Fig 6.4 XRD pattern of pure and Pr^{3+}-doped NZT glass materials.

6.3.3 Optical Properties

6.3.3.1 FTIR Spectra

Fig. 6.5 shows the structural behaviour of pure and Pr_2O_3 doped NZT glass samples in the wave number range 400-1500 cm^{-1}. The band at 424-450 cm^{-1} comes out due to the symmetric stretching vibration of the Zn-O bond. From Fig. 6.5, wave number band 448 cm^{-1} is found due to the stretching vibration of the Zn-O bond in ZnO_4 tetrahedral which is an indication of incorporation of ZnO into the glass network [255]. The structure of TeO_2-rich glasses contains mainly of a three-dimensional network of TeO_4 trigonal bipyramidal (tbp) units. These units have two equatorial and axial sites that are connected with oxygen atoms and the third equatorial site is occupied by a lone pair of electrons. The three-dimensional network can be modified with the transformation of TeO_4 units into TeO_{3+1} and TeO_3 units by using the proper modifier [201]. The intensity of the vibration band at 677 cm^{-1} in the tellurite host glass network indicates the modifications of trigonal bipyramidal (tbp) units. Here, the addition of ZnO acts as a glass modifier into a chain-like structure with Te_3O_8 groups built by TeO_4 and two TeO_{3+1} units connected by six coordinated Zn^{2+} ions. The contributions of stretching vibrations due to the Zn–O bond are also expected at this wavenumber. Zn^{2+} ions perform as an agent to split bonds and generate a modification in the glass structure [201]. For this result, TeO_{3+1} and TeO_3 can be twisted from TeO_4 units making non-bridging oxygen atoms [205]. The band 648 – 680 cm^{-1} occurred due to the stretching vibration of TeO_4 [254]. The peak position of the transmission line at 648 cm^{-1} for the host glass shifted due to the doping of Pr^{3+} ions motion of the fraction. The band at around 724 – 790 cm^{-1} is due to Te–Oeq bond vibrations of distorted TeO_4 units.

It has been observed that the 1222 cm^{-1} band arises for the deformed vibrations of OH-groups because the absorbed water molecules are bounded to the surface by the weak hydrogen bonds [38]. These bands are ascribed to the stretching vibration within the tellurium and the NBO of the trigonal pyramidal structure due to the glass modification with rare-earth ion (Pr^{3+}) [201].

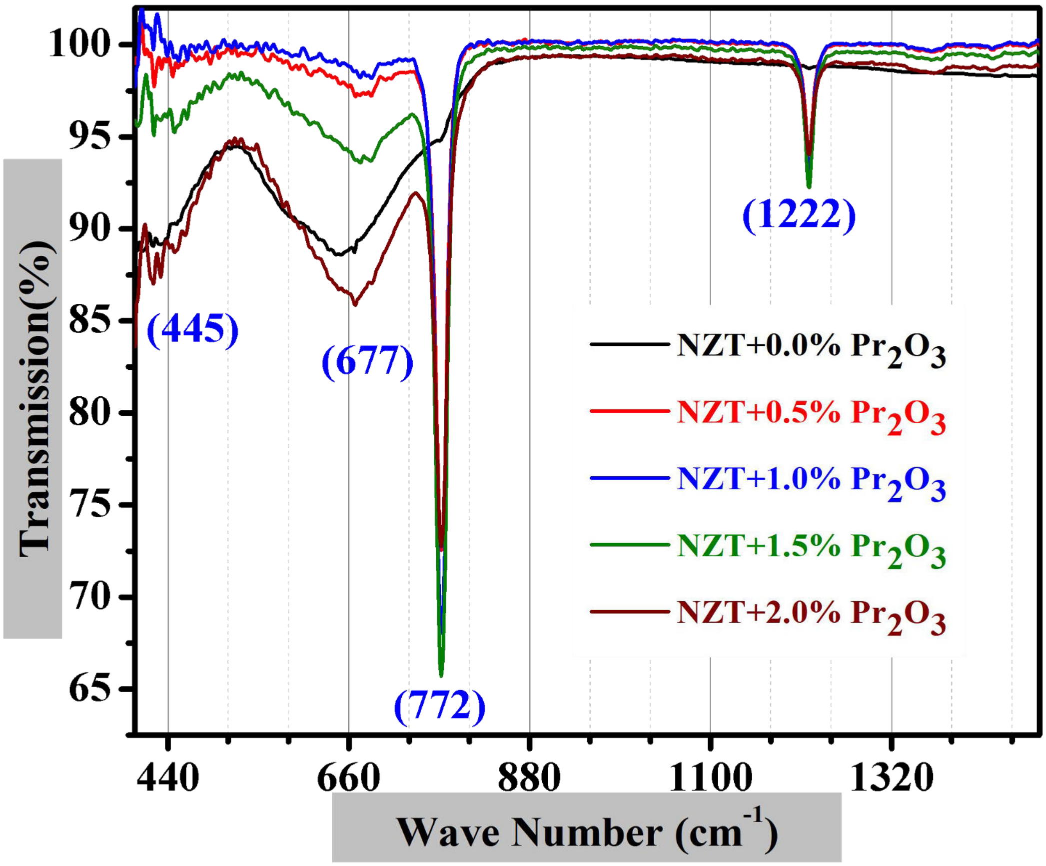

Fig 6.5 FTIR spectra of Pr_2O_3-doped NZT glass samples.

6.3.3.2 Raman Spectra

Fig. 6.6 shows the Raman spectra of pure and doped NZT glass samples. These spectra of glasses can be the signature of semi-crystallized glass materials as expected. The bands are sharper and the intensity of bands increases with the increase of doping concentration also confirmed from the XRD with hexagonal $Na_2Zn_2(TeO_3)_3$ crystalline phase. The wide band 442 cm^{-1} is assigned to the structural unit of TeO_4 tbps with symmetric bending vibration. Another sharp and strong band at peak 774 cm^{-1} is ascribed to the symmetric stretching vibration of TeO_4 tbps and at 700 cm^{-1} a band arises due to the asymmetric stretching vibration of Te-O-Te. The strong band around 774 cm^{-1} is associated with non-bridging-oxygens present in the glasses and more pronounced than the neighbouring bands at 700 cm^{-1}. The phonon energy of hosts glass and Pr_2O_3-doped glasses represent the vibrational energy in the Raman spectrum.

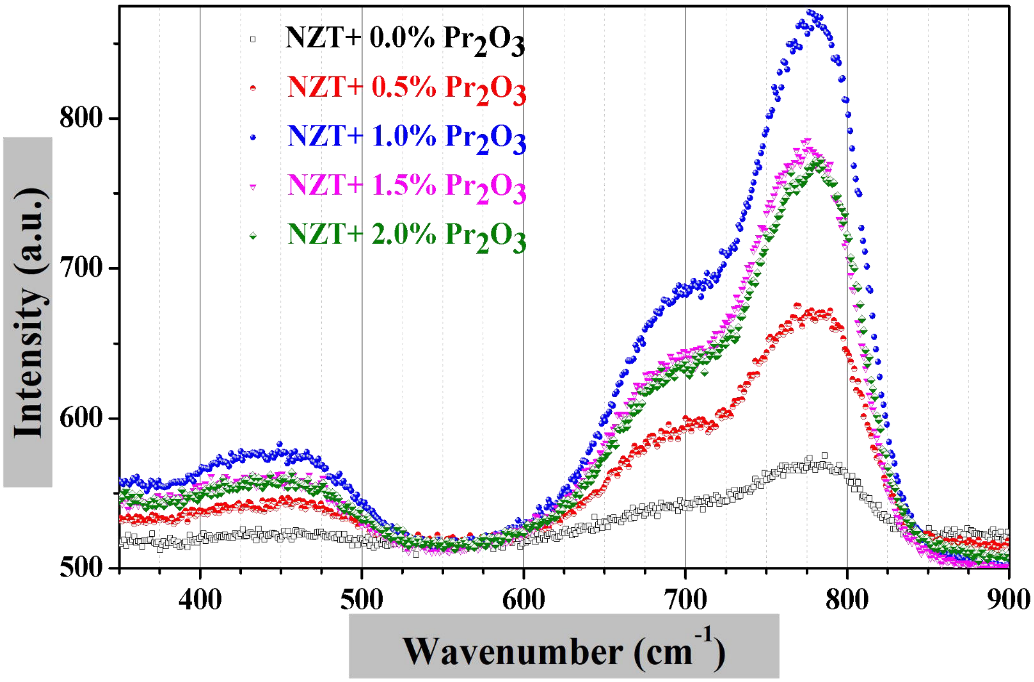

Fig 6.6 Raman spectra of pure and Pr_2O_3-doped NZT glass samples.

The atomic vibration corresponding to the band 442 cm^{-1} in TeO_2 glass may be the vibrations of oxygen atoms which is lighter than the immobile Te atoms. The bands 700 cm^{-1} and 774 cm^{-1} in the spectrum can be assigned for both TeO_3 tp units and TeO_4 tbps units [193, 198].

6.3.3.3 Absorption Spectra

Fig. 6.7 shows the absorption spectra of pure and Pr_2O_3-doped NZT glass samples. The recording of absorption data has been performed in the visible wavelength region (400 - 700 nm) at room temperature with intense band assignments. It is observed that the absorption intensity increases gradually with the increase of Pr^{3+} ions [295-299]. There is no transition occurred for the pure NZT glass sample, whereas the absorption peaks appeared at specific transitions in case of Pr^{3+} ions doping. The tail of the optical absorption band is not strongly identified due to the non-crystalline nature of glasses which is also established from XRD analysis.

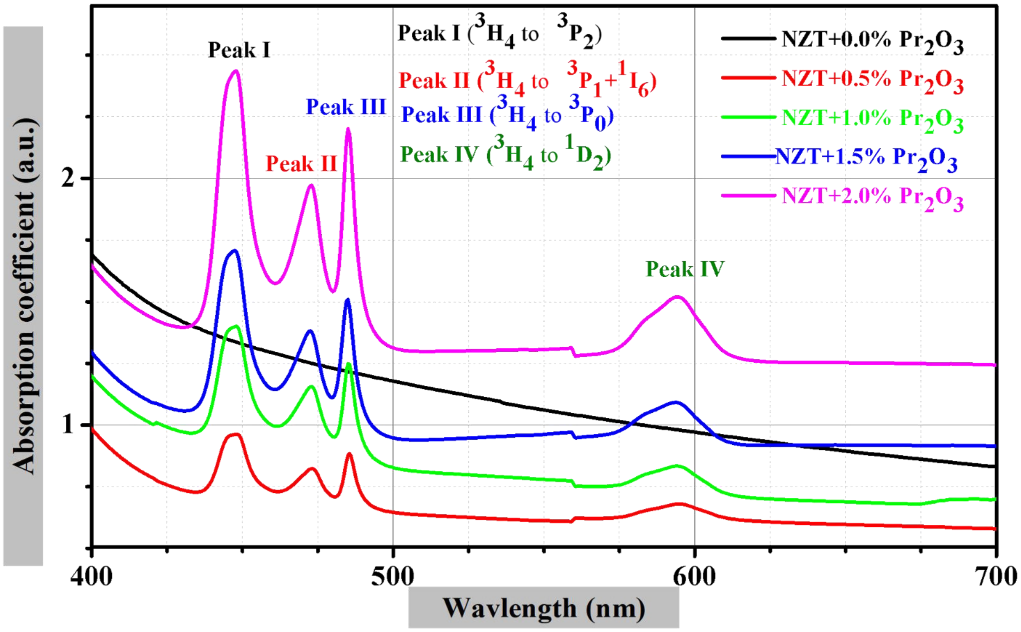

Fig 6.7 Absorption spectra of pure and Pr_2O_3-doped NZT glass samples.

The peak position of Pr^{3+}-doped NZT samples is obtained due to the interaction of 4f - 5d electronic configurations. It is found that there are four absorption peaks in Fig. 6.7. These transitions are $^3H_4 \rightarrow {}^3P_2$, $^3H_4 \rightarrow {}^3P_1 + {}^1I_6$, $^3H_4 \rightarrow {}^3P_0$, $^3H_4 \rightarrow {}^1D_2$ at 447, 472, 485 and 594 nm respectively. Carnall et al. approved these transitions [257]. The transition allowed to the selection rule $\Delta S = 0$, $\Delta L \leq 2$, $\Delta J \leq 2$ which are the same as those of a pure quadruple transition. The transition $^3H_4 \rightarrow {}^3P_2$ is the hypersensitive transition for the Pr^{3+} ion, and the peak intensity is modified significantly with the glass composition [296]. Fig. 6.8 shows the variation of absorption coefficient $\alpha(\nu)$ with corresponding energy. The absorption coefficient in many non-crystalline materials reflects the density of states at the band tails and can be determined from the absorption spectra using the relation.

$$\alpha(\nu) = \left(\frac{A_b}{t}\right) \dots \dots \dots \quad (6.2)$$

Where $\alpha(\nu)$ is absorption coefficient, A_b is the absorbance, and t is the thickness of the sample.

Again, the relation between the absorption coefficient and photon energy is

$$\alpha(\nu) = \frac{B\left(h\nu - E_g\right)^m}{h\nu} \quad \dots \dots \dots \quad (6.3)$$

Where B is the constant, m is the index number; E_g and h are optical band gap energy and Planck constant respectively.

The absorption coefficient has been determined for the indirect band gap energy with m = 2 by plotting the graph $(\alpha h\nu)^{1/2}$ vs. hν [258, 262, 300, 301]. For the indirect transitions, the corresponding value of E_g is obtained by extrapolating $(\alpha h\nu)^{1/2} = 0$.

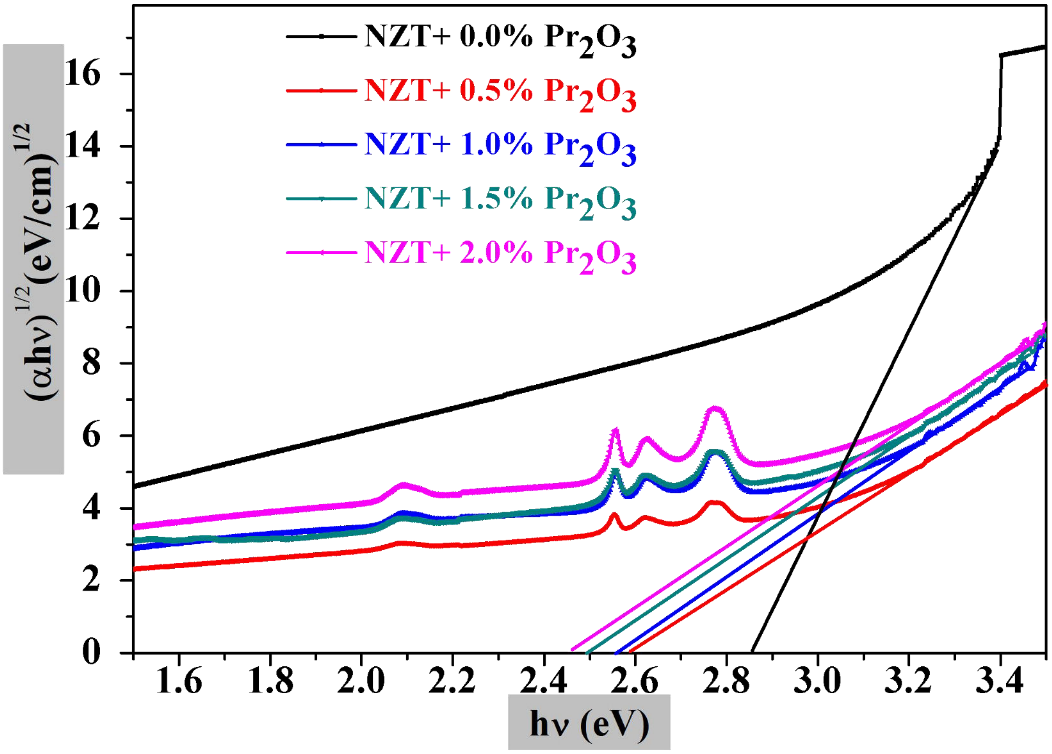

Fig 6.8 Tauc's plot for pure and Pr^{3+}-doped NZT glass materials.

The magnitudes of band gap energy for the glasses are represented in Table 6.2. The decrease of E_g with increasing Pr^{3+} ions in this glass network can be explained by the creation of a large number of NBO in the samples. The negative charges of oxygen ions in the NBO create active electrons with a higher value than that on the BO. These active electrons are distributed irregularly because NBOs are softly bounded by the tellurite atoms. The obtained values of the E_g and the refractive index (n) can be estimated using Eq. (6.4) [258, 262,302, 303].

$$(n^2 - 1)/(n^2 + 2) = 1 - \sqrt{(E_g/20)} \quad \dots\ \dots\ \dots \quad (6.4)$$

The refractive index increases from 2.44 to 2.56 with the increasing number of rare-earth ions due to the creation of non-bridging bonds [304, 305].

Table 6.2 Band gap energy and refractive index for pure and Pr_2O_3-doped NZT glasses.

Sample Name	Band gap energy (eV)	Refractive Index (n)
NZT+0.0% Pr_2O_3	2.86	2.44
NZT+0.5% Pr_2O_3	2.59	2.52
NZT+1.0% Pr_2O_3	2.55	2.53
NZT+1.5% Pr_2O_3	2.49	2.55
NZT+2.0% Pr_2O_3	2.46	2.56

This effect can be attributed to the dissociation of the bridging Te–O–Te bonds and created non-bridging bonds. The bond energy of NBO is lower with greater ionic character. The cation refractions have a higher magnitude for the NBO bonds which are calculated from this relation [290].

$$r_i = (1/N)^{1/3} \quad \dots\ \dots\ \dots \quad (6.5)$$

$$r_p = (\pi/48N)^{1/3} \quad \dots\ \dots\ \dots \quad (6.6)$$

$$F = \left(Z/{r_p}^2\right) \dots \dots \dots \quad (6.7)$$

Fig. 6.9 shows the variation of inter-ionic distance (r_i) and field strength (F) with ion concentration of Pr^{3+} ions. Inter-ionic distance (r_i) and polaron distance (r_p) decrease with the doping concentration Pr^{3+} ions. The field strength (F) is found by using Eq. (6.7) and the magnitude of field strength between Pr^{3+}- Pr^{3+} ions is increased with the ion concentration of Pr^{3+} ions.

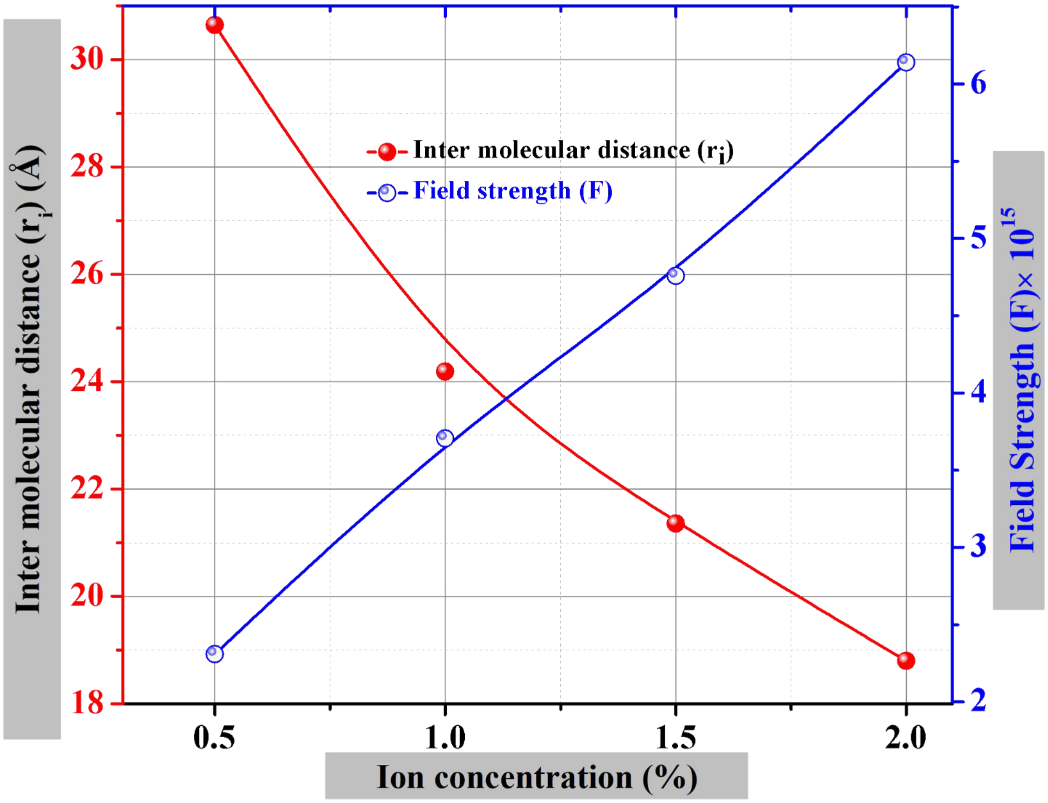

Fig 6.9 Inter-molecular distance and field strength with Pr^{3+} ions concentration of NZT glass samples.

Again, it has been observed that the inter-ionic and polaron distances decrease whereas, the field strength (F) increases with the variation of Pr^{3+} ions and has also been confirmed from the fluorescence spectra [217]. As the inter-ionic distance (r_i) decreases between two Pr^{3+} ions for the neatness of the glass network, the strapping interaction of Pr^{3+} ions can convey the excitation energy from one Pr^{3+} ion to the other ions [305].

6.3.3.4 Cross Section

The absorption cross-section of the glass materials for the $^3H_4 \rightarrow {}^3P_2$ transition has been estimated with the help of the Lambert-Beer formula:

$$\sigma_{ab}(\lambda) = 2.303\ A_b/(Nt) \quad \ldots \quad \ldots \quad \ldots \quad (6.8)$$

Where A_b is absorbance, t is the width of the sample and N is the density (ions/cm^3) of Pr^{3+} ion of the telluride glass [176]. Fig.6.10 shows the absorption cross-section decreasing for increasing the concentration of Pr^{3+} doped NZT glass samples. The emission cross-section is measured using MaCumber's (1964) theory.

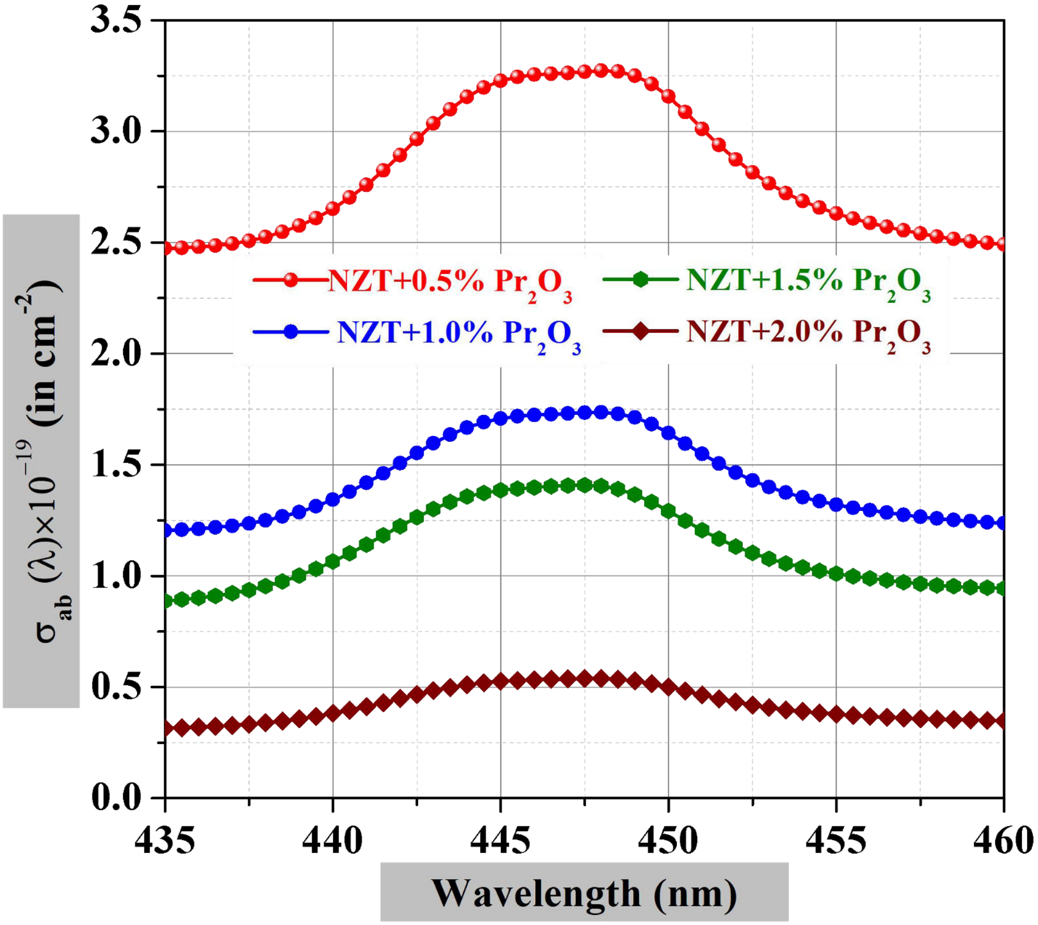

Fig 6.10 Wavelength dependence absorption cross-section of Pr_2O_3-doped NZT glasses.

The cross-section of emission and absorption spectra are associated with the formula:

$$\sigma_{emi}(\lambda) = \sigma_{ab}(\lambda) \exp[(E - h\nu)/K_B T] \quad \ldots \quad \ldots \quad \ldots \quad (6.9)$$

where ν is the phonon frequency, E is the free energy needed to excite Pr^{3+} from $^3H_4 \rightarrow {}^3P_2$ state at temperature T, h is Planck's constant, and K_B, Boltzmann constant. The emission cross-section of the $^3H_4 \rightarrow {}^3P_2$ transition of Pr^{3+} doped glass materials is shown in Fig. 6.11. The emission cross-section is decreased for a higher concentration of Pr^{3+} ions of NZT glasses [271, 306]. It is worth mentioning that the laser parameter can be estimated using absorption and emission cross-section.

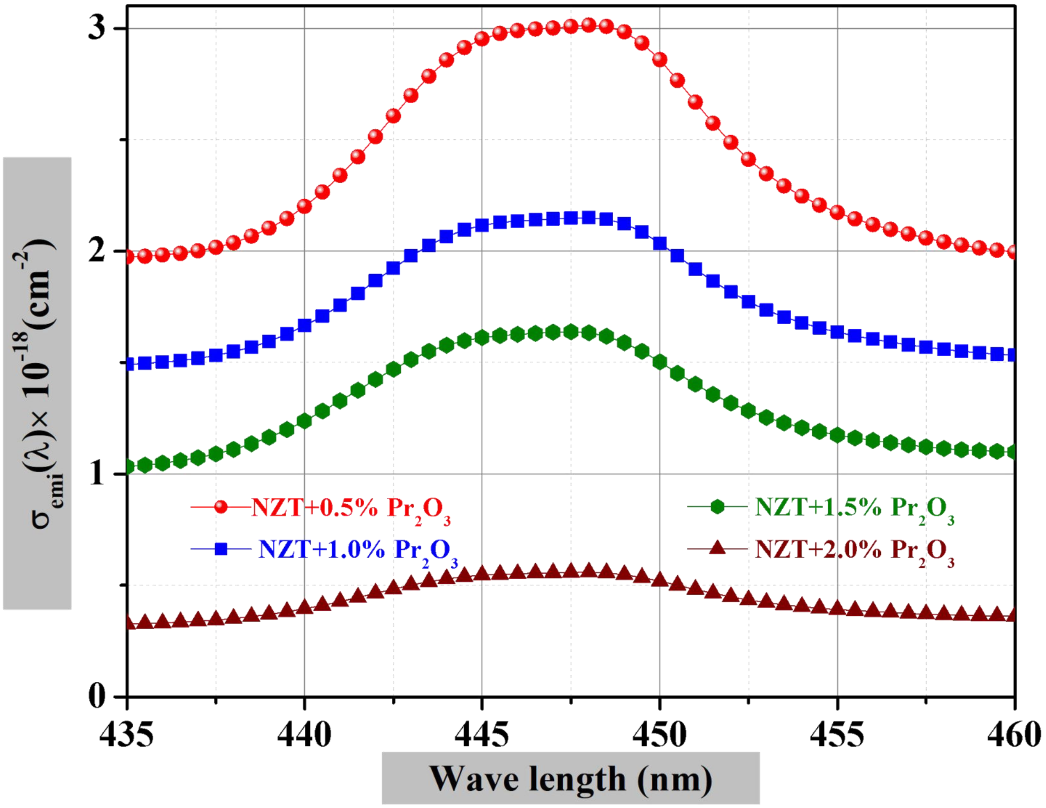

Fig 6.11 Wavelength dependence emission cross-section of Pr_2O_3-doped NZT glasses.

6.3.3.5 Fluorescence Spectra

Fig. 6.12 shows the emission spectra obtained at room temperature for the range of 470 - 700 nm regions with an excitation wavelength of 444 nm for different concentrations of Pr^{3+} ions incorporated in NZT glasses. The Pr^{3+} modified NZT glasses have exhibited five transitions $^3P_0 \rightarrow {}^3H_4$, $^3P_1 \rightarrow {}^3H_5$, $^3P_0 \rightarrow {}^3H_5$, $^1D_2 \rightarrow {}^3H_4$, $^3P_0 \rightarrow {}^3F_2$ at 490, 529, 545, 615, and 645 nm in the total visible region [295, 307-31041, 59-62]. Quite different context has been found in Pr^{3+} -doped tellurite glasses. The emission spectra are considered by two bands with a significant difference in intensity, connected to $^3P_0 \rightarrow {}^3H_4$ and $^1D_2 \rightarrow {}^3H_4$ transitions. The emission transition $^3P_0 \rightarrow {}^3H_4$ exhibits more sensitive intensity than the other transitions and increases with the increase of Pr^{3+} ions doped in the host matrix [311, 312].

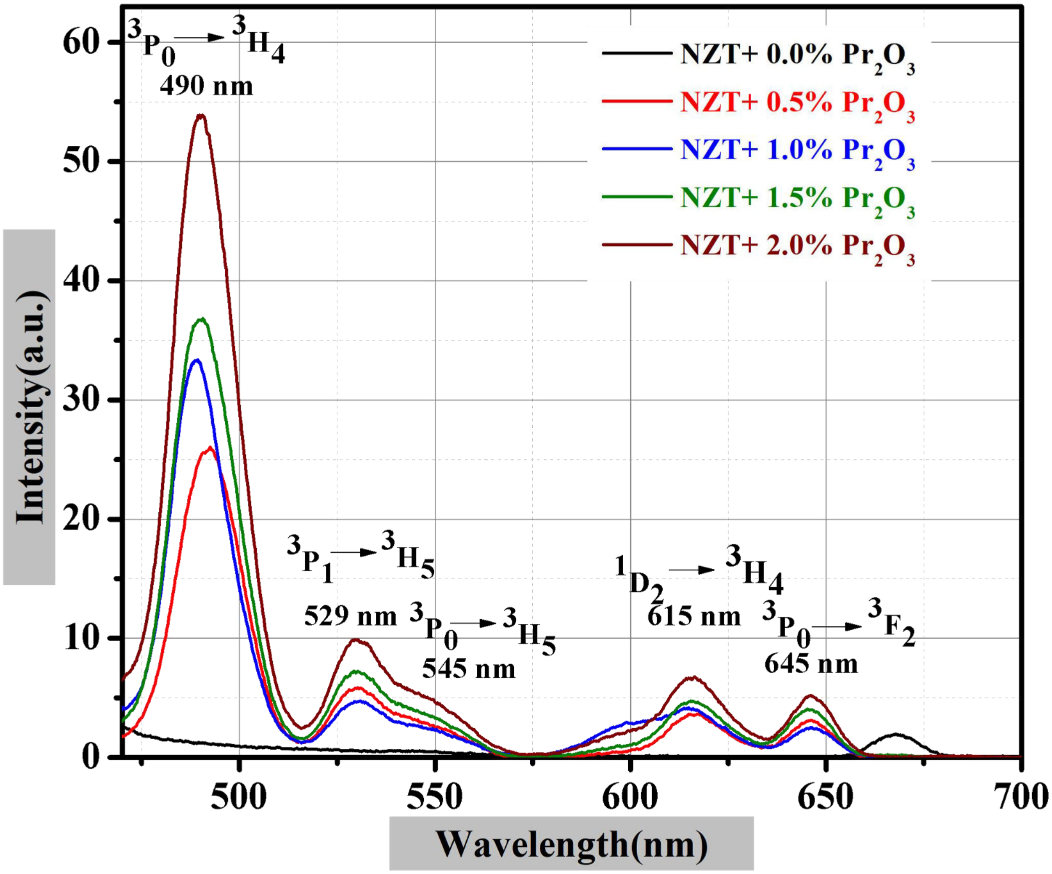

Fig 6.12 Luminescence spectra of pure, and Pr^{3+}-doped NZT glass materials, excited at 444 nm.

The emission intensity increases with the increasing Pr^{3+} ions in the glasses can be ascribed to the occurrence of radiative energy transfer (ET) between two adjacent Pr^{3+} ions. Generally, the emission of Pr^{3+}-doped tellurite glass can be observed for the electronic transitions from ^3P_J levels [313]. The phonon energy of the Pr^{3+}-doped tellurite glass matrix is lower (~700 cm^{-1}) compare to Pr^{3+}-doped borate glasses (~1400 cm^{-1}). However, on the emission spectrum, it has been found that the emitted transitions occurred from the $^1D_2$ level. This event may be the cause of non-radiative relaxation from the $^3P_0$ level. The intensity of $^3P_0 \rightarrow {}^3H_4$ and $^1D_2 \rightarrow {}^3H_4$ transitions is associated with non-radiative processes and excited states relaxation. The ion-ion interaction of rare-earth ions in the host glasses may lead to the energy transfer and cross relaxation (CR) processes. The transition $^1D_2 \rightarrow {}^3H_4$ may be occurred due to the cross relaxation (CR) and ET process [284]. Fig. 6.13 shows the energy level graph of the Pr_2O_3 doped NZT glass samples.

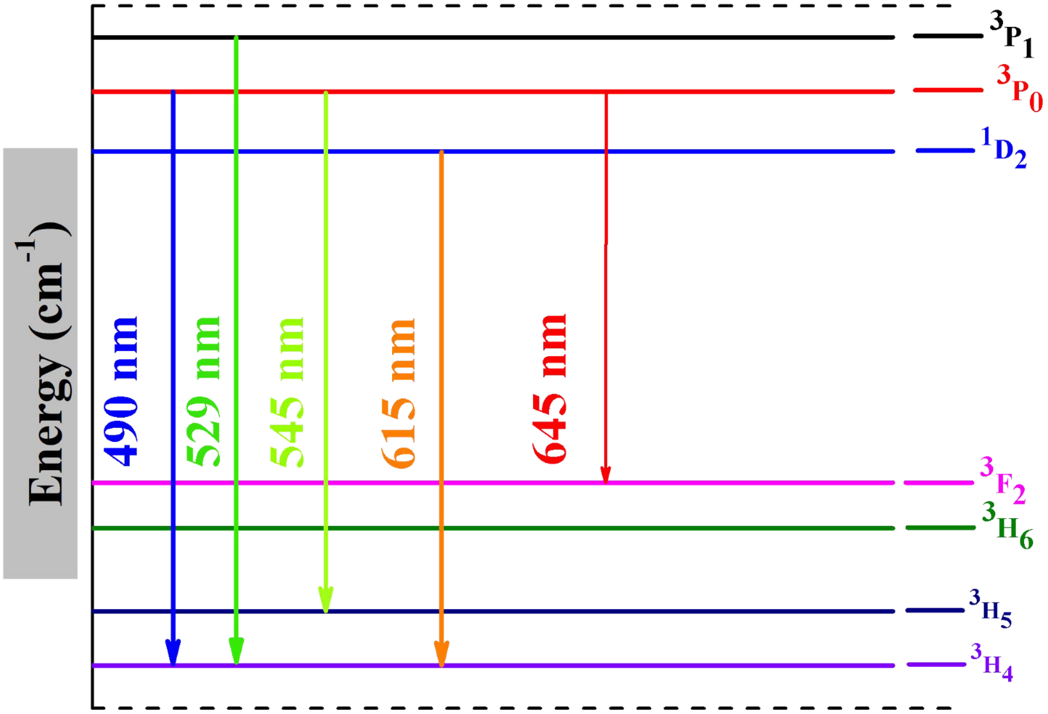

Fig 6.13 Energy level diagram and transitions of Pr^{3+}-doped NZT glasses.

The cross-section of stimulated emission (σ_{emi}) of emission transition is one of the important parameters used to identify a good optical material. A good optical material has a large emission cross-section [296]. Hence, rare-earth (Pr^{3+}) doped tellurite glass could be considered more appropriate for lasing material.

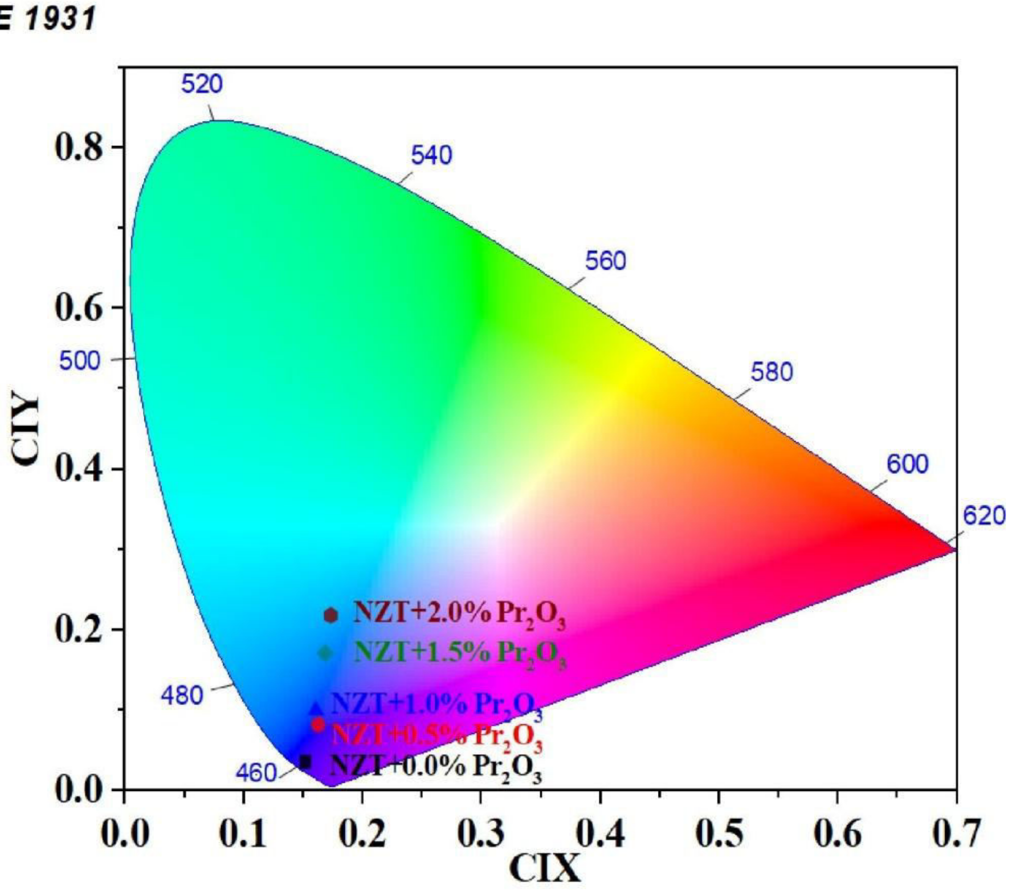

Fig 6.14 CIE chromaticity diagram of Pr_2O_3-doped NZT glass materials, excited at 444 nm.

The scattering wavelengths of emission spectra in the visible region can be measured using CIE 1931 colour coordinates, which is a physiologically clear colour vision of humans. The emission intensity of Pr_2O_3-doped NZT glass materials was designed using CIE 1931 (Fig. 6.14). The acquired colour confirmed the different colour of emission of all glass materials. The colour coordinates were (0.15215, 0.03578), (0.16257, 0.08245), (0.16057, 0.10072), (0.16845, 0.17109), and (0.1731, 0.21838) for Pr^{3+}-doped (0.5% wt-

2% wt) respectively. The non-emissive nature of the pure glass sample was confirmed from the coordinates out of the CIE plot [314]. The changes in coordinates specified that with increasing rare-earth oxide percent the emission moved towards higher wavelengths.

6.3.4 Electrical Properties

6.3.4.1 Dielectric Constant

The effect of frequency on dielectric constant for Pr_2O_3-doped NZT glasses is depicted in Fig. 6.15 in the frequency range 100 Hz - 8 MHz at room temperature. The numerical value of dielectric permittivity is associated with the electron density and ionic charges.

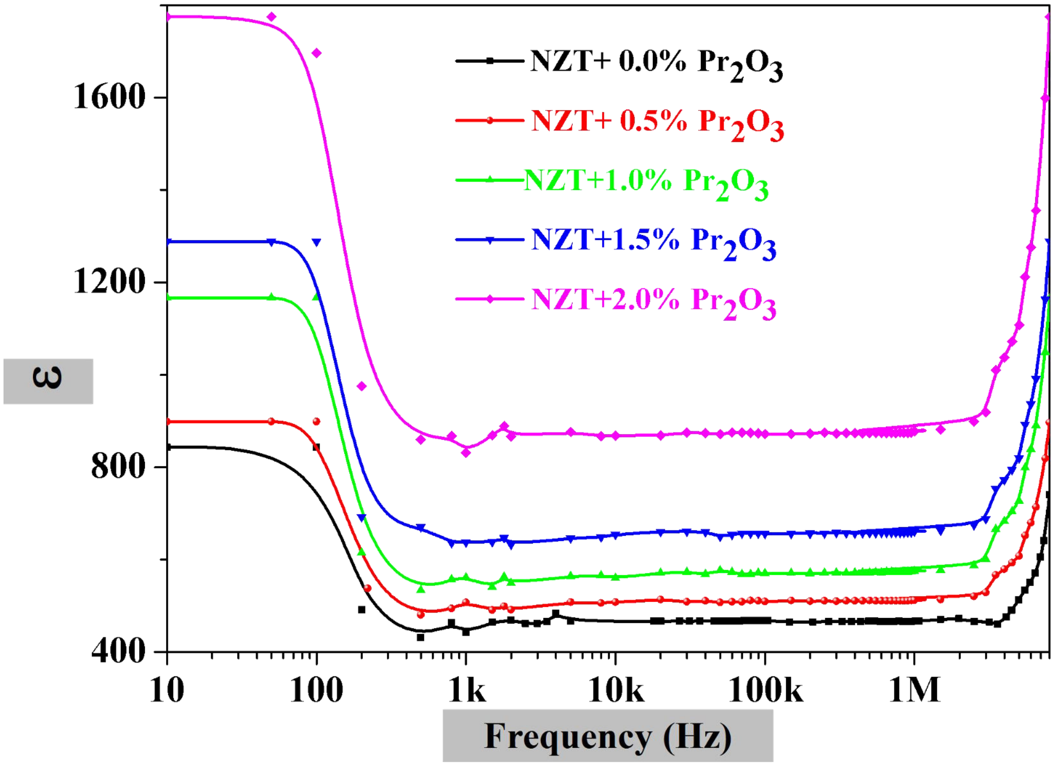

Fig 6.15 The variation of dielectric constant (ε) with frequency for pure and Pr^{3+}-doped NZT glasses at room temperature.

It is found that the magnitude of ε decreases quickly with increasing frequency up to 500 Hz. This could be ascribed to the dielectric dispersion from the delay of the polarizability process of the molecules in the applied electric field [273]. The dielectric constant is decreased with the increase of frequency for the lag of quick rearrangement, the molecular rotation, and the increasing friction between molecules [315]. The observed increasing dielectric constant towards the low-frequency region is ascribed to the interfacial polarization, space charge polarizations, motion of conducting charges, and absence of spontaneous polarization [277, 316]. Polarizability is mostly motivated by ionic and sources and decreased with the increase of frequency and ultimately develops into almost constant because of the inertia of ions and molecules [317].

The value of ε of these glasses is almost constant for the frequency 500 Hz to 2 MHz due to reducing of ionic, space charge and orientation polarization. The large value of the dielectric constant is obtained in the frequency range of 2 MHz to 8 MHz with a higher concentrations of rare-earth ions. This result is similar for rare-earth (Eu^{3+}, Nd^{3+} and Sm^{3+}) doped NZT glass materials [221, 279, 318, 319]. It describes the polarizing performance of the material in the presence of the applied electric field. The large value of dielectric constant at high frequency may be explained through the charge accumulation in the host glass due to rare-earth doping. This increase of dielectric constant at high frequency may also be explained through the electronic polarisation due to the excessive vibration of molecules in the host glass. From the plotted data, it is revealed that the tellurite glasses are not demonstrated any significant variation as there is no major modification in the orientation of the molecule. Again, the electron exchange between the ions does not follow the variations in the applied field. As the concentration of the rare-earth ions increased, these ions disrupt the glass network by creating dangling bonds and non-bridging ions which creates comfortable ways for the migration of charges. Thus, developed space charge polarization leads to the increase in dielectric constant as observed initially [154]. Here, the doping of Pr^{3+} ions may be creating more and more non-bridging oxygen ions. These non-bridging oxygen ions may create migration paths for the charge carriers which in turn increases space charge polarization and hence increases dielectric constant [320]. The dielectric constant increases with an increase in the substitution percentage of rare-earth ions and attains a maximum for 2 wt% Pr_2O_3 doped NZT glass. Other reasons are the impurities and imperfections in the crystal lattice. High porosity and low density led to a low dielectric constant. As the applied frequency increases, the ions are not able to respond quickly and it reveals an almost frequency-independent behavior [316, 278].

6.3.4.2 DC Conductivity

The variation of electrical conductivity with temperature is shown in Fig. 6.16. The conductivity increases with temperature and also with the doping of Pr^{3+} ions. This variation of conductivity with temperature found that the electrical conduction mechanism is Arrhenius type. This Arrhenius mechanism of electrical DC conductivity can be applied to establish the activation energy of the glass materials through the relation:

$$\sigma_{\mathrm{dc}} = \sigma_0 \exp[-\mathrm{E_a}/\mathrm{K_B}\mathrm{T}] \;\ldots\ldots\ldots\; (6.10)$$

Where E_a is the activation energy, σ_0 denotes the pre-exponential factor, T is the absolute temperature and K_B is the Boltzmann constant. The assessed activation energies for these samples have been measured from Fig. 6.16. The activation energy reduces (0.59 eV to 0.46 eV) due to the doping of Pr^{3+} ions. The interaction between the rare-earth ions and structural units of host glass explains the increment of DC conductivity due to the increasing concentration of rare-earth ions [221]. The mechanism of electrical DC conductivity in the glass structure depends on doping concentration, atomic weight, and position of Pr^{3+} ions. A large number of NBOs are produced due to the doping of rare-earth ions and hence the DC conductivity is enhanced for Pr_2O_3-doped NZT glasses [154].

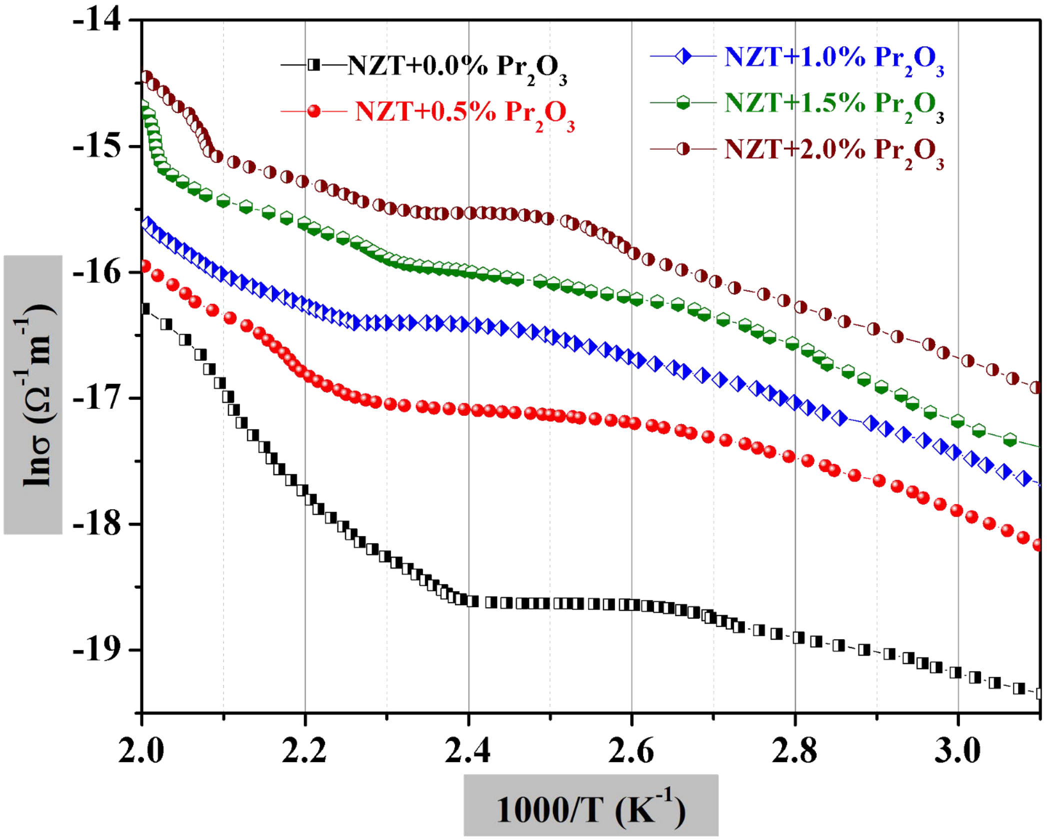

Fig 6.16 The variation of lnσ versus 1000/T.

6.4 Conclusions

Praseodymium-doped NZT glasses have been effectively made by the melt-quenching process. The X-ray diffraction characterization indicates the semi-crystalline nature of the materials for the incorporation of Pr^{3+} ions. FTIR spectra develop the creation of a new glass network of pure and Pr_2O_3-doped NZT glasses. The refractive index increases from 2.44 to 2.56 with the incorporation of Pr^{3+} ions. The absorption bands of the glass materials are found corresponding to the transitions $^3H_4 \rightarrow {}^3P_2$, $^3H_4 \rightarrow {}^3P_1 + {}^1I_6$, $^3H_4 \rightarrow {}^3P_0$, $^3H_4 \rightarrow {}^1D_2$ at 447, 472, 484, and 594 nm respectively. The emissions $^3P_0 \rightarrow {}^3H_4$, $^3P_1 \rightarrow {}^3H_4$, $^3P_1 \rightarrow {}^3H_5$, $^1D_2 \rightarrow {}^3H_4$, $^3P_0 \rightarrow {}^3F_2$ at 490, 529, 545, 615, and 645 nm are found in the photoluminescence spectra. Field strength (F) increases with increasing Pr^{3+} ions concentration and consequently, the inter-ionic distance (r_i), and polaron radius (r_p) are decreased. The indirect band gap energy (E_g) is decreased in the modified glass structure.

The dielectric constant for pure and doped NZT glass materials has been obtained for various frequencies and observed as a stable substance within the frequency of 500 Hz - 2 MHz. The DC conductivity increases with temperature whereas the activation energy reduces for the higher concentrations of Pr^{3+} ions in the usual approach. Hence, the present Pr^{3+} ions doped tellurite glasses can be exploited in optical devices.

[This work has been accepted in the Journal of Glass Physics and Chemistry 29th May 2023]

Chapter-7

Conclusion

The major results are summarized in the current thesis in concise form. Pure NZT and rare-earth (Eu, Nd, Sm, and Pr) doped Na_2O-ZnO-TeO_2 (NZT**)** glasses have been prepared by melt-quenching method and studied their thermal, structural, optical, and electrical characterizations.

7.1 Sample Preparation and Characterization

Amorphous and crystalline materials of the following tellurite glass systems have been prepared by normal and slow-quenching techniques:

1. $0.1Na_2O$-0.2ZnO-$0.7TeO_2$
2. (100-x) ($0.1Na_2O$-0.2ZnO-$0.7TeO_2$)-xEu_2O_3 (x = 0.5, 1.0, 1.5 and 2 wt %)
3. (100-x) ($0.1Na_2O$-0.2ZnO-$0.7TeO_2$)-xNd_2O_3 (x = 0.5, 1.0, 1.5 and 2 wt %)
4. (100-x) ($0.1Na_2O$-0.2ZnO-$0.7TeO_2$)-xSm_2O_3 (x = 0.5, 1.0, 1.5 and 2 wt %)
5. (100-x) ($0.1Na_2O$-0.2ZnO-$0.7TeO_2$)-xPr_2O_3 (x = 0.5, 1.0, 1.5 and 2 wt %)

The structural, optical, electrical, and thermal characteristics of all the glass samples have been characterized by using various analytical methods. The thermal factors including glass transition temperature, crystallization temperature, and melting temperature have been determined by Differential Thermal Analysis (DTA) and mass loss has been found by Thermo-Gravimetric Analysis (TGA). The optical absorption and luminescence properties have been investigated by UV-visible spectroscopy and photoluminescence (PL) spectroscopy respectively. An X-ray diffractometer has been used for the structural analysis of the glass samples.

7.2 Findings of the work on rare-earth doped NZT glass

The pattern of XRD of Eu^{3+} doped NZT samples shows no discrete sharp peaks and there are two broad peaks have been found in the region of glancing angle at 18^o to 34^o. The broad continuous pattern of X-ray diffraction reveals the amorphous nature of these glasses. A weak anomaly transition $^7F_1 \rightarrow {}^5D_1$ at 535 nm occurs in the absorption band of Eu^{3+}doped NZT glasses due to the spin-forbidden transitions. Six emission transitions

$^5D_1 \rightarrow {}^7F_1$ at 537 nm, $^5D_1 \rightarrow {}^7F_2$ at 556nm, $^5D_0 \rightarrow {}^7F_1$ at 591 nm, $^5D_0 \rightarrow {}^7F_2$ at 614 nm, $^5D_0 \rightarrow {}^7F_3$ at 653 nm, $^5D_0 \rightarrow {}^7F_4$ at 703 nm are observed with the excitation wavelength λ_{ex} = 395 nm. From the photoluminescence graph, it has been observed that the peak intensity of Eu^{3+}doped NZT glasses increases for the incorporation of Eu^{3+} ions. The intensity of the transition $^5D_0 \rightarrow {}^7F_2$ at 614 nm is maximum due to the electric dipole depending on the localized symmetry coordination surroundings of Eu^{3+} ions in the glass matrix. So, Eu^{3+}doped NZT glass samples have been used as a red laser source. The dielectric constant of glass samples was found as stable material within the frequency range 1 kHz to 1MHz with dielectric constant of 200 to 500. These glass samples may be useful as substrate devices as these materials show high dielectric constant. These glass materials can be used as a core material in optical fiber, as their refractive index is high. The variation of conductivity with temperature confirmed the Arrhenius conduction mechanism and the estimated activation energies were in the range of 0.64 eV to 0.53 eV. So, these samples have a high potential for application in optoelectronic devices.

In Chapter 4, we reported that the XRD pattern of Nd^{3+}-doped NZT glasses indicates the crystalline nature and decreases the crystalline nature due to the incorporation of Nd^{3+} ions. The absorption transition of Nd^{3+}-doped NZT glass materials are ($^4I_{9/2} \rightarrow {}^4G_{11/2}$) at 430 nm, ($^4I_{9/2}$–$^4G_{9/2}$) at 512 nm, ($^4I_{9/2} \rightarrow {}^4G_{7/2}$) at 525 nm, ($^4I_{9/2} \rightarrow {}^4G_{5/2}$) at 583 nm, ($^4I_{9/2} \rightarrow {}^4F_{9/2}$) at 683 nm, and ($^4I_{9/2} \rightarrow {}^4F_{7/2}$) at 746 nm. The peak intensity increases for higher concentrations of Nd^{3+} ions and is maxima for the transition ($^4I_{9/2} \rightarrow {}^4G_{5/2}$) at 583 nm. The peak value of photoluminescence spectra is slightly shifted due to the addition of the higher concentration of rare-earth ions in the NZT glass sample. Generally, the emission transition of Nd^{3+} doped tellurite glass materials is found near 1160 nm but the emission transition of Nd^{3+}-doped NZT glasses is observed in the visible region due to excitation of 325 nm. Nd^{3+}doped NZT glass samples have been used as a purple laser source. Polaron radius (r_p) and inter-ionic distance (r_i) decrease, and the corresponding value of field strength (F*)* increases for higher concentrations of Nd^{3+} ions. The value of optical band gap energy has been ascribed to the semi-conducting nature for doping of Nd^{3+} ions. The permittivity of Nd_2O_3-doped NZT glasses are seen as a stable substance within the frequency of 3 kHz to 1 MHz. So, these glass samples have a large prospect for application in optoelectronic devices.

In Chapter 5, we reported our investigation on samarium-doped NZT glasses the amorphous nature of the higher doping concentration of Sm^{3+} ions. FTIR spectra reveal the construction of a new glass structure of pure and Sm_2O_3-incorporated NZT glasses. The thermal stability of Sm^{3+} doped NZT glasses is increased with the increase of Hruby's parameter (H). The value of H is 0.57 for the higher doping of Sm^{3+} ions. The value of band gap energy decreases from 2.95 eV to 1.58 eV due to the doping of Sm^{3+} ions. The decreasing values of band gap energy of Sm^{3+} doped NZT glasses show the semi-conducting nature. The refractive index increases from 2.41 to 2.95 with the increase of Sm^{3+} ions. The absorption transitions $^6H_{5/2}\rightarrow{}^4P_{3/2}$, $^6H_{5/2}\rightarrow{}^4M_{19/2}$, $^6H_{5/2}\rightarrow{}^4I_{5/2}$, and $^6H_{5/2}\rightarrow{}^4I_{11/2}$ are observed at 402 nm, 418 nm, 462 nm, and 478 nm respectively. The emission transitions $^4G_{5/2}\rightarrow{}^6H_{5/2}$, $^4G_{5/2}\rightarrow{}^6H_{7/2}$, $^4G_{5/2}\rightarrow{}^6H_{9/2}$ are observed at 563 nm, 600 nm, 645 nm in the photoluminescence spectra with the excitation at 402 nm. Sm^{3+} doped NZT glass samples have been used as a red laser for emission at 600 nm corresponding to the $^4G_{5/2}\rightarrow{}^6H_{7/2}$ transition. The pattern of photoluminescence spectra has confirmed the quenching effect. The value of inter-ionic distance (r_i) and polaron radius (r_p) are decreased up to 1 wt% doping concentration and then increased up to the highest concentration of Sm^{3+} ions. The permittivity increases from 430 to 980 for Sm_2O_3 doping in the lower frequency at room temperature. The dielectric constant of Sm_2O_3-doped NZT glasses has been observed as a stable substance within the frequency range of 3 kHz to 2 MHz. Sm_2O_3-doped NZT glass samples have been used in optoelectronic devices. The DC conductivity increases with temperature whereas the activation energy decreases with the increase of ion concentration in the usual manner.

In Chapter 6, the preparation and characterization of Pr^{3+}-doped NZT glass has been reported. X-ray diffraction of Pr^{3+}-doped NZT glass materials has shown the hexagonal structure for the planes of $Na_2Zn_2(TeO_3)_3$ compound. FTIR spectra modify the creation of a new glass network of pure and Pr_2O_3-doped NZT glasses. The thermal stability of Pr^{3+} doped NZT glass samples is higher than other rare-earth doped NZT glass materials. The value of Hruby's parameter is 0.75 for the higher doping of Pr^{3+} ions. The absorption transitions of Pr_2O_3 doped NZT glasses are $^3H_4 \rightarrow {}^3P_2$, $^3H_4 \rightarrow {}^3P_1 + {}^1I_6$, $^3H_4 \rightarrow {}^3P_0$, $^3H_4 \rightarrow {}^1D_2$ at 447, 472, 484, and 594 nm respectively. The indirect band gap energy (E_g) is decreased in the modified glass structure. The refractive index increases from 2.44 to

2.56 with the incorporation of Pr^{3+} ions. These glass materials can be used as a core material in optical fiber, as their refractive index is high. The emission transitions $^3P_0 \rightarrow {}^3H_4$, $^3P_1 \rightarrow {}^3H_4$, $^3P_1 \rightarrow {}^3H_5$, $^1D_2 \rightarrow {}^3H_4$, $^3P_0 \rightarrow {}^3F_2$ at 490, 529, 545, 615, and 645 nm are found in the photoluminescence spectra with the excitation wavelength λ_{ex} = 444 nm. Field strength (F) increases with increasing Pr^{3+} ions concentration and consequently, the inter-ionic distance (r_i) and polaron radius (r_p) is decreased. The dielectric constant for pure and doped NZT glass materials has been observed as a stable substance within the frequency of 500 Hz-2 MHz. The DC conductivity increases and the activation energy reduces with temperature for a higher concentration of Pr^{3+} ions. Hence, the present Pr^{3+} ions doped tellurite glasses can be exploited in optical devices.

7.3 Future Scope

The simultaneous possessions of optical properties and environmental applications of the synthesized rare-earth-doped tellurite glasses present a striking opportunity for the innovation of smart optoelectronic devices in various fields. The production of reliable optoelectronic devices for today's speedy world is the ultimate aim. The prepared rare-earth doped tellurite glasses and their studied characterization might be supportive in the above aspect. In this research work, we have made an effort to enhance the optical properties of tellurite glasses by introducing some exciting rare-earth dopants. However, there are various scopes for enhancement in material properties of the different rare-earth compounds through proper doping/substitutions, which we would like to pursue in the future.

- Preparation of rare earth element gadolinium (Gd) doped tellurite glasses by low-cost method and to establish it as a good magnetic effect.
- Preparation of rare earth element lanthanum (La) doped tellurite glasses by low-cost method enhance the optical property in the visible region.
- Synthesis of tellurite glass semiconductor through inexpensive method for significant laser and optoelectronic device applications.

References:

[1] J. T. Berzelius, Ann. Phys. Chem., 1834, vol.32, pp.577.

[2] R. S. Kundu, S. Dhankhar, R. Punia , K. Nanda, N. Kishore, “Bismuth modified physical, structural and optical properties of mid-IR transparent zinc boro-tellurite glasses”, J. Alloys Comp., 2014, vol. 587, pp. 66-73. https://doi.org/10.1016/j.jallcom.2013.10.141.

[3] J. E. Shelby, “Introduction to Glass Science & Technology”, 2nd ed., Royal Soc. Chem., Cambridge, 2005.ISBN 0-85404-639-9.

[4] H. Tait, “Five Thousand Years of Glass”, British Museum Press, London, 1991.

[5] M. Bimson, I. C. Freestone, “Early Vitreous Materials”, British Museum Occasional Papers N°56 British Museum, London,1987.

[6] J. L. Adam, “Non-oxide glasses and their application in optics”, J. Non-Cryst. Solids, 2001, vol. 287, pp. 401-404. https://doi.org/10.1016/S0022-3093(01)00632-9.

[7] M. Poulain, “Halide Glasses”, J. Non-Cryst. Solids, 1981, vol. 56, pp. 1-14. https://doi.org/10.1016/0022-3093(83)90439-8.

[8] M. Chen, “A brief overview of bulk metallic glasses”, NPG Asia Mater., 2011, vol. 3, pp. 82-90. https://doi.org/10.1038/asiamat.2011.30.

[9] B. Bureau, X. H. Zhang, F. Smektala, J. L. Adam, J. Troles, H. L. Ma, C. B. Pledel, J. Lucas, P. Lucas, D. L. Coq, M. R. Riley, J. H. Simmons, “Recent advances in chalcogenide glasses”, J. Non-Cryst. Solids, 2004, vol. 345&346, pp. 276-283. https://doi.org/10.1016/j.jnoncrysol.2004.08.096.

[10] A. K. Mairaj, M. N. Petrovich, Y. W. West, A. Fu, D. W. J. Harwood, L. N. Ng, T. M. Monro, N. G. Broderick, D. W. Hewak, “Advances in gallium lanthanum sulphide glass for optical fibre and devices”, Int. Soc. Opt. Eng., 2001, vol. 4204, pp. 278-286. https://doi.org/10.1117/12.417421.

[11] J. Salbeck, N. Yu, J. Bauer, F. W. Grtel, H. Bestgen, “Low molecular organic glasses for blue electroluminescence”, Synth. Met., 1997, vol. 91, pp. 209-215.

[12] L. Deng, J. Du, “Development of boron oxide potentials for computer simulations of multi-component oxide glasses”, J. Am. Ceram. Soc., 2018, vol. 101. https://doi.org/10.1111/jace.16082.

[13] C. L. Babcock, “Substructure classification of silicate glasses”, J. Am. Ceram. Soc., 1969, vol. 52, pp. 151-153. https://doi.org/10.1111/j.1151-2916.1969.tb11202.x.

[14] S. C. Rasmussen, “A brief history of early silica glass: impact on science and society”, Substantia, 2019, vol. 5, pp. 125-138. https://doi.org/10.13128/Substantia-267.

[15] M. Guerette, M. R. Ackerson, J. Thomas, F. Yuan, E. B. Watson, D. Walker, L. Huang, “Structure and properties of silica glass densified in cold compression and hot compression”, Sci. Rep., 2015, vol. 5, pp. 1-10. https://doi.org/10.1038/srep15343.

[16] A. D. Wilson, S. Crisp, H. J. Prosser, B. G. Lewis, S. A. Merson, “A aluminosilicate glasses for polyelectrolyte cements”, Ind. Eng. Chem. Prod. Res. Dev., 1980, vol. 19, pp. 263-270. https://doi.org/10.1021/i360074a027.

[17] A. R. Allu, A. Gaddam, S. Ganisetti, S. Balaji, R. Siegel, G. C. Mather, M. Fabian, M. J. Pascual, N. Ditaranto, W. Milius, J. Senker, D. A. Agarkov, V. V. Kharton, J. M. F. Ferreira, “Structure and crystallization of alkaline-earth aluminosilicate glasses: Prevention of the alumina avoidance principle”, J. Phys. Chem. B, 2018, vol. 122, pp. 4737-4747. https://doi.org/10.1021/acs.jpcb.8b01811.

[18] S. Sundararaman, L. Huang, S. Ispas, W. Kob, “New interaction potentials for alkali and alkaline-earth aluminosilicate glasses”, J. Chem. Phys., 2019, vol. 150, pp. 154505-1-154505-13. https://doi.org/10.1063/1.5079663.

[19] F. Angeli, P. Jollivet, T. Charpentier, M. Fournier, S. Gin, “Structure and chemical durability of lead crystal glass”, Environ. Sci. Technol., 2016, vol. 50, pp.11549-11558. https://doi.org/10.1021/acs.est.6b02971.

[20] A. N. Trukhin, K. Smits, G. Chikvaidze, T. I. Dyuzheva, L. M. Lityagina, “Luminescence of silicon dioxide silica glass, α-quartz and stishovite”, Cent. Eur. J. Phys., 2011, vol. 9, pp. 1106-1113. https://doi.org/10.2478/s11534-011-0016-5.

[21] F. Nürnberg, B. Kühn, K. Rollmann, “Metrology of fused silica”, 2016, vol. 10014, pp. 42-54. https://doi.org/10.1117/12.2242487.

[22] C. J. Duflin,” Silicate Minerals: An Overview” BMS Occasional Paper No. 210, British Micromount Society, 2006, pp. 1-39.

[23] S. Hayat, M. Imran, “Computation of topological indices of certain networks”, Appl. Math. Comput., 2014, vol. 240, pp. 213-228. https://doi.org/10.1016/j.amc.2014.04.091.

[24] F. S. Spear, M. J. Kohn, S P Aetzold, “Petrology of the regional sillimanite zone, west-central New Hampshire, U.S.A., with implications for the development of inverted isograds”, Am. Mineral., 1995, vol. 80, pp. 361-376. https://doi.org/10.2138/am-1995-3-419.

[25] J. E. Bowey, A. M. Hofmeister, E. Keppel, “Infrared spectra of pyroxenes (crystalline chain silicates) at room temperature”, Royal Astron. Soc., 2020, vol. 497, pp. 3658-3673. https://doi.org/10.1093/mnras/staa2227.

[26] J. A. Cecilia, C. G. Sancho, E. V. Garcıa, J. J. Jimenez, E. R. Castellon, “Synthesis, characterization, uses and applications of porous clays hetero-structures: a review”, Chem. Rec. 2018, vol. 18, 1-21. https://doi.org/10.1002/tcr.201700107.

[27] V. R. Kulli, “Reverse Zagreb and Reverse Hyper-Zagreb indices and their polynomials of rhombus silicate networks”, Int. J. Pure Appl. Math., 2018, vol. 16, pp. 47-51. https://doi.org/10.22457/apam.v16n1a6.

[28] W. C. Lacourse, “Non silicate glass ceramics”, Mucchi Editore, Modena Italy, 1997, pp. 213-221.

[29] A. Karki, S. Feller, H. P. Lim, J. Starr, C. Sanchez, M. Shibata, “The density of sodium-borate glasses related to atomic arrangements”, J. Non-Cryst. Solids, 1987, vol. 92, pp. 11-19. https://doi.org/10.1016/S0022-3093(87)80355-1.

[30] A. I. Fu, J. C. Mauro, “Topology of alkali phosphate glass networks”, J. Non-Cryst. Solids, 2013, vol. 361, pp. 57-62. https://doi.org/10.1016/j.jnoncrysol.2012.11.001.

[31] H. T. Munasinghe, A. W. Beckmann, C. Schiele, D. Manzani, L. Wondraczek, S. A. V., T. M. Monro, H. E. Heidepriem, “Lead-germanate glasses and fibers: a practical alternative to tellurite for nonlinear fiber applications”, Opt. Mater. Express, 2013, vol. 3, pp. 1488-1503. https://doi.org/10.1364/OME.3.001488.

[32] P. Wang, S. Jia, X. Lu, Y. Jiang, J. Yu, X. Wang, S. Wang, E. Lewis, “Tellurite glass and its application in lasers”, Adv. Funct. Mater., https://doi.org/10.5772/intechopen.91338.

[33] D. Manara, G. Djean, D. Neuville, “Advances in understanding the structure of borosilicate glasses: A Raman spectroscopy study”, Am. Min., 2009, vol. 94, pp. 777-784. https://doi.org/10.2138/am.2009.3027.

[34] A. E. Nordberg, “Properties of some vycor-brand glasses”, Forty-Sixth Annual Meeting, Am. Cera. Soc., Pittsburgh, 1944, pp. 299-305. https://doi.org/10.1111/j.1151-2916.1944.tb14473.x.

[35] S. M. Bleay, V. D. Scott, “Microstructure property relationship in pyrex glass composites reinforced with Nicalon fibres”, J. Mater. Sci., 1991, vol. 26, pp. 2229-2239. https://doi.org/10.1007/BF00549193.

[36] M. N. N. Khan, P. K. Sarker, “Effect of waste glass fine aggregate on the strength, durability and high temperature resistance of alkali-activated fly ash and GGBFS blended

mortar", Constr. Build. Mater., 2020, vol. 263, pp. 1-12. https://doi.org/10.1016/j.conbuildmat.2020.120177.

[37] C. A. C. Souza, C. Bolfarini, W. J. B. Jr., L. R. P. A. Lima, M.F. Oliveira, C. S. Kiminami, "Corrosion resistance and glass forming ability of $Fe_{47}Co_{7}Cr_{15}M_{9}Si_{5}B_{15}Y_{2}$ (M = Mo, Nb) amorphous alloys", Mater. Res., 2013, vol. 16, pp. 1294-1298. https://doi.org/10.1590/S1516-14392013005000116.

[38] B. Jeong, J. S. Lee, M. J. Lee,T. Y. Lim, "Fabrication and properties of D-Glass fiber with low dielectric constant", Korean J. Mater., 2018, vol. 28, pp. 254-259. https://doi.org/10.3740/MRSK.2018.28.4.254.

[39] H. Li, P. Gu, J. Watson, J. Meng, "Acid corrosion resistance and mechanism of E-glass fibers: boron factor", J. Mater. Sci., 2013, vol. 48, pp. 3075–3087. https://doi.org/10.1007/s10853-012-7082-y.

[40] W. H. Kwana, C. B. Cheah, M. Ramli, K. Y. Chang., "Alkali-resistant glass fiber reinforced high strength concrete in simulated aggressive environment", Materiales de Construcción, 2018, vol. 68, pp. e147, (1-14). https://doi.org/10.3989/mc.2018.13216.

[41] M. Y. Ghugal, S. B. Deshmukh, "Performance of alkali-resistant glass fiber reinforced concrete", J. Reinf. Plast. Compos., 2006, vol. 25, pp. 617-630. https://doi.org/10.1177/0731684405058273.

[42] A. E. Krauklis, A. I. Gagani, K. Vegere, I. Kalnina, M. Klavins, A. T. Echtermeyer, "Dissolution kinetics of R glass fibres: influence of water acidity, temperature, and stress corrosion", Fibers, 2019, vol. 7, pp. 2-18. https://doi.org/10.3390/fib703002.

[43] C. Homrighausen, C. Wills, D. Fecko, A. Aiken, R. Fisher, "Fisher composite technologies, aiken, structural and ballistic comparison of various s-2 glass sizing/resin combinations", 2012.

[44] A. Daliri, A. Orifici, R. J. Curry, G. S. Langdon, H. Bornstein, R. Odish, "Experimental response of S-2 glass fibre reinforced composites subjected to localised blast loading", 1st Edition, CRC Press, 2019. ISBN9780429426506.

[45] U. Koklu, S. Morkavuk, C. Featherston, M. Haddad, D. Sanders, M. Aamir, D. Y. Pimenov, K. Giasin, "The effect of cryogenic machining of S-2 glass fibre composite on the hole form and dimensional tolerance", Int. J. Adv. Manuf. Technol., 2021, vol. 115, pp. 125-140. https://doi.org/10.1007/s00170-021-07150-y.

[46] D. Rawson, "The occurrence of parasitic worms in British freshwater fishes", Proc. 4th Int. Cong. on Glass, Imprimorice Chaix, Paris, 1952, vol. 62. pp. 877-887. https://doi.org/10.1080/00222935208654365M.

[47] M. Khanisanij, H. A. A. Sidek, “Elastic Behavior of Borate Glasses Containing Lead and Bismuth Oxides”, Adv. Mater. Sci. Eng., 2014, vol. 2014, pp. 1-8. https://doi.org/10.1155/2014/452830.

[48] D. R. Uhlmann, N.J. Kreidle, “Glass-science and technology”, Academic Press, New York, 1983, pp. 107.

[49] M. H. Huang, S. Mao, H. Feick, H. Yan, W. Yiying, H. Kind, E. Weber, R. Russo, P. Yang, “Room-temperature ultraviolet nano-wire nano-lasers”, Science, 2001, vol. 292 pp.1897-1899. https://doi.org/10.1126/science.1060367.

[50]. W. H. Dumbaugh, J. C. Lapp, “Heavy-Metal Oxide glasses”, Phys. Chem. Glasses, 1992, vol. 75, pp. 2315-2326. https://doi.org/10.1111/j.1151-2916.1992.tb05581.x.

[51] D. W. Hall, M. A. Newhouse, N. F. Borelli, W. H. Dumbaugh, D. L. Weidman, “Nonlinear optical susceptibilities of highindex glasses”, Appl. Phys. Lett., 1989, vol. 54, pp. 1293-1295. https://doi.org/10.1063/1.100697.

[52] C. Stehle, C. Vira, D. Vira, D. Hogan, S. Feller, M. Affatigato, “Optical and Physical Properties of Bismuth Borate Glasses Related to Structure”, Phys. Chem. Glasses, 1998, vol. 39, pp. 83-86.

[53] L. Baia, R. Stefan, W. Kiefer, J. Popp, S. Simon, “Structural investigations of copper doped B_2O_3-Bi_2O_3 glasses with high bismuth oxide content”, J. Non-Cryst. Solids, 2002, vol. 303, pp. 379-386. https://doi.org/10.1016/S0022-3093(02)01042-6.

[54] F. Miyaji, T. Yoko, S. Sakka, “Glass formation in Bi_2O_3-CaO-CuO and Bi_2O_3-SrO-CuO”, J. Non-Cryst. Solids, 1990, vol. 126, pp. 170-172. https://doi.org/10.1016/0022-3093(90)91035-P.

[55] J. Fu, “Novel bismuthate glasses”, J. Non-Cryst. Solids, 1996, vol. 194, pp. 207-209. https://doi.org/10.1016/0022-3093(95)00472-6.

[56] D. G. Hinnks, L. Soderholm, D. W. Capone, B. Dabrowski, A. W. Mitchell, D. Shi, “Preparation of Bi-Sr-Ca-Cu-O superconductors from oxide glass precursors”, Appl. Phys. Lett., 1988, vol. 53, pp. 423-425. https://doi.org/10.1063/1.100609.

[57] C. Feifei, D. Shixun, N. Qiuhua, X. Tiefeng, S. Xiang, W. Xunsi, “Glass formation and optical band gap studies on Bi_2O_3-B_2O_3-BaO ternary system”, J. Wuhan Uni., Tech. Mater. Sci. Ed., 2009, vol. 24, pp. 716-720. https://doi.org/10.1007/s11595-009-5716-y.

[58] G. D. Chryssikos, E. I. Kamistos, W. M. Risen, “A Raman investigation of cadmium borate and borogermanate glasses”, J. Non-Cryst. Solids, 1987, vol. 93, pp. 155-168. https://doi.org/10.1016/S0022-3093(87)80035-2.

[59] H. Bahari, S. H. A. Aziz, H. M. Kamari, W. M. Mat Yunus, F. R. M. Adikan, "The effect of bismuth on the structure and mechanical properties of GeO_2-PbO-Bi_2O_3 ternary bulk glass system" J. Ceram. Soc. Japan, 2012, vol. 120, pp. 280-285. https://doi.org/10.2109/jcersj2.120.280.

[60] R. A. H. El-Mallawany, "Tellurite glasses Hand book-physical properties and data", CRC Press LLC, 2002. ISBN 9781138075764.

[61] S. Singh, L. G. Van Uitert, W. H. Grodkiewicz, "Laser spectroscopic properties of Nd^{3+} - doped tellurite glasses", Optics Comm., 1976, vol. 17, pp. 315-319. https://doi.org/10.1016/0030-4018(76)90269-8.

[62] D. M. Martin, "TeO_2-based film glasses for photonic applications: structural and optical properties", Thesis, (2009) ISBN: 978-84-693-1813-3.

[63] J. E. Stanworth, "Tellurite Glasses", Nature, 1952, vol. 169, pp. 581-582. https://doi.org/10.1038/169581b0.

[64] J. S. Wang, E. M. Vogel, E. Snitzer, "Tellurite glass: a new candidate for fiber devices", Opt. Mater., 1994, vol. 3, pp. 187-203. https://doi.org/10.1016/0925-3467(94)90004-3.

[65] F. Désévédavy, C. Strutynski, A. Lemière, P. Mathey, G. Gadret, J. C. Jules, B. Kibler, F. Smektala, "Review of tellurite glasses purification issues for mid-IR optical fiber applications", J. Am. Ceram. Soc., 2020, vol. 103, pp. 4017-4034. http://doi.org/10.1111/jace.17078.

[66] C. B. A. Devi, S. Mahamuda, M. Venkateswarlu, K. Swapna, A. S. Rao, G. V. Prakash, "Dy^{3+} ions doped single and mixed alkali fluoro-tungsten tellurite glasses for laser and white LED applications", Opt. Mater., 2016, vol. 62, pp. 569-577. http://doi.org/101016/joptmat201611016.

[67] R. Mallawany, "Review tellurite glasses part 1. elastic properties", J. Mater. Chem. Phys. 1998, vol. 53, pp. 93-120. https://doi.org/10.1016/S0254-0584(97)02041-5.

[68] G. D Khattak, M. A. Salim, "X-ray photoelectron spectroscopic studies of zinc–tellurite glasses", J. Electron Spectrosc. Relat. Phenom., 2002, vol. 123, pp. 47-55. https://doi.org/10.1016/S0368-2048(01)00371-1.

[69] H. Burger, K. Nneipp, H. Hobert, W. Vogel, "Glass formation properties and structure of glasses in the TeO_2-ZnO system," J. Non-Cryst. Solids, 1992, vol. 151, pp. 134-142. https://doi.org/10.1016/0022-3093(92)90020-K.

[70] A. Gulenko, O. Masson, A. Berghout, D. Hamani, P. Thomas, "Atomistic simulations of TeO_2-based glasses: inter-atomic potentials and molecular dynamics", Phys. Chem. Chem. Phys, 2014. http://doi.org/10.1039/c4cp01273a.

[71] H. A. A. Sidek, S. Rosmawati, Z. A. Talib, M. K. Halimah, W. M. Daud, "Synthesis and optical properties of ZnO-TeO_2 glass system", Am. J. Applied Sci., 2009, vol. 6, pp. 1489-1494. http://doi.org/10.3844/ajassp.2009.1489.1494.

[72] M. R. Sahar, K. Sulhadi, M. S. Rohani, "Spectroscopic studies of TeO_2-ZnO-Er_2O_3 glass system", J. Mater. Sci., 2007, vol. 42, pp. 824-827. http://doi.org/10.1007/s10853-006-0095-7.

[73] A. Santic, A. M. Milankovic, K. Furic, M. R. Linaric Chandra S. Rayd, D. E. Dayd, "Structural properties and crystallization of sodium tellurite glasses", Croat. Chem. Acta, 2008, vol. 81, pp. 559-567. https://hrcak.srce.hr/file/49436.

[74] D. S. Yakovlev, A. P. Mirgorodskiœ, A. V. Tulub, B. F. Shchegolev, "Nonempirical calculation of linear and nonlinear polarizability of TeO_2-based molecular clusters and piezoelectric properties of crystalline tellurium oxide", Optics and Spectroscopy, 2002, vol. 92, pp. 449-454. https://doi.org/10.1134/1.1465473.

[75] J. M. Foster, S. F. Boys, "Canonical Cononigurational Interactional Procedure", Revs. Modern Phys., 1960, vol. 32, pp. 300-302. https://doi.org/10.1103/RevModPhys.32.300.

[76] G. W. Brady, "Structure of Tellurium Oxide Glass", J. Chern. Phys., 1957, vol. 27, pp. 300-303. https://doi.org/10.1063/1.1743690.

[77] H. Bürger, W. Vogel, V. M. Marinov, "Phase equilibrium, glass-forming, properties and structure of glasses in the TeO_2-B_2O_3 system", J. Mater. Sci., 1984, vol. 19, pp. 403-412. https://doi.org/10.1007/BF02403226.

[78] E. F. Lambson, G. A. Saunders, B. Bridge, R. A. El-Mallwany, "The elastic behaviour of TeO_2 glass under uniaxial and hydrostatic pressure," J. Non-Cryst. Solids, 1984, vol. 69, pp. 117-133. https://doi.org/10.1016/0022-3093(84)90128-5.

[79] M. M. El-Zaidia, A. A. Ammar, R. A. El-Mallwany, "Infra-red spectra, electron spin resonance spectra, and density of $(TeO_2)_{100-x}$-$(WO_3)_x$, and $(TeO_2)_{100-x}$-$(ZnCl_2)_x$ glasses", Phys. Stat. Sol. (a), 1985, vol. 91, pp. 637-642. https://doi.org/10.1002/pssa.2210910234.

[80] A. Ghosh, "Adiabatic hopping conduction in vanadium bismuth tellurite glasses", J. Phys.:Conden. Matter, 1993, vol. 5, pp. 8749-8754. https://doi.org/10.1088/0953-8984/5/46/012.

[81] M. M. Elkholy, R. A. El-Mallawany, "AC conductivity of tellurite glasses", Mater. Chem. Phys., 1995, vol. 40, pp. 163-167. https://doi.org/10.1016/0254-0584(95)01472-1.

[82] M. R. Sahar, A. K. Jehbu, M. M. Karim, "TeO-ZnO-ZnCl glasses for IR transmission", J. Non-Cryst. Solids, 1997, vol. 213 & 214, pp. 164-167. https://doi.org/10.1016/S0022-3093(97)00096-3.

[83] M. H. Bhat, M. Kandavel, M. Ganguli, K. J. Rao, "Li^+ ion conductivities in boro-tellurite", Bull. Mater. Sci., 2004, vol. 27, pp. 189-198. https://doi.org/10.1007/BF02708504.

[84] S. Szu, F. S. Chang, "Impedance study of V_2O_5-TeO_2-BaO glasses", Solid State Ion., 2005, vol. 176, pp. 2695-2699. https://doi.org/10.1016/j.ssi.2005.09.004.

[85] M. M. El-Desoky, "Characterization and transport properties of V_2O_5-Fe_2O_3-TeO_2 glasses", J. Non-Cryst. Solids, 2005, vol. 351, pp. 3139-3146. https://doi.org/10.1016/j.jnoncrysol.2005.08.004.

[86] J. Ozdanova, H. Ticha, L. Tichy, "Remark on the optical gap in ZnO–Bi_2O_3–TeO_2 glasses", J. Non-Cryst. Solids, 2007, vol. 353, pp. 2799-2802. https://doi.org/10.1016/j.jnoncrysol.2007.06.017.

[87] D. Saritha, Y. Markandeya, M. Salagram, M. Vithal, A.K. Singh, G. Bhikshamaiah, "Effect on Bi_2O_3 on physical, optical and structural studies of ZnO-Bi_2O_3- B_2O_3 glasses", J. Non-Cryst. Solids, 2008, vol. 354, pp. 5573-5579. https://doi.org/10.1016/jnoncrysol.2008.09.017.

[88] S. Rada, M. Culea, E. Culea, "Structure of TeO_2-B_2O_3 glasses infrared spectroscopy and DFT calculations", J. Non-Cryst. Solids, 2008, vol. 354, pp. 5491-5495. https://doi.org/10.1016/jnoncrysol.2008.09.009.

[89] M. P. Kumar, T. Sankarappa, "DC conductivity in some alkali doped vanado-tellurite glasses", Solid State Ionics, 2008, vol. 178, pp. 1719-1724. https://doi.org/10.1016/j.ssi.2007.11.003.

[90] M. Pant, D. K. Kanchan, N. Gondaliya, "Transport properties and relaxation studies in BaO substituted Ag_2O–V_2O_5–TeO_2 glass system", Mater. Chem. Phys., 2009, vol. 115, pp. 98-104. https://doi.org/10.1016/j.matchemphys.2008.11.047.

[91] B. Sujatha, C. N. Reddy, R. P. S. Chakradhar, "Dielectric relaxation and ion transport in silver-boro-tellurite glasses", Philos. Mag., 2010, vol. 90, pp. 2635–2650. https://doi.org/10.1080/14786431003662564.

[92] R. El-Mallawany, M. Sidky, H. Afifi, "Relaxation phenomena in tellurite glasses", J. Appl. Phys., 2010, vol. 107, pp. 053523-1-8. https://doi.org/10.1063/1.3311551.

[93] J. N. Ayuni, M. K. Halimah, Z. A. Talib, H. A. A. Sidek, W. M. Daud, A. W. Zaidan, A.M. Khamirul, "Optical properties of ternary TeO_2-B_2O_3-ZnO Glass System", IOP Conf.

Series: Mater. Sci .Engg., 2011, vol. 17, pp. 012027-1-7. https://doi.org/10.1088/1757-899X/17/1/012027.

[94] P. G. Pavani, K. Sadhana, V. C. Mouli, “Optical, physical and structural studies of boro-zinc tellurite glasses”, Phys. B, 2011, vol. 406, pp. 1242-1247. https://doi.org/10.1016/j.physb.2011.01.006.

[95] K. Linganna, K. Marimuthu, “Composition dependent structural and optical properties of Sm^{3+} doped boro-tellurite glasses”, J. Lumin., 2011, vol. 131, pp. 2746-2753. https://doi.org/10.1016/j.jlumin.2011.06.047.

[96] R. Punia, R. S. Kundu, J. Hooda, S. Dhankhar ,S. Dahiya, N. Kishore, “Effect of Bi_2O_3 on structural, optical, and other physical properties of semiconducting zinc vanadate glasses”, J. Appl. Phys., 2011, vol. 110, pp. 033527-1-6. https://doi.org/10.1063/1.3621188.

[97] H. M. Oo, H. M. Kamari, W. M. D. Wan-Yusoff, “Optical properties of bismuth tellurite based glass”, Int. J. Mol. Sci. 2012, vol. 13, pp. 4623-4631. https://doi.org/10.3390/ijms13044623.

[98] H. A. A. Sidek, S. Rosmawati, M. K. Halimah, K. A. Matori, Z. A. Talib, “Effect of AlF_3 on the density and elastic properties of zinc tellurite glass systems”, Materials, 2012, vol. 5, pp. 1361-1372. https://doi.org/10.3390/ma5081361.

[99] V. Kamalaker, G. Upender, C. Ramesh, V. C. Mouli, “Raman spectroscopy, thermal and optical properties of TeO_2-ZnO-Nb_2O_5-Nd_2O_3 glasses”, Spectrochim. Acta A Mol. Biomol. Spectrosc., 2012, vol. 89, pp. 149-154. https://doi.org/10.1016/j.saa.2011.12.057.

[100] G. Zhao, Y. Tian, H. Fan, J. Zhang, L. Hu, “Properties and structures of Bi_2O_3-B_2O_3-TeO_2 glass”, J. Mater. Sci. Technol., 2013, vol. 29, pp. 209-214. https://doi.org/10.1016/j.jmst.2012.11.003.

[101] V. Sreenivasulu, G. Upender, Swapna, V. V. Priya, V. C. Mouli, M. Prasad, “Raman, DSC, ESR and optical properties of lithium cadmium zinc tellurite glasses”, Phys. B, 2014, vol. 454, pp. 60-66. https://doi.org/10.1016/j.physb.2014.06.039.

[102] N. Berwal, R. S. Kundu, K. Nanda, R. Punia, N. Kishore, “Physical, structural and optical characterizations of borate modified bismuth-silicate-tellurite glasses”, J. Mol. Struc., 2015, vol. 1097, pp. 37-44. https://doi.org/10.1016/j.molstruc.2015.05.011.

[103] K. Nanda, N. Berwal, R. S. Kundu, R. Punia, N. Kishore, “Effect of doping of Nd^{3+} ions in BaO-TeO_2-B_2O_3 Glasses: A vibrational and optical study”, J. Mol. Struc., 2015, vol. 1088, pp. 147-154. https://doi.org/10.1016/j.molstruc.2015.02.021.

[104] S. Dhankhar, R. S. Kundu, M. Dult, S. Murugavel, R. Punia, N. Kishore, "Electrical conductivity and modulus formulation in zinc modified bismuth boro-tellurite glasses", Ind. J. Phys., 2016, vol. 90, pp. 1033-1040.https://doi.org/10.1007/s12648-016-0850-9.

[105] N. Berwal, S. Dhankhar, P. Sharma, R. S. Kundu, R. Punia, N. Kishore, "Physical, structural and optical characterization of silicate modified bismuth-borate-tellurite glasses", J. Mol. Struct., 2017, vol. 1127, pp. 636- 644. https://doi.org/10.1016/j.molstruc.2016.08.033.

[106] O. A. Zamyatin, V. G. Plotnichenko, M. F. Churbanov, E. V. Zamyatina, V. V. Karzanov, "Optical properties of zinc tellurite glasses doped with Cu^{2+} ions", J. Non-Cryst. Solids, 2017, vol. 480, pp. 81-89. https://doi.org/10.1016/j.jnoncrysol.2017.08.025.

[107] A. Gonçalves, V. S. Zanuto, G. A. S. Flizikowski, A. N. Medina, F. L. Hegeto, A. Somer, J. L. Gomes Jr., J. V. Gunha, G. K. Cruz, C. Jacinto, N. G. C. Astrath, A. Novatsk, "Luminescence and upconversion processes in Er^{3+}-doped tellurite glasses", J. Lumin., 2018, vol. 201, pp. 110-114. https://doi.org/10.1016/j.jlumin.2018.04.031.

[108] P. Yasaka, Y. Ruangthaweep, C. Wongdeeying, Herman, J. Kaewkhao, "Spectroscopic and structural characterization of zinc barium tellurite glass", Mater. Today: Proc., 2018, vol. 5, pp. 15072-15075. https://doi.org/10.1016/j.matpr.2018.04.059.

[109] N. N. Yusof, S. K. Ghoshal, R. Arifin, A. Awang, H. S. Tewari, K. Hamzah, "Self-cleaning and spectral attributes of erbium-doped sodium-zinc-tellurite glass: role of titania nano-particle", J. Non-Cryst. Solids, 2018, vol. 481, pp. 225-238. https://doi.org/10.1016/j.jnoncrysol.2017.10.044.

[110] A. I. Yakovlev, I. L. Snetkov, V. V. Dorofeev, S. E. Motorin, "Magneto-optical properties of high-purity zinc-tellurite glasses", J. Non-Cryst. Solids, 2018, vol. 480, pp. 90-94. https://doi.org/10.1016/j.jnoncrysol.2017.08.026.

[111] S. A. Tijani, S. M. Kamal, Y. Al-Hadeethi, M. Arib, M. A. Hussein, S. Wageh, L. A. Dim, "Radiation shielding properties of transparent erbium zinc tellurite glass system determined at medical diagnostic energies", J. Alloys Compd., 2018, vol. 741, pp. 293-299. https://doi.org/10.1016/j.jallcom.2018.01.109.

[112] M. I. Sayyed, H. O. Tekin, E. E. Altunsoy, S. S. Obaid, M. Almatari, "Radiation shielding study of tellurite tungsten glasses with different antimony oxide as transparent shielding materials using MCNPX code", J. Non-Cryst. Solids, 2018, vol. 498, pp. 167-172. https://doi.org/10.1016/j.jnoncrysol.2018.06.022.

[113] M. S. Al-Buriahi, K. S. Mann, “Radiation shielding investigations for selected tellurite-based glasses belonging to the TNW system”, Mater. Res. Express, 2019, vol. 6. pp. 105206-2-105206-11. https://doi.org/10.1088/2053-1591/ab3f85.

[114] B. T. Tonguc, H. Arslan, M. Sultan, Al-Buriahi, “Studies on mass attenuation coefficients, effective atomic numbers and electron densities for some biomolecules”, Radiat. Phys. Chem., 2018, pp. 86-91. https://doi.org/10.1016/j.radphyschem.2018.08.025.

[115] D. K. Gaikwad, M. I. Sayyed, S. N. Botewad, S. S. Obaid, Z. Y. Khattari, U. P. Gawai, F. Afaneh, M. D. Shirshat, P. P. Pawar, “Physical, structural, optical investigation and shielding features of tungsten bismuth tellurite based glasses”, J. Non-Cryst. Solids, 2019, vol. 503–504, pp. 158-168. https://doi.org/10.1016/j.jnoncrysol.2018.09.038.

[116] K.A. Matori, M.I. Sayyed, H.A.A. Sidek, M.H.M. Zaid, V.P. Singh, “Comprehensive study on physical, elastic and shielding properties of lead zinc phosphate glasses”, J. Non-Cryst. Solids, 2017, vol. 457, pp. 97-103. https://doi.org/10.1016/j.jnoncrysol.2016.11.029.

[117] H. M. Gomaa, M. I. Sayyed, H. O. Tekin, G. Lakshminarayana, A. H. El-Dosokey, “Correlate the structural changes to gamma radiation shielding performance evaluation for some calcium bismuth-borate glasses containing Nb_2O_5”,Phys. B: Condens. Matter, 2019, vol. 567, pp. 109-112. https://doi.org/10.1016/j.physb.2018.11.011.

[118] P. Vani, G. Vinitha, M. I. Sayyed, B. O. Elbashir, N. Manikandan, “Investigation on structural, optical, thermal and gamma photon shielding properties of zinc and barium doped fluorotellurite glasses”, J. Non-Cryst. Solids, 2019, vol. 511, pp. 194-200. https://doi.org/10.1016/j.jnoncrysol.2019.02.005.

[119] K. S. R. K. Reddy, K. Swapna, S. Mahamuda, M. Venkateswarlu, M. V. V. K. S. Prasad, A. S. Rao, G. V. Prakash, “Structural, optical absorption and photoluminescence spectral studies of Sm^{3+} ions in alkaline-earth boro-tellurite glasses”, Opt. Mater., 2018, vol. 79, pp. 21-32. https://doi.org/10.1016/j.optmat.2018.03.005.

[120] R. Sharma, A. S. Rao, N. Deopa, M. Venkateswarlu, M. Jayasimhadri, D. Haranath, G. V. Prakash, “Spectroscopic study of Pr^{3+} ions doped Zinc Lead Tungsten Tellurite glasses for visible photonic device applications”, Opt. Mater., 2018, vol. 78, pp. 457-464.doi: https://doi.org/10.1016/j.optmat.2018.02.054.

[121] Y. Ruan, D. A. Simpson, J. Jeske, H.E. Heidepriem, D. W. M. Lau, H. Ji, B. C. Johnson, T. Ohshima, S. Afshar V., L. Hollenberg, A. D. Greentree, T. M. Monro, B.C. Gibson, “Magnetically sensitive nano-diamond-doped tellurite glass fiber”, Sci. Rep., 2018, vol. 8, pp.1-6. https://doi.org/10.1038/s41598-018-19400-3.

[122] R. Kaur, A. Khanna, M. González-Barriuso, F. González, B. Chen, “Structural, optical and thermal properties of glass and anti-glass phases in strontium tellurite and borotellurite systems doped with europium”, Mater. Res. Bull., 2018, vol. 106, pp. 288-295. https://doi.org/10.1016/j.materresbull.2018.06.020.

[123] P. Cheng, Y. Zhou, X. Su, M. Zhou, Z. Zhou, H. Shao, “Pr^{3+}/Er^{3+} co-doped tellurite glass with ultra-broadband near-infrared fluorescence emission”, J. Lumin., 2018, vol. 197, pp. 31-37. https://doi.org/10.1016/j.jlumin.2018.01.005.

[124] L. Yuliantini, M. Djamal, R. Hidayat, K. Boonin, J. Kaewkhao, P. Yasaka, “Luminescence and Judd-Ofelt analysis of Nd^{3+} ion doped oxy-fluoride boro-tellurite glass for near-infrared laser application”, Mater. Today: Proc., 2021, vol. 43, pp. 2655-2662. https://doi.org/10.1016/j.matpr.2020.04.631.

[125] M. K. Narayanan, H. D. Shashikala, M. Manjaiah, “Statistical optimization of melt-quenching process parameters for multiple properties of ternary barium phosphate glasses”, Mater. Chem. Phys., 2015, vol. 152, pp. 127-134. https://doi.org/10.1016/j.matchemphys.2014.12.024.

[126] S. P. Mukherjee, “Sol-gel processes in glass science and technology”, J. Non-Cryst. Solids, 1980, vol. 42, pp. 477-488. https://doi.org/10.1016/0022-3093(80)90046-0.

[127] E. Zeimaran, S. Pourshahrestani, S. F. S. Shirazi, B. P. Murphy, N. A. Kadri, M. R. Towler, “Hydrothermal synthesis and characterisation of bioactive glass-ceramic nanorods”, J. Non-Cryst. Solids, 2016, vol. 443, pp. 118–124. https://doi.org/10.1016/j.jnoncrysol.2016.04.005.

[128] J. A. Dias, S. H. Santagneli, Y. Messaddeq, “Methods for lithium ion NASICON preparation: from solid-state synthesis to highly conductive glass-ceramics”, J. Phys. Chem. C, 2020, vol. 124, pp. 26518-26539. https://doi.org/10.1021/acs.jpcc.0c07385.

[129] V. Y. Vassiliev, J. Z. Zheng, S. K. Tang, W. Lu, J. Hua, Y. S. Lin, “Growth kinetics and deposition-related properties of sub-atmospheric pressure chemical vapor deposited borophosphosilicate glass film”, J. Electrochem. Soc., 1999, vol. 146, pp. 3039-3051. https://doi.org/10.1149/1.1392048.

[130] A. J. G. Zarbin, R. Bertholdo, M. A. F. C. Oliveira, “Preparation, characterization and pyrolysis of poly(furfuryl alcohol)/porous silica glass nano-composites: novel route to carbon template”, Carbon, 2002, vol. 40, pp. 2413–2422. https://doi.org/10.1016/S0008-6223(02)00130-6.

[131] D. Bokov, A. T. Jalil, S. Chupradit, W. Suksatan, M. J. Ansari, I. H. Shewael, G. H. Valiev, E. Kianfar, "Nanomaterial by Sol-Gel Method: Synthesis and Application", Adv. Mater. Sci. Eng., 2021, vol. 2021, pp. 1-21. https://doi.org/10.1155/2021/5102014.

[132] A. P. Chiriac, I. Neamtu, L. E. Nita, M. T. Nistor, "Sol-Gel method performed for biomedical products implementation", Mini-Rev. Med. Chem., 2010, vol. 10, pp. pp. 990-1013. https://doi.org/10.2174/138955710793177449.

[133] S. N. B. Hodgson, L. Weng, "Chemical and sol-gel processing of tellurite glasses for optoelectronics", J. Mater. Sci: Mater Electron., 2006, vol. 17, pp. 723-733. https://doi.org/10.1007/s10854-006-0016-1.

[134] H. O. Pierson, "Handbook of chemical vapor deposition (CVD) principles, technology and applications", second ed., LLC Norwich, New York, U.S.A. 1999.

[135] G. L. Doll, B. A. Mensah, H. Mohseni, T. W. Scharf, "Chemical vapor deposition and atomic layer deposition of coatings for mechanical applications", J. Therm. Spray Technol., 2010, vol. 19, pp. 510-516. https://doi.org/10.1007/s11666-009-9364-8.

[136] M. Saeed, Y. Alshammari, S. A. Majeed, E. Al-Nasrallah, "Chemical vapour deposition of graphene-synthesis, characterization and applications: a review", Molecules, 2020, vol. 25, pp. 1-62. https://doi.org/10.3390/molecules25173856.

[137] Y. Hamedani, P. Macha, T. J. Bunning, R. R. Naik, M. C. Vasudev, "Plasma-enhanced chemical vapor deposition: where we are and the outlook for the future", pp. 247-278. https://doi.org/10.5772/64654.

[138] T. L. Chu, S. S. Chu, C. Ferekides, J. Britt, C. Q. Wu, "Thin film junctions of cadmium telluride by metal organic chemical vapor deposition", J. Appl. Phys., 1992, vol. 71, pp. 3870-3876. https://doi.org/10.1063/1.350852.

[139] A. N. Moiseev, A. V. Chilyasov, V. V. Dorofeev, O. A. Vostrukhin, E. M. Dianov, B. G. Plotnichenko, V. V. Koltashev, "Production of TeO_2-ZnO glasses by chemical vapor deposition from organo-metallic compounds", J. Optoelectron. Adv. Mater., 2005, Vol. 7, pp. 1875-1879.

[140] M. Diba, A. R. Boccaccini, "Precious metals for biomedical applications", 2014, pp. 177-211. https://doi.org/10.1533/9780857099051.2.177.

[141] N. Kaur, A. Khanna, P. S. R. Krishna, "Preparation and characterization of boro-tellurite glasses", Solid State Phys., AIP Conf. Proc., 2014, vol. 1591, pp. 802-804. https://doi.org/10.1063/1.4872761.

[142] B. A. E. Ben-Arfa, R. C. Pullar, "A comparison of bioactive glass scaffolds fabricated by robocasting from powders made by sol-gel and melt-quenching methods", Processes, 2020, vol. 8, pp. 1-18. https://doi.org/10.3390/pr8050615.

[143] Z. Khurshid, S. Husain, H. Alotaibi, R. Rehman, M. S. Zafar, I. Farooq, A. S. Khan, "Biomedical, Therapeutic and Clinical Applications of Bioactive Glasses", Novel techniques of scaffold fabrication for bioactive glasses, Woodhead Publishing Series in Biomaterials, 2019, pp. 497-519. https://doi.org/10.1016/B978-0-08-102196-5.00018-5.

[144] G. Kaur, G. Pickrell, N. Sriranganathan, V. Kumar, D. Homa, "Review and the state of the art: Sol-gel and melt quenched bioactive glasses for tissue engineering", J. Biomed. Mater. Res. Part B Appl. Biomater., 2015, vol. 00B, pp.1248-1275. https://doi.org/10.1002/jbm.b.33443.

[145] A. Ali, Y. W. Chiang, R. M. Santos, "X-ray diffraction techniques for mineral characterization: a review for engineers of the fundamentals, applications, and research directions", Minerals, 2022, vol.12, pp. 1-25. https://doi.org/10.3390/ min12020205.

[146] S. S. Bhokare, V. R. Biradar, R. D. Chakole, M. S. Charde, "Applications of FTIR spectroscopy: Review", Int. J. Sci. Dev. Res., 2022, vol. 7, pp. 213-219. ISSN: 2455-2631.

[147] J. Ryczkowski, "IR spectroscopy in catalysis", Catalysis Today, 2001, vol. 68, pp. 263-381. https://doi:10.1016/S0920-5861(01)00334-0.

[148] R. J. Bell, "Introductory fourier transform spectroscopy," Academic Press, INC, New York, 1972, Library of Congress Catalog Card no. 70-182606.

[149] S. Gordon, "Differential thermal analysis", J Chem. Educ., 1963, vol. 40, pp. A87-A116. . https://doi.org/10.1021/ed040pa87.

[150] E. O. Ortega, H. Hosseinian, I. B. A. Meza, M. J. R. López, A. R. Vera, S. Hossein, "Material characterization techniques and application", 2022, vol. 19, ISBN: 978-981-16-9568-1.

[151] C. A. D. Caro, H. Claudia, "UV/VIS spectro-photometry fundamentals and applications", Mettler Toledo AG, 2015, pp. 1-53. https://www.researchgate.net/publication/321017142.

[152] M. U. M. Patel, R. Dominko, "Application of in operando UV/Vis spectroscopy in lithium-sulfur batteries", Chem. Sus. Chem., 2014, 7, 2167-2175. https://doi.org/10.1002/cssc.201402215.

[153] S. Simula, S. Ikäläinen, K. Niskanen, "Measurement of the dielectric properties of paper", J. Imaging Sci. Technol., 1999, vol. 43, pp. 472-477.

[154] A. A. Ali, M. H. Shaaban, "Electrical properties of LiBBaTe glass doped with Nd_2O_3", Solid State Sci., 2010, vol. 12, pp. 2148-2154. https://doi.org/10.1016/j.solidstatesciences.2010.09.016.

[155] S. Indris, P. Heitjans, M. Ulrich, A. Bunde, "AC and DC conductivity in nano and microcrystalline Li_2O:B_2O_3 composites: experimental results and theoretical models", Z. Phys. Chem., vol. 219, pp. 89-103. https://doi.org/10.1524/zpch.219.1.89.55015.

[156] A. Jha, B. Richards, G. Jose, T. T. Fernandez, P. Joshi, X. Jiang, J. Lousteau, "Rare-earth ion doped TeO_2 and GeO_2 glasses as laser materials", Prog. Mat. Sci., 2012, vol. 57, pp. 1426-1491. https://doi.org/10.1016/j.pmatsci.2012.04.003.

[157] A. Wagh, Y. Raviprakash, V. Upadhyaya, S. D. Kamath, "Composition dependent structural and optical properties of PbF_2-TeO_2-B_2O_3-Eu_2O_3 glasses", Spectrochim. Acta A Mol. Biomol. Spectrosc., 2015, vol. 151, pp. 696-706. https://doi.org/10.1016/j.saa.2015.07.016.

[158] A. Jha, B. D. O. Richards, G. Jose, T. T. Fernandez, C. J. Hill, J. Lousteau, P. Joshi, "Review on structural, thermal, optical and spectroscopic properties of tellurium oxide based glasses for fibre optic and waveguide applications", Int. Mater. Rev., 2012, vol. 57, pp. 357-382. https://doi.org/10.1179/1743280412Y.0000000005.

[159] A. N. Begum, V. Rajendran, "Structure investigation of TeO_2–BaO glass employing ultrasonic study", Mat. Lett., 2007, vol. 61, pp. 2143-2146. https://doi.org/10.1016/j.matlet.2006.08.034.

[160] A. K. Yakhind, "Tellurite Glasses", J. Am. Ceram. Soc., 1966, vol. 49, pp. 670-675. https://doi.org/10.1111/j.1151-2916.1966.tb13197.x

[161] S. Neov, V. Kozhukharov, I. Gerasimove, K. Krezhov, B. Sidzhimov, "A model for structural recombination in tellurite glasses", J. Phys. C: Solid State Phys., 1979, vol. 12, pp. 2475-2485. https://iopscience.iop.org/article/10.1088/0022-3719/12/13/012.

[162] S. Neov, I. Gerasimove, K. Krezhov, B. Sidzhimov, V. Kozhukharov, "Atomic arrangement in tellurite glasses studied by neutron diffraction", Phys. Stat. Sol., 1978, vol. 47, pp. 743-750. https://doi.org/10.1002/pssa.2210470249.

[163] P. Roychoudhury, S. K. Batabyal, A. Paul, C. Basu, S. Mukherjee, K. Goswami, "Acoustic and optical properties of $(Li_2O)_{0.2-x}(Na_2O)_x(TeO_2)_{0.8}$ glasses", J. Appl. Phys., 2012, vol. 92, pp. 3530-3539. https://doi.org/10.1063/1.1503385.

[164] R. D. Almeida, M. Davinson, L. R. P. Kassab, "Eu^{3+} luminescence in tellurite glasses with gold nanostructures", Opt. Commun., 2008, vol. 281, pp. 108-112. https://doi.org/10.1016/j.optcom.2007.08.072.

[165] E. S. Sazali, M. R. Sahar, S. K. Ghoshal, “Influence of europium ion on structural, mechanical and luminescence behavior of tellurite nanoglass”, J. Phys. Conf. Ser., 2013, vol. 431, pp. 1-8. https://doi.org/10.1088/1742-6596/431/1/012008.

[166] K. Ghorbel, H. Litaiem, L. Ktari, M. Dammak, “Ionic-protonic conduction analysis and dielectric relaxation behavior of the rubidium ammonium arsenate tellurate, Ionics, 2015, vol. 22, pp. 251-260. https:/doi.org/10.1007/s11581-015-1538-4.

[167] E. H. P. Cordfunke, V. M. Smit-Groen, “A DSC Study of the phase diagram of the system TeO-CsTeO$_3$”, Therm. Acta, 1984, vol. 80, pp. 181-183. https://doi.org/10.1016/0040-6031(84)87195-6.

[168] M. I. Khalil, M. M. Al-qunaibit, A. M. Al-zahem, J. P. Labis, “Synthesis and characterization of ZnO nanoparticles by thermal decomposition of a curcumin zinc complex”, Arab. J. Chem., 2014, vol. 7, pp. 1178-1184. https://doi.org/10.1016/j.arabjc.2013.10.025.

[169] S. H. Alazoumi, S. A. Aziz, R. E. Mallawany, U. S. Aliyu, H. M. Kamari, M. H. M. M. Zaid, K. A. Matori, A. Ushah, “Optical properties of zinc lead tellurite glasses”, Res. Phys., 2018, vol. 9, pp. 1371-1376. https://doi.org/10.1016/j.rinp.2018.04.041.

[170] G. Lakshminarayana, S. Buddhudu, “Spectral analysis of Eu^{3+} and Tb^{3+}:B$_2$O$_3$-ZnO-PbO glasses”, Mater. Chem., 2007, vol. 102, pp. 181-186. https://doi.org/10.1016/j.matchemphys.2006.11.020.

[171] P. Babu, C. K. Jayasankar, “Optical spectroscopy of Eu^{3+} ions in lithium borate and lithium fluoroborate glasses”, Physica B, 2000, vol. 279, pp. 262-281. https://doi.org/10.1016/S0921-4526(99)00876-5.

[172] K.V. Raju, S. Sailaja, C. N. Raju, B. S. Reddy, “Optical characterization of Eu^{3+} and Tb^{3+} ions doped cadmium lithium alumino fluoro boro tellurite glasses”, Spectrochim. Acta A Mol. Biomol. Spectrosc., 2011, vol. 79, pp. 87-91. https://doi.org/10.1016/j.saa.2011.02.009.

[173] L. R. P. Kassab, R. D. Almeida, D. M. da Silva, T. A. A. de-Assumpção, C. B. de-Araújo, “Enhanced luminescence of Tb^{3+}/Eu^{3+} doped tellurium oxide glass containing silver nanostructures”, J. Appl. Phys., 2009, vol. 105, pp. 1-3. https://doi.org/10.1063/1.3126489.

[174] V. Venkatramu, P. Babu, C. K. Jayasankar, “Fluorescence properties of Eu^{3+} ions doped borate and fluoroborate glasses containing lithium, zinc and lead”, Spectrochim. Acta A Mol. Biomol. Spectrosc., 2006, vol. 63, pp. 276-281. https://doi.org/10.1016/j.saa.2005.05.010.

[175] K. U. Kumar, S. S. Babu, C. Srinivasa, C. K. Jayasankar, “Optical and fluorescence spectroscopy of Eu_2O_3-doped P_2O_5-K_2O-KF-MO-Al_2O_3 (M = Mg, Sr and Ba) glasses”, Opt. Commun., 2011, vol. 284, pp. 2909–2914. https://doi.org/10.1016/j.optcom.2011.02.033.

[176] D. Mandal, H. D. Banerjee, M. L. N. Goswami, H. N. Acharya, “Synthesis of Er^{3+} and Er^{3+}: Yb^{3+} doped sol-gel derived silica glass and studies on their optical properties”, Bull. Mat. Sci., 2004, vol. 27, pp. 367-372. https://doi.org/10.1007/BF02704774.

[177] A. Wang, Y. Raviprakash, S. D. Kamnath, “Dielectric properties and relaxation dynamics in PbF_2-TeO_2-B_2O_3-Eu_2O_3 glasses”, Trans. Nonferrous Met. Soc. China., 2015, vol. 25, pp. 2637-2645. https://doi.org/10.1016/S1003-6326(15)63886-9.

[178] S. Yilmaz, O. Turkoglu, M. Ari, I. Belenli, “Electrical conductivity of the ionic conductor tetragonal $(Bi_2O_3)_{1-x}(Eu_2O_3)_x$”, Cerâmica, 2011, vol. 57, pp. 185-192. https://doi.org/10.1590/S0366-69132011000200009.

[179] G. V. Prakash, D. N. Rao, A. K. Bhatnagar, “Linear optical properties of niobium-based tellurite glasses”, Solid State Commun. 2001, vol. 119, pp. 39-44. https://doi.org/10.1016/S0038-1098(01)00195-800195-8.

[180] M. R. Dousti, P. Ghassemi, M. R. Sahar, Z. A. Mahraz, “Chemical durability and thermal stability of Er^{3+} zinc doped tellurite glass containing silver nanoparticles”, Chalcogenide Lett., 2014, vol. 11, pp. 111-119. https://www.researchgate.net/publication/260424871.

[181] E. Yousef, M. Hotzel, C. Russel, “Effect of ZnO and Bi_2O_3 addition on linear and non-linear optical properties of tellurite glasses”, J. Non-Cryst. Solid., 2007, vol. 353, pp. 333-338. https://doi.org/10.1016/j.jnoncrysol.2006.12.009.

[182] P. Damas, J. Coelho, G. Hungerford, N. S. Hssain, “Structural studies of lithium boro-tellurite glasses doped with praseodymium and oxides,” Mater. Res. Bull. 2012, pp. 3489-3494. https://doi.org/10.1016/j.materresbull.2012.06.071.

[183] S. J. Japari, M. I. Sayyed, A. K. Yahya, A. L. Anis, S. M. Iskandar, M. H. M. Zaid, M. N. Azlan, R. Hisam, “Effects of Na_2O on optical and radiation shielding properties of $x$$Na_2O$-(20-$x$)$K_2O-30V_2O_5-50TeO_2$ mixed alkali glasses”, Results in Physics*,* 2021, vol. 22, pp. 1-11. https://doi.org/10.1016/j.rinp.2021.103946.

[184] T. M. Machado, R. F. Falci, G. F. S. Andrade, M. J. V. Bell, M. A. P. Da-Silva, “Unprecedented multiphonon vibronic transitions of erbium ions on copper nanoparticles-containing tellurite glasses”, Phys. Chem. Chem. Phys., 2020, vol. *22, pp.* 13118-13122. https://doi.org/10.1039/d0cp01690j.

[185] S. N. S. Yaacob, M. R. Sahar, S. A. Jupri, E. S. Sazali, R. Zainal, P. Marwoto, "Physical, absorption and photoluminescence performance of Eu^{3+} doped lithium chloride tellurite glass", Solid State Phenomena, 2020, vol. 307, pp. 307-313. https://www.scientific.net/SSP.307.307.

[186] J. Yuan, G. Zheng, Y. Ye, Y. Chen, T. Deng, P. Xiao, Y. Ye.; W. Wang, "Enhanced 1.5 µm emission from Yb^{3+}/Er^{3+} co-doped tungsten tellurite glasses for broadband near-infrared optical fiber amplifiers and tunable fiber lasers", RSC Adv., 2021, vol. 11, pp. 27992–27999. https://doi.org/10.1039/d1ra05269a.

[187] E. A. Anashkina, "Laser sources based on rare-earth ion doped tellurite glass fibers and microspheres", Fibers, 2020, vol. 8, pp. 1-17. https://doi.org/10.3390/fib8050030.

[188] M. Azam, V. K. Rai, D. K. Mohanty, "Spectroscopy and enhanced frequency up-conversion in Nd^{3+}-Yb^{3+} codoped TPO glasses: energy transfer and NIR to visible up converter", Methods Appl. Fluoresc., 2017, vol. 5, pp. 1-13. https://doi.org/10.1088/2050-6120/aa7ac1.

[189] K. U. Kumar, V. A. Prathyusha, P. Babu, C. K. Jayasankar, A. S. Joshi, A. Speghini, M. Bettinelli, "Fluorescence properties of Nd^{3+}-doped tellurite glasses", Spectrochim. Acta Part A, 2007, vol. 67, pp. 702-708. https://doi.org/10.1016/j.saa.2006.08.027.

[190] A. Kasim, W. A. W. Razali, H. Azhan, M. R. Sahar, "Luminescence spectra of TeO_2-PbO-Li_2O doped Nd_2O_3 glass", Adv. Mater. Res., 2012, vol. 501, pp. 121-125. https://doi.org/10.4028/www.scientific.net/AMR.501.121.

[191] R. Balda, J. Fernandez, M. A. Arriandiaga, J. M. F. Navarro, "Spectroscopy and frequency up-conversion in Nd^{3+}-doped TeO_2-TiO_2-Nb_2O_5 glass", J. Phys.: Condens. Matter, 2007, vol. 19, pp. 1-12. https://doi.org/10.1088/0953-8984/19/8/086223.

[192] R. Situmorang, A. Marbun, A. Hakim, D. D. Panggabean, J. Rajagukguk, J. Kaewkhao, "Preparation and characterization of Nd^{3+} doped P_2O_5-Bi_2O_3-Na_2O-Gd_2O_3 glasses system for laser medium application", J. Phys.: Conf. Ser., 2018, vol. 1120, pp. 1-9. https://doi.org/10.1088/1742-6596/1120/1/012048.

[193] W. L. Fong, S. O. Baki, N. M. Arifin, Y. Mansor, A. Nazri, B. K. Abbas, "Structural, thermal and optical properties of rare-earth doped lead- tellurite oxide glasses", J. Adv. Res. Fluid Mech. Therm. Sci., 2021, vol. 81, pp. 52-58. https://doi.org/10.37934/arfmts.81.2.5258.

[194] B. Hauke, E. R. Barney, E. Pakhomenko, M. Jesuit, M. Packard, A. Crego, G. Tarantino, M. Affatigato, S. Feller, "Structure and glass transition temperatures of tellurite glasses",

Phys. Chem. Glasses: Eur. J. Glass Sci. Technol. B, 2020, vol. 61, pp. 21-26. https://doi.org/10.13036/17533562.61.1.11.

[195] R. Kaur, A. Khanna, "Structural and thermal properties of magnesium tellurite glasses", AIP Conf. Proc., 2020, vol. 2265, pp. 030238-1-030238-4. https://doi.org/10.1063/5.0017748.

[196] A. Kaur, A. Khanna, P. S. R. Krishna, A. B. Shinde, M. G. Barriuso, F. Gonzalez, B. Chen, "Structure of copper tellurite and borotellurite glasses by neutron diffraction, Raman, ^{11}B MASNMR and FTIR spectroscopy", Phys. Chem. Glasses: Eur. J. Glass Sci. Technol. B, 2020, vol. 61, pp. 27–39. https://doi.org/10.13036/17533562.61.1.007.

[197] J. D. M. Dias, G. H. A. Melo, T. A. Lodi, J. O. Carvalho, P. F. F. Filho, M. J. Barboza, A. Steimacher, F. Pedrochi, "Thermal and structural properties of Nd_2O_3 doped calcium boroaluminate glasses", J. Rare-earths, 2016, vol. 34, pp. 521-528. https://doi.org/10.1016/S1002-0721(16)60057-1.

[198] A. G. Kalampounias, G. Tsilomelekis, S. Boghosian, "Glass-forming ability of TeO_2 and temperature-induced changes on the structure of the glassy, super-cooled and molten states", J. Chem. Phys., 2015, vol. 142, pp. 154503-1-154503-10. https://doi.org/10.1063/1.4917536.

[199] J. V. Gunha, A. Goncalves, A. Somer, A. V. C. Andrade, D. T. Dias, A. Novatski, "Thermal, structural and optical properties of TeO_2-Na_2O-TiO_2 glassy system", J. Mater. Sci.: Mater. Electron, 2019, vol. 30, pp. 16695-16701. https://doi.org/10.1007/s10854-019-01496-6.

[200] V. N. Jambhale, A. L. Patil, U. B. Chanshetti, "FT-IR and density studies on neodymium doped zinc borotellurite glass system", Int. J. Sci. Res., 2017, vol. 7, pp. 562-565. https://www.researchgate.net/publication/326624820.

[201] N. Elkhoshkhany, S. Y. Marzouk, M. A. Khattab, S. A. Dessouki, "Influence of Sm_2O_3 addition on Judd-Ofelt parameters, thermal and optical properties of the TeO_2-Li_2O-ZnO-Nb_2O_5 glass system", Mater. Charact., 2018, vol. 144, pp. 274–286. https://doi.org/10.1016/j.matchar.2018.07.021.

[202] K. Selvaraju, K. Marimuthu, "Stucture of spectroscopic studies on concentration-dependent Er^{3+} dopped boro-tellurite glasses", J. Lumin., 2012, vol. 132, pp. 1171-1178. https://doi.org/10.1016/j.jlumin.2011.12.056.

[203] V. O. Sokolov, V. G. Plotnichenko, V. V. Koltashev, E. M. Dianov, "On the structure of tungstate–tellurite glasses", J. Non-Cryst. Solids, 2006, vol. 352, pp. 5618-5632. https://doi.org/10.1016/j.jnoncrysol.2006.09.006.

[204] K. Linganna, J.H. In, S.H. Kim, K. Han, J.H. Choi, "Engineering of TeO_2-ZnO-BaO-based glasses for mid-infrared transmitting optics", Materials, 2020, vol. 13, pp. 1-14. https://doi.org/10.3390/ma13245829.

[205] M.I. Sayyed, A.A. Ati, M.H.A. Mhareb, K.A. Mahmoud, K.M. Kaky, S.O. Baki, M.A. Mahdi, "Novel tellurite glass (60-x)TeO_2-10GeO_2-20ZnO-10BaO-xBi_2O_3 for radiation shielding", J. Alloys Compd., 2020. https://doi.org/10.1016/j.jallcom.2020.155668.

[206] E. Mansour, "FTIR spectra of pseudo-binary sodium borate glasses containing TeO_2", J. Mol. Struct., 2012, vol. 1014, pp. 1-6. https://doi.org/10.1016/j.molstruc.2012.01.034.

[207] Y. A. Tanko, M. R. Sahar, S. K. Ghoshal, "Prominent spectral features of Sm^{3+} ion in disordered zinc tellurite glass", Results Phys., 2016, vol. 6, pp. 7-11. https://doi.org/10.1016/j.rinp.2015.12.001.

[208] J. F. M. Dos-santos, V. S. Zanuto, C. R. Kesavulu, G. Venkataiah, C. K. Jayasankar, L. A. O. Nunes, T.Catunda, "Photothermal and spectroscopic characterization of Tb^{3+}-doped tungsten-zirconium-tellurite glasses", J. Appl. Phys., 2020, vol. 128, pp. 13103-1-13103-9. https://doi.org/10.1063/5.0020655.

[209] C. K. Jayasankar, V. V. R. K. Kumar, "Optical properties of Nd^{3+} ions cadmium boro-sulphate glasses and comparative energy level analyses of Nd^{3+} ions in various glasses", Physica B, 1996, vol. 226, pp. 313-330. https://doi.org/10.1016/0921-4526(96)00288-8.

[210] D. L. Sidebottom, M. A. Hruschka, B. G. Potter, R. K. Brow, "Structure and optical properties of rare-earth doped zinc oxyhalide tellurite glasses", J. Non-Cryst. Solids, 1997, vol. 222, pp. 282-289. https://doi.org/10.1016/S0022-3093(97)90125-3.

[211] R. E. Mallawany, M. D. Abdalla, I. A. Ahmed, "New tellurite glass: Optical properties", Mater. Chem. Phys., 2008, vol. 109, pp. 291-296. https://doi.org/10.1016/j.matchemphys.2007.11.040.

[212] Y. Yamsuk, P. Yasaka, J. Keawkhao, N. Sangwaranatee, "Nd^{3+} doped in zinc barium tellurite oxyfluoride glasses for laser application", J. Phys.: Conf. Ser. 2020, vol. 1428, pp. 1-9. https://doi.org/10.1088/1742-6596/1428/1/012028.

[213] N. A. M. Jan, M. R. Sahar, S. K. Ghoshal, R. Ariffin, M. S. Rohani, K. Hamzah, "Absorption spectra of neodymium doped tellurite glass", Adv. Mater. Res., 2014, vol. 895, pp. 395-399. https://doi.org/10.4028/www.scientific.net/AMR.895.395.

[214] M. R. Babu, N. M. Rao, A. M. Babu, "Effect of erbium ion concentration on structural and luminescence properties of lead borosilicate glasses for fiber amplifiers", J. Biol. Chem. Lumin., 2017, vol. 33, pp. 71-78. https://doi.org/10.1002/bio.3374.

[215] M. R. Babu, A. M. Babu, L. R. Moorthy, "Structural and optical properties of Nd^{3+}-doped lead borosilicate glasses for broadband laser amplification", Int. J. Appl. Eng. Res. 2018, vol. 13, pp. 7692-7700.

[216] K. Mariselvama, R. A. Kumara, P. Manasa, "Spectroscopic investigations of neodymium doped barium bismuth fluoro-borate glasses." Infrared Phys. Technol., 2018, vol. 91, pp. 18-26. https://doi.org/10.1016/j.infrared.2018.03.021.

[217] D. D. Ramteke, V. Y. Ganvira, S. R. Munishwar, R. S. Gedam, "Concentration effect of Sm^{3+} ions on structural and luminescence properties of lithium borate glasses", Phys. Procedia, 2015, vol. 76, pp. 25-30. https://doi.org/10.1016/j.phpro.2015.10.005.

[218] M. Hasnat, V. Lahti, H. Byron, M. Lastusaari, L. Petit, "Micro-luminescence measurement to evidence decomposition of persistent luminescent particles during the preparation of novel persistent luminescent tellurite glasses", Scripta Materialia, 2021, vol. 199, pp. 1-7. https://doi.org/10.1016/j.scriptamat.2021.113864.

[219] N. A. M. Jan, M. R. Sahar, S. K. Ghoshal, R. Ariffin, M. S. Rohani, "Thermal and photoluminescence properties of Nd^{3+} doped tellurite nanoglass", Nano Hybrids, 2013, vol. 3, pp. 81-92. https://doi.org/10.4028/www.scientific.net/NH.3.81.

[220] A. A. Ali, M. H. Shaaban, "Optical and electrical properties of Nd^{3+} doped TeBiY borate glasses", Silicon, 2018, vol. 10, pp. 1503-1511. https://doi.org/10.1007/s12633-017-9633-y.

[221] J. N. Mirdda, S. Mukhopadhyay, K. R. Sahu, M. N. Goswami, "Enhancement of optical emission and dielectric properties of Eu^{3+}-doped Na_2O–ZnO–TeO_2 glass material", Glass Phys. Chem., 2020, vol. 46, pp. 218-227. https://doi.org/10.1134/S1087659620030104.

[222] R. Hisam, A. K. Yahya, H. M. Kamari, Z. A. Talib, R. H. Y. Subban, "Anomalous dielectric constant and AC conductivity in mixed transition-metal-ion xFe_2O_3–$(20-x)MnO_2$–$80TeO_2$ glass system", Mater. Express, 2016, vol. 6, pp. 149-160. https://doi.org/10.1166/mex.2016.1286.

[223] J. C. S. Moraes, J. A. Nardi, S. M. Sidel, B. G. Mantovani, K. Yukimitu, V. C. S. Reynoso, L. F. Malmonge, N. Ghofraniha, G. Ruocco, L. H. C. Andrade, S. M. Lima, "Relation among optical, thermal and thermo-optical properties and niobium concentration in tellurite glasses", J. Non-Cryst. Solids, 2010, vol. 356 pp. 2146-2150. https://doi.org/10.1016/j.jnoncrysol.2010.07.044.

[224] V. Rajendran, N. Palanivelu, B. K. Chaudhuri, K. Goswami, "Characterization of semiconducting V_2O_5–Bi_2O_3–TeO_2 glasses through ultrasonic measurements", J. Non

Cryst. Solids, 2003, vol. 320, pp. 195-209. https://doi.org/10.1016/S0022-3093(03)00018-8.

[225] M. S. Al-Buriahi, C. Sriwunkum, H. Arslan, B. T. Tonguc, M. A. Bourham, “Investigation of barium borate glasses for radiation shielding applications”, Appl. Phys. A, 2020, vol. 126, pp. 1-9. https://doi.org/10.1007/s00339-019-3254-9.

[226] M. S. Al-Buriahi, E. M. Bakhsh, B. Tonguc, S. B. Khan, “Mechanical and radiation shielding properties of tellurite glasses doped with ZnO and NiO”, Ceram. Int., 2020, vol. 46, pp. 19078-19083. https://doi.org/10.1016/j.ceramint.2020.04.240.

[227] M. S. Al-Buriahi, V. P. Singh, A. Alalawi, C. Sriwunkumd, B. T. Tonguc, “Mechanical features and radiation shielding properties of TeO_2–Ag_2O-WO_3 glasses”, Ceram. Int., 2020, vol. 46, pp. 15464-15472. https://doi.org/10.1016/j.ceramint.2020.03.091.

[228] M. S. Al-Buriahi, Y. S. M. Alajerami, A. S. Abouhaswa, A. Alalawi, T. Nutaro, B. Tonguc, “Effect of chromium oxide on the physical, optical, and radiation shielding properties of lead sodium borate glasses”, J. Non-Cryst. Solids, 2020, vol. 544, pp. 120171. https://doi.org/10.1016/j.jnoncrysol.2020.120171.

[229] M. S. Al-Buriahi, H. H. Hegazy, F. Alresheedi, H. H. Somaily, C. Sriwunkum, I. O. Olarinoye, “Effect of Sb_2O_3 addition on radiation attenuation properties of tellurite glasses containing V_2O_5 and Nb_2O_5”, Appl. Phys. A, 2021, vol. 127, pp. 1-12. https://doi.org/10.1007/s00339-020-04265-z.

[230] H. H. Hegazy, M. S. Al-Buriahi, F. Alresheedi, S. Alraddadi, H. Arslan, H. Algarni, “The effects of TeO_2 on polarizability, optical transmission, and photon/neutron attenuation properties of boro-zinc-tellurite glasses”, J. Inorg. Organomet. Polym. Mater., 2021, vol. 31, pp. 2331-2338. https://doi.org/10.1007/s10904-021-01933-2.

[231] M. S. Al-Buriahi, H. H. Somaily, A. Alalawi, S. Alraddadi, “Polarizability, optical basicity and photon attenuation properties of Ag_2O–MoO_3–V_2O_5–TeO_2 glasses: the role of silver oxide”, J. Inorg. Organomet. Polym. Mater., 2021, vol. 31, pp. 1047-1056. https://doi.org/10.1007/s10904-020-01750-z.

[232] J. S. Alzahrani, M. A. Alothman, C. Eke, H. Al-Ghamdi, D. A. Aloraini, M. S. Al-Buriahi, “Simulating the radiation shielding properties of TeO_2–Na_2O–TiO glass system using PHITS Monte Carlo code”, Comput. Mater. Sci., 2021, vol. 196, pp. 110566. https://doi.org/10.1016/j.commatsci.2021.110566.

[233] S. S. Hajer, M. K. Halimah, Z. Azmi, M. N. Azlan, “Optical properties of zinc-borotellurite doped samarium”, Chalcogenide Lett., 2014, vol. 11, pp. 553-566.

[234] B. Eraiah, “Optical properties of samarium doped zinc–tellurite glasses”, Bull. Mater. Sci., 2006, vol. 29, pp. 375-378. https://doi.org/10.1007/BF02704138.

[235] S. R. Munishwar, K. Roy, R.S. Gedam, “Photoluminescence study of Sm^{3+} containing sodium borosilicate glasses and glass-ceramics”, Mater. Res. Express, 2017, vol. 4, pp. 105201-1-8. https://doi.org/10.1088/2053-1591/aa8c91.

[236] W. Stambouli, H. Elhouichet, B. Gelloz, M. Ferid, “Optical and spectroscopic properties of Eu-doped tellurite glasses and glass ceramics”, J. Lumin., 2013, vol. 138, pp. 201-208. https://doi.org/10.1016/j.jlumin.2013.01.019.

[237] R. S. Gedam, D. D. Ramteke, “Electrical and optical properties of lithium borate glasses doped with Nd_2O_3”, J. Rare-earths, 2012, vol. 30, pp. 785-788. https://doi.org/10.1016/S1002-0721(12)60130-6.

[238] D. D. Ramteke, K. Annapurna, V. K. Deshpande, R. S. Gedam, “Effect of Nd^{3+} on spectroscopic properties of lithium borate glasses”, J. Rare-earths, 2014, vol. 32, pp. 1148-1153. https://doi.org/10.1016/S1002-0721(14)60196-4.

[239] C. Lurin, C. Parent, G. Leflem, P. Hagenmuller, “Energy transfer in a Nd^{3+}-Yb^{3+} borate glass”, J. Phys. Chem. Solids, 1985, vol. 46, pp. 1083-1092. https://doi.org/10.1016/0022-3697(85)90024-1.

[240] S. S. L. Surana, Y. K. Sharma, S. P. Tandon, “Laser action in neodymium doped zinc chloride boro-phosphate glasses”, Mater. Sci. Eng. B, 2001, vol. 83, pp. 204-209. https://doi.org/10.1016/S0921-5107(01)00517-7.

[241] P. Babu, K. H. Jang, E. S. Kim, L. Shi, H. J. Seo, “Optical properties and white-light emission in Dy^{3+}-doped transparent oxy-fluoride glass and glass ceramics containing CaF_2 nano-crystals”, J. Korean Phys. Soc., 2009, vol. 54, pp. 1488-1491. https://doi.org/10.3938/jkps.54.1488.

[242] R. S. E. S. Dawaud, S. Hashim, Y. S. M. Alajerami, M. H. A. Mhareb, M. M. Maqableh, “Structural and optical properties of lithium sodium borate glasses doped with Sm^{3+} ions”, Int. J. Mod. Phys. B, 2014, vol. 28, pp. 1450182-1-12. https://doi.org/10.1142/S0217979214501823.

[243] H. Lin, E. Y. B. Pun, X. Wang, X. Liu, “Intense visible fluorescence and energy transfer in Dy^{3+}, Tb^{3+}, Sm^{3+} and Eu^{3+} doped rare-earth borate glasses”, J. Alloys Compound., 2005, vol. 390, pp. 197-201. https://doi.org/10.1016/j.jallcom.2004.07.068.

[244] M. A. Marzouk, H. A. E. Batal, Y. M. Hamdy, F. M. E. Eldin, “Collective optical, FTIR and photoluminescence spectra of CeO_2 and/or Sm_2O_3 doped Na_2O-ZnO-P_2O_5 glasses”, Int. J. Optics., 2019, pp. 1-11. https://doi.org/10.1155/2019/6527327.

[245] S. Q. Mawlud, M. M. Ameen, M. R. Sahar, K. F. Ahmed, “Influence of Sm_2O_3 ion concentration on structural and thermal modification of TeO_2-Na_2O glasses”, J. Appl. Mech. Eng., 2016, vol. 5, pp. 1-5. https://doi.org/10.4172/2168-9873.1000222.

[246] S. O. Baki, L. S. Tan, C. S. Kan, H. M. Kamari, A. S. M. Noor, M. A. Mahdi, “Structural and optical properties of Er^{3+}-Yb^{3+} co-doped multi-composition TeO_2-ZnO-PbO-TiO_2-Na_2O glass”, J. Non-Cryst. Solids, 2013, vol. 362, pp. 156-161. https://doi.org/10.1016/j.jnoncrysol.2012.11.042.

[247] M. Wang, L. Yi, L. Zhang, G. Wang, L. Hu, J. Zhang, “2-µm fluorescence and Raman spectra in high and low $Al(PO_3)_3$ content fluorophosphates glasses doped with Er-Tm-Ho”, Chin. Opt. Lett., 2009, vol. 7, pp. 1035-1037. https://doi.org/10.3788/COL20090711.1035.

[248] A. A. C. Jr, C. Fredericci, E. D. Zanotto, “A test of the Hruby parameter to estimate glass-forming ability”, J. Non-Cryst. Solids, 1997, vol. 219, pp. 182-186. https://doi.org/10.1016/S0022-3093(97)00327-X.

[249] S. Badamasi, Y. A. Tanko, “Thermal properties of TeO_2-ZnO-Na_2O glasses: effect of Dy_2O_3 doping”, Sci. World J., 2018, vol. 13, pp. 95-99.

[250] M. N. Azlan, M. K. Halimah, S. S. Hajer, A. B. Suriani, Y. Azlina, S. A. Umar, “Enhanced optical performance of tellurite glass doped with samarium nano-particles for fiber optics application”, Chalcogenide Lett., 2019, vol. 16, pp. 215-229. https://chalcogen.ro/215_AzlanMN.pdf.

[251] M. N. Azlan, S. S. Hajer, M. K. Halimah, S. A. Umar, M. H. M. Zaid, R. Hisam, S. M. Iskandar, B. K. Kenzhaliyev, G. K. Kassymova, N. N. Yusof, “Comprehensive comparison on optical properties of samarium oxide (micro/nano) particles doped tellurite glass for optoelectronics applications”, J Mater Sci: Mater Electron, 2021, vol. 32, pp. 14174-14185. https://doi.org/10.1007/s10854-021-05961-z.

[252] S. K. Ahmmad, M. A. Samee, S. M. Taqiullah, S. Rahman, “FT-IR and Raman spectroscopic studies of ZnF_2-ZnO-As_2O_3-TeO_2 glasses”, J. Taibah Univ. Sci., 2016, vol. 10, pp. 329-339. https://doi.org/10.1016/j.jtusci.2014.12.008.

[253] S. Marjanovic, J. Toulouse, H. Jain, C. Sandmann, V. Dierolf, A. R. Kortan, N. Kopylov, R. G. Ahrens, “Characterization of new erbium-doped tellurite glasses and fibers”, J. Non-Cryst. Solids, 2003, vol. 322, pp. 311-318. https://doi.org/10.1016/S0022-3093(03)00278-3.

[254] S. F. Mansour, E. S. Yousef, M. Y. Hassaan, A. M. Emara, “Thermal, IR, Raman characteristics, Raman gain coefficient and bandwidths in quaternary glasses”, Solid

State Sci., 2014, vol. 37, pp. 33-39. https://doi.org/10.1016/j.solidstatesciences.2014.08.004.

[255] N. Elkhoshkhany, M. A. Khatab, M. A. Kabary, “Thermal, FTIR and UV spectral studies on tellurite glasses doped with cerium oxide”, Ceram. Int., 2018, vol. 44, pp. 2789-2796. https://doi.org/10.1016/j.ceramint.2017.11.019.

[256] N. Hasim, M. S. Rohani, M. R. Sahar, “Structural characteristics of Er^{3+} and Nd^{3+} doped Lithium Niobate Tellurite Glass”, Mater. Sci. Forum, 2017, vol. 846, pp.126-130. https://doi.org/10.4028/www.scientific.net/MSF.846.126.

[257] W. T. Carnall, P. R. Fields, K. Rajnak, “Electronic energy levels in the trivalent lanthanide aquo ions Pr^{3+}, Nd^{3+}, Pm^{3+}, Sm^{3+}, Dy^{3+}, Ho^{3+}, Er^{3+} and Tm^{3+}”, J. Chem. Phys., 1968, vol. 49, pp. 4424-4442. https://doi.org/10.1063/1.1669893.

[258] S. Q. Mawlud, M. M. Ameen, M. R. Sahar, N. M. Yusof, K. F. Ahmed, Y. A. Tanko, “Absorption and luminescence spectral properties study of Sm^{3+} doped TeO_2-Na_2O glasses”, Proc. Int. Sci. Postgraduate Conf., 2016, pp. 1-10.

[259] M. Anis, S. S. Hussaini, M. I. Baig, M. I. Anis, E. E. S. Massoud, “Investigating optical, electrical, and mechanical traits of thiourea admixtured KDP single crystals to explore NLO device applications”, J. Mater Sci: Mater Electron., 2021, vol. 32, pp. 23206-23214. https://doi.org/10.1007/s10854-021-06806-5.

[260] S. P. Ramteke, S. M. Azhar, G. G. Muley, M. I. Baig, A. M. Alshehri, H. H. Somaily, M. Anis, “Growth and optimization of optical traits of copper sulfate crystal exploiting L-ascorbic acid for photonic device applications”, Chin. J. Phys., 2021, vol. 71, pp. 168-174. https://doi.org/10.1016/j.cjph.2020.04.006.

[261] M. Shwetha, B. Eraiah, “Influence of samarium ions Sm^{3+} on the optical properties of lithium zinc phosphate glasses”, AIP Conf. Proc., 2018, vol. 1953, pp. 090002-1-4. https://doi.org/10.1063/1.5032849.

[262] G. Upender, S. Ramesha, M. Prasada, V. G. Sathe, V. C. Mouli, “Optical band gap, glass transition temperature and structural studies of $(100-2x)TeO_2$–xAg_2O–xWO_3 glass system”, J. Alloys Compound., 2010, vol. 504, pp. 468-474. https://doi.org/10.1016/j.jallcom.2010.06.006.

[263] E. A. Mohamed, F. Ahmad, K. A. Aly, “Effect of lithium addition on thermal and optical properties of zinc-tellurite glass”, J. Alloys Compound., 2012, vol. 538, pp. 230-236. https://doi.org/10.1016/j.jallcom.2012.05.044.

[264] S. P. Ramteke, S. Kalainathan, M. Anis, G. G. Muley, M. I. Baig, H. Algarni, “Novel report on luminescence, linear and laser-induced optical traits of potassium aluminium

sulfate crystal for photonic device applications", Optik, 2019, pp. 1-13. https://doi.org/10.1016/j.ijleo.2019.163509.

[265] M. Anis, M. I. Baig, G. G. Muley, S. AlFaify, M. A. Khan, "Impact of increasing concentration of L-alanine environment on structural, UV–Vis, SHG efficiency, luminescence and dielectric traits of zinc thiourea chloride (ZTC) crystal", Optik, 2019, vol. 185, pp. 317-324. https://doi.org/10.1016/j.ijleo.2019.03.081.

[266] S. Arunkumar, K. Marimuthu, "Concentration effect of Sm^{3+} ions in B_2O_3–PbO–PbF_2–Bi_2O_3–ZnO glasses structural and luminescence investigations", J. Alloys Compd., 2013, vol. 565, pp. 104-114. https://doi.org/10.1016/j.jallcom.2013.02.151.

[267] C. R. Kesavulu, C. K. Jayasankar, "Concentration effect of Sm^{3+} ions in B_2O_3–PbO–PbF_2–Bi_2O_3–ZnO glasses-structural and luminescence investigations", J. Lumin. 2012, vol. 132, pp. 2802-2809. https://doi.org/10.1016/j.jlumin.2012.05.031.

[268] S. S. Sundari, K. Marimuthu, M. Sivraman, S. S. Babu, "Composition dependent structural and optical properties of Sm^{3+}-doped sodium borate and sodium fluoro-borate glasses", J. Lumin. 2010, vol. 130, pp. 1313-1319. https://doi.org/10.1016/j.jlumin.2010.02.046.

[269] V. Lavın, I. R. Martın, C. K. Jayasankar, T. Troster, "Pressure-induced energy transfer processes between Sm^{3+} ions in lithium fluoroborate glasses", Phys. Rev. B, 2002, vol. 66, pp. 064207-1-7. https://doi.org/10.1103/PhysRevB.66.064207.

[270] S. Thomas, R. George, S. N. Rasool, M. Rathaiah, V. Venkatramu, C. Joseph, N. V. Unnikrishnan, "Optical properties of Sm^{3+} ions in zinc potassium fluorophosphate glasses", Opt. Mater., 2013, vol. 36, pp. 242-250. https://doi.org/10.1016/j.optmat.2013.09.002.

[271] T. Suhasini, J. S. Kumar, T. Sasikala, K. Jang, H. S. Lee, M. Jayasimhadri, J. H. Jeong, S. S. Yi, L. R. Moorthy, "Absorption and fluorescence properties of Sm^{3+} ions in fluoride containing phosphate glasses", Opt. Mater., 2009, vol. 31, pp. 1167-1172. https://doi.org/10.1016/j.optmat.2008.12.008.

[272] P. Solarz, W. R. Romanowski, "Luminescence and energy transfer processes of Sm^{3+} in $K_5Li_2LaF_{10}$:Sm^{3+}-$K_5Li_2SmF_{10}$ single crystals", Phys. Rev. B, vol. 72, pp. 075105-1-8. https://doi.org/10.1103/PhysRevB.72.075105.

[273] S. E. Ibrahim, Y. S. Rammah, I. Z. Hager, R. E. Mallawany, "UV and electrical properties of TeO_2-WO_3-Li_2O-Nb_2O_5/Sm_2O_3/Pr_6O_{11}/ Er_2O_3 glasses", J. Non-Cryst. Solids, 2018, vol. 498, pp. 443-447. https://doi.org/10.1016/j.jnoncrysol.2018.02.019.

[274] M. Anis, M. I. Baig, A. M. Alshehri, H. H. Somaily, “Experimental analysis of pure and L-tyrosine influenced bis-thiourea zinc acetate (BTZA) crystal for NLO device applications”, Optik, 2020, vol. 220, pp. 165100. https://doi.org/10.1016/j.ijleo.2020.165100.

[275] M. I. Baig, M. Anis, M. D. Shirsat, S. S. Hussaini, H. Algarni, “Comparative analysis of pristine and Cd^{2+} influenced potassium hydrogen phthalate single crystal for photonic device applications”, Optik, 2019, vol. 203, pp. 163903. https://doi.org/10.1016/j.ijleo.2019.163903.

[276] M. I. Baig, M. Anis, M. D. Shirsat, A. M. Alshehri, H. H. Somaily, S. S. Hussaini, “Influence impact of Zn^{2+} on laser-induced optical and electrical traits of KH_2PO_4 crystal for NLO device applications”, Optik, 2021,vol. 227, pp.165998. https://doi.org/10.1016/j.ijleo.2020.165998.

[277] S. S. Zulkefly, H. M. Kamari, M. N. A. Azis, W. M. D. W. Yusoff, “Influence of erbium doping on dielectric properties of zinc borotellurite glass system”, Mater. Sci. Forum., 2015, vol. 846, pp. 161-171. http://doi.org/10.4028/www.scientific.net/MSF.846.161.

[278] M. P. F. Graca, H. Fawzy, Y. Badr, M. M. Elokr, C. Nico, R. Soares, L. C. Costa, M. A. Valente, “Electrical, dielectric and structural properties of boro-vanadate glass systems doped with samarium oxide”, Phys. Status Solidi C, 2011, vol. 8, pp. 3107-3110. http://doi.org/10.1002/pssc.201000762.

[279] H. M. Li, C. H. Ra, G. Zhang, W. J. Yoo, “Frequency and temperature dependence of the dielectric properties of a PCB substrate for advanced packaging applications”, J. Korean Phys. Soc., 2009, vol. 54, pp. 1096-1099.

[280] A. Bergh, G. Craford, A. Duggal. R. Haitz, “The promise and challenge of solid-state lighting”, Phys. Today, 2001, vol. 54, pp. 42-47. http://doi.org/101063/11445547.

[281] J. M. Park, H. J. Kim, S. Kim, P. Limsuwan, J. Kaewkhao, “Luminescence property of rare-earth doped bismuth-borate glasses”, Procedia Eng., 2012, vol. 32, pp. 855-861. http://doi.org/101016/jproeng201202023.

[282] J. Sun, X. Zhang, Z. Xia, H. Du, “Luminescent properties of $LiBaPO_4$:RE (RE = Eu^{2+}, Tb^{3+}, Sm^{3+}) phosphors for white light-emitting diodes”, J. Appl. Phys., 2012, vol. 111, pp. 1-7. http://doi.org/101063/13673331.

[283] J. S. Kim, P. E. Jeonny, J. C. Choi, H. L. Park, S. I. Mho, G. C. Kim, “Warm-white-light emitting diode utilizing a single-phase full-color $Ba_3MgSi_2O_8$:Eu^{2+}, Mn^{2+}, phosphor”, Appl. Phys. Lett., 2004, vol. 84, pp. 2931–2933. http://doi.org/101063/11695441.

[284] P. Suthanthirakumar, C. Basavapoornima, K. Marimuthu, “Effect of Pr^{3+} ions

concentration on the spectroscopic properties of Zinc telluro-fluoroborate glasses for laser and optical fiber applications", J. Lumin., 2017, vol. 187, pp. 392-402. http://doi.org/101016/jjlumin201703052.

[285] Y. Al-Hadeethi, M. I. Sayyed, S. A. Tijania, "Gamma radiation attenuation properties of tellurite glasses: A comparative study", Nucl. Eng. Technol. 2019, vol. 51, pp. 2005-2012. https://doi.org/101016/jnet201906014.

[286] L. D. A. Florencio, L. A. G. Malagón, B. C. Lima, A. S. L. Gomes, J. A. M. Garcia, L. R. P. Kassab, "Efficiency enhancement in solar cells using photon down-conversion in Tb/Yb-doped tellurite glass", Sol. Energy Mater. Sol. Cells, 2016, vol. 157, pp. 468-475. https://doi.org/10.1016/j.solmat.2016.07.024.

[287] M. R. Henderson, B. C. Gibson, H. E. Heidepriem, K. Kuan, V. S. Afshar, J. O. Orwa, I. Aharonovich, S. Tomljenovic-Hanic, A. D. Greentree, S. Prawer, T.M. Monro, "Diamond in tellurite glass: a new medium for quantum information", Adv. Mater., 2011, vol. 23, pp. 2806-2810. https://doi.org/101002/adma201100151.

[288] F. Zhang, Z. Bi, A. Huang, Z. Xiao, "Luminescence and Judd-Ofelt analysis of the Pr^{3+} doped fluorotellurite glass", J. Lumin., 2015, vol. 160, pp. 85-89. https://doi.org/10.1016/j.jlumin.2014.11.047.

[289] V. K. Rai, D. K. Rai, S. B. Rai, "Pr^{3+} doped lithium tellurite glass as a temperature sensor", Sens. Actuator A, 2006, vol. 128, pp. 14-17. https://doi.org/10.1016/j.sna.2005.12.030.

[290] Z. A. S. Mahraz, M. R. Sahar, S. K. Ghoshal. "Band gap and polarizability of boro-tellurite glass: Influence of erbium ions", J. Mol. Struct., 2014, vol. 1072, pp. 238-241. https://doi.org/10.1016/j.molstruc.2014.05.017.

[291] M. Shaalan, G. El-Damrawi, A. Hassan, M. H. Misbah, "Structural role of Nd_2O_3 as a dopant material in modified borate glasses and glass ceramics", J. Mater. Sci: Mater. Electron, 2021, vol. 32, pp. 12348-12357. https://doi.org/101007/s10854-021-05866-x.

[292] J. D. C. Gallerande, D. Taniguchi, M. Colas, P. Thomas, T. Hayakawa, "Influence of Nd^{3+} modifying on $80TeO_2$– xZnO–(20−x)Na_2O ternary glass system", A.P.L. Mater., 2021, vol. 9, pp. 1-17. https://doi.org/10.1063/5.0061880.

[293] J. D. C. Gallerande, D. Taniguchi, M. Colas, P. Thomas, T. Hayakawa, "High-temperature investigation of TeO_2–Na_2O–ZnO glasses", Phys. Status Solidi B, 2022, vol. 259, pp. 1-7. https://doi.org/10.1002/pssb.202200065.

[294] T. Bezrodna, G. Puchkovska, V. Shymanovska, J. Baran, H. Ratajczak, "IR-analysis of H-bonded H_2O on the pure TiO_2 surface", J. Mol. Struct., 2004, vol. 700, pp. 175–181. https://doi.org/10.1016/j.molstruc.2003.12.057.

[295] K. A. Bashar, G. Lakshminarayana, S. O. Baki, A. B. F. A. Mohammed, U. Caldino, A. N. M. Rocha, V. Singh, I. V. Kityk, M. A. Mahdi, "Tunable white-light emission from Pr^{3+}/Dy^{3+} co-doped B_2O_3-TeO_2–PbO-ZnO-Li_2O-Na_2O glasses", Opt. Mater., 2019, vol. 88, pp. 558-569. https://doi.org/10.1016/j.optmat.2018.12.028.

[296] B. Haritha, V. R. Prasad, S. Damodaraiah, Y. C. Ratnakaram, "Spectroscopic properties of Pr^{3+} ions embedded in different multi-component phosphate glasses", Am. J. Eng. Res., 2017, vol. 6, pp. 315-322.

[297] S. Bodył, M. Czaja, Z. Mazurak, "Optical properties of Pr^{3+}, Sm^{3+} and Er^{3+} ions in apatite, fluorite and phosphate glasses", Phys. Procedia, 2009, vol. 2, pp. 515-525. https://doi.org/10.1016/j.phpro.2009.07.037.

[298] L. Vijayalakshmi, V. Naresh, B. H. Rudramadevi, S. Buddhudu, "Emission analysis of Pr^{3+} & Dy^{3+} ions doped Li_2O-LiF-B_2O_3-ZnO glasses", Int. J. Eng. Sci., 2014, vol. 4, pp. 19-25.

[299] K. Annapurna, R. Chakrabarti, S. Buddhudu, "Absorption and emission spectral analysis of Pr^{3+}: Tellurite glasses", J. Mater. Sci., 2007, vol. 42, pp. 6755-6761.

[300] S. B. Kolavekar, N. H. Ayachit, R. V. Anavekar, "Characterization and optical properties of Pr_2O_3-doped molybdenum lead-borate glasses", Bull. Mater. Sci., 2017, vol. 40, pp. 523-526. https://doi.org/10.1007/s12034-017-1400-6.

[301] C. R. Kesavulu, R. P. S. Chakradhar, C. K. Jayasankar, J. L. Rao, "EPR, optical. Photoluminescence studies of Cr^{3+} ions in Li_2O-Cs_2O-B_2O_3 glasses-an evidence of mixed alkali effect", J. Mol. Struct., 2010, vol. 975, pp. 93-99. https://doi.org/10.1016/j.molstruc.2010.03.091.

[302] Z. A. S. Mahraz, M. R. Sahar, S. K. Ghoshal. M. R. Dousti, "Concentration dependent luminescence quenching of Er^{3+}-doped zinc boro-tellurite glass", J. Lumin., 2013, vol. 144, pp. 139-145. https://doi.org/10.1016/j.jlumin.2013.06.050.

[303] V. Dimitrov, S. Sakka, "Electronic oxide polarizability and optical basicity of simple oxides", J. Appl. Phys., 1996, vol. 79, pp. 1736-1740. https://doi.org/10.1063/1.360962.

[304] H. R. Shaari, M. N. Azlan, Y. Azlina, S. N. Hajer, S. S. Nazrin, S. A. Umar, B. K. Kenzhaliyev, I. Boukhris, N. M. A. Hada, "Investigation of structural and optical properties of graphene oxide coated neodymium nanoparticles doped zinc-tellurite glass for glass fiber", J. Inorg. Organomet Polym. Mater., 2021, vol. 31, pp. 4349-4359.

https://doi.org/10.1007/s10904-021-02061-7.

[305] S. B. Kolavekar, N. H. Ayachit, "Impact of Pr_2O_3 on the physical and optical properties of multi-component borate glasses", Mater. Chem. Phys., 2021, vol. 257, pp. 1-10. https://doi.org/10.1016/j.matchemphys.2020.123796.

[306] K. Maheshvaran, S. Arunkumar, K. V. Krishnaiah, K. Marimuthu, "Investigations on luminescence behavior of Er^{3+}/Yb^{3+} co-doped boro-tellurite glasses", J. Mol. Struct., 2015, vol. 1079, pp. 130-138. https://doi.org/10.1016/j.molstruc.2014.09.038.

[307] M. V. V. Kumar, K. R. Gopal. R. R. Reddy, G. V. L. Reddy, N. S. Hussain, B. C. Jamalaiah, "Application of modified Judd-Ofelt theory and the evaluation of radiative properties of Pr^{3+}-doped lead telluroborate glasses for laser applications", J. Non-Cryst. Solids, 2013, vol. 364, pp. 20-27. https://doi.org/10.1016/j.jnoncrysol.2012.11.049.

[308] M. A. Marzouk, I. M. Elkashef, A. M. Fayad, H. A. Elbatal. "Photoluminescence, optical and structural properties of Pr^{3+}-doped fluorophosphate glasses and their induced defects by gamma irradiation", J. Mater. Sci.: Mater. Electron., 2018, vol. 29, pp. 10561-10572. https://doi.org/10.1007/s10854-018-9120-2.

[309] S. Kaewjaeng, W. Boonpa, F. Khrongchaiyaphum, S. Kothan, H. J. Kim, N. Intachai, R. Rajaramakrishna, S. Kiatwattanacharoen, J. Kaewkhao, "Influence of trivalent praseodymium ion on SiO_2–B_2O_3–Al_2O_3–BaO–CaO–Sb_2O_3–Na_2O–Pr_2O_3 glasses for X-Rays shielding and luminescence materials", Radiat. Phys. Chem., 2021, vol. 184, pp. 1-5.

[310] B. Zhou, V. Tao, Y. H. Tsang, W. Jin, E. Y. B. Pun, "Super broadband near-IR photoluminescence from Pr^{3+}-doped fluorite tellurite glasses", J. Opt. Soc. Am., 2012, vol. 20, pp. 3803-3813. https://doi.org/10.1364/OE.20.003803.

[311] D. Rajesh, M. R. Dousti, R. J. Amjad, A. S. S. D. Camargo, "Quantum cutting and up-conversion investigations in Pr^{3+}/Yb^{3+} co-doped oxyfluoro-tellurite glasses", J. Non-Cryst. Solids, 2016, vol. 450, pp. 149-155. https://doi.org/10.1016/j.jnoncrysol.2016.08.009.

[312] L. J. B. Gonzalez, G. Galleani, D. Manzani, L. A. O. Nunes, S. J. L. Ribeiro, "Visible to infrared energy conversion in Pr^{3+}-Yb^{3+}co-doped fluoroindate glasses", Opt. Mater, 2013, vol. 35, pp. 2085-2089. https://doi.org/10.1016/j.optmat.2013.05.024.

[313] L. Żur, J. Janek, M. Sołtys, J. Pisarska, W. A. Pisarski, J. Ballato, "Effect of BaF_2 content on luminescence of rare-earth ions in borate and germanate glasses", J. Am. Ceram. Soc., 2016, vol. 99, pp. 2009-2016. https://doi.org/10.1111/jace.14223.

[314] T. Wei, W. Bo, C. Yan, C. Yeqing, L. Jun, Z. Qingguang, "Single Pr $^{3+}$-activated high-color-stability fluoride white-light phosphor for white-light-emitting diodes", Opt. Mater Express, 2019, vol. 9, pp. 223-233.https://doi.org/10.1364/OME.9.000223.

[315] G. A. Khater, B. S. Nabawy, J. Kang, M. A. Mahmoud, "Dielectric properties of basaltic glass and glass-ceramics: modeling and applications as insulators and semiconductors", Silicon, 2019, vol. 11, pp. 579-592. https://doi.org/10.1007/s12633-018-9963-4.

[316] D. A. Vasumathy, P. Murugasen, S. Sagadevan, "Preparation and characterization of the structural, optical, spectroscopic, and electrical properties of Pr_2O_5 doped borate glass", Mater. Res., 2016, vol. 19, pp. 923-927. http://dx.doi.org/10.1590/1980-5373-MR-2016-0014.

[317] A. Malge, T. Sankarappa, G. B. Devidas, J. S. Ashwajeet, A. Devidas, M. Heerasingh, "Dielectric and relaxation studies in multioxides doped borotellurite glasses", IOP Conf Ser: Mater. Sci. Eng., 2022, vol. 1221, pp. 012015-1-012015-6. https://doi.org/10.1088/1757-899X/1221/1/012015.

[318] J. N. Mirdda, S. Mukhopadhyay, K. R. Sahu, M. N. Goswami, "Optical and electrical properties of Nd^{3+} doped Na_2O-ZnO-TeO_2 material", Biointerface Res. Appl. Chem., 2022, vol. 12, pp. 7927- 7941. https://doi.org/10.48550/arXiv.2106.04545.

[319] J. N. Mirdda, S. Mukhopadhyay, K. R. Sahu, M. N. Goswami, "Enhancement of optical properties and dielectric nature of Sm^{3+} doped Na_2O–ZnO–TeO_2 glass materials", J. Phys. Chem. Solids, 2022, vol. 167, pp. 110776-1-9. https://doi.org/10.1016/j.jpcs.2022.110776.

[320] J. S. Ashwajeet, T. Sankarappa, "Dielectric and AC conductivity studies in Li_2O-CoO-B_2O_3-TeO_2 glasses", Ionics, 2017, vol. 23, pp. 627-636. https://doi.org/10.1007/s11581-016-1819-6.